Electrodeposition of nanostructured SnO2 films for DNA label-free electrochemical detection

Hai Le Minh

UNIVERSITÉ DE GRENOBLE

THÈSE

Pour obtenir le grade de

DOCTEUR DE L'UNIVERSITÉ DE GRENOBLE

Spécialité : **Matériaux, Mécanique, Génie Civil, Electrochimie**
Arrêté ministériel : 7 août 2006

Et de

DOCTEUR DE L'INSTITUT POLYTECHNIQUE DE HANOI

Spécialité : **Science et Technologie des Matériaux**

Présentée par

Minh Hai LE

Thèse dirigée par **Valérie Stambouli** et
codirigée par **Anh Tuan MAI**

préparée au sein du **Laboratoire des Matériaux et du Génie Physique**
dans **l'École Doctorale:** Ingénierie – Matériaux, Mécanique, Environnement, Energétique, Procédés, Production
et de **l'Institut International de Formation de Science en Matériaux**

Electrodéposition de films de SnO_2 nanostructurés pour la détection électrochimique sans marquage d'ADN

Thèse soutenue publiquement le **19 Décembre 2013**,
devant le jury composé de:

M. Eric CHAINET
Directeur de Recherche CNRS, LEPMI, Président
Mme. Catherine DEBIEMME-CHOUVY
Chargée de Recherche CNRS, LISE, Rapporteur
M. Mathieu LAZERGES
Maître de conférences, Université Paris Descartes, Rapporteur
Mme. Eliane SOUTEYRAND
Directrice de Recherche CNRS, INL, Examinateur
Mme. Nicole JAFFREZIC-RENAULT
Directrice de Recherche CNRS, ISA, Examinateur
M. Abdelkader ZEBDA
Chargé de Recherche INSERM, TIMC-IMAG, Invité
M. Anh Tuan MAI
Maître de conférences, IPH-Vietnam, Co-encadrant
Mme. Valérie STAMBOULI
Chargée de Recherche CNRS, LMGP, Directrice de thèse

Electrodeposition of nanostructured SnO_2 films for DNA label-free electrochemical detection

This thesis is dedicated to the memory of my beloved grandfather,
Pham Ngoc Bich

ACKNOWLEDGEMENTS

I would like to express my deepest gratitude to my main supervisor, Dr. Valerie Stambouli, for her excellent guidance, caring, providing me with an excellent atmosphere for doing research and patiently correcting my writing. I have been extremely lucky to have a supervisor who cared so much about my work. I am also grateful to my co-supervisors, Dr. Anh Tuan Mai, from - Hanoi University of Science and Technology, for his support and advice in my studies.

I would like to thank Dr. Catherine Debiemme-Chouvy and Dr. Mathieu Lazerges for the honor they gave me by accepting to evaluate my work, and Dr. Eliane Souteyrand, Dr. Nicole Jaffrezic-Renault, Dr. Eric Chainet and Dr. Abdelkader Zebda for accepting to participate in the thesis committee.

I would like to express my deep gratitude and respect to Dr. Eric Chainet. The electrodeposition experiment would not be fully finished without his very kind and enthusiastic help. Also, I would like to thank Dr. Carmen Jimenez and Joseph La-Manna for their help for developing the experimental system. This work would not be possible without our excellent microscopy and diffraction engineers Béatrice Doisneau, Laetitia Rapenne, Odette Chaix, Isabelle Paintrand, Patrick Chaudouet and Hervé Roussel. Many thanks to Raphael Guillot and Fabien Dalonneau for their willing helps in particular issues related to my biology experiment.

I would like to thank Dr. Catherine Picart, Dr. Didier Delabouglise, Dr. Franz Bruckert, Dr. Marianne Weidenhaupt and Dr. Thomas Boudou for their fruitful scientific discussions and advice.

I thank Virginie Charrière, Josiane Viboud, Anne Fracchia, Nicole Douard, Michele San Martin and Augustine Allesio for their administrative assistance.

My greatest appreciation and friendship goes to Louis Fradetal, who always willing helps me with everything. Members of IMBM team also deserve my sincerest thanks for their friendship and assistances. I met some very nice people who made my lab life enjoyable at LMGP, among them Varvara Gribova, Pauline Serre, Sophie Guillemin, Claire Monge, Claire Holzinger, Flora Gilde, Sofia Caridade, Lijie He, Xiqiu Liu, Martin Seisse, Daniel Langley, Naresh Saha.

I express my gratitude to all my Vietnamese friends in Grenoble, who made me home away from home. These acknowledgments would not be complete without thanking my family: ba Phong, me Yen and Hoang beo, for their constant support and care. I would like to mention two other people who are very important in my life: my wife, Thanh Huong and my little son, Minh Nguyen. I thank my wife for everything. I thank my little son for making me so happy with his cute smile.

TABLE OF CONTENTS

ABSTRACT

For environmental *in situ* diagnostic, as well as for medical point of care diagnostic, quick and affordable sensing devices are of importance. Label-free biosensors based on electrical or electrochemical detection methods can provide such features. In previous studies, we have demonstrated for the first time the feasibility of using semiconductive SnO_2 2D dense films for non-faradic electrochemical impedance DNA detection. The aim of the present study is (i) to improve the sensing performances by using SnO_2 nanostructures in order to benefit from high specific surface, and (ii) to study the influence of the morphology and microstructure on the impedimetric DNA detection signal.

We performed the cathodic electrodeposition of SnO_2 nanostructures. By changing relevant processing parameters, two kinds of nanostructures were deposited: **3D nanoporous films** and **1D nanowires**. Both nanostructures have been characterized in terms of morphology, microstructure and electrochemical properties.

Our results emphasize the importance of both the microstructural and morphological organizations on the impedimetric signal upon DNA hybridization. Opposite tendencies are found. DNA hybridization induces a decrease of the impedance in the case of 3D-nanoporous films, whereas an increase of impedance is obtained in the case of 1D NWs. Indeed, following the dimensionality of the nanostructures, either external cause - ion transport - or internal cause - field effect phenomenon - can contribute to the impedance variation.

The performances of the sensors have also been analyzed, namely: sensitivity, selectivity and reusability. Compared to the 2D dense and 3D nanoporous films, the 1D SnO_2 nanowires are more favorable in term of sensitivity, showing a detection limit of 2 nM.

Key words: SnO_2, nanostructure, electrodeposition, DNA biosensor, impedance spectroscopy.

INTRODUCTION

For environmental *in situ* diagnostic, as well as for medical point of care diagnostic, quick and affordable sensing devices are of importance. Label-free biosensors based on electrical or electrochemical detection methods can provide such features. However their development is still challenging mainly due to low reproducibility, limited detection sensitivity, weak robustness and stability.

A label-free biosensor is a sensor where the detection of the biological element is directly linked to a variation of a specific physical parameter of the sensitive element (transducer). More specifically, in the case of non-faradic electrochemical impedance spectroscopy (EIS) for DNA hybridization detection, the response is based on the impedance change of the sensor transduction element. The latter is generally a semiconductive material. The presence of charged molecules such as DNA strands on its surface induces the creation of a subsurface space charge layer, via the field effect phenomenon (FET). The space charge layer is characterized by band bending introduced into the flat-band potential near the surface of the semiconductor. As a result, the impedance of the interface electrolyte/DNA/semiconductor is modified depending on the n or p type doping of the semiconductor.

In previous studies carried out by our group, A. Zebda demonstrated, during his thesis [1] for the first time, the feasibility of the use of semiconductive metallic oxide film electrodes as sensitive elements for DNA detection based on non-faradic electrochemical impedance spectroscopy. These films were $CdIn_2O_4$, pure or doped SnO_2. They were deposited by the aerosol pyrolysis technique and they exhibited 2D dense polycrystalline film surfaces.

The results have shown that although $CdIn_2O_4$ is much more sensitive than SnO_2, this metallic oxide presents many drawbacks. It is affected and chemically weakened by the functionalization steps, which is not the case of SnO_2. Indeed, SnO_2 is well known for its chemical inertness. Moreover SnO_2 deposition is easier than $CdIn_20_4$ and does not involve toxic compounds such as Cd, or scarce and expensive compounds such as In. For these reasons, it is of interest to develop SnO_2 based DNA biosensors.

In this context, the aim of the present study is twofold:

(i) to improve the performances of SnO_2 based DNA sensors through the use of controlled SnO_2 nanostructured surfaces, namely 1D nanowires or 3D nanoporous matrix in order to develop the specific surface to volume ratio compared to a 2D surface electrode,

(ii) by the same method, to study how the morphology and microstructure variations of the SnO_2 electrode can influence the DNA impedance signal.

To fabricate the SnO_2 nanostructures, the chosen strategy is based on the electrodeposition method which is a simple and low cost technique. During the first months of the thesis, this technique was set up and optimized to obtain reproducible films. The desired morphology, 1D nanowires or 3D nanoporous matrix, was obtained by modifying relevant deposition parameters. The characteristics of the obtained nanostructures - microstructure, morphology, chemistry and electrochemical properties - have been thoroughly investigated using XRD, SEM, TEM, XPS and EIS.

Then, a multi-step functionnalization process using a silanization method, either in liquid or in vapor phase, has been tested in order to covalently graft the single strand (ss) DNA probes on the different nanostructured surfaces.

Finally the DNA detection has been thouroughly investigated using EIS on both 3D and 1D nanostructures. In parallel, the detection was also performed using fluorescence microscopy, in either epifluorecence mode or confocal mode, to validate and to locate DNA hybridization on the SnO_2 nanostructures.

Finally, the performances of the sensors were also analyzed, namely: sensitivity, selectivity and reusability.

This thesis is divided into four main parts:

The first chapter presents a literature review of non-faradic electrochemical impedance DNA biosensors. Their characteristics and related sensing electrode materials are reported via a listing of the different kinds of semiconductor materials such as Si or metallic oxides. A review on the different techniques available to deposit SnO_2 nanostructures closes this chapter.

The second chapter is dedicated to the description of the experimental fabrication of the SnO_2 based DNA sensors. It includes the electrodeposition process and the different characterization techniques to analyze the SnO_2 nanostructures, as well as the impedance technique. Then the process for DNA grafting via silanization and its hybridization is presented.

In the two following chapters (chapters 3 and 4), we detail the results corresponding to the two different SnO_2 nanostructure morphologies: 3D (chapter 3) and 1D (chapter 4). For each chapter, the presentation is similar. First, we detail the properties of the obtained SnO_2 nanostructures as a function of the electrodeposition parameters. Then, we present their performances in terms of impedance and fluorescence response signals upon DNA hybridization.

The end of chapter 4 presents several comparisons and a discussion regarding the different impedance behaviors upon DNA hybridization obtained with the different SnO_2 nanostructures.

CHAPTER I: State of the art: Non-faradic electrochemical impedance DNA biosensors and sensitive materials

1.1 Label-free impedance DNA biosensors

1.1.1 What is a DNA biosensor?

The origin of the field of biosensor technology was initiated in 1956 when Professor Leland C Clark, known as the father of biosensor concept, published an experiment [1] in which glucose oxidase (GOX) was entrapped in a Clark oxygen electrode using dialysis membrane [2]. Consequently, the term "biosensor" began to spread in scientific literature in 1977 when Rechnitz et al. [3] immobilized living microorganisms at the surface of an ammonia gas sensing electrode to construct a selective electrode for the amino acid arginine, which they called a "bio-selective sensor". Later, bio-selective sensor was shortened to "biosensor" and has remained for the combination between a material of biological origin and a physical transducer.

According to the International Union of Pure and Applied Chemistry (IUPAC) in 1996 [4], a biosensor is a self-contained integrated receptor-transducer device, which is capable of providing selective quantitative or semi-quantitative analytical information. Basically, a biosensor consists of a biological recognition element, so-called bioreceptor, connected in series with a physico-chemical transduction element, a transducer, which converts the biological recognition event into a usable output signal [5].

Figure 1.1 schematically represents a biosensor. The bioreceptor recognizes the target analyte and translates the information into a chemical or physical output signal with a defined sensitivity. The transducer then converts the signal from the output domain of the recognition system, mostly to an electrical signal which is proportional to the concentration of the analyte. The amplified signal is then processed by signal processor where it can be stored, displayed and analyzed [6].

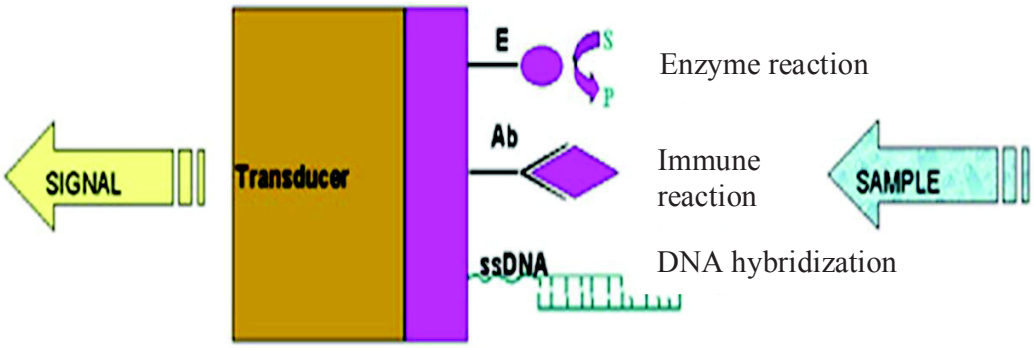

Figure 1.1: Schematic diagram of a biosensor device.

On the basis of the bio-recognition element, biosensors can be divided into different major categories as shown in **Table 1.1**. The bio-recognition elements (or bioreceptor) consist of a biological material or a biologically derived material: a tissue, a microorganism, enzymes, antibodies, nucleic acids, etc. These bioreceptors are responsible for binding the analyte of interest to the sensor for the measurement.

Table 1.1 Classification of biosensors according to bio-recognition element.

Name of Biosensor	**Types of Biological Recognition**
Enzyme sensor	Enzymes Proteins
Immunosensor	Antibody/antigen
DNA sensor	***Nucleic acids (DNA/RNA)***
Microbial sensor	Microbial cells Plant and animal tissues

DNA biosensors are defined as a subgroup of the broad biosensor field. Their principle relies on the hybridization of deoxyribonucleic acid (DNA). The DNA structure, represented in **Figure 1.2**, is a double helix configuration of two complementary polynucleotide strands.

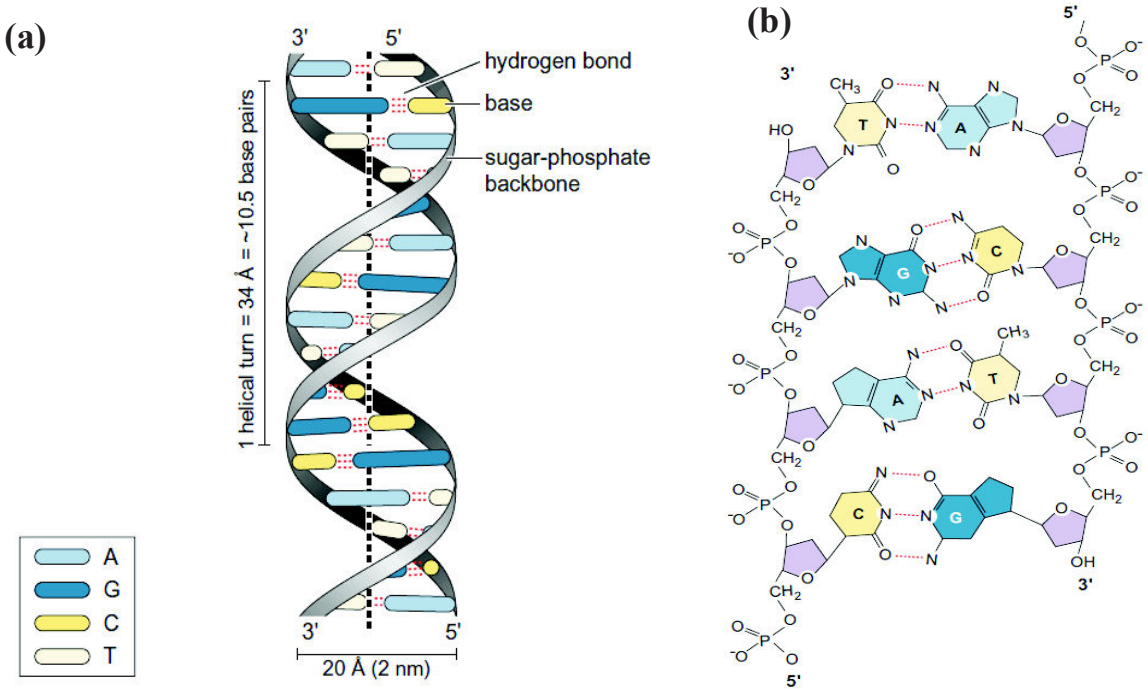

Figure 1.2: The helical structure of DNA. (a) Schematic model and (b) Detailed structure showing base pairings and the phosphodiester linkages of the backbone.

The sugar-phosphate backbone forms the structural framework DNA and RNA. This backbone is composed of alternating sugar and negatively charged phosphate groups, and defines directionality of the molecule. Each strand is constituted of a polymeric chain that contains bases: Adenine, Thymine, Cytosine and Guanine. These bases are complementary by two through two hydrogen bonds in the Adenine-Thymine (A-T) base pair and three in the Guanine-Cytosine (G-C) base pair. This base-pairing interaction forms the basis for the specificity of bio-recognition in DNA biosensor [2]. In other words, it provides the ability of one single strand to recognize its complementary strand to form a duplex (hybridization process).

In a typical configuration as presented in **Figure 1.3**, a well-defined single-stranded probe sequence is immobilized onto a solid platform within recognition layer. Then, a DNA target sequence is added from an unknown sample. If the DNA target is complementary with the probe DNA, base-pairing interaction recruits the DNA target to the surface, detection and identification are performed [7].

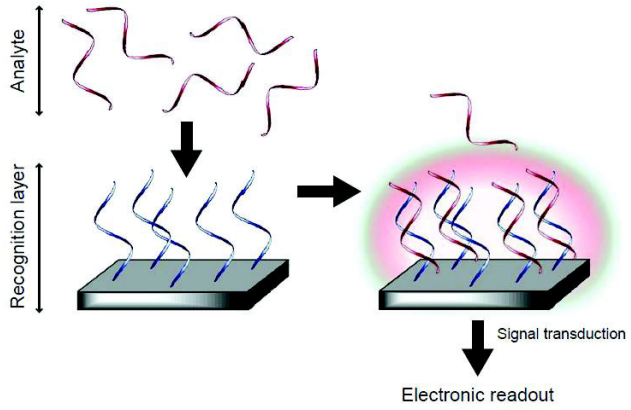

Figure 1.3: Typical configuration of a DNA biosensor [7].

Because of the difficulty in detecting biological analyses directly through their intrinsic physical properties (mass, size, electrical, etc), biological research has relied upon attachment of various labels to the molecules being studied.

The common labels used in molecular biology studies to analyze DNA hybridization involve fluorescent dyes, redox active enzymes magnetic particles or different kinds of nanoparticles [8]. For example, the DNA target sequence is labeled with a proper fluorescent tag. With the aid of a fluorescence microscope, fluorescence is observed at place where complementary hybridization takes place. Although the technique is highly sensitive, fluorescence markers are photochemically unstable and they require extra time, expense, sample handling. Additionally, labels might, in some cases, interfere with the detection, the base-pairing interaction, thus resulting in false-positives [9].

The challenge is to develop simple, reliable and economical methods. Label-free strategies have emerged as potential methods for detecting DNA hybridization with lower cost and at high sensitivity.

Label-free biosensors, by definition, do not require the use of reporter elements to facilitate measurements [6]. Unlike label methods that simply confirm the presence or absence of a molecule to be detected, label-free techniques can provide direct information on target molecules in the form of changes in a physical bulk property of a sample. Basically, label-free DNA sensors rely on the modification of a given physical parameter of the supporting material (transducer), which is induced by DNA hybridization.

The choice of suitable substrate/platform to immobilize the DNA is a fundamental part since the immobilized single stranded ss-DNA has to be stable and efficiently attached to the surface to facilitate the hybridization event.

1.1.2 DNA immobilization on electrodes

The ability to immobilize the DNA probes on an electrode while maintaining their affinity for complementary DNA targets is a crucial aspect of DNA biosensor development. Consequently, the immobilization of DNA probes on the electrode surface needs to be well controlled for the achievement of high sensitive and selective DNA biosensors. It is necessary to ensure that the functionalized-DNA-probe-surface is highly reactive and stable without non-specific bonding. DNA probes can be immobilized on solid electrode using several methods: adsorption, film entrapment, affinity binding and covalent attachment. The appropriate immobilization is strictly dependent on the characteristics of the electrode. Each of the different immobilization strategies can lead to the proper orientation of DNA probes, allowing to control the probe conformational freedom, making them accessible for interaction with DNA target.

Physisorption: DNA immobilization by physical adsorption is the simplest method. This technique is based on ionic interaction between the negatively charged groups present on DNA probes and positive charges covering the surface [10-11]. This method has been widely used on carbon electrodes such as glassy carbon [12] or carbon paste electrodes [13], and to a lesser extent, on Au [14] and ITO [15] electrodes. In some cases [16-18], the adsorption of the DNA probes on the electrode surfaces is carried out under positive potential which favors the adsorption of the polyanions through the phosphate skeleton.

Film entrapment: Direct DNA entrapment has been mostly employed onto polymers, dialysis membranes and cationic layers [11]. Based on polyanionic nature, DNA molecules are immobilized as dopant anions [19] or by electrostatic way on cationic electrode surface [20]. This

method is carried out by applying an appropriate potential to the working electrode immerging in solution containing DNA probes and an electropolymerizable monomer. However, the conformational mobility of the DNA is restricted leading to kinetic and barriers to hybridization.

Affinity binding: The strong interaction between avidin and biotin is the form of affinity binding which is the most often used for immobilization purposes. Biotinylated DNA molecules are immobilized by use of two approachs:

- Electrode / avidin / biotinylated DNA [21-22].
- Electrode / biotin / avidin / biotinylated DNA [23-24].

Variations of the first strategy rely on the way in which avidin is attached to the surface-physical adsorption onto Au [21] or C electrodes [25], cross-linking with glutaraldehyde or covalent binding onto a SAM on gold electrodes. Regarding to the second scheme, biotin-bearing mercapto [23] or pyrrole groups [24] have been synthesized onto gold electrodes by chemisorptions or electropolymerisation, respectively.

Covalent bonding (chemisorption): Among different techniques for DNA immobilization, covalent attachment is the most often used strategy with different methods on different supports.

Thiol-modified DNA probes are frequently immobilized onto gold electrode surface due to the strong affinity of the thiol groups for the Au metal surface, which formed the covalent bonds between the sulfur and gold atoms [10]. For example, Sun et al. [26] immobilized of ssDNA monolayer on the gold electrode surface with self-assembled aminoethanethiol monolayer for voltammetric detection of sequence-specific DNA. By the same way, DNA sequences also could be attached onto gold micropads [27] or gold ultra-microelectrode arrays [28].

Carbodiimide is often used as a regent for covalent reactions to form the bonding between the DNA probes and the functionalized groups of the surface such as amino, phosphonate, carboxylate [11]. For example, DNA probe molecules are immobilized to the carboxylated or aminated single walled carbon nanotube multilayer films using 1-Ethyl-3-(3-dimethylaminopropyl) carbodiimide (EDC) [29]. DNA probes are also covalently attached on conducting polymer electrode such as polythiophene [30], polypyrrole [31] and poly(aniline) [32] with the aid of EDC. For example, Peng et al. reported an acid functionalized polypyrrole, poly[pyrrole-co-4-(3-pyrrolyl) butanoic acid], where amino-functionalized DNA was covalently attached to the polypyrrole polymer film using EDC as catalyst [31].

Another way to graft DNA onto electrode surface is via self assembled monolayers (SAMs) with appropriate group. Functionalized surfaces are created by chemical treatment using silanization process with differently functionalized organosilanes. Silanization process has been successfully performed on Pt [33], carbon nanotubes [34] and silicon/silicon oxide [35] film surfaces.

Especially, 3-aminopropyltriethoxysilane (APTES) is commonly used for the modification of silica surfaces for biological implants or lab-on-a-chip applications [36-37]. Surface modification of metal oxide thin films with organosilanes is developed from the protocol of modifying silica surface as represented in **Figure 1.4**. Silanization of the oxide surface involves the coupling of the functionalized silane on the metal oxide at the hydroxylated sites. The metal oxide electrodes could be hydroxylated by immerging either in a NaOH solution [38-39] or in a piranha solution of 1/3 H_2O_2 and 2/3 H_2SO_4 [35], or by treating with oxygen plasma [40].

Self-assembly of organosilane molecules, with general formula $(X)_3$-Si-Y, where X is an alkoxy group (O-CH_3 or O-CH_2-CH_3) or halogen (-Cl) ligand, occurs via the reaction of the X groups with hydroxyl (-OH) groups at substrate surface to form Si-O-Si linkage [41]. The silanization reaction is performed in liquid phase with the use of hydrocarbon solvents such as ethanol, toluene, and benzene. Then, a cross linker glutaraldehyde ($HCO(CH_2)_3CHO$) is used to achieve a strong covalent bonding between the APTES and the DNA probes. This strong link between the DNA strands and the electrode is important in the context of electrochemical detection [42].

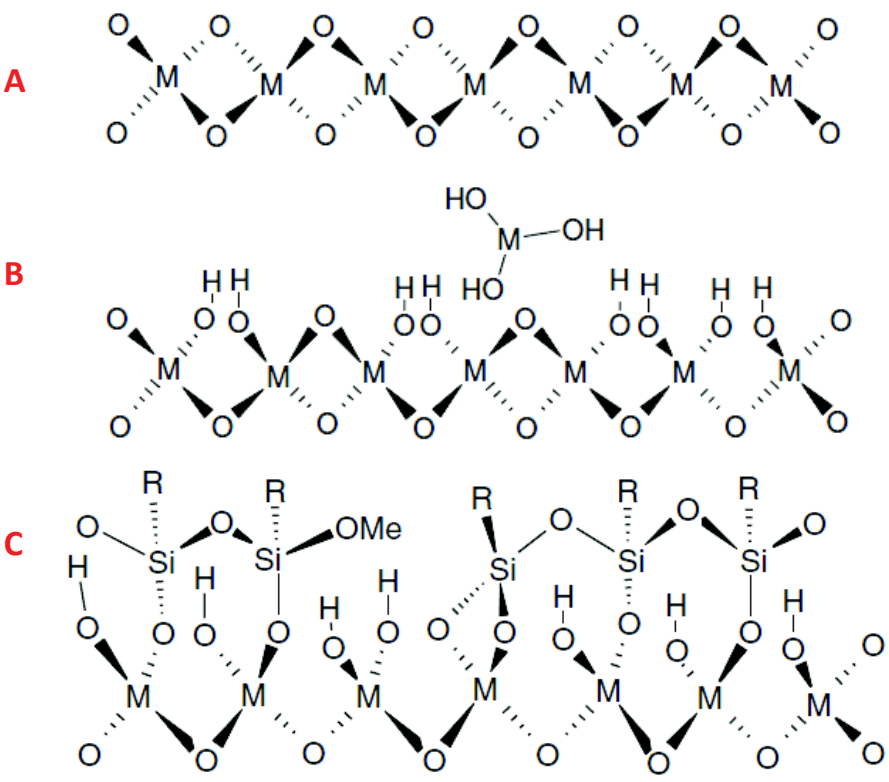

Figure 1.4: Schematic view of (a) an ideal metal oxide surface (b) an oxide surface undergoing hydrolysis to produce hydroxylated sites and (c) a cross-linking silane surface, with relatively few unreacted –OH groups left on the oxide surface [41].

1.1.3 Classification of label-free DNA sensors

Depending on the nature of transducers, label-free DNA sensors are divided into several approaches including optical, mass-based, electrochemical and electronic methods. Although all these types of transducers are constantly developed for use in biosensors, the electrochemical transduction is given importance in this thesis. Hence, electrochemical detection will be further discussed in detail in this review. Optical, mass based sensors are only briefly mentioned.

Label-free optical detection: This type of DNA sensor is based on the measurement of light absorbed or emitted as a consequence of DNA hybridization. Commonly used techniques are Surface Plasmon Resonance (SPR) and Surface Enhanced Raman Spectroscopy (SERS).

SPR biosensors, represented in **Figure 1.5**, investigate changes in refractive index caused by structural alterations in the vicinity of a thin film metal substrate [43]. SPR occurs when polarized light is directed from a layer of higher refractive index (RI) to a layer of lower RI (typically gold film). Incident light travels through the higher RI layer and is totally reflected back into the high RI layer when the angle of reflection is greater than or equal to the critical angle. When the light is incident on the prism side at a particular angle called the resonance angle, the intensity of the reflected light is at its minimum.

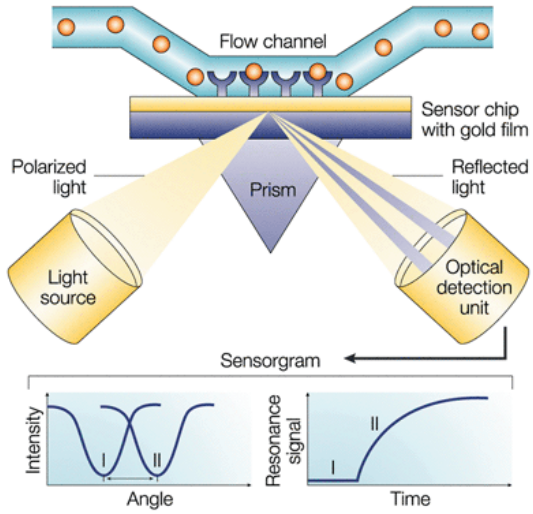

Figure 1.5: Typical set-up of a SPR biosensor

In the presence of the biomolecules on the gold surface, this angle variation is very sensitive. By measuring the shift of resonance angle in response to the biomolecular interactions, SPR biosensors can detect various binding reactions on a quantitative basis in real time [44-46]. As a label-free technique, this technique has been used frequently to develop biosensors, especially to detect DNA hybridization. To detect DNA hybridization, DNA probe is immobilized onto the gold surface either via a thiol linker [47] or using enzymatically digested DNA [48]. However, if short-

chain DNA molecules are involved, the resonance angle shifts are very small and SPR is not sensitive enough to monitor the binding events accurately [10]. Besides, due to its complex and costly system, SPR is generally more suitable for research application [6].

SERS is another label-free optical technique for the detection of DNA hybridization. To remind, SERS is a surface sensitive technique that results in the enhancement of Raman scattering of molecules adsorbed on rough metal surfaces or metal nanoparticles. The enhancement of the Raman scattering cross-section ($>10^6$) is believed to be due to a surface plasmon providing stronger electromagnetic coupling at the analyte site. SERS-active systems depends critically on (among other parameters) the geometry of the metal nanostructures. Different sensing platforms have been proposed including silver mirror substrate [49], roughened silver sheets [50], SiO_2/Si substrates coated with Ag° nanoparticles (NPs) [51] and Ag NPs distributed on TiO_2 thin film [52]. **Figure 1.6** shows the obtained Raman spectra of ssDNA and dsDNA grafted on an Ag^o/TiO_2 platform [52]. The comparison between ssDNA and ds DNA spectra indicates significant modifications in the relative intensities of Adenine (A) and Cytosine (C) lines located near 731 cm^{-1} and 784 cm^{-1}, respectively. Accordingly, the A:C intensity ratio appears to be about 2:1 in the case of ss DNA probes, while it is closer to 1:1 after DNA hybridization. SERS-based method of DNA detection is feasible, however, SERS spectra reproducibility is still challenging.

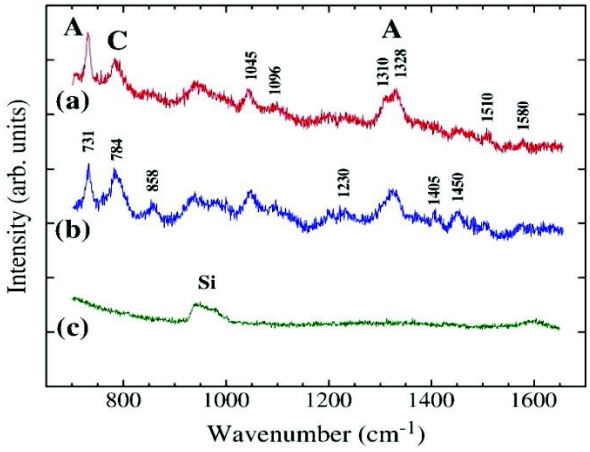

Figure 1.6: Raman spectra of single strand (a) and label-free double strand (b) DNA grafted on an Ag°/TiO_2 heterostructure. (c) Raman spectrum of the Ag°/TiO_2 heterostructure without DNA grafting where only the second order Si Raman spectrum is visible [52].

Label-free mass detection: Mass sensors are also capable of detecting label-free DNA hybridization. These DNA biosensors are based on small changes in mass due to the presence of DNA molecules. The main type of mass based biosensor is Quartz Crystal Microbalance (QCM). Basically, mass changes are measured by using QCM. The frequency of vibration varies according to the mass of single stranded DNA or double stranded DNA immobilized on the surface of QCM.

Therefore, when the mass increases due to hybridization process between probe and target DNA, the frequency of the crystal changes. This change is then analyzed to distinguish the double stranded from a single stranded DNA [53-55]. Although reliable and high sensitivity, QCM has been a technical challenge (specialized technician is often required).

Recently, microcantilever sensors, represented in **Figure 1.7**, have emerged as a promising tool for label-free detect biomolecular interactions. This technique is based on a response due to either stress variation or mass loading [10]. Hybridization of the DNA target to the immobilized DNA on the cantilever surface causes a change of the surface stress of the cantilever, which can be detected as changes in the cantilever deflection [56].

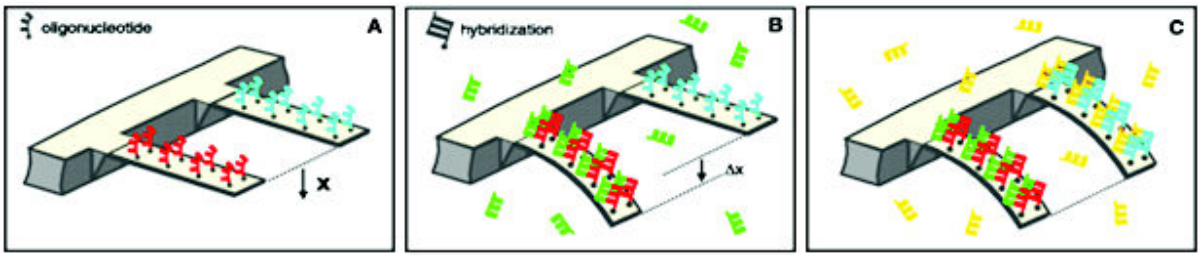

Figure 1.7: Microcantilever DNA sensor [56].

Label –free electrochemical detection: Electrochemistry has received much attention recently for the DNA hybridization detection. As a result, almost recent reviews dealing with DNA biosensors focus on electrochemical transduction [7-10, 57-60]. These systems offer several advantages over their optical or mass-based counterparts such as low cost, simple design and small dimension. The DNA probe sequences can be readily confined to variety of electrode substrates such as Au, conductive polymers, semi-conductive materials. Finally, the compatibility between electrochemical DNA sensors and micro-fabrication technologies make them excellent candidates for DNA diagnostics [7, 57-59].

Electrochemical DNA biosensors are based on the investigation of current or potential evolution due to interactions occurring at the sensor-sample matrix interface. The different methods are usually classified into two main categories: label or label-free approaches, depending on the nature of the electrochemical signal.

Label-based approaches are mainly based on the differences in the electrochemical behavior of labels with single-stranded DNA (ss-DNA) or double stranded DNA (ds-DNA) modified electrode. A label is an electroactive species which is used with the aim of enhancing the difference in the signal obtained between the probe immobilization and the hybridization with a complementary sequence. Different protocols (represented in **Figure 1.8**) have been recently employed for labeled-DNA detection by electrochemical techniques with the use of redox markers

[61], metal nanoparticles [62-63], redox active enzymes [64-65] and intercalators [66-67]. In this case, the response signal upon DNA hybridization is a current measured at a given potential depending on the involved redox species.

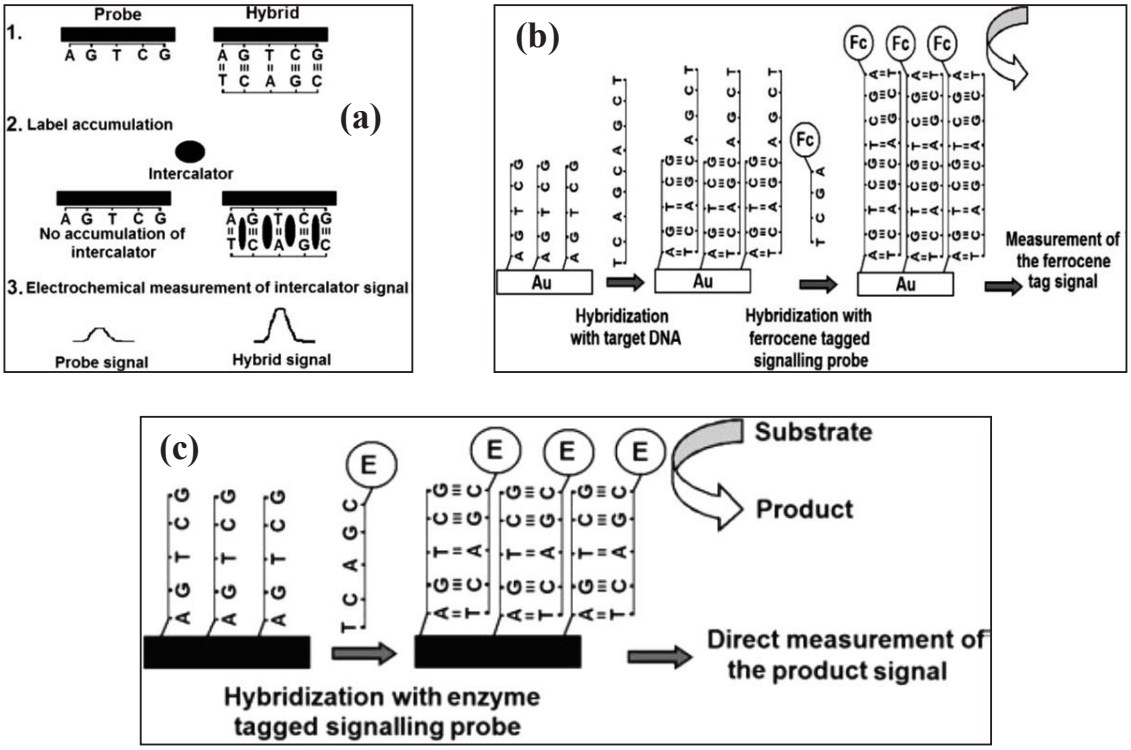

Figure 1.8: The basic schemes using labels for electrochemical DNA detection. (A) Intercalator. (B) Redox marker (Fc = ferrocene). (C) Enzyme [68].

On the other hand, in label-free methods the signal arises from the hybridization event by itself, without the need of any special electroactive species.

The label free detection is based on different strategies. A first approach can be based on the intrinsic electroactivity of the nucleotide residues present in DNA. Palecek [69] proved that DNA is an electroactive compound producing reduction and oxidation signals after hybridization. Signals of adenine, cytosine and guanine are observed on oscillopolarograms in the case of ssDNA but absent with dsDNA. Among the bases, Guanine is the most redox-active base in DNA and thus, the oxidation of guanine moieties can be exploited for sequence-specific DNA detection. However, if both DNA probes and targets contain Guanine residues, it is difficult to assign the oxidation signal to the probes or to the targets. The problem can be solved by substituting guanine by inosine which can also base-pair with cytosine in the probe DNA [70]. The detection limit was estimated at $1.25.10^{-8}$ M of DNA target.

The second strategy is based on some intrinsic properties of DNA, such as the negative charges from phosphate groups which are used for the direct detection of hybridization. As the consequence, DNA hybridization alters the dielectric properties of conductive surfaces. Thus, DNA hybridization events can be detected from a measured electrical signal. The Electrochemical Impedance Spectroscopy (EIS), an effective method for probing interfacial properties (capacitance, electron transfer resistance) of the modified electrode primarily used for affinity biosensors, is rapidly developing as a tool for studying DNA hybridization. Because EIS detection is the major technique to detect DNA hybridization in this thesis, it will be reviewed and discussed in more detail.

1.2 Impedimetric DNA biosensors

1.2.1 Theoritical background

Electrochemical Impedance Spectroscopy (EIS) is a characterization technique which measures both the resistive and capacitive properties of an electrode upon perturbation of the electrode/electrolyte interface by a small amplitude sinusoidal ac excitation signal [9].

Electrochemical impedance is measured by applying an AC potential to an electrochemical cell and by measuring the resulting current across the cell.

If the applied sinusoidal potential is $E_t = E_o \sin(\omega t)$ (**Figure 1.9a**), the resulting current is $I_t = I_o \sin(\omega t + \varphi)$, where, E_t and I_t is the potential and the current at time t; E_o and I_o is the amplitude, $\omega = 2\pi f$ is radial frequency, f is the frequency.

According to Ohm's law, the impedance of the system is:

$$Z(\omega) = \frac{E_t}{I_t} = \frac{E_o \sin \omega t}{I_o \sin(\omega t + \varphi)} = Z_o \frac{\sin \omega t}{\sin(\omega t + \varphi)} \qquad (1.1)$$

The impedance $Z(\omega)$ has magnitude Z_o and a phase shift φ. An impedimetric spectrum is obtained when a small AC excitation voltage is applied to the system within a frequency range, resulting in an AC current response for each frequency value. In impedance biosensor, excitation voltage is usually less than 10mV or less to avoid damaging the probe layer [9].

A common way to represent the impedance is vector model with the real and imaginary axes (**Figure 1.9b**). Herein, all the components related to the formation of insulating layer (double layer, barrier) that generate a phase shift (capacitance) contribute to the imaginary part of the impedance Z_i, while the ones that do not induce any phase shift (resistance) contribute to the real part Z_r [8].

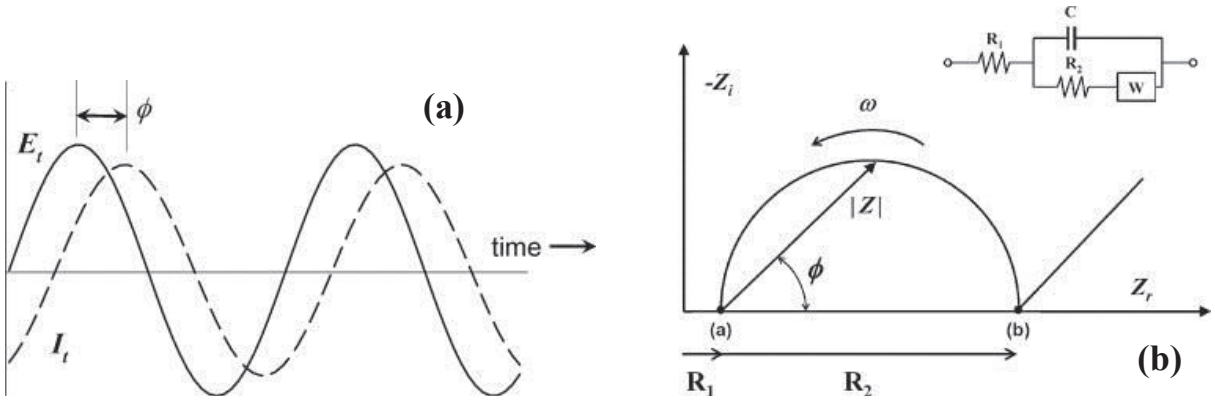

Figure 1.9: (a) AC excitation signal applied and sinusoidal current response at an electrical system; (b) a typical Nyquist diagram [8].

"Nyquist plot", in which the imaginary part Z_i is plotted versus the real part Z_r of the impedance, is mostly used to represent impedimetric data. Each data point corresponds to a different frequency. The low frequency data are represented in the right part of the diagram and high frequency data are on the left one. The impedance spectrum ideally exhibits a semicircle beginning in the point R_1 and ending in the point corresponding to the sum of $R_1 + R_2$ (**Figure 1.9b**) which represents the semicircle diameter.

The interpretation of this Nyquist plot is based on the correlation between the obtained data and an equivalent electrical circuit formed by basic electrical elements such as resistance, capacitance, etc (presented in the inset of Figure 1.9b). Since all the current must pass through the electrolyte and the electrode, the ohmic resistance R_1 represents the sum of the resistance of the solution and the one of the electrode. R_2, in most cases, corresponds to the polarization resistance of the interface which has to be overcome during the charge transfer to/from the electroactive species [59]. The capacitance C is the double layer capacitance which can be calculated by maximum value of Z_i. Once the electron transfer gets started the Warburg impedance W due to mass transport begins to play a role in determining the electrode kinetics.

However, the semicircles of Nyquist diagrams commonly present a not completely symmetric shape in many systems under study. It is due to the non-ideal behavior of most capacitors. In this case, the use of a Constant Phase Element (CPE) instead of a capacitor is required. The impedance of a CPE is given by: $Z_{CPE} = (j\omega)^{-\alpha}/C$. where α is an empirical coefficient [71].

Based on its ability of directly investigating the interfacial properties of a modified electrode, EIS is developing as an attractive method for studying biorecognition events especially for detection of DNA hybridization.

Currently, EIS has emerged as an attractive technique to investigate the interfacial properties of the modified electrode for studying biorecognition events [72] notably for DNA hybridization detection. The most important advantage for studying impedimetric DNA biosensors is that DNA labeling is not required [73]. The changes in the electrical properties of the modified electrode surface can result from the presence of the target molecules (i.e. DNA target). It is important to distinguish between nonfaradic and faradic sensors.

1.2.2 Faradic EIS for DNA detection

In the case of Faradic impedance spectroscopy, charges are transferred across the electrode/electrolyte interface. The addition of a redox-active species, such as $[Fe(CN)_6]^{3-/4-}$ or $[Ru(NH_3)_6]^{2+/3+}$, is required. An electrode/electrolyte interface may be simplified as shown in **Figure 1.10a**.

When a dc voltage is applied to the electrode, the solvated counter ions form an electrical double layer along the electrode surface. Depending on the applied voltage, the added redox species in the electrolyte are alternately oxidized and reduced by the transfer of an electron to and from working electrode surface. Their activity is altered by DNA hybridization. As a consequence, the EIS signal is acquired at the redox voltage of this compound. In this case, redox species is not considered as a label because it is indirectly concerned to the sensing events.

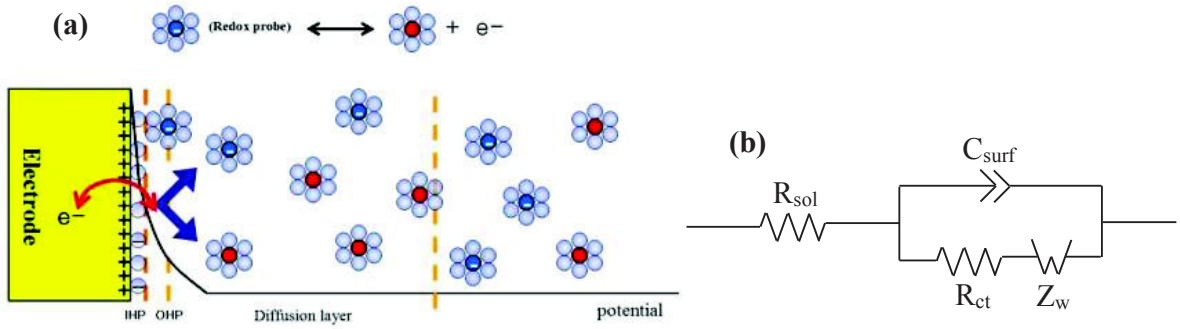

Figure 1.10: (a) Schematic diagram for an electrode/electrolyte interface and (b) Common circuit models for faradic interfaces [9].

Figure 1.10b shows the most common equivalent circuit used to fit the faradic impedance data [9, 71, 74]. The capacitance C_{surf} between the electrode surface and the ions in the solution depends on the thickness and the dielectric constant of the modified layer. The charge transfer resistance (R_{ct}) is a manifestation of two effects: (1) the energy potential associated with the oxidation or reduction event at the electrode, (2) the energy barrier of the redox species reaching the electrode due to electrostatic repulsion or steric hindrance.

Faradic EIS detection of DNA hybridization is generally based on the variation of the charge transfer resistance between the solution and the electrode surface. In most cases, because of nature negative charges of phosphate groups, the immobilization of DNA sequences on the electrode surface generates a repulsion of the anionic redox species, thus inhibiting the redox reaction and enhancing R_{ct} [59].

1.2.3 Non-faradic EIS for DNA detection: what causes an impedance change according the electrode material?

Redox indicator with a certain volume can reduce the accessibility of the DNA target, leading to a modification of the yield of probe/target coupling process. To encounter this problem, it is essential to avoid the use of redox species. According to Daniels and Pourmand [9], transient current can flow without charge transfer in nonfaradic process. No additional reagent is needed. In this case, a sufficiently sensitive electrode material is needed. Bio-modification of the electrode leads to the variation of the capacitance of the double layer formed between the solution and the electrode surface. **Figure 1.11** shows the most common models used to fit impedance spectra for nonfaradic measurements. In non-faradic mode, the resistive part is modeled as R_{leak}. For an ideal insulator or when no redox species is present, R_{leak} is theoretically infinite.

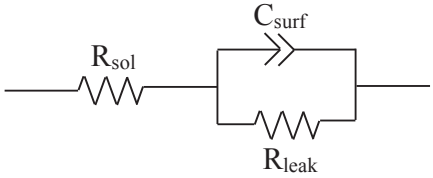

Figure 1.11: Common circuit models for non-faradic interfaces [9]

In non-faradic detection, the relation between DNA target binding and impedance change might not be easy to interpret. Various theoretical models have been proposed to explain the observed change of the impedance upon DNA hybridization according to the electrode materials.

a. Case of metal electrodes

For the DNA-modified-metallic electrode, the changes in the impedimetric response are usually discussed in term of variation of capacitance of the probe layer. The DNA hybridization event results in a capacitance change at the metal-solution interface due to alterations of the electrical double layer created in close proximity to the electrode [71, 75].

Gold (Au) nanoparticles have received extensive attention in view of their easy synthesis and good stability in aqueous solution. Many efforts have been made to explore Au nanomaterials-based impedimetric biosensors. First, in 1999, Berggren et al. [75] demonstrated that the decrease in capacitance of a probe-modified gold film, accrued to the DNA hybridisation can be used for monitoring with high sensitivity and speed the hybridisation event. The decrease of capacitance upon DNA hybridization is explained by displacement water and solvated ions away from the electrode surface. Similar phenomenon was observed by An-Lai et al. [76] who presented non-faradic impedimetric detection of avian influenza virus (AIV) DNA on modified Pt electrode.

b. Case of semiconductive electrodes

Semiconductive materials are the promising platforms for non-Faradic EIS detection. The reason is that investigating the interfaces "semiconductor/solutions" may lead to the information of the part played by charge transfer at the interface of biological system.

- **Inner cause: internal part of the electrode**

The negatively charged DNA probe immobilization followed by the additional increase of negative charges upon DNA hybridization induced an electrical perturbation near to the surface of the semiconductor through a field effect. Theoretically, an increase of negative charges induced a decrease of the electronic density in the space charge region [77]. As a result, a negative shift of the flat-band potential from the starting position leads to an increase in the energies levels of flat-bands.

Depending on semiconductor type, n-doped (electrons act as charge carriers) or p-doped (holes act as charge carriers), different changes in impedance modulus are obtained in relation of what occurs beneath the surface, in the space charge layer [78].

- When the electrode is p-doped semiconductor, DNA hybridization results in a decrease in the resistive part of the impedance due to an increase of the holes density [79-80].
- In contrary, the measurement showed an increase of the real part of the impedance in the case of n-type semiconductor due to a decrease of the electron density [38-39, 81].

Schematic representations of the energy diagrams at the n-type or p-type semiconductor/electrolyte interfaces are showed in **Figure 1.12**.

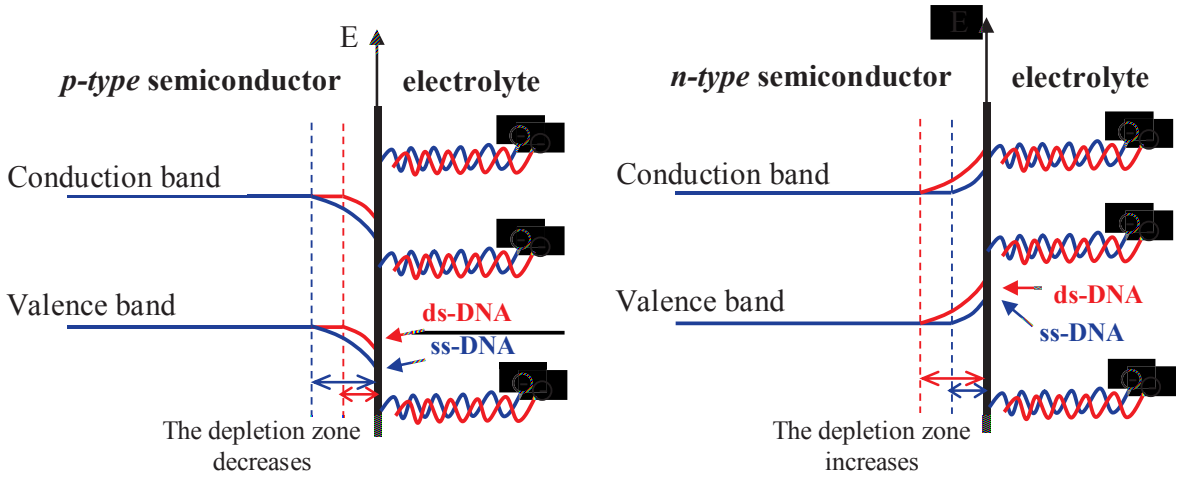

Figure 1.12: Schematic representations of the energy diagram at the semiconductor/electrolyte interface. Extra negative charges, located at the surface upon DNA hybridization, will change the electric field and the band bending in the space charge region in different ways according to the semiconductor types.

- **External cause: outer part of the electrode**

Elsewhere, the change of the non-faradic impedance could be caused by the conformation changes of the DNA [82-83] and hydrophilic character of hybridized DNA [84]. According to Piro et al. [82], DNA conformation changes from random coils on the probe-immobilized film to rigid helix double stranded upon hybridization (**Figure 1.13**). Consequently, the electrode surface is liberated and the ion-exchange process at the electrode/electrolyte interface is easier. Besides, hydrophilic character of ds-DNA could partially facilitate the ions reaching the electrode surface and consequently, speed up the rate of electron transfer at the electrode electrolyte interface.

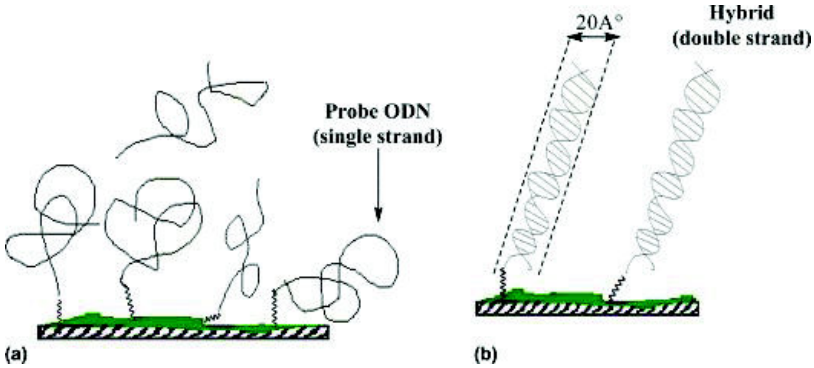

Figure 1.13: Schematic representation of DNA conformation on the poly(JUG-co-JUGA) film. (a) before, and (b) after hybridization [82].

b1. Silicon based materials

In 1997, Souteyrand pioneered in applying semiconductive material to develop label-free impedimetric DNA biosensors with the use of Si/SiO_2 substrates as a transducer to detect homo-oligomer DNA sequences [77, 80, 85]. Impedance measurements allow the detection of the charge distribution changes at the oxide/solution interface following modifications of the oxide surface. When the Si/SiO_2 substrate surface is modified, the impedance measurements show that the flat band potential of the semiconductor shifts negatively of 150 and 100mV following the immobilization of DNA probe (1mg/1mL) and the complementary hybridization (1mg/1mL), respectively (**Figure 1.14**).

The limit of the detection presented is 10^{-4} µg/µL with the use of peptide nucleic acid (PNA) as the probe layer [85].

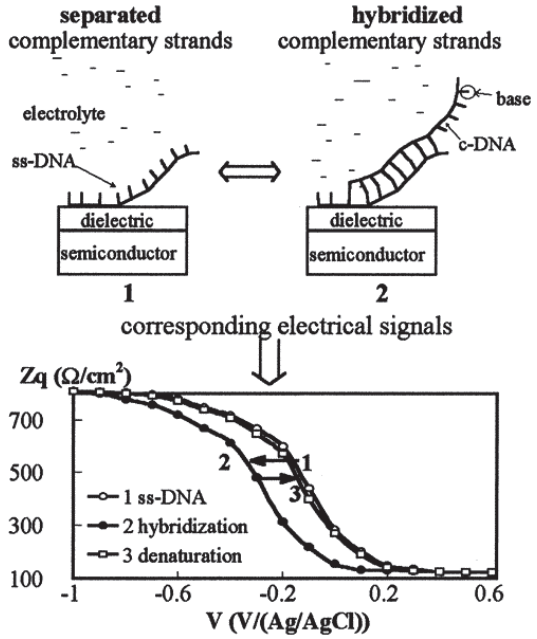

Figure 1.14: Electrical effects induced by hybridization between complementary strands. Curve 1 was recorded after immobilization of ssDNA onto the substrate. Curve 2 corresponds to the impedance measurements after hybridization. Curve 3 shows the impedance measurements after denaturation [80].

In 2005, Cai et al. [78] investigated interfacial electrical changes when DNA-modified either n-type or p-type Si (111) surfaces are exposed to the solution containing DNA targets. The impedance spectra show that incubation with the complementary sequences produces the increase in magnitude of both real and imaginary components of the impedance on the n-type samples. In contrast, when a p-type sample is used, hybridization causes the impedance to decrease. Moreover, from the comparison of results on different silicon bulk doping it can be concluded that the sensitivity to DNA hybridization arises from DNA-induced changes in the resistance of the silicon substrate and the resistance of the molecular layers.

An impedimetric DNA sensor based on nanoporous silicon platform was developed by Vamvakaki and Chaniotakis [86]. The controlled pore size in the range of 20 to 40nm matches with the size of the 21-mer dsDNA molecules. It allows the efficient adsorption and stabilization of DNA molecules inside the pores of p-Si. The DNA double helix formed based on the strong hydrogen bonds between the base pairs leads to a decrease in the hydrated sphere and thus the amount of electrolyte surrounding the initial single strands of DNA. The resulting decrease of interface charge density upon the presence of the complementary DNA strand justifies the observed impedance increase.

b2. Conductive polymers

Conducting polymers (CPs) have emerged as potential candidates for biosensors. CPs are polyconjugated polymers which possess their unique electronic structure regarding to their electrical conductivity, low ionization potentials and high electron affinity [87]. The immobilization of DNA probes and the hybridization reaction induce the changes both in the intrinsic properties of the CPs and in the interfacial film properties [88]. The most widely studied CPs for EIS detection of DNA hybridization includes polypyrrole (PPy) [83-84, 89-91], polyaniline [92-93], and polythiophene [94-96].

In 2001, the non-faradic EIS detection of the DNA hybridization reaction was accomplished by Lee *et al.* [30] on carboxylated polythiophene films prepared on glassy carbon electrode. A significant decrease in impedance was observed only for the complementary target, not in the mismatched targets. The difference in impedance values before and after hybridization is attributed to a higher conductivity of ds-DNA compared to ss-DNA.

Later in 2005, Tlili et al. [83] reported non-Faradic DNA detection based on DNA immobilized precursor copolymer, poly(3-acetic-acid pyrrole, 3N-hydrophthalimide pyrrole). The impedance measurements were performed at a DC potential of -1.4V (vs. ref) at which polypyrrole is in semiconducting state. The resulting impedance spectra **(Figure 1.15)** showed a decrease of charge-transfer-resistance upon grafting DNA probes and an increase upon complementary hybridization. According to the authors, these phenomena are explained due to the effect of the negative charges of ss-DNA and ds-DNA and their conformational structures. Under the experimental condition, polypyrrole is considered as a p-type semiconductor. Consequently, immobilization of the negatively charged DNA probes led to an increase in the majority carrier density and a decrease in the resistance of the space charge region. Another possible reason is that the DNA probes can penetrate into the pores to increase the ionic concentration in the polymer electrode. On the other hand, ds-DNA is in helical conformation, which results in significant stiffness of the functionalized polypyrrole leading to a decrease in intrinsic conjugation of the polymer backbone and causing an increase in the charge transfer resistance. The charge transfer resistance shows a linear variation versus the complementary targer DNA concentration. The detection limit of this sensor is 0.2 nM.

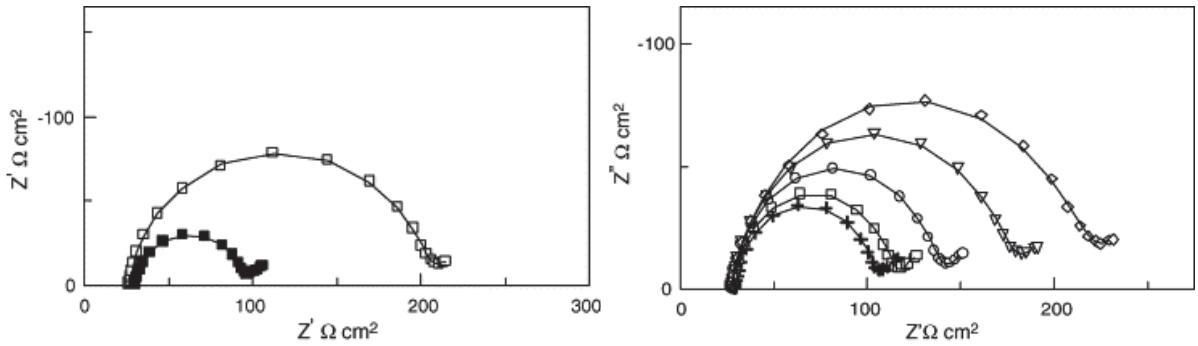

Figure 1.15: (a) Nyquist plots of PPy films prepared at the bare gold (□) before and after grafted of ss-DNA probe (■). (b) Nyquist plot of the PPy-DNA films after hybridization reaction with its complementary target under various concentrations: 0 nmol ml−1 (+); 0.5 nmol ml−1 (□); 2 nmol ml−1 (○); 3.5 nmol ml−1 (▽) and 5.5 nmol ml−1 (◊) [83].

In 2006, Gautier et al. [94-96] studied the differences between the impedance modulus obtained either in Faradic and non-Faradic EIS detection of DNA hybridization on functionalized polythiophene sensing matrix. In the case non-Faradic impedance, the hybridization caused a decrease in the semicircle diameter in Nyquist plot (**Figure 1.16a**). The authors suggested that the decrease of the resistive components under hybridization was caused by the formation of the double helix structure which liberates the surface from the random coil conformation of the ss-DNA and restores a partial anionic exchange at the interface between film and the electrolyte. That means that the DNA free surface coverage increases after hybridization, enhancing the ionic exchanges. Besides, the increase in the density of negative phosphate groups at the surface was attributed for the raised of the capacitance. In contrast, the results showed an increase in the impedance after hybridization in the case of the Faradic measurement (**Figure 1.16b**). It is due to electrostatic repulsion between negative charges of the $[Fe(CN)_6]^{3-/4-}$ redox indicator and the negatively charged DNA.

Additionally, the same authors also investigated the influence of the length of the DNA target sequence on the non-Faradic response signal [94]. Results proved that when the probes and the target have the same length (37 bases), hybridization event makes a decrease in the impedance modulus, in accordance with an opening of the interface to the mobile ions in the solution. In contrast, when the DNA target (675 bases) is much longer than the DNA probe (37 bases), the double helix is extended in the solution, which prevents the ion access. This phenomenon finally leads to an increase of the total impedance.

In 2007, Peng's group studied the use of terthiophene for non-Faradic EIS detection of DNA hybridization [97-98]. The impedance spectra also showed a decrease in the impedance similarly to ref [30]. The authors attempted to study the mechanism by using electrochemical quatz crystal microbalance (EQCM) and recognized the important role of the dopants in the impedance change.

EQCM results illustrated the dominant ion movement during the process is cation movement. As a result, the increase of the negative charges due to DNA hybridization facilitated cation movement during doping process, causing an increase in the conductance of the polymer film.

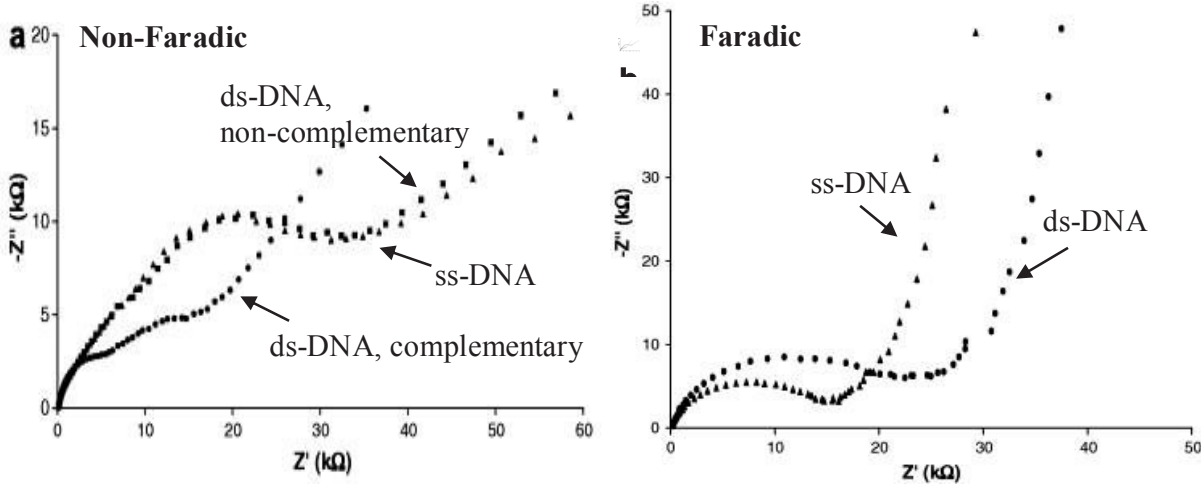

Figure 1.16: Nyquist plot for (a) Non-Faradic and (b) Faradic impedance measurements of DNA probe-modified copolymer before (▲) and after exposure to the non-complementary (■) or complementary 37 bases DNA target (●) [94].

b3. Diamond

In 2007, Vemeeren et al [99] used nanostructured ***p-type diamond*** (NCD) to improve the performance of impedimetric DNA sensors. The ***decrease of the impedance*** upon DNA hybridization was demonstrated, mainly due to the negative charges of the DNA target molecules inducing a field effect in the semiconductor substrate. Upon DNA hybridization, the amount of negative charges near the diamond surface increases. It reduces the electric field at the interface leading to a less pronounced band bending. Consequently, the depletion zone will be smaller for samples with dsDNA.

b4. GaN

In 2008, Chen et al. [100] developed a label-free DNA sensor based on ***p-type semiconductive GaN nanowires*** (represented in **Figure 1.17**). According to the authors, the immobilization of DNA probes on the NWs surface provides a negative charge layer, which creates an additional capacitive element in series with NWs. Hybridization occurs recruiting DNA targets to the electrode surface leading to more negative charges accumulation on the surface. Consequently, ***the impedance of the DNA/electrolyte interface increases*** due to electrostatic repulsion, while ***the impedance of the GaN/DNA interface decreases***. The schematic diagrams of immobilization and

hybridization of DNA on GaN NWs, the band bending evolution due to each step and Nyquist plots and corresponding Bode plots of as-grown, pLF-modified, and dsDNA-modified GaNNWs are presented in **Figure 1.17.** The detection limit of detection is 50nM of target DNA.

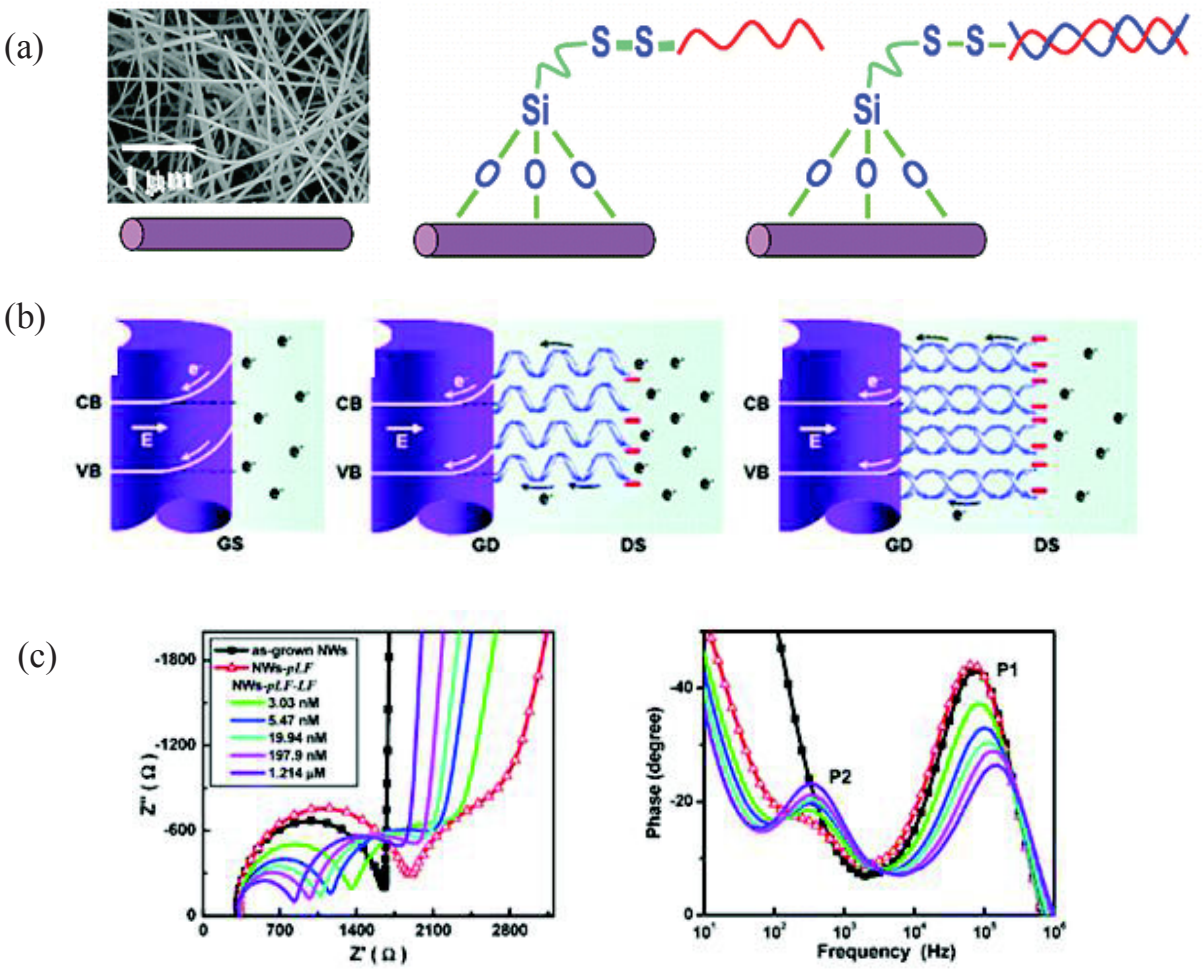

Figure 1.17: (A) Schematic diagram of immobilization and hybridization of DNA on GaN NWs. (B) The band-bending of GaN NWs: bare GaN NWs, reduce band-bending due to immobilization of probe DNA and Further flattening by hybridization [100]. (C) Nyquist plots and corresponding Bode plots of as-grown, pLF-modified, and dsDNA-modified GaNNWs (at different concentrations of LF targets, in situ DNA hybridization detection).

b5. Metal oxides

In the previous work performed in our team by Zebda [101], the non-Faradic impedance detection of DNA hybridization have been developed on different kinds of semiconductive metal-oxide thin films such as Sb-doped-SnO_2, $CdIn_2O_4$ [38-39, 81]. The impedance measurements showed a

significant increase in the impedance modulus in both used electrode upon DNA hybridization. The observed increase of the impedance is particularly much higher in the case of $CdInO_4$ than in the case of SnO_2. The increase has been explained by the field effect phenomenon occurred at the modified semiconductive metal oxide surfaces.

To the best of our knowledge, no other publication reports on this kind of semiconductive material for non-faradic EIS detection of DNA.

b6. Conclusion

Non-faradic EIS DNA sensors involve various semiconductive sensitive materials: silicon, conducting polymers, diamond, GaN and metal oxides. The comparison between the obtained detected signals is not straight forward. It can be concluded that depending on both the doping and on the intrinsic-characteristics of semiconductive materials, increase or decrease of the impedance characteristics such as resistance charge transfer are obtained upon DNA hybridization.

1.2.4 Metal oxide thin films as sensing matrix

Metal oxides are TCOs films which exhibit simultaneously high visible wavelength transparency and electrical conductivity. The majority of known TCO materials are n-type semiconductors where defects such as oxygen vacancies, impurity substitutions and interstitials donate electrons to the conduction band providing charge carriers for the flow of electric current [102-103]. These films are used in low emissivity windows, gas sensors, flat panel displays, thin film transistors, light emitting diodes and solar cells.

Thanks to their semiconductor characteristics and particularly to their chemical stability, DNA sensing platforms constituted of TCOs are an interesting alternative over the commonly used type for electrochemical detection of DNA hybridization. Reported electrochemical DNA sensors based on TCOs films are listed in Table 1.2.

Table 1.2: Different TCOs sensing platforms used in electrochemical DNA sensors.

Electrode	Technique	Immobilization method	Redox mediator	Year [Ref]
With label redox mediators: Faradic mode				
ITO	CV	Covalent link	$Ru(bpy)_3^{2+}$	1997 [104]
ITO	CV, EIS, DPV	Adsorption	$Co(phen)_3^{3+}$	2001 [105]
ITO	CV	Covalent link	$Ru(bpy)_3^{2+}$	2001 [106]
ITO	CV, CA	Covalent link	$Ru(bpy)_3^{2+}$	2002 [107]
ITO	CV	Covalent link	Au-NPs	2007 [108]
ns-ZnO/ITO	DPV	Physisorption	$[Fe(CN)_6]^{3-/4-}$	2009 [109]
ns-ZnO/ITO	EIS	Electrostatic	Methylene blue	2010 [110]
ZrO_2	EIS, DPV	Affinity	Methylene blue	2009 [111]
ZrO_2/Au	DPV	Covalent link	Methylene blue	2010 [112]
ZrO_2/Diamond	DPV	Covalent link	Methylene blue	2012 [113]
SnO_2-QDs	EIS, DPV	Electrostatic	$[Fe(CN)_6]^{3-/4-}$	2013 [114]
Without label redox mediators: Non-faradic mode				
$CdIn_2O_4$	EIS	Covalent link	No	2006 [38]*
Sb-doped SnO_2 and $CdIn_2O_4$	EIS	Covalent link	No	2006 [39]*
$CdIn_2O_4$	EIS	Covalent link	No	2010 [81]*

CV = Cyclic Voltammetry, EIS = Electrochemical Impedance Spectroscopy, DPV = Differential pulse voltammetry, CA = chroamprometry
** from our group.*

1.2.4.1 Faradic mode

From this review, various TCOs based electrochemical DNA sensors have been developed with number of DNA immobilization strategies. However, most of fabricated TCOs based DNA sensors rely on the use of different kinds of redox labels including $Ru(bpy)_3^{2+}$, $Co(phen)_3^{3+}$, $[Fe(CN)_6]^{3-/4-}$ and Methylene blue to enhance the response signals.

a. Indium tin oxide (ITO)

The most widely used TCO is a solid solution of indium (III) oxide (In_2O_3) and tin (IV) oxide (SnO_2), with typically 90%wt In_2O_3, 10%wt SnO_2. The use of ITO for electrochemical DNA detection was first reported by Napier et al. [104] in 1997. In this work, the DNA probes were immobilized to the ITO surface through self-assembled-monolayer of 12-dodecanedicarboxylic acid (DDCA). DNA hybridization was electrochemical detected by cyclic voltammetry technique

via the catalytic oxidation of guanine using $Ru(bpy)_3^{2+}$ as the mediator. The development of ITO based electrochemical DNA sensors later focused on the immobilization method of DNA on the electrode surface. Xu et al. [105] fabricated electrochemical DNA sensors in which the DNA probes were immobilized on the ITO surface by adsorption. According to the authors, the DNA molecules could be adsorbed onto the silanized ITO surface with high concentration. On the other hand, Yang et al. [106] performed DNA immobilization by direct attachment of nucleic acid molecules to the ITO electrode, which is realized by treating the electrode with a solution of DNA in 9:1 DMF/acetate solution. In addition, sensitivity of detection of DNA hybridization on ITO surface could be much enhanced by labeling the target ssDNA with Au nanoparticles [108].

b. Zinc oxide (ZnO)

Nontoxicity, high chemical stability, and high electron transfer capability make ZnO as a promising material for immobilization of biomolecule. Hence ZnO can be employed for developing biosensors, especially DNA sensors. Furthermore, the high isoelectric point (IEP) of ZnO results in unique property to immobilize biomolecules having low isoelectric point through electrostatic interaction. Consequently, ZnO has wide applications in biosensors. Different kinds of electrochemical biosensors based on ZnO or various nanostructured ZnO have been fabricated. They include enzymes, antigens, glucose, etc. However, only a few of papers have been reported, that utilized ZnO platform for electrochemical detection of DNA hybridization. Ansari et al. [109] presented a sol–gel derived nano-structured zinc oxide (ZnO) film dip-coated onto an ITO glass substrate for the fabrication of a DNA biosensor for sexually transmitted disease (gonorrhoea) detection. A 20-mer thiolated oligonucleotide probe (th-ssDNA) specific to Neisseria gonorrhoeae was immobilized on the sensing electrode. Electrochemical measurements show that the sol–gel derived nano-structured ZnO film is an excellent matrix for the immobilization of th-ssDNA onto the ZnO/ITO electrode surface. The detection limit was 7.0×10^{-4} fM. Das et al. [110] fabricated an electrochemical DNA sensor based on electrodeposited nanostructured ZnO on ITO substrate. DNA probes were immobilized via physisorption based on strong electrostatic interactions between positively charged ZnO and negatively charged DNA. The DNA–nsZnO/ITO sensor has detection range of 1.0×10^{-6} to 1.0×10^{-12} M, with a detection limit of 1.0×10^{-12} M (complementary target).

c. Zirconium oxide (ZrO_2)

In recent years, the fabrications of electrochemical DNA sensors on zirconium oxide (ZrO_2) have drawn much attention due to their unique physical, chemical and optical properties such as thermally stable and chemically inert. Besides, ZrO_2 has affinity for groups containing oxygen which facilitates covalent immobilization of biomolecules. The use of ssDNA immobilized sol-gel-derived nanostructured ZrO_2 sensing platform to detect specific-sequence of Escherichia coli was reported by Solanki et al. [111]. This DNA sensor showed a high selectivity and sensitivity

with the detection range of 10^{-6} to 10^{6} pM of DNA target. In another study, electrodeposited nanostructured ZrO_2 on gold substrate was used as the sensing matrix of a DNA sensor for Mycobacterium tubercolosis detection with detection limit of 20nM [112]. Recently, Liu et al. [113] reported a DNA sensor based on electrodeposited ZrO_2 on a diamond substrate. This device shows a selective and linear response to the logarithm of complementary DNA concentration in the range of 10^{-10} to 10^{-7} M.

d. Tin oxide (SnO_2)

SnO_2 is a chemically robust material which is known to be highly sensitive to its chemical and charged environment by inducing an electronic band bending in relation with an electrical field effect. SnO_2 films and nanostructured SnO_2 have been widely used as gas sensing materials for detecting NO_x, CO_x, H_2, C_2H_5OH, and H_2S [115]. Moreover, due to its ability to be functionalized by OH^- groups on the surface, tin oxide exhibited as a promising sensing material for electrochemical DNA sensors. However, only one paper reports about the use of SnO_2 for DNA faradic electrochemical detection. Indeed, Patel et al. [114] reported the application of tin oxide quantum dots (SnO_2-QDs) for electrochemical detection of Vibrio cholerae based on DNA hybridization technique. SnO_2-QDs have been synthesized by laser ablation technique onto hydrolyzed surface of indium tin oxide (ITO) coated glass electrode. It is showed that the developed DNA sensor of ssDNA/SnO_2-QDs/ITO exhibits high sensitivity with detection limit of 31.5ng/L.

1.2.4.2 Non-faradic mode

We are the only group to present non-faradic label-free detection of DNA hybridization based on TCOs films [38-39, 81]. Label-free detection of DNA using EIS has been studied for several years in our group. We demonstrated the feasibility of using Sb doped SnO_2 [39] and $CdIn_2O_4$ [38-39, 81] thin films to act as sensing element for label-free electrochemical impedance DNA sensors. The TCOs films were deposited directly on glass substrates using an aerosol pyrolysis deposition technique. The deposited films revealed dense and polycrystalline structure with a naturally rough 2D surface. Importantly, these films show a strong adherence on the substrate.

The process of DNA functionalization involving a covalent DNA grafting via APTES was performed on the deposited films. The impedance spectra measured before and after DNA hybridization showed a significant increase of the real part at low frequencies of the impedance in both used electrodes. We evidenced that the sensitivity is strongly dependent on the resistivity of the sensing electrode [81]. This phenomenon could be explained by the relationship between the

thickness of the space charge region and the film electrical resistivity. Indeed, an increase of the sensitivity to the DNA detection with the electrode resistivity has been found indicating that the more resistive is the oxide, the more sensitive is the sensor. A comparison of the performances between Sb-doped-SnO_2 and $CdIn_2O_4$ films was performed. The results indicated a much higher sensitivity for $CdIn_2O_4$ over Sb-doped-SnO_2 film [39]. However, $CdIn_2O_4$ possesses several limits. This oxide is chemically fragile and suffers from aging. On the contrary, SnO_2 is particularly robust and stable oxide.

Besides, the usually used planar configuration of the surface suffers from limited probe immobilization capacity and inaccessibility of targets to probes due to steric hindrances. In contrast, the collective use of high aspect ratio nanostructures increases the immobilized probe concentration and hence the number of available sites for target-probe recognition thereby reducing steric hindrance. Thus, because of their high specific surface area and excellent biological compabilities, nano-materials are used to increase the amount of DNA immobilization. Consequently, nanostructured materials based DNA sensors may possess several advanced features including high sensitivity, high selectivity, and fast response time [8]. That is why in the present work, our objective is to fabricate SnO_2 nanostructures based DNA sensors in order to enhance the sensitivity.

In recent years, the development of advanced electrochemical DNA sensing strategies based on nanomaterials have been considered as important tool in the field of genomics, diagnosis and drug-DNA interation [116-117]. A wide variety of nanoscale materials of different sizes, shapes and compositions are now available. The aim of using nanomaterials in impedimetric DNA sensors is to enhance the sensitivity of the technique (i.e the impedimetric response). In this review, different types of impedimetric DNA biosensors are discussed following the kind of substrates.

As for other kinds of sensing materials including carbon-based materials, nanostructures such as nanowires, nanotubes, nanoparticles and nanoporous with their large surface areas promote the performance of the DNA biosensors compared to their bulk counterparts.

Hence it is expected that nanostructured semiconductive SnO_2 opens the opportunities and future challenges for the development of label-free DNA sensors. Up to date, no paper which reports the use of nanostructured semiconductive metal oxide for label-free EIS detection of DNA hybridization has been found.

In the following, we present a brief review on SnO_2 crystal physical properties as well as on some different SnO_2 nanostructures and their ways of elaboration.

1.3 Tin dioxide SnO_2

SnO_2 is one of typical kinds of transparent conducting oxide (TCO) materials with ITO and ZnO. It has been widely used in many applications such as catalysts agent [118-119], heat reflecting mirrors [120], varistors [121], transparent conducting electrodes for solar cells [122-123], and optoelectronic devices [124]. Especially, SnO_2 is the most attractive material for gas sensor applications [125].

1.3.1 Crystal structure and physical properties of SnO_2

Tin oxide is special in the respect that tin possesses a dual valency, with tin preferably attaining an oxidation state of 2+ (stannous oxide SnO) or 4+ (stannic oxide SnO_2). This dual valency facilitates a variation of the surface oxygen composition. It is the key for understanding many aspects of SnO_2 surface [126].

SnO_2 crystallizes with tetragonal rutile structure with symmetry D^{14}_{4h} (C_{2v}, P_42/mnm point group) [126]. The unit cell contains six atoms, two tin and four oxygen atoms as illustrated in **Figure 1.18**. Each tin atom is at the center of six oxygen atoms placed approximately at the corners of a regular octahedron, and every oxygen atom is surrounded by three tin atoms approximately at the corners of an equilateral triangle. Thus, it is the structure of 6/3 coordination. The lattice parameters are a = b = 4.737 Å and c = 3.185Å. The c/a ratio is 0.673. The ionic radii for O^{2-} and Sn^{4+} are 1.40 and 0.71 Å, respectively. The corresponding heat of formation is $\Delta H = 1.9 \times 10^3$ J mol^{-1}, the heat capacity of Tin dioxide is $C_p = 52.59$ J mol^{-1} K^{-1}, the density at 300 K is 6.95 g cm^{-3} and the melting point is 1630°C.

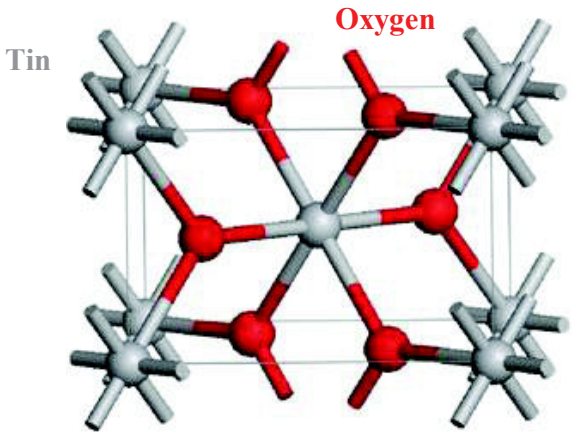

Figure 1.18: The crystal structure of SnO_2 [126].

Remarkably, SnO_2 is an unique "transparent conductor" presenting the contradictory properties of high conductivity due to massive structural non-stoichiometry with nearly insulator-like

transparency with up to 97% optical transparency in the visible range (for films of thickness 0.1 - 1.0 μm) in the visible range [127].

In the case of intrinsic semiconductor, it was shown that Sn interstitials and O vacancies, which dominate the defect structure of SnO_2 due to the multivalence of Sn, explained the natural non-stoichiometry of this material and produced shallow donor levels, turning the material into an extrinsic "n-type" semiconductor. Hence, SnO_2 is an n-type broad-band gap (3.6eV) oxide semiconductor. Particularly, undoped SnO_2 has a carrier density of up to 10^{20} cm^{-3} which is comparable to that of semimetals (10^{17} to 10^{20} cm^{-3}) [127].

In addition to its natural non-stoichiometry, the electrical properties of tin dioxide nanostructures also critically depend on amount of dopants present and on their size and shape. In order to improve the electrical properties of SnO_2 for certain application, selective doping of the SnO_2 films by normal, transition or inner transition elements offers a broad variation in the optical and electrical properties. The dopants can give off either electrons to the conduction bands (*donors*) or holes to the valence band *(acceptors)* to provide free carriers.

The optical properties of SnO_2 including transmission, reflection and absorption are determined intrinsically by its solid structure and extrinsically by its geometry including film thickness, thickness uniformity and surface roughness.

Additionally, SnO_2 is chemically inert, mechanically hard, and can resist to high temperatures [128].

1.3.2 SnO_2 nanostructures

1.3.2.1 Physical properties and related applications

Semiconductor nanomaterials have attracted much attention due to their potential scientific significance and technological applications [129]. Owing to their small size, metal oxides nanostructures with large surface areas exhibit superior chemical and physical properties that are different from those of bulk materials and can be used to enhance the performance of sensing devices. Among the variety of nanostructured metal oxides, SnO_2 semiconducting nanostructures are particularly interesting because of their promising applications in electronic devices and especially in gas sensors.

In fact, the synthesis of SnO_2 nanostructures including nanoparticles [130-132], nanowires [133-134], nanorods [135-137], nanotubes [138], etc, has been mostly performed for gas sensing application in which structural properties play a key role. As mentioned above, SnO_2 is an n-type semiconductor with oxygen deficiency. The chemical sensing mechanism of semiconductive metal

oxides is governed by the fact that the oxygen vacancies on the oxide surfaces are electrically and chemically active. Thus, the conductivity of oxide is strongly affected by the adsorbed molecules. That is why with a large surface-to-volume ratio, the electronic properties of the nanostructures being strongly influenced by the surface processes, yield superior sensitivity than the thin film counterpart.

In addition, SnO_2 has been presented to act as an excellent subwavelength waveguide because of its defect-related bands at 2.5eV and 2.1eV [139]. As a result, SnO_2 nanostructures are attractive in developing nanophotonic devices including light-emitting-diodes (LEDs), lasers and detectors.

Elsewhere, by using nanoindentation, Mao et al. [140] investigated the mechanical strength of SnO_2 nanobelts. Their results showed the possibility of nanomachining these nanobelts using an atomic force microscope tip. Additionally, the thermal conductivity of a single nanobelt was found to be significant lower than the bulk values of SnO_2 [141]. This phenomenon could be attributed to the increased phonon boundary scattering and modified phonon dispersion.

Besides, the SnO_2 nanostructures show an extraordinary electrochemical behavior based on their ability to provide more reaction sites on the surface which enhance the charge transfer in electrochemical reactions. As a result, the SnO_2 nanostructures have represented a promising strategy to achieve high-power-density as well as high-energy-density Lithium-ion batteries (LIBs). Young-Dae et al. [142] presented a SnO_2-nanowire-electrode which exhibited high electrochemical performance with stable cycling behaviors and delivering a high specific discharged capacity. In other research [143], SnO_2 nanorod-arrays present an excellent performance as a LIB anode in properties such as capacity retention and rate capability.

For biosensor applications, metal oxide nanostructures have good conductivity and catalytic properties, which could enhance electron transfer between the redox species and the electrode surface for electrochemical sensors. Ansari et al. [144] prepared sol-gel derived nanostructured SnO_2 film onto indium-tin oxide (ITO) for glucose sensing. A high bioaffinity of the enzyme (GOx) was observed which can be attributed to higher GOx loading due to microenvironment of nanoporous sol–gel derived SnO_2 film. The proposed sensor was highly sensitive and selective toward glucose sensing. In 2013, Patel et al. [114] applied nano crystalline tin oxide quantum dots (SnO_2-QDs) for electrochemical detection of Vibrio cholerae based on DNA hybridization technique. DNA probes (23 bases) have been designed form the virulent gene sequence of V. cholerae and have been immobilized onto SnO_2-QDs/ITO surface. The electrochemical response indicated that SnO_2 QDs provides an effective surface to bind with the phosphate group of DNA. The hybridized electrode exhibits linear response high sensitivity 35.20 nA/ng/cm^2, low detection limit (31.5 ng/μL), faster response time (3 s) and high stability of 0–120 days when stored under refrigerated conditions.

1.3.2.2 Different ways of elaboration of SnO_2 nanostructures

Different methods have been used to prepare SnO_2 nanostructures exhibiting 2 or 3 dimensions: thermal vapor evaporation, carbothermal reduction, chemical vapor deposition (CVD), laser ablation, sol-gel, oxidation of tin metal nanostructures and electrodeposition.

Thermal evaporation method involving a vapor-liquid-solid (VLS) growth process has been considered as an effective technique to synthesize semiconductor NWs with a good level of geometry. A typical diagram of the setup is showed in **Figure 1.19**.

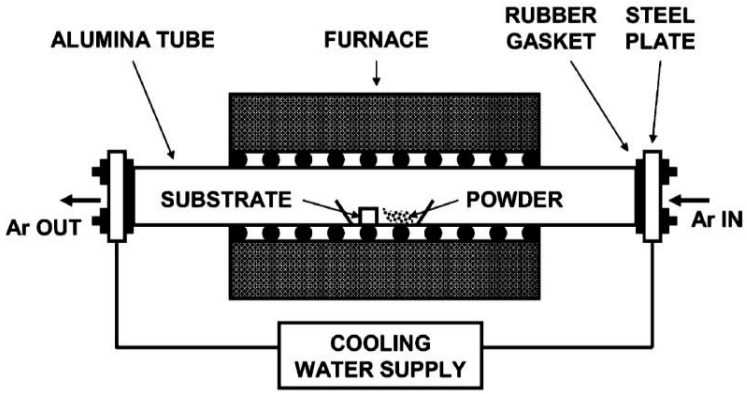

Figure 1.19: Schematic diagram describing the furnace setup used for growing the SnO_2 nanorods via thermal evaporation process [145].

Tin oxide powder is first evaporated at temperatures higher than 1300°C at one end or at the center of a furnace and then transported in a gas flow to other side of the tube where tin oxide molecules condense onto a cold substrate. This technique has been used for the formation of SnO_2 nanowires/nanobelts of high quality from SnO_2 or SnO powders [135-137, 145-147]. Although, the growth mechanism has not been completely resolved, it is important to point out that the SnO_2 nanostructures do not require a metal-catalyst to grow. In addition to nanowires and nanobelts, other SnO_2 nanostructures can be elaborated by this technique such as nanodiskettes [148], fishbone-like nanoribbons [149]. Furthermore, by employing RuO_2 as a nucleating agent, Ramgir et al [150] found the formation of SnO_2 nanobipyramids and cubes.

SnO_2 nanowires and nanoribbons can also be elaborated by carbothermal reduction technique which is a slight modification of thermal evaporation technique performed at lower synthesis temperature (about 800°C) [151-152]. Besides, laser ablation method has a similar mechanism of SnO_2 formation to thermal evaporation method. The difference comes from the way to obtain metal oxide which results from the ablation of the Sn target with suitable laser power. This technique is efficient in large-scale synthesis of SnO_2 nanowires with controlled diameters [153].

Chemical vapor deposition (CVD) is a chemical process often used to produce semiconductor thin films. CVD is practiced in a variety of formats classified according to which the chemical reactions are initiated. Via CVD, Ma et al. [154] successfully prepared SnO_2 nanowires. SnO_2 nanoboxbeams, or nanotubes with square or rectangular cross-sections (**Figure 1.20**) were synthesized on quartz substrates using a combustion chemical vapor deposition (CCVD) method in an opened atmosphere from 850 °C to 1150 °C [155]. Mathur et al. [156] fabricated single-crystalline SnO_2 nanowires with a control over diameter and morphology by employing a molecular precursor, $Sn(OtBu)_4$ in molecule-based chemical vapor deposition MB-CVD process using Au nanoparticles as catalyst.

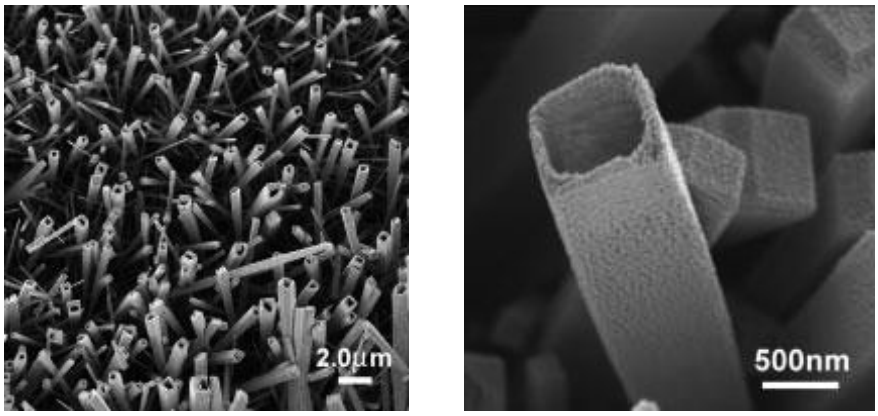

Figure 1.20: SEM images of SnO_2 tubes synthesized by combustion chemical vapor deposition (CCVD) (a) tilted view (b) a single tube [155].

Sol-gel approach is a solution-phase technique for the fabrication of SnO_2 nanostructures starting either from a chemical solution (sol) or colloidal nanoparticles to produce an integrated network (gel). Different precursors may be used for preparation of SnO_2 using a sol-gel process such as tin alkoxide and tin tetrachloride [157]. The precursor sol can either be deposited on a substrate to form a film or infiltration cast into a suitable template such as nanoporous membranes or carbon-nanotubes with the desired shapes and sizes. SnO_2 nanoparticles [157-158], nanorods [159], nanotubes [160-162] have been successfully fabricated via sol-gel route. However, the morphologies of the nanostructures are limited due to the difficulty in fabricating templates with various shapes and sizes.

In addition to sol-gel, hydrothermal method is another solution-phase route that has been used to prepare SnO_2 nanostructures [163]. For the synthesis of SnO_2 nanowires, a tin salt such as chloride or oxalate is reflxed in a suitable solvent with a boiling point of 100 – 300°C. In short, the solution methods have the disadvantages of low levels of crystallinity compared to those involving higher temperatures [164].

Additionally, SnO_2 nanowires [165] nanofibers [166] and porous nanobelts [167] could be prepared by electrospinning method. Especially, Kumar et al. [168] reported a SnO_2 nanoflower-like morphology by controlling the Sn precursor concentration in a polymeric solution. The nanoflowers (**Figure 1.21**) were made up of 70-100 nm nanofibrils, which in turn consisted of linear arrays of single crystalline SnO_2 nanoparticles. Their size is between 20–30 nm. Moreover, Mott–Schottky analysis shows that flowers have an order of magnitude higher electron density compared with the fibers despite their chemical similarity.

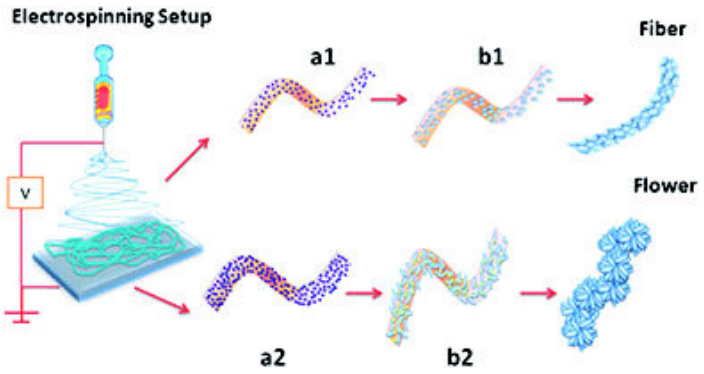

Figure 1.21: Schematics showing the evolution of flower morphology in electrospun inorganic nanostructures with (a1) low (a2) high precursor concentration. (b2) Highly populated growth of SnO_2 grains outstrips the fiber boundary giving rise to flower morphology [168].

The SnO_2 nanostructures could be achieved using a two-step process involving the deposition of Sn metal nanostructures followed by oxidizing the deposited Sn to form SnO_2. The oxidation process could be performed either by anodization process [169] or by heat-treatment [170]. Moreover, metal anodization is a promising way to prepare porous structures of corresponding metal oxides. Yamaguchi et al. [171] fabricated a transparent nanoporous tin oxide film by anodizing a tin film on a fluorine-doped tin oxide (FTO) electrode. By the same way, Hossain [172] prepared mesoporous SnO_2 spheres of tunable particle size by facile anodization of tin foil in alkaline media.

Finally, electrodeposition is a powerful process that can be applied to synthesized films and powders. Compared to the other techniques, electrodepostion offers several advantages which include: low-temperature process, low cost for material and devices and the ability to deposit thin films on complex surface. This technique has been used to synthesize metallic coatings for long time. In the past decade, electrodeposition has emerged as an effective technique to prepare metal oxides. Nanostructured coatings with a variety of morphologies could be achieved through a proper parameter control. The important processing parameters are: nature and concentration of precursors, the bath temperature, current density, the applied potential, charge passed density

during the deposition and deposition temperature. The electrodeposition of SnO_2 films and SnO_2 nanostructures are reviewed and discussed in more detail in the next section.

1.3.2.3 Electrodeposition of SnO_2 thin film and nanostructures

a. Anodic method

An oxide film can be grown by anodic oxidation of a metal surface. Depending on the process condition and the electrolytes, either a thin dense oxide film or a film containing high density of microscopic pores is grown.

In 1974, SnO_2 films were prepared Giani and Kelly [173] by anodizing Sn sheets from an ethylene-glycol-based electrolyte at voltages ranging from 6 to 50 V. The anodic SnO_2 films exhibited a polycrystalline structure with thickness ranging from 250 to 690 nm. Later in 2010, Hossain et al. [172] reported the synthesis of mesoporous SnO_2 spheres of tunable particle size were synthesized by electrochemical of tin foil in alkaline media containing NaOH and NH_4F in ethylene glycol. The obtained mesoporous SnO_2 spheres have a uniform size of 60 nm. These spherical particles are composed of agglomeration of SnO_2 nanocrystals with grain size 5-6nm (**Figure 1.22**). In the same year, a transparent tin oxide film was fabricated by anodizing a tin film on a fluorine-doped tin oxide (FTO) by Yamaguchi et al [171]. The resulting anodized nanoporous tin oxide film has a columnar-type pore channels with around 50 nm in diameter.

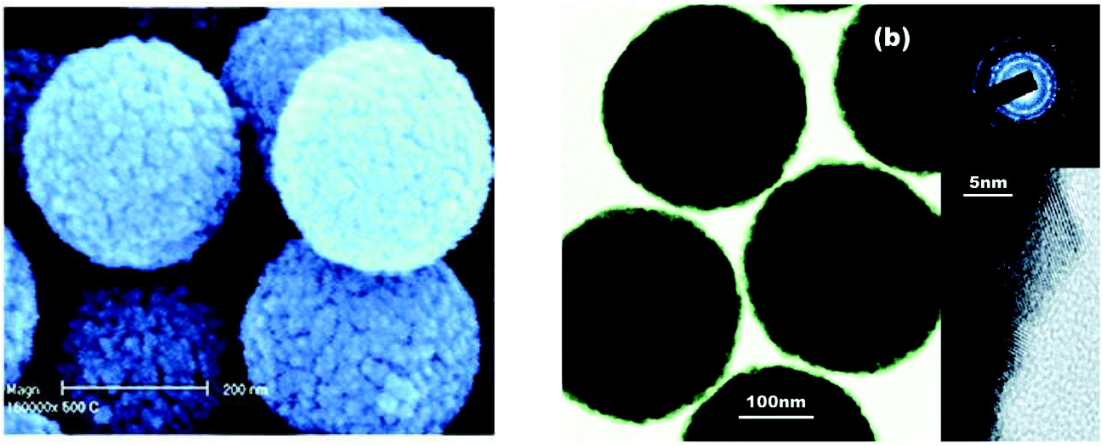

Figure 1.22: SEM and TEM images of mesoporous SnO2 spheres.

b. Cathodic method

- **SnO_2 nanoporous films (3D)**

To perform the electrodeposition of SnO_2 or any metal oxide, the presence of either the hydroxyl ions (OH^-) or O-radical on or near the working electrode is necessary [174]. Different types of oxygen precursors have been used namely, hydrogen peroxide [175], nitrate ions [176] and blown oxygen [177]. Depending on the type of the oxygen source, different two-half reactions on the working electrode occur as follows:

- Nitrate ions (NO_3^-): $NO_3^- + H_2O + 2e^- \rightarrow NO_2^- + 2OH^-$ (1)
- Hydrogen peroxide: $H_2O_2 + 2e^- \rightarrow 2OH^-$ (2)
- Dissolved oxygen: $O_2 + 2H_2O + 4e^- \rightarrow 4OH^-$ (3)
  $O_2 + 2H_2O + 2e^- \rightarrow H_2O_2 + 2OH^-$ (4)

Typically, for electrodeposition of SnO_2, when the potential is applied to the working electrode, the reduction reaction of the oxygen precursors leads to the formation of OH^- groups. These formed anions then accumulate on the electrode surface and cause an increase of the local pH. Subsequently, the Sn^{4+} ions derived from tin salts present in the solution react with the OH^- ions to form tin hydroxide ($Sn(OH)_4$) on the cathode. This hydroxide compound is unstable. It rapidly dehydrates and precipitates to form SnO_2), as described in the following reaction:

$$Sn^{4+} + 4OH^- \rightarrow Sn(OH)_4 \rightarrow \mathbf{SnO_2} + 2H_2O \quad (5)$$

The published conditions for SnO_2 cathodic electrodeposition are listed in **Table 1.3**.

Commonly, SnO_2 is electrodeposited at temperatures lower than 100°C in aqueous solutions of tin salts. Several salts have been used as precursors of cations Sn^{4+} including $SnCl_2.2H_2O$ [178-183], $SnCl_4.5H_2O$ [184] and $SnSO_4$ [185]. In the case where $SnCl_2.2H_2O$ and $SnSO_4$ were used as precursors, HNO_3 is most often served as the oxidizing agent to transform Sn^{2+} ions to Sn^{4+} ions in the solution.

Table 1.3: Preparation of tin oxide (SnO_2) by cathodic electrodeposition

Electrode	Electrolyte	Conditions	Mode	References	Year
Cu	25 mM $SnCl_2.2H_2O$ 100 mM $NaNO_3$ 75 mM HNO_3	The electrolyte is kept at 85 °C for 3 h before and during experiment	Galvanostatically 1 to 15 mA cm^{-2} (for 10 - 200 min)	Chang et al. [178]	2002
Cu	25 mM $SnCl_2.2H_2O$ 150 mM HNO_3	Oxygen is blown into the electrolyte with a rate of 300 sccm for 1h before experiment. The electrolyte is kept at 85 °C before and during experiment	Potentiostatically -0.2 to -0.6V vs. Ag/AgCl (for 10 min)	Chang et al. [179]	2004
Au	25 mM $SnCl_2.2H_2O$ 100 mM $NaNO_3$ 75 mM HNO_3	Polycarbonate membrane with pore radius of 100 nm is used	Potentiostatically -0.3 to -0.5V vs. Ag/AgCl (for 50 to 120 min)	Lai et al. [183]	2006
Pt	100 mM $SnCl_2.2H_2O$ 400 mM $NaNO_3$ 500 mM HNO_3 0.2 wt.% SDS	The temperature is kept at 45 °C	Potentiostatically -0.25 V vs. Ag/AgCl	Spray et al. [180]	2007
ITO	20 mM $SnCl_2.2H_2O$ 100 mM $NaNO_3$ 75 mM HNO_3 5 mM SDS	The temperature is kept at 50 °C	Potentiostatically -0.6 to -0.9V vs. Ag/AgCl (for 10 min)	Ishizaki et al. [181]	2009
Cu	20 mM $SnCl_4.5H_2O$ 80 mM HNO_3	The temperature is kept at 65 to 85 °C	Potentiostatically 0.1 to 0.7V vs. Tin plate (for 10 min)	Chen et al . [184]	2010
ITO	30 mM $SnSO_4$ 1.07M HNO_3	Oxygen bubbling 0.5 L/min during the process	Potentiostatically 0.1 to 0.7V vs. Ag/AgCl (for 10 min)	Vequizo et al. [185]	2010
Cu	100 mM $SnCl_2.2H_2O$ 500 mM $NaNO_3$ 400 mM HNO_3	The temperature is kept at 50 °C	Potentiostatically -0.4 to -0.8V vs. Ag/AgCl (for 2 min)	Kim et al. [182]	2012

In 2002, Chang et al. [178-179] were the first authors who reported the fabrication of nanostructured SnO_2 films on Cu electrode by electrodepostion from a solution containing nitrate ions at 85°C via both potentiostatic and galvanostatic manners. In their work, pre-treatment of the electrolyte is required to convert Sn^{2+} ions to Sn^{4+} ions. The deposited SnO_2 layers presented a low degree of crystallinity with two layer microstructure composed of an upper porous layer and an underlying dense layer (**Figure 1.23**). Later, various electrodeposition setups of SnO_2 thin films were developed by other authors with controlled deposition parameters [182, 184-185].

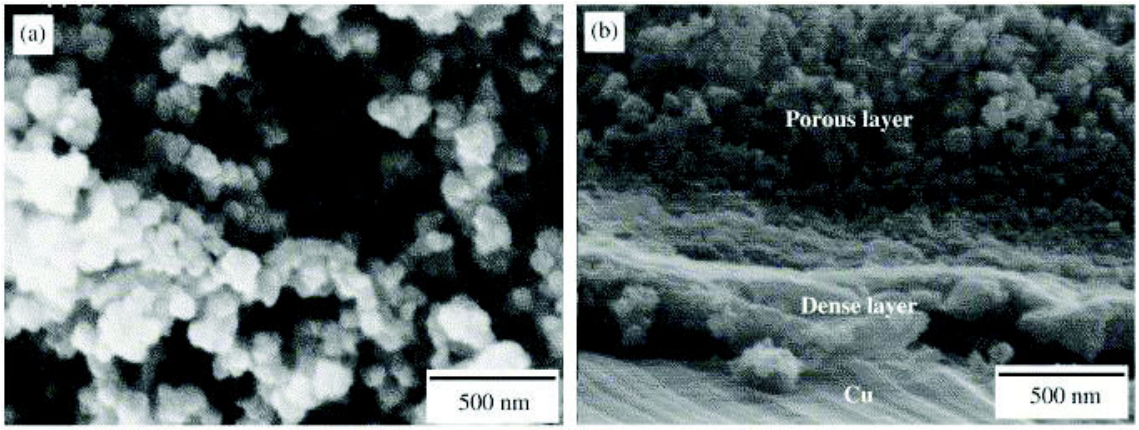

Figure 1.23: SEM micrographs of (a) top view and (b) cross-sectional view for the as-deposited SnO_2 coatings [179].

- **1D SnO_2 nanostructures: nanowires**

The template-assisted electrodeposition is one of the most effective methods for the synthesis of controlled nanostructures of metals and metal oxides. The templates are either so-called "hard" templates such as porous membranes with 1D channel that present on the surfaces of a solid substrate, or "soft" templates such as mesoscale structures which are self-assembled from block copolymers, liquid crystal materials and surfactants [186].

By using a hard template of nanoporous polycarbonate membrane, Lai et al. [183] successfully electrodeposited large aspect ratio SnO_2 nanotubes. The template was then dissolved by dichloromethane. The as-deposited nanotubes were recovered by centrifugation. Spray et al [180] used sodium docedyl sulfate (SDS) as a surfactant. According to the authors, well-organized arrangements of Sn^{4+} ions can be achieved on the working electrode by the presence of interfacial SDS assemblies. When the electrodeposition begins, this arrangement of Sn^{4+} ions becomes directly the skeleton of the SnO_2 film forming mesoporous frameworks (**Figure 1.24**).

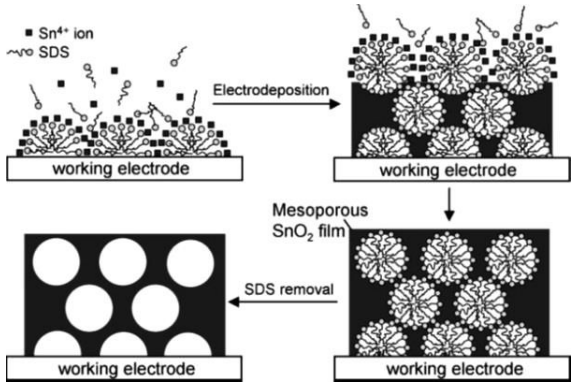

Figure 1.24: Schematic representation of electrochemical interfacial SDS surfactant [180].

Recently, Ishizaki et al. [181] used a surfactant assisted electrodeposition process to synthesize SnO_2 nanowires by using SDS surfactant (**Figure 1.25**). It was proposed that the micelles of SDS in the solution led to the aggregation of the SnO_2 particles and the anisotropic growth of the SnO_2 nanowires.

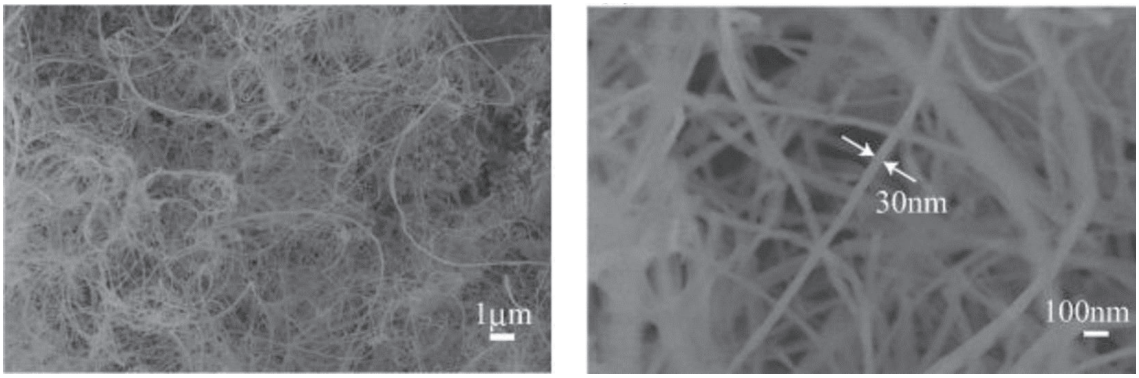

Figure 1.25: FESEM images of the surface morphologies of the SnO_2 NWs deposited at −0.8 V with SDS [181].

1.4 Conclusions

Non-faradic EIS DNA sensors involve various semiconductive sensitive materials: silicon, conducting polymers, diamond and GaN. The comparison between the obtained detected signals is not straight forward. Depending on both the doping and the intrinsic characteristics of semiconductive materials, increase or decrease of the impedance characteristics such as resistance charge transfer are obtained upon DNA hybridization.

Over these commonly used semiconductive materials, metal oxides (or TCOs) are an interesting alternative particularly thanks to their chemical stability. However, most of fabricated TCOs based DNA sensors rely on the use of redox labels to enhance the response signals.

Our group pioneered to study the non-faradic label-free detection of DNA hybridization based on TCOs films. The feasibility of using polycrystalline SnO_2 film electrode has been demonstrated. As a n type semiconductor, SnO_2 is sensitive to the negative charges of DNA immobilized on the surface which induces a change in its space charge layer by field effect phenomenon. As a result, an increase of the impedance was obtained. However, the 2D planar configuration of SnO_2 film surfaces is a limiting factor reducing both the DNA probe immobilization capacity and accessibility of targets to probe. To overcome this issue and to increase the response signal performances, efforts must be put to increase the developed specific surface through the controlled elaboration of SnO_2 nanostructures. No paper has been reported on the elaboration of SnO_2 nanostructures for label-free detection by non-faradic EIS measurements.

Among the different ways to elaborate SnO_2 nanotructures, it appears that the electrodeposition technique offers several advantages: low-temperature process, low cost for material and devices. In the past decade, authors have shown that several kinds of SnO_2 nanostructures can be obtained by cathodic electrodeposition: **SnO_2 nanoporous films (3D)** and **1D SnO_2 nanowires** via a hard or soft template-assisted electrodeposition process.

In this context, and based on these different backgrounds, the following parts of the thesis will present:

(i) the study of the elaboration of different SnO_2 nanostructures -nanoporous films and nanowires- by electrodeposition process,

(ii) for the first time, the study and investigation of their performances in term of functionnalization and label-free non-faradic electrochemical DNA detection.

REFERENCES

[1] L. C. Clark and C. Lyons, "Electrode systems for continuous monitoring in cardiovascular surgery", *Annals of the New York Academy of Sciences,* vol. 102, pp. 29-45, 1962.

[2] R. Monosik, M. Stredansky, and E. Sturdik, "Biosensor - classification, characterization and new trends", *Acta Chimica Slovaca,* vol. 5, pp. 109-120, 2012.

[3] G. A. Rechnitz, R. K. Kobos, and R. S. J., "A bio-selective membrane electrode prepared with living bacterial cells", *Analytica Chimica Acta,* vol. 94, pp. 357-36, 1977.

[4] IUPAC: International Union of Pure and Applied Chemistry (IUPAC), 1996.

[5] D. R. Thévenot, K. Toth, R. A. Durst, and G. S. Wilson, "Electrochemical biosensors: recommended definitions and classification", *Biosensors and Bioelectronics,* vol. 16, pp. 121-131, 2001.

[6] M. Nirschl, F. Reuter, and J. Vörös, "Review of Transducer Principles for Label-Free Biomolecular Interaction Analysis", *Biosensors and Bioelectronics,* vol. 1, pp. 70-92, 2011.

[7] T. G. Drummond, G. M. Hill, and K. J. Barton, "Electrochemical DNA sensors", *Nature biotechnology,* vol. 21, pp. 1192-1199, 2003.

[8] A. Bonanni and M. Del Valle, "Use of nanomaterials for impedimetric DNA sensors: A review", *Analytica Chimica Acta,* vol. 678, pp. 7-17, 2010.

[9] J. S. Daniels and N. Pourmand, "Label-Free Impedance Biosensors: Opportunities and Challenges", *Electroanalysis,* vol. 19, pp. 1239-1257, 2007.

[10] A. Sassolas, B. D. Leca-Bouvier, and L. J. Blum, "DNA biosensors and Microarrays", *Chemical Review,* vol. 108, pp. 109-139, 2008.

[11] P. de-los-Santos-Alvarez, M. Lobo-Castañón, A. Miranda-Ordieres, and P. Tuñón-Blanco, "Current strategies for electrochemical detection of DNA with solid electrodes", *Analytical and Bioanalytical Chemistry,* vol. 378, pp. 104-118, 2004.

[12] C. M. A. Brett, A. M. Oliveira Brett, and S. H. P. Serrano, "On the adsorption and electrochemical oxidation of DNA at glassy carbon electrodes", *Journal of Electroanalytical Chemistry,* vol. 366, pp. 225-231, 1994.

[13] J. Wang, J. R. Fernandes, and L. T. Kubota, "Polishable and Renewable DNA Hybridization Biosensors", *Analytical Chemistry,* vol. 70, pp. 3699-3702, 1998.

[14] Z. Yuan-Di, P. Dai-Wen, W. Zong-Li, C. Jie-Ke, and Q. Yi-Peng, "DNA-modified electrodes. Part 2. Electrochemical characterization of gold electrodes modified with DNA", *Journal of Electroanalytical Chemistry,* vol. 431, pp. 203-209, 1997.

[15] P. M. Armistead and H. H. Thorp, "Modification of Indium Tin Oxide Electrodes with Nucleic Acids: Detection of Attomole Quantities of Immobilized DNA by Electrocatalysis", *Analytical Chemistry,* vol. 72, pp. 3764-3770, 2000.

[16] H.-S. Wang, H.-X. Ju, and H.-Y. Chen, "Adsorptive Stripping Voltammetric Detection of Single-Stranded DNA at Electrochemically Modified Glassy Carbon Electrode", *Electroanalysis,* vol. 14, pp. 1615-1620, 2002.

[17] J. Xu, J.-J. Zhu, Y. Zhu, K. Gu, and H.-Y. Chen, "A novel biosensor of DNA immobilization on nano-gold modified ITO for the determination of mifepristone", *Analytical Letters,* vol. 34, pp. 503-512, 2001.

[18] X. Lin, S. Zheng, Q. Miao, and B. Jin, "DNA sensor for base mismatch detection based on a gold colloid modified glassy carbon electrode", *Analytical Letters,* vol. 35, pp. 1373-1385, 2002.

[19] J. Wang, M. Jiang, A. Fortes, and B. Mukherjee, "New label-free DNA recognition based on doping nucleic-acid probes within conducting polymer films", *Analytica Chimica Acta,* vol. 402, pp. 7-12, 1999.

[20] P. Kara, K. Kerman, D. Ozkan, B. Meric, A. Erdem, P. E. Nielsen, and M. Ozsoz, "Label-Free and Label Based Electrochemical Detection of Hybridization by Using Methylene Blue and Peptide Nucleic Acid Probes at Chitosan Modified Carbon Paste Electrodes", *Electroanalysis,* vol. 14, pp. 1685-1690, 2002.

[21] M. Wojciechowski, R. Sundseth, M. Moreno, and R. Henkens, "Multichannel Electrochemical Detection System for Quantitative Monitoring of PCR Amplification", *Clinical Chemistry,* vol. 45, pp. 1690-1693, 1999.

[22] C. N. Campbell, D. Gal, N. Cristler, C. Banditrat, and A. Heller, "Enzyme-Amplified Amperometric Sandwich Test for RNA and DNA", *Analytical Chemistry,* vol. 74, pp. 158-162, 2001.

[23] J. Gau, Jr., E. H. Lan, B. Dunn, C.-M. Ho, and J. C. S. Woo, "A MEMS based amperometric detector for E. Coli bacteria using self-assembled monolayers", *Biosensors and Bioelectronics,* vol. 16, pp. 745-755, 2001.

[24] A. Dupont-Filliard, A. Roget, T. Livache, and M. Billon, "Reversible oligonucleotide immobilisation based on biotinylated polypyrrole film", *Analytica Chimica Acta,* vol. 449, pp. 45-50, 2001.

[25] K. Ikebukuro, Y. Kohiki, and K. Sode, "Amperometric DNA sensor using the pyrroquinoline quinone glucose dehydrogenase–avidin conjugate", *Biosensors and Bioelectronics,* vol. 17, pp. 1075-1080, 2002.

[26] X. Sun, P. He, S. Liu, J. Ye, and Y. Fang, "Immobilization of single-stranded deoxyribonucleic acid on gold electrode with self-assembled aminoethanethiol monolayer for DNA electrochemical sensor applications", *Talanta,* vol. 47, pp. 487-495, 1998.

[27] G. Legay, E. Finot, R. Meunier-Prest, M. Cherkaoui-Malki, N. Latruffe, and A. Dereux, "DNA nanofilm thickness measurement on microarray in air and in liquid using an atomic force microscope", *Biosensors and Bioelectronics,* vol. 21, pp. 627-636, 2005.

[28] V. Dharuman, E. Nebling, T. Grunwald, J. Albers, L. Blohm, B. Elsholz, R. Wörl, and R. Hintsche, "DNA hybridization detection on electrical microarrays using coulostatic pulse technique", *Biosensors and Bioelectronics,* vol. 22, pp. 744-751, 2006.

[29] D.-H. Jung, B. H. Kim, Y. K. Ko, M. S. Jung, S. Jung, S. Y. Lee, and H.-T. Jung, "Covalent Attachment and Hybridization of DNA Oligonucleotides on Patterned Single-Walled Carbon Nanotube Films", *Langmuir,* vol. 20, pp. 8886-8891, 2004.

[30] T.-Y. Lee and Y.-B. Shim, "Direct DNA Hybridization Detection Based on the Oligonucleotide-Functionalized Conductive Polymer", *Analytical Chemistry,* vol. 73, pp. 5629-5632, 2001.

[31] H. Peng, C. Soeller, N. Vigar, P. A. Kilmartin, M. B. Cannell, G. A. Bowmaker, R. P. Cooney, and J. Travas-Sejdic, "Label-free electrochemical DNA sensor based on functionalised conducting copolymer", *Biosensors and Bioelectronics,* vol. 20, pp. 1821-1828, 2005.

[32] N. Prabhakar, K. Arora, H. Singh, and B. D. Malhotra, "Polyaniline Based Nucleic Acid Sensor", *The Journal of Physical Chemistry B,* vol. 112, pp. 4808-4816, 2008.

[33] I. Moser, T. Schalkhammer, F. Pittner, and G. Urban, "Surface techniques for an electrochemical DNA biosensor", *Biosensors and Bioelectronics,* vol. 12, pp. 729-737, 1997.

[34] C. Velasco-Santos, A. L. Martínez-Hernández, M. Lozada-Cassou, A. Alvarez-Castillo, and V. M. Castaño, "Chemical funtionalization of carbon nanotubes through an organosilane", *Nanotechnology,* vol. 13, pp. 495-498, 2002.

[35] D. Peyrade, J. E. Mendez, L. Drazek, V. Stambouli, M. Labeau, J.-M. Terrot, C. Uzel, P. Barritault, A. Hoang, and P. Peletie, "A DNA chip microstructured on silicon", *Applied Nanoscience,* vol. 1, pp. 63-69, 2004.

[36] J. A. Howarter and J. P. Youngblood, "Optimization of Silica Silanization by 3-Aminopropyltriethoxysilane", *Langmuir,* vol. 22, pp. 11142-11147, 2006.

[37] T. Nakagawa, T. Tanaka, D. Niwa, T. Osaka, H. Takeyama, and T. Matsunaga, "Fabrication of amino silane-coated microchip for DNA extraction from whole blood", *Journal of Biotechnology,* vol. 116, pp. 105-111, 2005.

[38] A. Zebda, V. Stambouli, M. Labeau, C. Guiducci, J. P. Diard, and B. Le Gorrec, "Metallic oxide $CdIn_2O_4$ films for the label free electrochemical detection of DNA hybridization", *Biosens Bioelectron,* vol. 22, pp. 178-84, 2006.

[39] V. Stambouli, A. Zebda, E. Appert, C. Guiducci, M. Labeau, J. P. Diard, B. Le Gorrec, N. Brack, and P. J. Pigram, "Semiconductor oxide based electrodes for the label-free electrical detection of DNA hybridization: Comparison between Sb doped SnO_2 and $CdIn_2O_4$", *Electrochimica Acta,* vol. 51, pp. 5206-5214, 2006.

[40] P. Serre, C. Ternon, V. Stambouli, P. Periwal, and T. Baron, "Fabrication of silicon nanowire networks for biological sensing", *Sensors and Actuators B: Chemical,* vol. 182, pp. 390-395, 2013.

[41] M. Brumbach and A. N. R., "Preparation of Monolayer Modified Electrodes", in *Encyclopedia of Electrochemistry*. vol. 10, A. J. Bard*, et al.*, Eds., ed Weinheim: Wiley-VCH, 2007.

[42] V. Stambouli, M. Labeau, I. Matko, B. Chenevier, O. Renault, C. Guiducci, P. Chaudouët, H. Roussel, D. Nibkin, and E. Dupuis, "Development and functionalisation of Sb doped SnO_2 thin films for DNA biochip applications", *Sensors and Actuators B: Chemical,* vol. 113, pp. 1025-1033, 2006.

[43] M. Manesse, R. Sanjines, V. Stambouli, C. Jorel, B. Pelissier, M. Pisarek, R. Boukherroub, and S. Szunerits, "Preparation and characterization of silver substrates coated with antimony-doped SnO_2 thin films for surface plasmon resonance studies", *Langmuir,* vol. 25, pp. 8036-41, 2009.

[44] M. A. Cooper, "Optical biosensors in drug discovery", *Nat Rev Drug Discov,* vol. 1, pp. 515-528, 2002.

[45] K. M. Byun, N.-H. Kim, Y. H. Ko, and J. S. Yu, "Enhanced surface plasmon resonance detection of DNA hybridization based on ZnO nanorod arrays", *Sensors and Actuators B: Chemical,* vol. 155, pp. 375-379, 2011.

[46] B. P. Nelson, M. R. Liles, K. B. Frederick, R. M. Corn, and R. M. Goodman, "Label-free detection of 16S ribosomal RNA hybridization on reusable DNA arrays using surface plasmon resonance imaging", *Environmental Microbiology,* vol. 4, pp. 735-743, 2002.

[47] F. Nakamura, E. Ito, T. Hayashi, and M. Hara, "Fabrication of COOH-terminated self-assembled monolayers for DNA sensors", *Colloids and Surfaces A: Physicochemical and Engineering Aspects,* vol. 284–285, pp. 495-498, 2006.

[48] I. Mannelli, M. Minunni, S. Tombelli, R. Wang, M. Michela Spiriti, and M. Mascini, "Direct immobilisation of DNA probes for the development of affinity biosensors", *Bioelectrochemistry,* vol. 66, pp. 129-138, 2005.

[49] C. J. Lee, J. S. Kang, M. S. Kim, K. P. Lee, and M. S. Lee, "The Study of Doxorubicin and its Complex with DNA by SERS and UV-resonance Raman Spectroscopy ", *Bulletin of the Korean Chemical Society,* vol. 25, pp. 1211-1216, 2004.

[50] K.-H. Yang, Y.-C. Liu, and C.-C. Yu, "Simple Strategy To Improve Surface-Enhanced Raman Scattering Based on Electrochemically Prepared Roughened Silver Substrates", *Langmuir,* vol. 26, pp. 11512-11517, 2010.

[51] M. Green, F.-M. Liu, L. Cohen, P. Kollensperger, and T. Cass, "SERS platforms for high density DNA arrays", *Faraday Discussions,* vol. 132, pp. 269-280, 2006.

[52] M. Langlet, I. Sow, S. Briche, M. Messaoud, O. Chaix-Pluchery, F. Dherbey-Roussel, P. Chaudouët, and V. Stambouli, "Elaboration of an Ag°/TiO_2 platform for DNA detection by surface enhanced Raman spectroscopy", *Surface Science,* vol. 605, pp. 2067-2072, 2011.

[53] M. Dizdaroglu, P. W. Jaruga, and H. Rodriguez, "Measurement of 8-hydroxy-2'-deoxyguanosine in DNA by high-performance liquid chromatography-mass spectrometry: comparison with measurement by gas chromatography-mass spectrometry", *Nucleic Acids Research,* vol. 29, p. e12, 2001.

[54] J. R. Soglia, R. J. Turesky, A. Paehler, and P. Vouros, "Quantification of the heterocyclic aromatic amine DNA adduct N-(Deoxyguanosin-8-yl)-2-amino-3-methylimidazo[4,5-f]quinoline in livers of rats/Microelectrospray Mass Spectrometry: a dose-response study", *Analytical Chemistry,* vol. 73, pp. 2819-2827, 2001.

[55] D.-S. Kim, Y.-T. Jeong, H.-J. Park, J.-K. Shin, P. Choi, J.-H. Lee, and G. Lim, "An FET-type charge sensor for highly sensitive detection of DNA sequence", *Biosensors and Bioelectronics,* vol. 20, pp. 69-74, 2004.

[56] H. P. Lang, M. Hegner, and C. Gerber, "Cantilever array sensors", *Materials Today,* vol. 8, pp. 30-36, 2005.

[57] J. Wang, "Electrochemical nucleic acid biosensors", *Analytica Chimica Acta,* vol. 469, pp. 63-71, 2002.

[58] J. J. Gooding, "Electrochemical DNA hybridization biosensors", *Electroanalysis,* vol. 14, pp. 1149-1156, 2002.

[59] J. Y. Park and S.-M. Park, "DNA hybridization sensors based on electrochemical impedance spectroscopy as a detection tool", *Sensors,* vol. 9, pp. 9513-9532, 2009.

[60] M. Lazerges and F. Bedioui, "Analysis of the evolution of the detection limits of electrochemical DNA biosensors", *Analytical and Bioanalytical Chemistry,* vol. 405, pp. 3705-3714, 2013.

[61] Y. Xu, H. Cai, P.-G. He, and Y.-Z. Fang, "Probing DNA Hybridization by Impedance Measurement Based on CdS-Oligonucleotide Nanoconjugates", *Electroanalysis,* vol. 16, pp. 150-155, 2004.

[62] Y. Fu, R. Yuan, L. Xu, Y. Chai, X. Zhong, and D. Tang, "Indicator free DNA hybridization detection via EIS based on self-assembled gold nanoparticles and bilayer two-dimensional 3-mercaptopropyltrimethoxysilane onto a gold substrate", *Biochemical Engineering Journal,* vol. 23, pp. 37-44, 2005.

[63] M. Ozsoz, A. Erdem, K. Kerman, D. Ozkan, B. Tugrul, N. Topcuoglu, H. Ekren, and M. Taylan, "Electrochemical Genosensor Based on Colloidal Gold Nanoparticles for the Detection of Factor V Leiden Mutation Using Disposable Pencil Graphite Electrodes", *Analytical Chemistry,* vol. 75, pp. 2181-2187, 2003.

[64] F. Patolsky, A. Leichtenstein, and I. Willner, "Detection of single-base DNA mutations by enzyme-amplified electronic transduction", *Nature biotechnology,* vol. 19, pp. 253-257, 2001.
[65] F. Lucarelli, G. Marrazza, and M. Mascini, "Enzyme-based impedimetric detection of PCR products using oligonucleotide-modified screen-printed gold electrodes", *Biosensors and Bioelectronics,* vol. 20, pp. 2001-2009, 2005.
[66] S.-f. Liu, Y.-f. Li, J.-r. Li, and L. Jiang, "Enhancement of DNA immobilization and hybridization on gold electrode modified by nanogold aggregates", *Biosensors and Bioelectronics,* vol. 21, pp. 789-795, 2005.
[67] Y. Jin, X. Yao, Q. Liu, and J. Li, "Hairpin DNA probe based electrochemical biosensor using methylene blue as hybridization indicator", *Biosensors and Bioelectronics,* vol. 22, pp. 1126-1130, 2007.
[68] K. Kagan, K. Masaaki, and T. Eiichi, "Recent trends in electrochemical DNA biosensor technology", *Measurement Science and Technology,* vol. 15, p. R1, 2004.
[69] E. Palecek, "Oscillographic Polarography of Highly Polymerized Deoxyribonucleic Acid", *Nature,* vol. 188, pp. 656-657, 1960.
[70] J. Wang and A.-N. Kawde, "Pencil-based renewable biosensor for label-free electrochemical detection of DNA hybridization", *Analytica Chimica Acta,* vol. 431, pp. 219-224, 2001.
[71] E. Katz and I. Willner, "Probing Biomolecular Interactions at Conductive and Semiconductive Surfaces by Impedance Spectroscopy: Routes to Impedimetric Immunosensors, DNA-Sensors, and Enzyme Biosensors", *Electroanalysis,* vol. 15, pp. 913-947, 2003.
[72] C. Gabrielli, "Use and application of electrochemical impedance techniques", *Solartron analytical,* vol. Technical report number 24, 1997.
[73] A. Bonanni, M. Esplandiu, M. Pividori, S. Alegret, and M. Del Valle, "Impedimetric genosensors for the detection of DNA hybridization", *Analytical and Bioanalytical Chemistry,* vol. 385, pp. 1195-1201, 2006.
[74] D. D. Macdonald, "Reflections on the history of electrochemical impedance spectroscopy", *Electrochimica Acta,* vol. 51, pp. 1376-1388, 2006.
[75] C. Berggren, P. Stålhandske, J. Brundell, and G. Johansson, "A Feasibility Study of a Capacitive Biosensor for Direct Detection of DNA Hybridization", *Electroanalysis,* vol. 11, pp. 156-160, 1999.
[76] Y.-T. Long, C.-Z. Li, H.-B. Kraatz, and J. S. Lee, "AC Impedance Spectroscopy of Native DNA and M-DNA", *Biophysical Journal,* vol. 84, pp. 3218-3225, 2003.
[77] E. Souteyrand, J. P. Cloarec, J. R. Martin, C. Wilson, I. Lawrence, S. Mikkelsen, and M. F. Lawrence, "Direct Detection of the Hybridization of Synthetic Homo-Oligomer DNA Sequences by Field Effect", *The Journal of Physical Chemistry B,* vol. 101, pp. 2980-2985, 1997.
[78] W. Cai, J. R. Peck, D. W. van der Weide, and R. J. Hamers, "Direct electrical detection of hybridization at DNA-modified silicon surfaces", *Biosensors and Bioelectronics,* vol. 19, pp. 1013-1019, 2004.
[79] C. Schyberg, C. Plossu, D. Barbier, N. Jaffrezic-Renault, C. Martelet, H. Maupas, E. Souteyrand, M. H. Charles, T. Delair, and B. Mandrand, "Impedance analysis of Si/SiO_2 structures grafted with biomolecules for the elaboration of an immunosensor", *Sensors and Actuators B: Chemical,* vol. 27, pp. 457-460, 1995.

[80] J. P. Cloarec, J. R. Martin, C. Polychronakos, I. Lawrence, M. F. Lawrence, and E. Souteyrand, "Functionalization of Si/SiO_2 substrates with homooligonucleotides for a DNA biosensor", *Sensors and Actuators B: Chemical,* vol. 58, pp. 394-398, 1999.

[81] A. Zebda, M. Labeau, J. P. Diard, V. Lavalley, and V. Stambouli, "Electrical resistivity dependence of semi-conductive oxide electrode on the label-free electrochemical detection of DNA", *Sensors and Actuators B: Chemical,* vol. 144, pp. 176-182, 2010.

[82] B. Piro, J. Haccoun, M. C. Pham, L. D. Tran, A.Rubin, H. Perrot, and C. Gabrielli, "Study of the DNA hybridization transduction behavior of a quinone-containing electroactive polymer by cyclic voltammetry and electrochemical impedance spectroscopy", *Journal of Electroanalytical Chemistry,* vol. 577, pp. 155-165, 2005.

[83] C. Tlili, H. Korri-Youssoufi, L. Ponsonnet, C. Martelet, and N. J. Jaffrezic-Renault, "Electrochemical impedance probing of DNA hybridisation on oligonucleotide-functionalised polypyrrole", *Talanta,* vol. 68, pp. 131-137, 2005.

[84] H. Korri-Youssoufi and B. Makrouf, "Electrochemical biosensing of DNA hybridization by ferrocenyl groups functionalized polypyrrole", *Analytica Chimica Acta,* vol. 469, pp. 85-92, 2002.

[85] A. Macanovic, C. Marquette, C. Polychronakos, and M. F. Lawrence, "Impedance based detection of DNA sequences using a silicon transducer with PNA as the probe layer", *Nucleic Acids Research,* vol. 32, p. e20, 2004.

[86] V. Vamvakaki and N. A. Chaniotakis, "DNA Stabilization and Hybridization Detection on Porous Silicon Surface by EIS and Total Reflection FT-IR Spectroscopy", *Electroanalysis,* vol. 20, pp. 1845-1850, 2008.

[87] H. Peng, L. Zhang, C. Soeller, and J. Travas-Sejdic, "Conducting polymers for electrochemical DNA sensing", *Biomaterials,* vol. 30, pp. 2132-2148, 2009.

[88] J. Wang, "Towards Genoelectronics: Electrochemical Biosensing of DNA Hybridization", *Chemistry – A European Journal,* vol. 5, pp. 1681-1685, 1999.

[89] H. Korri-Youssoufi and A. Yassar, "Electrochemical Probing of DNA Based on Oligonucleotide-Functionalized Polypyrrole", *Biomacromolecules,* vol. 2, pp. 58-64, 2001.

[90] M. A. Booth, S. Harbison, and J. Travas-Sejdic, "Development of an electrochemical polypyrrole-based DNA sensor and subsequent studies on the effects of probe and target length on performance", *Biosensors and Bioelectronics,* vol. 28, pp. 362-367, 2011.

[91] V. Velusamy, K. Arshak, C. F. Yang, L. Yu, O. Korostynska, and C. Adley, "Comparison between DNA Immobilization Techniques on a Redox Polymer Matrix", *American Journal of Analytical Chemistry,* vol. 2, pp. 392-400, 2011.

[92] W. Zhang, T. Yang, X. Li, D. Wang, and K. Jiao, "Conductive architecture of Fe_2O_3 microspheres/self-doped polyaniline nanofibers on carbon ionic liquid electrode for impedance sensing of DNA hybridization", *Biosensors and Bioelectronics,* vol. 25, pp. 428-434, 2009.

[93] Y. Feng, T. Yang, W. Zhang, C. Jiang, and K. Jiao, "Enhanced sensitivity for deoxyribonucleic acid electrochemical impedance sensor: gold nanoparticle/polyaniline nanotube membranes", *Anal Chim Acta,* vol. 616, pp. 144-51, 2008.

[94] C. Gautier, C. Esnault, C. Cougnon, J.-F. Pilard, N. Casse, and B. Chénais, "Hybridization-induced interfacial changes detected by non-Faradaic impedimetric measurements compared to Faradaic approach", *Journal of Electroanalytical Chemistry,* vol. 610, pp. 227-233, 2007.

[95] C. Gautier, C. Cougnon, J.-F. Pilard, and N. Casse, "Label-free detection of DNA hybridization based on EIS investigation of conducting properties of functionalized polythiophene matrix", *Journal of Electroanalytical Chemistry,* vol. 587, pp. 276-283, 2006.

[96] C. Gautier, C. Cougnon, J.-F. Pilard, N. Casse, B. Chénais, and M. Laulier, "Detection and modelling of DNA hybridization by EIS measurements: Mention of a polythiophene matrix suitable for electrochemically controlled gene delivery", *Biosensors and Bioelectronics,* vol. 22, pp. 2025-2031, 2007.

[97] P. Hui, C. Soeller, and J. Travas-Sejdic, "DNA Sensors based on Conducting Polymers Functionalized with Conjugated Side Chain", in *Sensors, 2007 IEEE*, 2007, pp. 1124-1127.

[98] H. Peng, L. Zhang, J. Spires, C. Soeller, and J. Travas-Sejdic, "Synthesis of a functionalized polythiophene as an active substrate for a label-free electrochemical genosensor", *Polymer,* vol. 48, pp. 3413-3419, 2007.

[99] V. Vermeeren, N. Bijnens, S. Wenmackers, M. Daenen, K. Haenen, O. A. Williams, M. Ameloot, M. vandeVen, P. Wagner, and L. Michiels, "Towards a real-time, label-free, diamond-based DNA sensor", *Langmuir,* vol. 23, pp. 13193-202, 2007.

[100] C.-P. Chen, A. Ganguly, C.-H. Wang, C.-W. Hsu, S. Chattopadhyay, Y.-K. Hsu, Y.-C. Chang, K.-H. Chen, and L.-C. Chen, "Label-Free Dual Sensing of DNA Molecules Using GaN Nanowires", *Analytical Chemistry,* vol. 81, pp. 36-42, 2008.

[101] A. Zebda, "Propriétés microstructurales et électriques d'électrodes d'oxydes SnO_2 et $Cdln_2O_4$: application à la détection électrochimique directe de l'hybridation de l'ADN", Docteur, Grenoble INP, Grenoble, 2007.

[102] S. Calnan and A. N. Tiwari, "High mobility transparent conducting oxides for thin film solar cells", *Thin Solid Films,* vol. 518, pp. 1839-1849, 2010.

[103] K. Chopra and I. Kaur, "Thin Film Technology: An Introduction", in *Thin Film Device Applications*, K. Chopra and I. Kaur, Eds., ed: Springer US, 1983, pp. 1-54.

[104] M. E. Napier and H. H. Thorp, "Modification of Electrodes with Dicarboxylate Self-Assembled Monolayers for Attachment and Detection of Nucleic Acids", *Langmuir,* vol. 13, pp. 6342-6344, 1997.

[105] J. Xu, J.-J. Zhu, Q. Huang, and H.-Y. Chen, "A novel DNA-modified indium tin oxide electrode", *Electrochemistry Communications,* vol. 3, pp. 665-669, 2001.

[106] I. V. Yang and H. H. Thorp, "Modification of Indium Tin Oxide Electrodes with Repeat Polynucleotides: Electrochemical Detection of Trinucleotide Repeat Expansion", *Analytical Chemistry,* vol. 73, pp. 5316-5322, 2001.

[107] N. D. Popovich, A. E. Eckhardt, J. C. Mikulecky, M. E. Napier, and R. S. Thomas, "Electrochemical sensor for detection of unmodified nucleic acids", *Talanta,* vol. 56, pp. 821-828, 2002.

[108] S. Moses, S. H. Brewer, S. Kraemer, R. R. Fuierer, L. B. Lowe, C. Agbasi, M. Sauthier, and S. Franzen, "Detection of DNA hybridization on indium tin oxide surfaces", *Sensors and Actuators B: Chemical,* vol. 125, pp. 574-580, 2007.

[109] A. A. Ansari, R. Singh, G. Sumana, and B. D. Malhotra, "Sol–gel derived nano-structured zinc oxide film for sexually transmitted disease sensor", *Analyst,* vol. 134, pp. 997-1002, 2009.

[110] M. Das, G. Sumana, R. Nagarajan, and B. D. Malhotra, "Application of nanostructured ZnO films for electrochemical DNA biosensor", *Thin Solid Films,* vol. 519, pp. 1196-1201, 2010.

[111] P. R. Solanki, A. Kaushik, P. M. Chavhan, S. N. Maheshwari, and B. D. Malhotra, "Nanostructured zirconium oxide based genosensor for Escherichia coli detection", *Electrochemistry Communications,* vol. 11, pp. 2272-2277, 2009.
[112] M. Das, G. Sumana, R. Nagarajan, and B. D. Malhotra, "Zirconia based nucleic acid sensor for Mycobacterium tuberculosis detection", *Applied Physics Letters,* vol. 96, p. 133703, 2010.
[113] B. Liu, J. Hu, and J. S. Foord, "Electrochemical detection of DNA hybridization by a zirconia modified diamond electrode", *Electrochemistry Communications,* vol. 19, pp. 46-49, 2012.
[114] M. K. Patel, J. Singh, M. K. Singh, V. V. Agrawal, S. G. Ansari, and B. D. Malhotra, "Tin Oxide Quantum Dot Based DNA Sensor for Pathogen Detection", *Journal of Nanoscience and Nanotechnology,* vol. 13, pp. 1671-1678, 2013.
[115] A. M. Azad, S. A. Akbar, S. G. Mhaisalkar, L. D. Birkefeld, and K. S. Goto, "Solid-State Gas Sensors: A Review", *Journal of The Electrochemical Society,* vol. 139, pp. 3690-3704, 1992.
[116] F. Patolsky and C. M. Lieber, "Nanowire nanosensors", *Materials Today,* vol. 8, pp. 20-28, 2005.
[117] J. Wang, "Nanomaterial-based electrochemical biosensors", *Analyst,* vol. 130, pp. 421-426, 2005.
[118] L. Chou, Y. Cai, B. Zhang, J. Niu, S. Ji, and S. Li, "Influence of SnO_2-doped W-Mn/SiO_2 for oxidative conversion of methane to high hydrocarbons at elevated pressure", *Applied Catalysis A: General,* vol. 238, pp. 185-191, 2003.
[119] P. T. Wierzchowski and L. W. Zatorski, "Kinetics of catalytic oxidation of carbon monoxide and methane combustion over alumina supported Ga_2O_3, SnO_2 or V_2O_5", *Applied Catalysis B: Environmental,* vol. 44, pp. 53-65, 2003.
[120] M. Kojima, F. Takahashi, K. Kinoshita, T. Nishibe, and M. Ichidate, "Transparent furnace made of heat mirror", *Thin Solid Films,* vol. 392, pp. 349-354, 2001.
[121] M. R. C. Santos, P. R. Bueno, E. Longo, and J. A. Varela, "Effect of oxidizing and reducing atmospheres on the electrical properties of dense SnO_2-based varistors", *Journal of the European Ceramic Society,* vol. 21, pp. 161-167, 2001.
[122] T. El Moustafid, H. Cachet, B. Tribollet, and D. Festy, "Modified transparent SnO_2 electrodes as efficient and stable cathodes for oxygen reduction", *Electrochimica Acta,* vol. 47, pp. 1209-1215, 2002.
[123] M. Okuya, S. Kaneko, K. Hiroshima, I. Yagi, and K. Murakami, "Low temperature deposition of SnO_2 thin films as transparent electrodes by spray pyrolysis of tetra-n-butyltin(IV)", *Journal of the European Ceramic Society,* vol. 21, pp. 2099-2102, 2001.
[124] T. W. Kim, D. U. Lee, D. C. Choo, J. H. Kim, H. J. Kim, J. H. Jeong, M. Jung, J. H. Bahang, H. L. Park, Y. S. Yoon, and J. Y. Kim, "Optical parameters in SnO_2 nanocrystalline textured films grown on p-InSb (111) substrates", *Journal of Physics and Chemistry of Solids,* vol. 63, pp. 881-885, 2002.
[125] D. D. Vuong, G. Sakai, K. Shimanoe, and N. Yamazoe, "Preparation of grain size-controlled tin oxide sols by hydrothermal treatment for thin film sensor application", *Sensors and Actuators B: Chemical,* vol. 103, pp. 386-391, 2004.
[126] M. Batzill and U. Diebold, "The surface and materials science of tin oxide", *Progress in Surface Science,* vol. 79, pp. 47-154, 2005.

[127] Ç. Kılıç and A. Zunger, "Origins of Coexistence of Conductivity and Transparency in SnO_2", *Physical Review Letters,* vol. 88, p. 095501, 2002.
[128] H. Salehi, M. Aryadoust, and M. Farbod, "Electronic And Structural Properties Of Tin Dioxide In Cubic Phase", *Iranian Journal of Science and Technology - Transaction A: Science,* vol. 34, pp. 131-139, 2010.
[129] H. Y. Dang, J. Wang, and S. S. Fan, "The synthesis of metal oxide nanowires by directly heating metal samples in appropriate oxygen atmospheres", *Nanotechnology,* vol. 14, p. 738, 2003.
[130] M. Vaezi and S. Sadrnezhaad, "Gas sensing behavior of nanostructured sensors based on tin oxide synthesized with different methods", *Materials Science and Engineering: B,* vol. 140, pp. 73-80, 2007.
[131] F. Li, J. Xu, X. Yu, L. Chen, J. Zhu, Z. Yang, and X. Xin, "One-step solid-state reaction synthesis and gas sensing property of tin oxide nanoparticles", *Sensors and Actuators B: Chemical,* vol. 81, pp. 165-169, 2002.
[132] E. Leite, I. Weber, E. Longo, and J. Varela, "A new method to control particle size and particle size distribution of SnO_2 nanoparticles for gas sensor applications", *Advanced Materials,* vol. 12, pp. 965-968, 2000.
[133] A. Kolmakov, Y. Zhang, G. Cheng, and M. Moskovits, "Detection of CO and O_2 using tin oxide nanowire sensors", *Advanced Materials,* vol. 15, pp. 997-1000, 2003.
[134] Y. Wang, X. Jiang, and Y. Xia, "A solution-phase, precursor route to polycrystalline SnO2 nanowires that can be used for gas sensing under ambient conditions", *Journal of the American Chemical Society,* vol. 125, pp. 16176-16177, 2003.
[135] E. Comini, G. Faglia, G. Sberveglieri, Z. Pan, and Z. L. Wang, "Stable and highly sensitive gas sensors based on semiconducting oxide nanobelts", *Applied Physics Letters,* vol. 81, pp. 1869-1871, 2002.
[136] E. Comini, G. Faglia, G. Sberveglieri, D. Calestani, L. Zanotti, and M. Zha, "Tin oxide nanobelts electrical and sensing properties", *Sensors and Actuators B: Chemical,* vol. 111, pp. 2-6, 2005.
[137] E. Comini, "Metal oxide nano-crystals for gas sensing", *Analytica Chimica Acta,* vol. 568, pp. 28-40, 2006.
[138] G. Wang, J. Park, M. Park, and X. L. Gou, "Synthesis and high gas sensitivity of tin oxide nanotubes", *Sensors and Actuators B: Chemical,* vol. 131, pp. 313-317, 2008.
[139] M. Law, D. J. Sirbuly, J. C. Johnson, J. Goldberger, R. J. Saykally, and P. Yang, "Nanoribbon Waveguides for Subwavelength Photonics Integration", *Science,* vol. 305, pp. 1269-1273, 2004.
[140] S. X. Mao, M. Zhao, and Z. L. Wang, "Nanoscale mechanical behavior of individual semiconducting nanobelts", *Applied Physics Letters,* vol. 83, pp. 993-995, 2003.
[141] L. Shi, Q. Hao, C. Yu, N. Mingo, X. Kong, and Z. L. Wang, "Thermal conductivities of individual tin dioxide nanobelts", *Applied Physics Letters,* vol. 84, pp. 2638-2640, 2004.
[142] K. Young-Dae, K. Jin-Gu, P. Jae-Gwan, L. Sungjun, and K. Dong-Wan, "Self-supported SnO_2 nanowire electrodes for high-power lithium-ion batteries", *Nanotechnology,* vol. 20, p. 455701, 2009.
[143] J. Liu, Y. Li, X. Huang, R. Ding, Y. Hu, J. Jiang, and L. Liao, "Direct growth of SnO_2 nanorod array electrodes for lithium-ion batteries", *Journal of Materials Chemistry,* vol. 19, pp. 1859-1864, 2009.

[144] A. A. Ansari, P. R. Solanki, and B. D. Malhotra, "Sol-gel Derived Nanostructured Tin Oxide Film for Glucose Sensor", *Sensor Letters,* vol. 7, pp. 64-71, 2009.
[145] S. Shukla, V. Venkatachalapathy, and S. Seal, "Thermal evaporation processing of nano and submicron tin oxide rods", *J Phys Chem B,* vol. 110, pp. 11210-6, 2006.
[146] Z. R. Dai, Z. W. Pan, and Z. L. Wang, "Novel Nanostructures of Functional Oxides Synthesized by Thermal Evaporation", *Advanced Functional Materials,* vol. 13, pp. 9-24, 2003.
[147] M.-R. Yang, S.-Y. Chu, and R.-C. Chang, "Synthesis and study of the SnO_2 nanowires growth", *Sensors and Actuators B: Chemical,* vol. 122, pp. 269-273, 2007.
[148] Z. R. Dai, Z. W. Pan, and Z. L. Wang, "Growth and Structure Evolution of Novel Tin Oxide Diskettes", *Journal of the American Chemical Society,* vol. 124, pp. 8673-8680, 2002.
[149] J. Q. Hu, Y. Bando, and D. Golberg, "Self-catalyst growth and optical properties of novel SnO_2 fishbone-like nanoribbons", *Chemical Physics Letters,* vol. 372, pp. 758-762, 2003.
[150] N. S. Ramgir, I. S. Mulla, and K. P. Vijayamohanan, "Effect of RuO_2 in the Shape Selectivity of Submicron-Sized SnO_2 Structures", *The Journal of Physical Chemistry B,* vol. 109, pp. 12297-12303, 2005.
[151] A. Kar, J. Yang, M. Dutta, M. A. Stroscio, J. Kumari, and M. Meyyappan, "Rapid thermal annealing effects on tin oxide nanowires prepared by vapor-liquid-solid technique", *Nanotechnology,* vol. 20, p. 065704, 2009.
[152] E. R. Leite, J. W. Gomes, M. M. Oliveira, E. J. Lee, E. Longo, J. A. Varela, C. A. Paskocimas, T. M. Boschi, J. F. Lanciotti, P. S. Pizani, and P. C. Soares Junior, "Synthesis of SnO_2 nanoribbons by a carbothermal reduction process", *J Nanosci Nanotechnol,* vol. 2, pp. 125-8, 2002.
[153] Z. Liu, D. Zhang, S. Han, C. Li, T. Tang, W. Jin, X. Liu, B. Lei, and C. Zhou, "Laser Ablation Synthesis and Electron Transport Studies of Tin Oxide Nanowires", *Advanced Materials,* vol. 15, pp. 1754-1757, 2003.
[154] Y.-J. Ma, F. Zhou, L. Lu, and Z. Zhang, "Low-temperature transport properties of individual SnO_2 nanowires", *Solid State Communications,* vol. 130, pp. 313-316, 2004.
[155] Y. Liu and M. Liu, "Growth of Aligned Square-Shaped SnO_2 Tube Arrays", *Advanced Functional Materials,* vol. 15, pp. 57-62, 2005.
[156] S. Mathur, S. Barth, H. Shen, J.-C. Pyun, and U. Werner, "Size-Dependent Photoconductance in SnO_2 Nanowires", *Small,* vol. 1, pp. 713-717, 2005.
[157] G. Zhang and M. Liu, "Preparation of nanostructured tin oxide using a sol-gel process based on tin tetrachloride and ethylene glycol", *Journal of Materials Science,* vol. 34, pp. 3213-3219, 1999.
[158] S. V. Manorama, C. V. Gopal Reddy, and V. J. Rao, "Tin dioxide nanoparticles prepared by sol-gel method for an improved hydrogen sulfide sensor", *Nanostructured Materials,* vol. 11, pp. 643-649, 1999.
[159] H. Wang, J. Liang, H. Fan, B. Xi, M. Zhang, S. Xiong, Y. Zhu, and Y. Qian, "Synthesis and gas sensitivities of SnO_2 nanorods and hollow microspheres", *Journal of Solid State Chemistry,* vol. 181, pp. 122-129, 2008.
[160] Y. Wang, J. Y. Lee, and H. C. Zeng, "Polycrystalline SnO_2 Nanotubes Prepared via Infiltration Casting of Nanocrystallites and Their Electrochemical Application", *Chemistry of Materials,* vol. 17, pp. 3899-3903, 2005.

[161] J. Huang, N. Matsunaga, K. Shimanoe, N. Yamazoe, and T. Kunitake, "Nanotubular SnO_2 Templated by Cellulose Fibers: Synthesis and Gas Sensing", *Chemistry of Materials,* vol. 17, pp. 3513-3518, 2005.
[162] W. Zhu, W. Wang, H. Xu, and J. Shi, "Fabrication of ordered SnO_2 nanotube arrays via a template route", *Materials Chemistry and Physics,* vol. 99, pp. 127-130, 2006.
[163] D. F. Zhang, L. D. Sun, J. L. Yin, and C. H. Yan, "Low-Temperature Fabrication of Highly Crystalline SnO_2 Nanorods", *Advanced Materials,* vol. 15, pp. 1022-1025, 2003.
[164] M. Samal and D. K. Yi, "Tin Dioxide Nanowires: Evolution and Perspective of the Doped and Nondoped Systems", *Critical Reviews in Solid State and Materials Sciences,* vol. 38, pp. 91-127, 2013.
[165] D. Li, Y. Wang, and Y. Xia, "Electrospinning of Polymeric and Ceramic Nanofibers as Uniaxially Aligned Arrays", *Nano Letters,* vol. 3, pp. 1167-1171, 2003.
[166] J. T. McCann, D. Li, and Y. Xia, "Electrospinning of nanofibers with core-sheath, hollow, or porous structures", *Journal of Materials Chemistry,* vol. 15, pp. 735-738, 2005.
[167] A. Yang, X. Tao, G. K. H. Pang, and K. G. G. Siu, "Preparation of Porous Tin Oxide Nanobelts Using the Electrospinning Technique", *Journal of the American Ceramic Society,* vol. 91, pp. 257-262, 2008.
[168] E. N. Kumar, R. Jose, P. S. Archana, C. Vijila, M. M. Yusoff, and S. Ramakrishna, "High performance dye-sensitized solar cells with record open circuit voltage using tin oxide nanoflowers developed by electrospinning", *Energy & Environmental Science,* vol. 5, pp. 5401-5407, 2012.
[169] C.-Y. Kuo, K.-H. Huang, and S.-Y. Lu, "Fabrication of synthetic opals composed of mesoporous SnO_2 spheres with an anodization-assisted double template process", *Electrochemistry Communications,* vol. 9, pp. 2867-2870, 2007.
[170] A. Kolmakov, Y. Zhang, and M. Moskovits, "Topotactic Thermal Oxidation of Sn Nanowires: Intermediate Suboxides and Core−Shell Metastable Structures", *Nano Letters,* vol. 3, pp. 1125-1129, 2003.
[171] A. Yamaguchi, T. Iimura, K. Hotta, and N. Teramae, "Transparent nanoporous tin-oxide film electrode fabricated by anodization", *Thin Solid Films,* vol. 519, pp. 2415-2420, 2011.
[172] M. A. Hossain, G. Yang, M. Parameswaran, J. R. Jennings, and Q. Wang, "Mesoporous SnO_2 Spheres Synthesized by Electrochemical Anodization and Their Application in CdSe-Sensitized Solar Cells", *The Journal of Physical Chemistry C,* vol. 114, pp. 21878-21884, 2010.
[173] E. Giani and R. Kelly, "A Study of SnO2 Thin Films Formed by Sputtering and by Anodizing", *Journal of The Electrochemical Society,* vol. 121, pp. 394-399, 1974.
[174] G. H. A. Therese and P. V. Kamath, "Electrochemical Synthesis of Metal Oxides and Hydroxides", *Chemistry of Materials,* vol. 12, pp. 1195-1204, 2000.
[175] T. Pauporté and D. Lincot, "Hydrogen peroxide oxygen precursor for zinc oxide electrodeposition II—Mechanistic aspects", *Journal of Electroanalytical Chemistry,* vol. 517, pp. 54-62, 2001.
[176] M. Izaki and T. Omi, "Characterization of Transparent Zinc Oxide Films Prepared by Electrochemical Reaction", *Journal of The Electrochemical Society,* vol. 144, pp. 1949-1952, 1997.
[177] S. Peulon and D. Lincot, "Mechanistic Study of Cathodic Electrodeposition of Zinc Oxide and Zinc Hydroxychloride Films from Oxygenated Aqueous Zinc Chloride Solutions", *Journal of The Electrochemical Society,* vol. 145, pp. 864-874, 1998.

[178] S.-T. Chang, I.-C. Leu, and M.-H. Hon, "Preparation and characterization of nanostructured tin oxide films by electrochemical deposition", *Electrochemical and solid-state letters,* vol. 5, pp. C71-C74, 2002.
[179] S. T. Chang, I. C. Leu, and M. H. Hon, "Electrodeposition of nanocrystalline SnO_2 coatings with two-layer microstructure", *Journal of Crystal Growth,* vol. 273, pp. 195-202, 2004.
[180] R. L. Spray and K.-S. Choi, "Electrochemical synthesis of SnO_2 films containing three-dimensionally organized uniform mesopores via interfacial surfactant templating", *Chemical Communications,* vol. 0, pp. 3655-3657, 2007.
[181] T. Ishizaki, N. Saito, and O. Takai, "Surfactant-Assisted Fabrication of Tin Oxide Nanowires Through One-Step Electrochemically Induced Chemical Deposition", *Journal of The Electrochemical Society,* vol. 156, pp. D413-D417, 2009.
[182] S. Kim, H. Lee, C. M. Park, and Y. Jung, "Synthesis of tin oxide nanoparticle film by cathodic electrodeposition", *J Nanosci Nanotechnol,* vol. 12, pp. 1616-9, 2012.
[183] M. Lai, J. A. Gonzalez Martinez, M. Gratzel, and D. J. Riley, "Preparation of tin dioxide nanotubes via electrosynthesis in a template", *Journal of Materials Chemistry,* vol. 16, pp. 2843-2845, 2006.
[184] X. Chen, J. Liang, Z. Zhou, H. Duan, B. Li, and Q. Yang, "The preparation of SnO_2 film by electrodeposition", *Materials Research Bulletin,* vol. 45, pp. 2006-2011, 2010.
[185] Junie Jhon M. Vequizo, Jun Wang, and Masaya Ichimura, "Electrodeposition of SnO_2 Thin Films from Aqueous Tin Sulfate Solutions", *Japanese Journal of Applied Physics,* vol. 49, pp. 125502-125506, 2010.
[186] G. She, L. Mu, and W. Shi, "Electrodeposition of one-dimensional nanostructures", *Recent Pat Nanotechnol,* vol. 3, pp. 182-91, 2009.

CHAPTER II: **Experimental procedures**

This chapter describes the whole experimental process leading to the final DNA biosensor. It is schematically presented in **Figure 2.1**.

In the first part, we present how the different SnO_2 nanostructures are fabricated using the electrodeposition method according to different experimental conditions.

The second part presents different characterization techniques used to study their morphology, microstructure and electrical properties.

The third part deals with the functionalization process used to bio-modify the deposited SnO_2 nanostructures including silanization, DNA probe immobilization and DNA hybridization.

Finally, in the last part, we describe the detection of DNA hybridization by both impedance and fluorescence techniques.

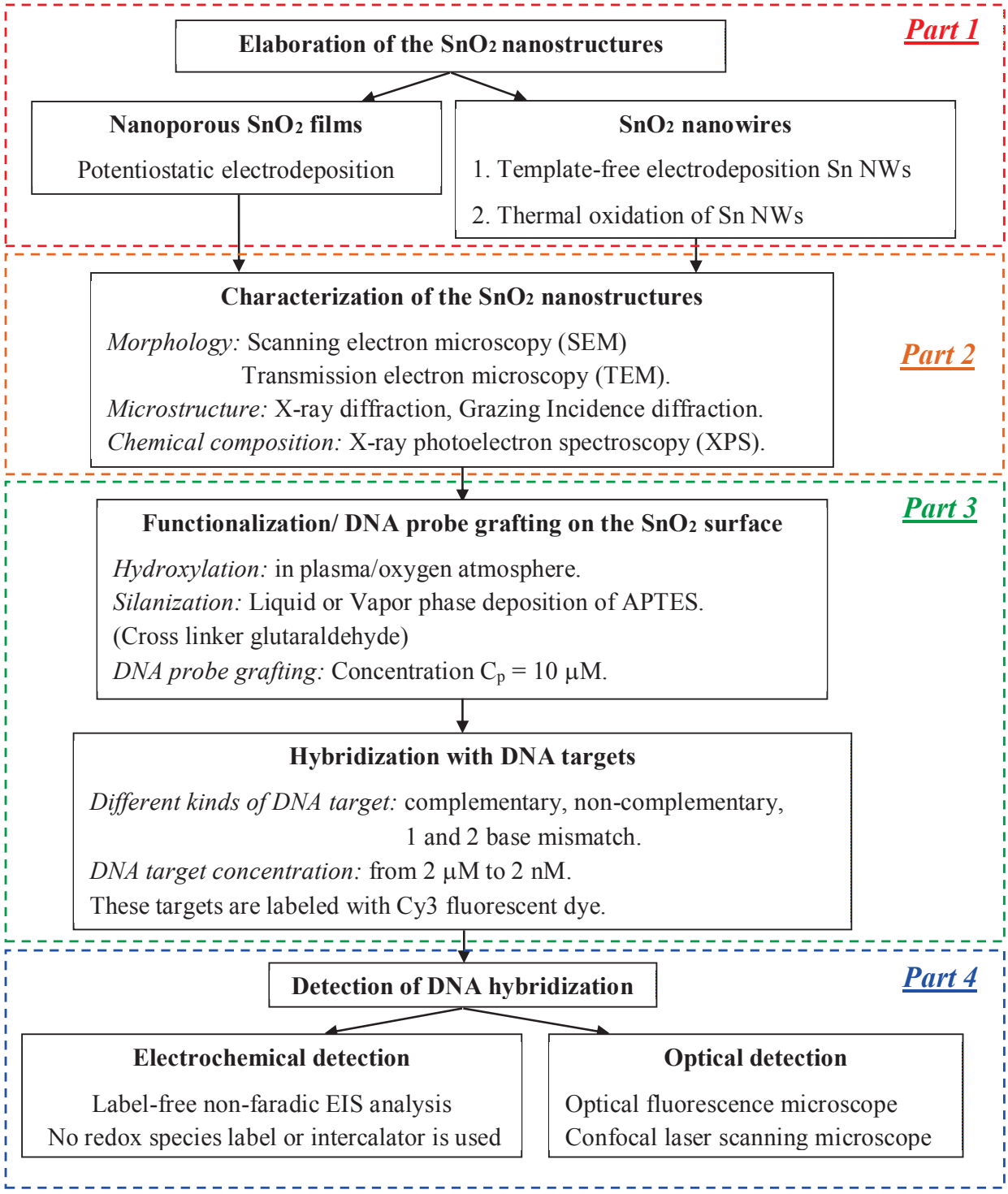

Figure 2.1: Flow chart of overall work in this study

2.1 Elaboration of SnO_2 nanostructures

2.1.1 Electrodeposition system

The electrodepostion system that we have mounted is the same for the deposition of both nanoporous SnO_2 films and Sn NWs. It is described first, and then the specific conditions for each case are reported.

The electrodeposition is performed in a 3-electrode-electrochemical configuration (**Figure 2.2-left**). Practically, the electrochemical cell could be made up of two electrodes. In this case, the second electrode must maintain a constant potential to gauge the potential of the working electrode while passing current to counter redox events at the working electrode during the process. However, a current passing through an electrode can also change its potential. Therefore, it is extremely difficult for an electrode to do both of the works at the same time. By using 3-electrode cell, the roles of supplying electrons and providing a reference potential are divided between two separate electrodes. The reference electrode, with a known potential, acts as reference in measuring and controlling the working electrode potential. On the other hand, the counter electrode passes all the current needed to balance the current observed at the working electrode.

Electrochemical cell: A rounded glass cell with 3 necks is used. Its volume is 250 ml. The temperature of the solution inside the cell is regulated using a programmed heater and a thermometer.

Working electrode: Commercial ITO (Indium tin-oxide) coated soda-lime-glass substrates, purchased from Advanced Film Services Company, USA, are used for all electrodeposition. The size of one commercial sheet is 200 x 200 x 1.1 mm. The thickness of the ITO layer is 300 nm, with a sheet resistance of 10Ω/□. Before performing electrodeposition process of SnO_2 on the ITO surface, the sheets are cut to a final size of 10 x 25 mm and are subjected to a cleaning process in order to remove all the impurities on the surface collected after fabrication or during the storage.

These substrates are first cleaned with commercial soap and rinsed with boiled deionized water. Then the substrates are sonicated with the following sequence: 15 minutes in ethanol, 15 minutes in acetone and 15 minutes in iso-propanol. Between each bath of solvent, the substrates are rinsed with boiled deionized water and dried by cleanroom-tissues. Then, the ITO/glass substrate is installed into the cell with a vertical arrangement by using a specific Teflon holder which has been made in our laboratory (**Figure 2.2-middle**). It also controls the area of the working electrode exposed to the electrolyte, the surface of which is 1 cm^2 for all experiments.

Reference electrode: A commercial Ag/AgCl (KCl saturated) purchased from Radiometer Analytical. Its potential is determined by the reaction $AgCl(s) + e^- = Ag(s) + Cl^-$ of which relative

to the normal hydrogen electrode (NHE) is 0.208 V at room temperature. The reference electrode is located as close as possible to the working electrode in the cell.

Counter electrode: A rolled platinum wire (d = 0.5 mm) (**Figure 2.2-right**). The counter electrode is mounted parallel and with a distance of 10 mm from the working electrode surface.

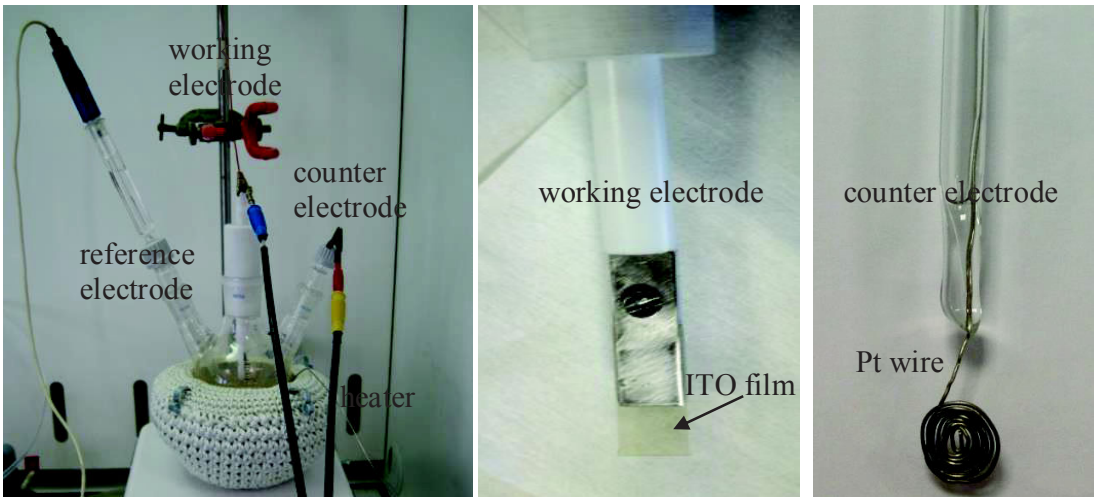

Figure 2.2: Pictures of the electrodeposition sytem, working electrode and counter electrode.

Electrolyte: To prevent the contamination, the electrodeposition experiments were carried out with solutions freshly prepared with MilliQ water. The volume of the electrolyte is 80 ml for all experiments. All the reagents employed are of analytical grade. The composition of the electrolyte is adapted according to the kind of SnO_2 nanostructures (**Table 2.1**).

Table 2.1: Chemicals used for the electrolyte preparation

Chemical	Formula	Supplier	Purity
Dihydrated tin chloride	$SnCl_2.2H_2O$	Sigma Aldrich	(> 99.99%)
Nitric acid	HNO_3	Sigma Aldrich	(> 65%)
Sodium nitrate	$NaNO_3$	Sigma Aldrich	(>99%)

Instrumentation: The three electrodes of the electrochemical cell are connected to a potentiostat/galvanostat Model 263A (Princeton Applied Research) controlled by the software Powersuite (**Figure 2.3**).

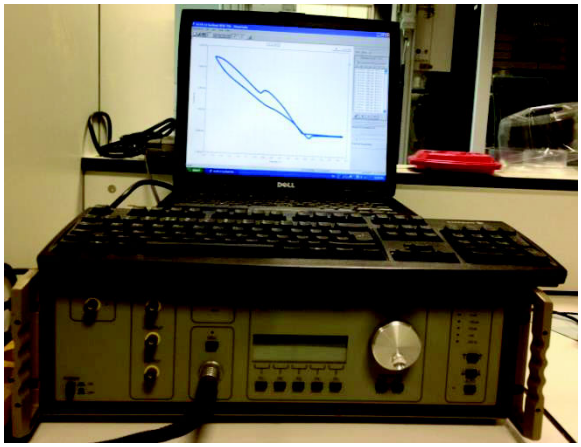

Figure 2.3: Picture of the electrochemical equipment: potentiostat/galvanostat Model 263A (Princeton Applied Research)

2.1.2 Electrochemical techniques

Cyclic voltametry: This technique consists of scanning the potential of the working electrode, which is immersed in a solution, and measuring the resulting current. It is a popular tool for studying the general electrochemical behavior of the different solutions used to grow the material nanostructures under both unstirring and stirring conditions.

The voltage applied to the working electrode is scanned linearly versus time from open circuit potential E_{oc}, at which no current is detected toward negative potentials. E_{oc} is automatically determined from the potentiostat. During the negative scan, the reduction of the electroactive species takes place. When the potential reaches a predetermined negative limit, the scan is reversed. During scanning toward positive potential, the total or partial oxidation of the species previously electrodeposited on the working electrode occurs. The cycle completes when the scan returns to the initial potential E_{oc}. The potential limits are adjusted to cover all the range where the electrochemical reactions of the electroactive species happen. Usually, cyclic voltammetry is carried out at a scan rate of 50 mV s^{-1}.

Cyclic voltammetry allows us to determine the potentials at which the electrochemical reaction takes place on the electrode surface. In addition, by comparing the charges recorded (or the sizes of the peaks) during both reduction and oxidation processes, we can evaluate the presence of side reactions taking place simultaneously with electrodeposition.

Electrodeposition: Depending on the applied signal, electrodeposition can be conducted following a chronoamperometry regime (potentiostatic technique) or a chronopotentiometry regime (galvanostatic technique).

A potentiostatic synthesis is performed by polarizing the working electrode to a desired potential with respect to the reference electrode. The variation of the cell current is recorded as a function of time (I-t). During the process, the cell current decays as electrochemical reaction begins. It is due to the low rates of diffusion of the reactants from the bulk solution to the electrode surface or due to reduction in activity of the reactant. Generally, a pure single-phase product is obtained. The nature of the product relies on the electrochemical reaction occurring on electrode surface at the selected applied potential. Usually, the deposition potential is chosen from the cyclic voltammogram of the system.

In a galvanostatic synthesis, the cell current is held at a constant value and the potential-time curve is recorded (E-t). Because the rate of the reaction is monitored, the deposits often present a good adhesion and a controlled morphology. However, the cell potential drifts as the reactant activity decreases at the working electrode surface. It may lead to a multiplicity of products.

In practice, in addition to applied potential (E) and cell current (I), the deposit characteristics also depend on other processing parameters. For example, concentration of the electroactive species strongly affects the rate of electrode reaction. Consequently, it will much influence on the deposit characteristics: microstructure and morphology of the deposit. The important parameters in the electrochemical cell are shown in **Figure 2.4**.

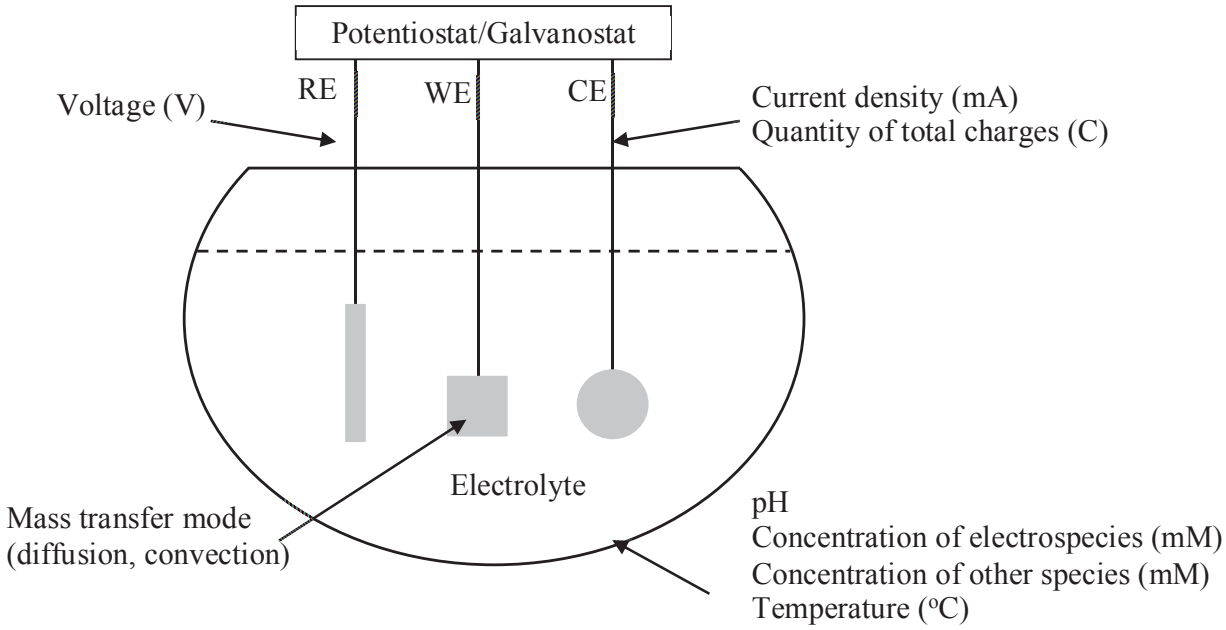

Figure 2.4: Important parameters in an electrochemical cell.

2.1.3 Electrodeposition of SnO_2 nanoporous films

The nanoporous SnO_2 thin films are potentiostatically electrodeposited onto ITO substrates in an electrolyte with composition as showed in **Table 2.2**. For all the experiments, the concentration of HNO_3 is fixed at 75mM, in which the solution pH is approximately 1.25. For deposition conducted at a temperature, the cell is first heated up to reach the desired temperature. Then it is maintained at this point for 10 minutes to achieve temperature homogeneity for whole the cell before the experiment is started. To avoid a decrease in the volume of the electrolyte due to water evaporation at high temperatures, a water-circulated condenser is used during heating process.

The present work started from the deposition process proposed by Chang et al. [1] but with some important modifications that are listed in the following table (**Table 2.2**).

Table 2.2: Comparison of processing parameters between the Chang et al. deposition process and our process

Parameters	***Chang et al. [1-2]***	***Our work***
Substrate	Cu	ITO
Pre-treatment	The electrolyte was held at 85°C for 3h without oxygen blowing or for 1h with oxygen blowing	No
T° electrolyte (during process)	85 °C	50 °C
Electrolyte	20 mM $SnCl_2.2H_2O$ 100 mM $NaNO_3$ 75 mM HNO_3	20 mM $SnCl_2.2H_2O$ 100 mM $NaNO_3$ 75 mM HNO_3
Stirring	Not mentioned	No
Regime	Galvanostatic I = 1 to 15 mA cm^{-2}	Potentiostatic Deposition voltage is selected from the cyclic voltammogram, which is from -1.0 to -0.5 V (vs. Ag/AgCl).

First, Chang et al [1] deposited SnO_2 on Cu electrode which is not the case here as we use ITO. Second, the electrolyte was held at a temperature of 85°C for 3h prior to deposition experiment in order to obtain stabilized solution. In this study, as will be explained in section 3.1 chapter 3, such process is omitted and the temperature of the cell is kept at 50°C during deposition process. The nanoporous SnO_2 thin films are electrodeposited potentiostatically onto ITO electrodes in an electrolyte consisted of 20 mM $SnCl_2.2H_2O$, 100 mM $NaNO_3$ and 75 mM HNO_3 under unstirring

condition. The deposition potentials are selected from the voltammograms obtained in these same conditions. To achieve the desired thickness of the film, total passed charge density is controlled.

We also investigated the impact of some experimental factors including: convection force (stirring speed), concentration of $SnCl_2.2H_2O$ and $NaNO_3$, cell temperature on the electrochemical behavior and the obtained phases and morphology of the as-deposited films.

2.1.4 Elaboration of SnO_2 nanowires

The elaboration of the 1D SnO_2 NWs based on a two-step-process. The first step is the template-free electrodeposition of Sn NWs on the ITO electrodes. The second step deals with converting these deposited Sn NWs to form SnO_2 NWs by thermal oxidation.

2.1.4.1 Electrodeposition of Sn nanowires

Although template-assisted electrodeposition has been successfully employed for the preparation of 1-D Sn morphology [3], to our knowledge, no other reported in template-free electrodeposition of Sn NWs.

In our work, Sn nanowires are galvanostatic electrodeposited on the ITO/glass substrate from a colloidal solution of 20mM $SnCl_2.2H_2O$ in 80 ml of deionized water. Processing parameters of the electrodeposition process are detailed in **Table 2.3**.

Table 2.3: Processing parameters of electrodeposition Sn NWs process

Substrate	ITO
Pre-treatment	The electrolyte is sonicated for 10 min
T° electrolyte (during process)	22±2 °C
Electrolyte	20 mM $SnCl_2.2H_2O$
Stirring	No
Regime	Galvanostatic Current density: 5 mA cm^{-2} Deposition time: 20 s

The electrolyte is sonicated for 10 minutes before pouring it into the cell to obtain a homogeneous colloidal solution. The deposition experiments are performed at room temperature, 22±2 °C. The

effects of current density and the deposition time on the Sn NWs growth process as well as on the morphology of the NWs are investigated.

2.1.4.2 Thermal oxidation of Sn nanowires

To convert the deposited Sn nanowires to SnO_2 nanowires, thermal oxidation is carried out in a process approximating rheotaxial growth and thermal oxidation (RGTO) published elsewhere [4]. The RGTO method has proved to be effective for complete oxidation of Sn films, and nanowires [4-5]. The crucial feature of this process is that the shapes of the Sn nanowires are maintained during their conversion to tin oxide. The first stage of the process involves heating the Sn sample (in ambient condition) to a temperature just below the melting point of Sn (about 200 ºC) in order to grow on the surface of the tin nanowires a thin supporting oxide skin. This oxide supports the Sn core and resists deformation during a subsequent higher temperature process (500 ºC) which completes the oxidation of the tin nanowires to tin oxide nanowires. The heat-treatment profile is shown in the **Figure 2.5**.

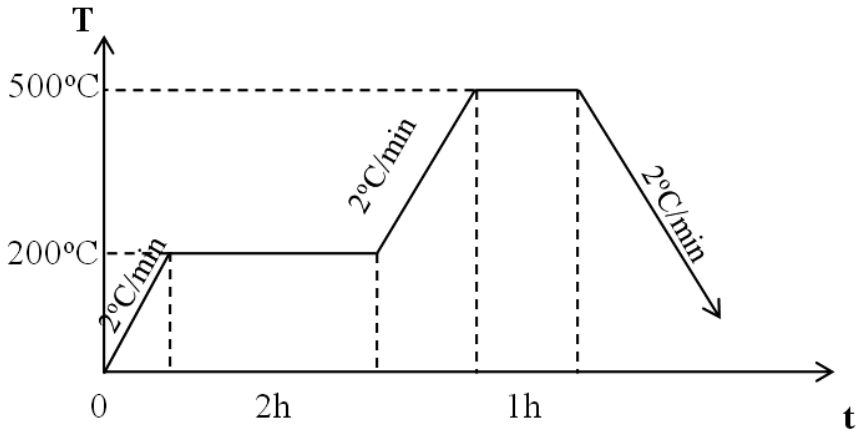

Figure 2.5: Profile of the heat-treatment process for full oxidation of electrodeposited Sn NWs

2.2 Characterization of the elaborated SnO_2 nanostructures

2.2.1 Morphology

The morphology of the electrodeposited SnO_2 nanostructures is observed by scanning electron microscopy (SEM). The type of apparatus used is a Quanta 200 FEG / ESEM (FEI Phillips). The electron microscope is operated at a 5kV accelerating voltage in high vacuum mode (total vacuum of 10^{-6} mbar) and has a resolution of 3 nm. The two signals mainly used in microscopy are the secondary and backscattered electrons (**Figure 2.6**). The secondary electrons are of low energy

electrons (<50eV) which emitted by atoms near the surface of a sample material when their electrons become excited and have sufficient energy to escape the sample surface. On the other hand, the backscattered electrons have higher energy, which are the electrons that have been scattered out of the sample by elastic collision with the sample atoms. Of the two, secondary electron imaging has greater resolution. However, backscattered electrons have the advantage that they are sensitive to the atomic mass of the atoms they scatter from. As a result, heavier elements which backscatter more efficiently appear brighter than lighter elements in a backscattered electron image.

Due to their low conductivity resulting in a charging of the films, the deposited SnO_2 films are often coated with a thin carbon layer before SEM observation. Film thickness, diameters and lengths of the nanowires are measured from the SEM image taken in cross-sectional view. The cross-sectional view could be achieved by cutting the samples. The cutting process consists of making a scratched line at the back side of the sample using a diamond tip and separating it into two parts at this line by a specific tool.

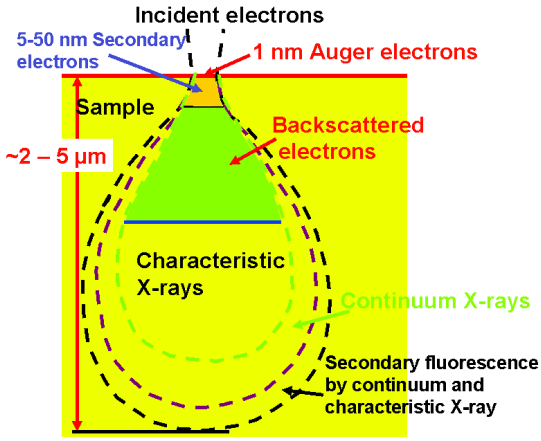

Figure 2.6: Electron beam interaction with the analyzed surface diagram

The morphology of the deposited SnO_2 nanostructures is also studied by a high resolution transmission electron microscopy (HRTEM). From the cross-sectional observation, the substrate, the thin film layers, and the interfaces between them can be imaged either simultaneously or individually.

Importantly, selected area electron diffraction (SAED) can be performed inside a transmission electron microscope (TEM). This crystallographic technique obtains diffraction patterns that result from the electron beam scattered by the sample lattice. From an SAED pattern the structural information of the sample: crystalline symmetry, unit cell parameter and space group, can be obtained.

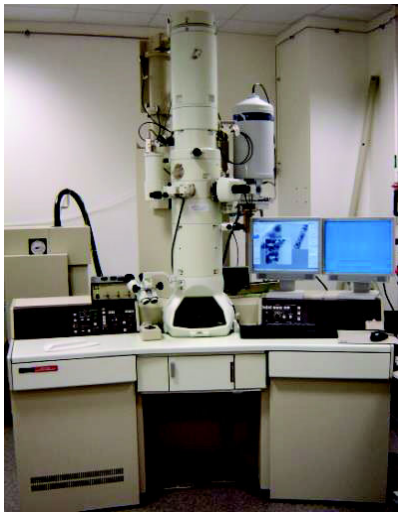

Figure 2.7: Transmission electron microscopy JEOL 2011

TEM and electron diffraction were carried out on a JEOL 2011 (**Figure 2.7**) operating at 200 kV with a 0.19-nm point-to point resolution. Cross-section samples were obtained by the tripod method. Samples were polished on both sides using diamond impregnated films from 15 mm sequentially down to 0.5 mm until they were less than 15 mm thick. Low-angle ion Ar^+ beam milling was used for final perforation of the samples and to minimize contamination.

2.2.2 Microstructure

The X-ray diffraction (XRD) is a technique commonly used to determine the structure and the crystallographic orientation of a solid material. In this method, the sample is irradiated with an X-rays monochromatic beam at an incident angle (represented in Figure 2.8). The incident X-ray radiation excites the atoms in the crystal and relaxes by emitting radiation of spherical waves. When the sample has a crystalline structure, diffraction is observed when the waves associated with X-rays are in phase together (constructive interferences). This phenomenon happens when the Bragg condition following is satisfied:

$$n\lambda = 2d_{hkl}.\sin\theta \qquad (2.1)$$

where, d_{hkl} is the distance between the lattice planes (hkl) of the crystal lattice, θ is the incident angle of X-rays relative to the surface of the sample, λ is the wavelength of the incident beam and n is an integer representing the order of diffraction mode.

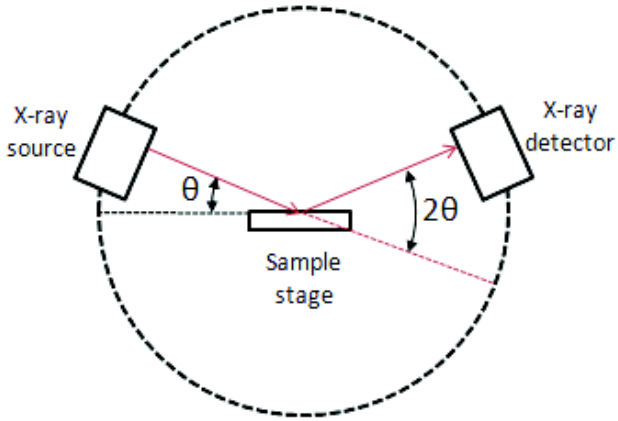

Figure 2.8: Schematic of Bragg spectrometer

In the present work, measurements are performed on a Siemens X-ray diffractometer Bruker D5000 Diffraktometer using the Bragg-Brentano geometry (θ-2θscans). X-rays were produced from a source of copper Kα radiation (λ = 0.154 nm), with an accelerating voltage of 40 kV and a current of 20 mA. The scans are performed between 20 and 70° with a step of 0.02°.

The phase identification and crystal orientation could be done by comparing the obtained spectra (positions and intensities of the diffracted rays) with the spectra of known phases of reference compounds stored in the database JCPDS-ICDD data.

Peak widths and shapes provide important information about the structural and microstructural properties of the material: crystallite size and defects. The crystallite size can be calculated from the peak widths at half maximum or FWHM (Full Width at Half Maximum) according to the Scherrer formula (assuming that the crystallites are spherical), which is defined by:

$$d = \frac{0.9\,\lambda}{\beta \cos\theta} \qquad (2.2)$$

Where, λ is the X-ray wavelength (in the case of Cu target, λ = 0.154 nm), d is the average crystalline size, θ is the half of the diffraction angle, β is the full width at half maximum (FWHM).

Grazing Incidence Diffraction (GID): X-ray radiation has a large penetration depth into any matter. Consequently, this technique is difficult to analyze thin films due to their small diffracting volumes, which results in low diffracted intensities compared to the substrate and background. Grazing Incidence Diffraction (GID) is the technique to overcome this restriction. GID measurements are performed at very low incident angles to maximize the signal from the thin layers.

For the GID, the incident and diffracted beams are made nearly parallel by means of a narrow slit on the incident beam and along Soller slit on the detector side. The stationary incident beam makes

a very small angle with the sample surface (typically 0.3°to 3°), which increases the path length of the X-ray beam through the film. This helps to increase the diffracted intensity, while at the same time, reduces the diffracted intensity from the substrate. During the collection of the diffraction spectrum, only the detector rotates through the angular range, thus keeping the incident angle, the beam path length, and the irradiated area constant. Grazing incidence analysis is performed by the same apparatus as that of X-ray diffraction test.

2.2.3 Chemical composition of the extreme surface

X-ray photoelectron spectroscopy (XPS) is a quantitative spectroscopic technique that measures the elemental composition, empirical formula, chemical state and electronic state of the elements that exist within a material. XPS measurements are performed by irradiating a material with a beam of X-rays while simultaneously measuring the kinetic energy and number of electrons that escape from the top 1 to 10 nm of the analyzed material. The kinetic energy of the photoelectrons detected is:

$$E_{kinetic} = h\upsilon - E_{binding} \quad (2.3)$$

Where, $h\upsilon$ is the energy of incident X photons and $E_{binding}$ is the binding energy of the photoelectron emitted.

The calculation of the binding energy of the detected electrons allows knowing the nature of the photoelectron emitting atom (except hydrogen and helium) and the orbital from which the electron originates. The measured area of the detected peak determines the relative concentrations of these species in the studied material. The obtained chemical shift provides the information about the chemical groups presenting in the film. Thus the decomposition of an XPS peak is commonly used to calculate the concentrations of various chemical groups and to have an idea of the structure of the material.

XPS analysis were carried-out by means of XPS (XR3E2) located at laboratory SIMAP – Grenoble INP, in an UHV chamber (10^{-10} mbar), using a Mg K_α radiation. The samples were irradiated under normal incidence and the probed thickness was around 10 nm. To study compositions of the deposited thin films, the measurement is only qualitative. Moreover, the measurements do not reflect the overall structure of the sample and on the other hand, the absorbed surface species (such as carbon, oxygen) take a significant part in the quantification of elements.

2.2.4 Electrochemical properties

Electrochemical impedance spectroscopy (EIS) has been well established as a powerful tool for investigating the mechanism of electrochemical reactions, for measuring the dielectric and transport properties of materials, for exploring the properties of the porous electrodes and for investigating passive surfaces [6].

In present work, the study of the electrochemical properties of the elaborated and bio-modified SnO_2 nanostructures has been performed. The impedance measurements are carried out on the deposited SnO_2 electrode by using a laboratory-made microfluidics cell involving a Plexiglass three-electrode setup (**Figure 2.9-left**).

The electrolyte used is the pure DNA hybridization buffer (NaCl: 0.5M, PBS 0.01M without DNA molecules). The volume of the liquid in the cell is 500 µL for each measurement. The SnO_2 films act as the working electrode with an area of 0.19cm^2 which is exposed to the electrolyte. The reference electrode Ag/AgCl is made by immerging an Ag wire (0.5 mm diameter) into the solution of $FeCl_2$ for a few seconds. The counter electrode is a platinum wire with a diameter of 0.5 mm.

A multi-potentiostat (VMP, Biologic S.A, France) is used for the electrochemical measurements (**Figure 2.9-right**). It is linked to a computer for data acquisition and monitored by EC – Lab program. For EIS measurements, this apparatus is used between 10 mHz to 200 kHz with potentials ranging from -0.5 to 0.5 V (vs. ref) and a modulation of 10 mV.

The impedance spectra are analyzed with Z-fit within EC-lab software using Non linear Least Squares Fit principles.

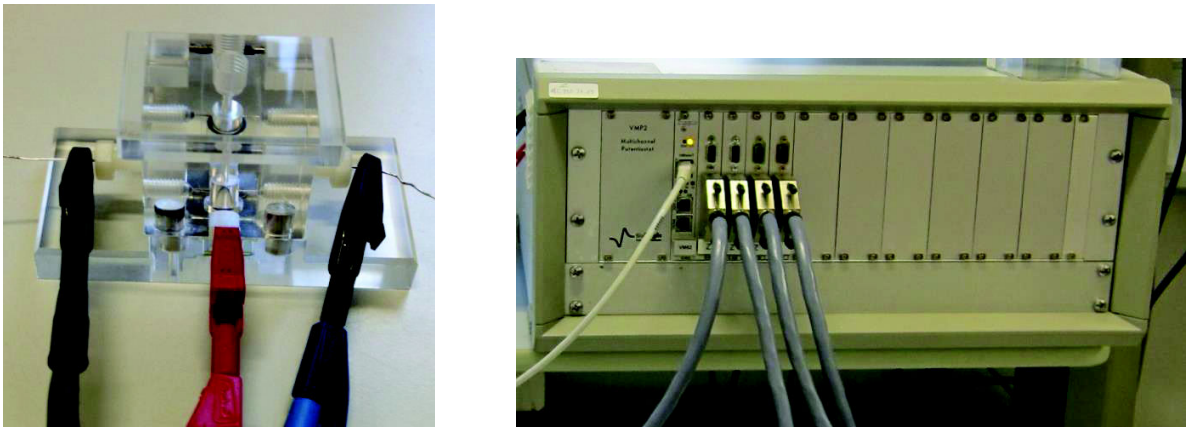

Figure 2.9: Equipments used for impedance measurement: Plexiglass three-electrode cell and multi-potentiostat VMP2, Biologic S.A, France.

2.3 Functionalization, DNA grafting and hybridization

The functionalization process is similar to the one used previously for dense 2D oxide films, except for the vapor silanization part, which has been experimented in this thesis.

Hydroxylation step: The electrodeposited SnO_2 surfaces are treated with oxygen plasma for 4 minutes. RF power is set at 12W and air pressure is about 0.4 Torr. The plasma ionizes the dioxygen molecules of air which removes the carbonic pollution on the sample and creates hydroxyl groups on the surface (**Figure 2.10a**). As a result, the surface becomes hydrophilic. These OH groups allow obtaining a chemically bonding of the functional silane onto the SnO_2 surface (**Figure 2.10b**).

Silanization step: Both liquid-phase and vapor-phase procedures have been tested for deposition of 3-aminopropyl-tri-ethoxyl-silane (APTES) on SnO_2 surface.

Liquid phase deposition of APTES: The silanization is carried out in an organic solvent. The samples are located into a solution containing 0.5M of APTES (Sigma-Aldrich) in 95% absolute ethanol and 5% deionized water under agitation for a night (**Figure 2.11a**). To remove the unbound silane, the samples are carefully rinsed with ethanol and then, with deionized water. This process is followed by curing the samples in an oven at 110°C for 3 hours.

Vapor phase deposition of APTES: The samples first are placed in a teflon holder, which then is put into a glove bag (**Figure 2.11b**). The next step is to draw out the air from the bag using a rotary pump and fill the bag with an argon gas. This step is repeated three times to make sure that the humidity in the bag is as low as about 5%. After 200 µL of APTES is delivered, the lid of the sample holder is closed tightly. This holder is kept at 82°C for 1 hour to cause the evaporation of APTES. To finish, the samples are rinsed carefully with absolute ethanol and deionized water to remove unreacted silane and cured in an oven at 110°C for 1 hour.

In order to achieve a cross binding between NH_2 termination of APTES and the 5'NH_2 termination of the DNA probes, molecules of glutaraldehyde (GA, Sigma-Aldrich) are grafted onto the APTES functionalized surface (**Figure 2.10c**). To perform this step, the samples are immersed in a solution of 10% GA for 90 minutes at room temperature. The double aldehyde terminations are very reactive and bind immediately with each NH_2 termination.

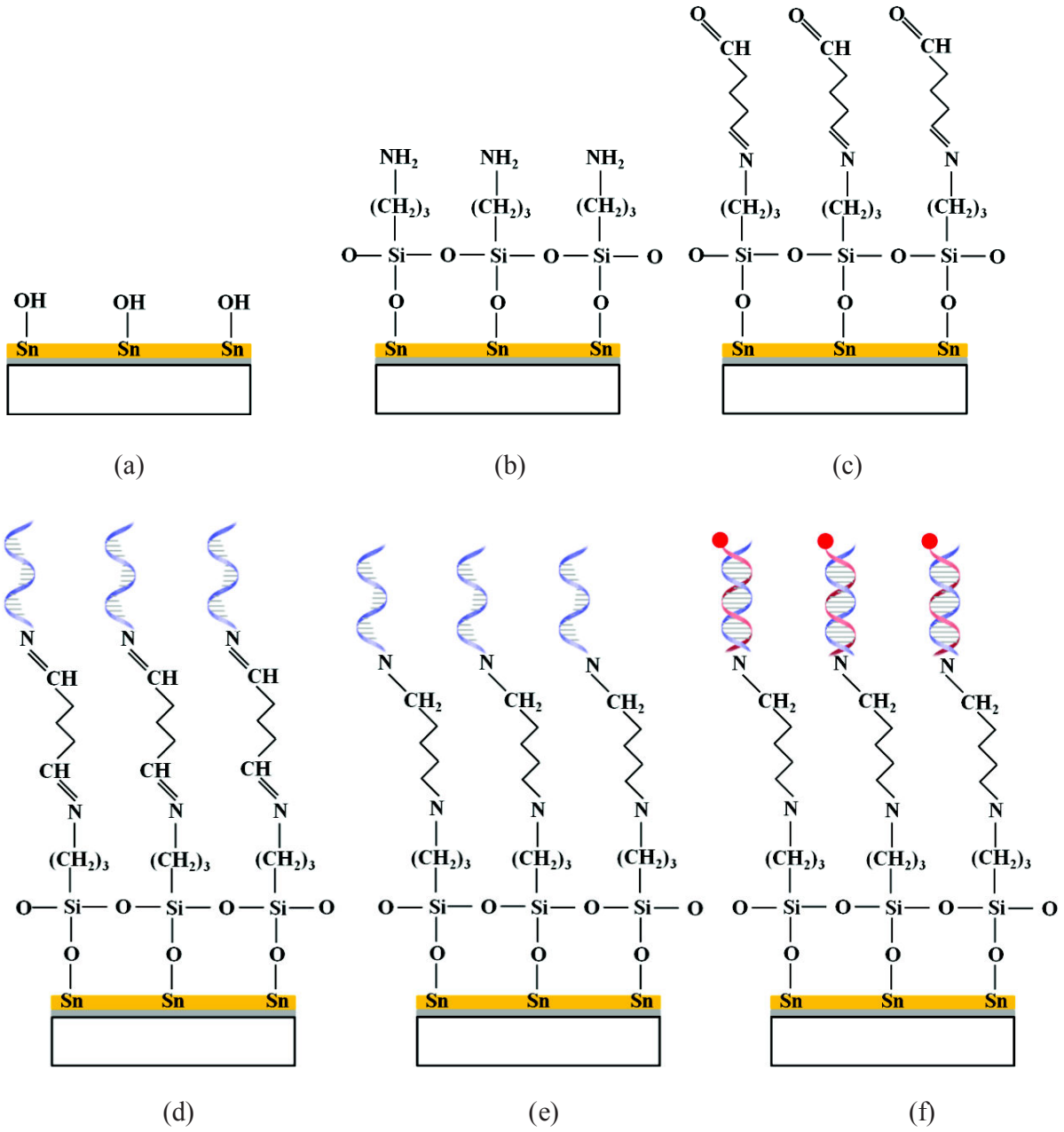

Figure 2.10: Schematic representation of successive functionalization steps performed on all SnO_2 nanostructure surfaces (a) hydroxylation (b) silanization (c) glutaraldehyde grafted onto the silane (d) DNA probe (with NH_2 termination) grafted onto the glutaraldehyde (e) stabilization of the molecule by modifying imine bonding into amine bonding (f) DNA hybridization with DNA targets

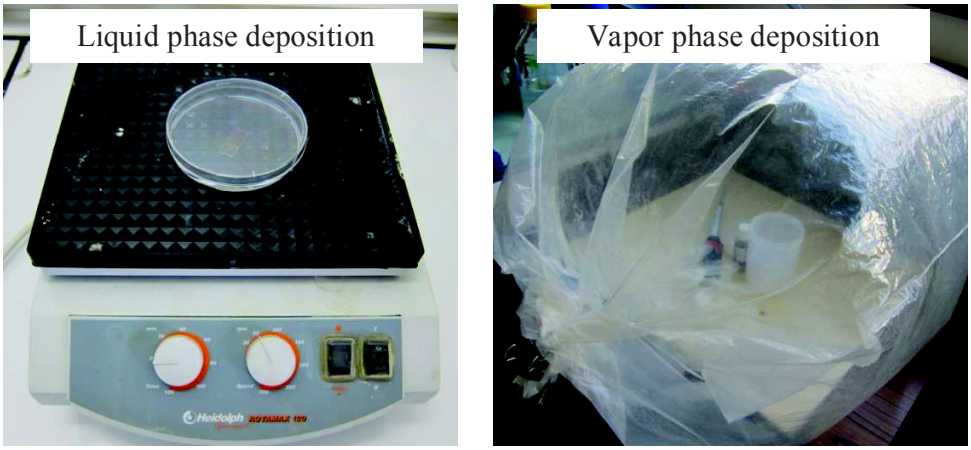

Figure 2.11: Manipulation of liquid and vapor phase deposition of the APTES on the hydroxylated SnO_2 surface.

20-base pre-synthesized DNA probes are used (purchased from Biomers). A standard-type probe sequence was chosen: 5'-NH_2-TTTTT GAT AAA CCC ACT CTA-3'. These DNA probes are diluted in a sodium phosphate solution 0.3M/H_2O to a concentration of 10 µM. 3 µL drops of this solution are manually applied on the sample surface (**Figure 2.12-left**) and incubated for 2 hours at room temperature (**Figure 2.10d**). The probes were then reduced and stabilized using a $NaBH_4$ solution (0.1M) which modifies the CH=N imine into a CH_2-NH amine bond and also deactivates the non-bonded CHO termination of the glutaraldehyde transforming them into CH_2-OH (**Figure 2.10e**).

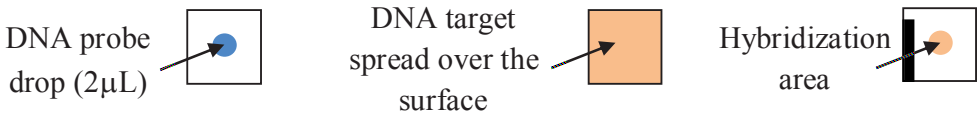

Figure 2.12: Top-view schema of DNA immobilization and hybridization on SnO_2 surface.

The hybridization is carried out using DNA targets labeled with a Cy3 fluorescent dye (**Figure 2.10f**). The DNA target solution is diluted in a hybridization buffer solution (phosphate buffer (PBS): 10mM, NaCl: 0.5M at pH 7.0) to a desired concentration and spread throughout the sample surface (10 drops per samples, each drop of 2µL) (**Figure 2.12-middle**). The target DNA concentration has been varied from 2 nM to 2 µM. The samples are then covered by a hybrislip and placed into a hybridization chamber at 42°C for 45 minutes. Finally, the samples are rinsed with saline-sodium citrate (SSC) buffer to remove all the unbound DNA targets from the surface and dried with nitrogen (**Figure 2.12-right**).

In order to study the selectivity of the process, different types of DNA target have been used in this experiment including complementary, non-complementary, 1- and 2-base mismatch as represented in Table 2.4.

Table 2.4: Different types of DNA target have been used in this study.

DNA target	
Complementary	3' AC CTA TTT GGG TGA GAT AC-Cy3 5'
Non-complementary	3' AC TGG CGC AAT CAC TCT AC-Cy3 5'
1-base mismatch	3' AC CTA TTT G**C**G TGA GAT AC-Cy3 5'
2-base mismatch	3' AC CTA TTT G**CA** TGA GAT AC-Cy3 5'

2.4 Detection of DNA hybridization

Although the present work is aimed at the development of label-free impedimetric DNA detection by EIS, the use of Cy3 labeled DNA targets allows the systematic comparison of electrical results with fluorescence results.

2.4.1 Optical fluorescence detection

2.4.1.1 Epifluorescence detection

Fluorescence measurements are achieved using an Olympus microscope (BX41M), fitted with a 100W mercury lamp, a cyanide Cy3 dichroic cube filter (excitation 550nm, emission 580nm) and a cooled Spot RT monochrome camera (Diagnostic). The Image Pro plus software is used for image analysis. The processing parameters are detailed in Table 2.5.

Table 2.5: Processing parameters of fluorescence measurement

Objective	10 x
Gain	1
Bining	1
Acquisition time	Usually, the time is set at 2s. In some certain cases, the time is adjusted.

The fluorescence intensity is measured at two distinct regions of the sample: the spot where DNA probes were grafted and the background outside the spot where no DNA probes were immobilized. This background intensity is then subtracted from the intensity of each spot. An average intensity value from different parts of the drop is reported.

2.4.1.2 Confocal fluorescence detection

Fluorescence measurements are also performed with a confocal laser scanning microscope Zeiss LSM700. The wavelength emission of the laser diode source is 550 nm. Confocal images were collected (pinhole set at 1 Airy Unit) with MBS405 dichroics from 560 to 700 nm. A 3D stereoscopic view of the surface can be built by assembling several pictures taken on numerous consecutive focusing plans.

2.4.2 Impedimetric detection of DNA hybridization

The impedance measurements are performed without any redox species on the bio-modified films in the same cell configuration with the same process as for the bare electrodes.

These measurements are carried out either on the silanized electrodes, and on DNA probe grafted electrodes before and after DNA hybridization. The obtained impedance spectra are often represented by Nyquist diagram in which the negative part of the imaginary part (-ImZ) of the impedance is plotted versus the real part (ReZ). Each point corresponds to different frequency. The interpretation of the impedance spectra is based on the corresponding equivalent circuit used to fit it. As will be detailed in the result part, the sensitivity to DNA detection is evaluated based on the difference between the values of resistances obtained at high and low frequencies before and after DNA hybridization.

REFERENCES

[1] S.-T. Chang, I.-C. Leu, and M.-H. Hon, "Preparation and characterization of nanostructured tin oxide films by electrochemical deposition", *Electrochemical and solid-state letters,* vol. 5, pp. C71-C74, 2002.

[2] S. T. Chang, I. C. Leu, and M. H. Hon, "Electrodeposition of nanocrystalline SnO_2 coatings with two-layer microstructure", *Journal of Crystal Growth,* vol. 273, pp. 195-202, 2004.

[3] T. Djenizian, H. Ilie, D. P. Yesudas, V. Florence, and K. Philippe, "Electrochemical fabrication of Sn nanowires on titania nanotube guide layers", *Nanotechnology,* vol. 19, p. 205601, 2008.

[4] A. Kolmakov, Y. Zhang, and M. Moskovits, "Topotactic Thermal Oxidation of Sn Nanowires: Intermediate Suboxides and Core−Shell Metastable Structures", *Nano Letters,* vol. 3, pp. 1125-1129, 2003.

[5] X. Q. Pan and L. Fu, "Oxidation and phase transitions of epitaxial tin oxide thin films on (1-bar 012) sapphire", *Journal of Applied Physics,* vol. 89, pp. 6048-6055, 2001.

[6] D. D. Macdonald, "Reflections on the history of electrochemical impedance spectroscopy", *Electrochimica Acta,* vol. 51, pp. 1376-1388, 2006.

CHAPTER III: Label-free DNA biosensors based on SnO_2 nanoporous films

In this chapter, we will study the steps of fabrication the label-free DNA biosensors based on SnO_2 nanoporous films.

In the first part (**part 3.1**), we will study the signal responses of DNA sensors obtained from SnO_2 films electrodeposited by varying the deposition potential at a fixed time.

In the second part (**part 3.2**), we will study the signal responses of DNA sensors obtained from SnO_2 films electrodeposited by varying the passed charge density at a fixed potential.

The third part **(part 3.3)** will be devoted to the study of some characteristics of the DNA sensors based on SnO_2 films giving the highest variation signal upon DNA hybridization.

The detailed presentation of each part is presented as following:

Part 3.1: Influence of the deposition potential: micrometer-thick films
- Film deposition
- Film characterization:
  - Morphology: SEM, TEM
  - Microstructure: XRD, GID
  - Chemical composition : XPS
  - Electrochemical properties: EIS
- DNA detection
  - Non-faradic EIS
  - Epifluorescence

Part 3.2: From nanometer to micrometer thick films: Influence of the passed charge density
- Film deposition
- Film characterization:
  - Morphology: SEM, TEM
  - Microstructure: XRD, GID
  - Electrochemical properties: EIS
- DNA detection
  - Non-faradic EIS
  - Epifluorescence
  - Confocal laser microscopy

Part 3.3: Characteristics of DNA biosensors based on SnO_2 nanoporous nanometer-thick film
- Comparison between vapor and liquid phase deposition of APTES
- Sensitivity
- Selectivity
- Reusability

3.1 Influence of the deposition voltage: micrometer-thick films

3.1.1 Cyclic voltammetry

The electrochemical reactions related to the electrodeposition of tin dioxide film onto the ITO/glass substrate have been studied by cyclic voltammetry. The experimental conditions are detailed in **Table 3.1**.

Table 3.1: Processing parameters of the electrochemical cell used for cyclic voltammetry test

Electrolyte	Condition			Cyclic voltammetry	
	T (^oC)	pH	Stirring	Scan rate ($mV\ s^{-1}$)	E_{oc} (V vs. Ag/AgCl)
20 mM $SnCl_2.2H_2O$ 100 mM $NaNO_3$ 75 mM HNO_3	50	1.23	No	50	-0.15 ± 0.05

First of all, in a strong oxidizing environment as nitric acid solution, the Sn^{2+} ions dissolved from tin dichloride are oxidized to Sn^{4+} as follows:

$$Sn^{2+} + NO_3^- + 2H^+ \rightarrow Sn^{4+} + NO_2^- + H_2O \qquad (3.1)$$

By this way, we assumed that the Sn^{2+} ions are completely oxidized to Sn^{4+} in acid nitric solution. **Figure 3.1** shows a typical cyclic voltammogram recorded at potentials between -1.5 and 0 V (vs. Ag/AgCl). The arrows show the scan direction. The potential is scanned from open-circuit potential E_{oc} (-0.15 ± 0.05 V), reversed at -1.5 V to 0 V (vs. Ag/AgCl), and terminated at E_{oc}.

When the potential of the electrode is moved negatively from E_{oc} to -1.5 V (vs. Ag/AgCl), the cathodic current appears from about -0.5 V. Then a cathodic peak (peak 1) located between -0.75 and -0.9 V (vs. Ag/AgCl) is observed. It may be ascribed to the reduction of nitrate ions on the electrode surface via electron transfer step as follows:

$$NO_3^- + 2H^+ + 2e^- \rightarrow NO_2^- + 2OH^- \qquad E^o = 0.01\ V \text{ vs. NHE} \qquad (3.2)$$

All the values of standard potential E_o are versus the normal hydrogen electrode (NHE).

However, because of the complexity of the system, the following two reactions might coexist and result in the deposition of metallic Sn on the electrode surface as follows:

$$Sn^{4+} + 2e^- \rightarrow Sn^{2+} \qquad E^o = 0.15\ V \text{ vs. NHE} \qquad (3.3)$$

$$Sn^{2+} + 2e^- \rightarrow Sn \qquad E^o = -0.136\ V \text{ vs. NHE} \qquad (3.4)$$

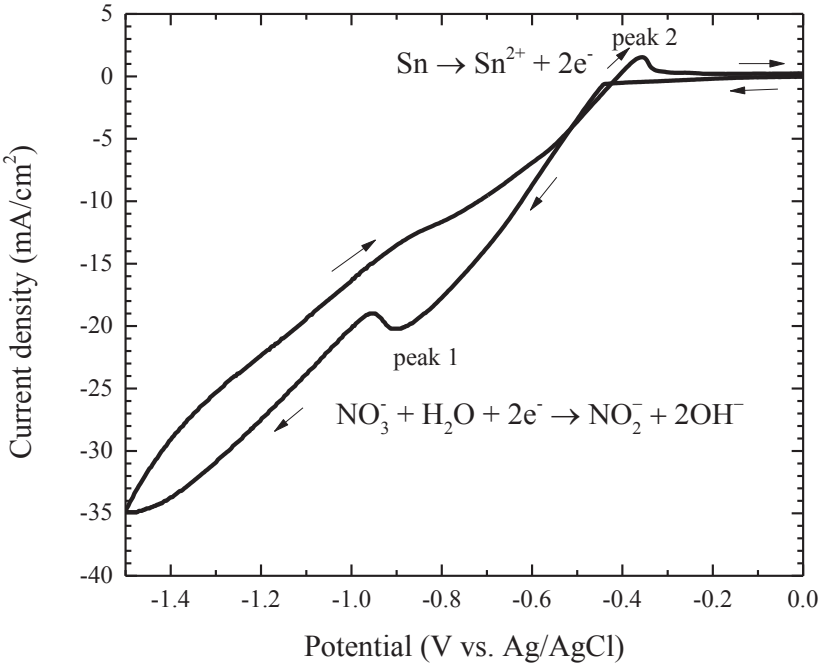

Figure 3.1: Typical CV curve obtained at ITO/glass electrode in 20 mM $SnCl_2.2H_2O$, 100 mM $NaNO_3$ and 75 mM HNO_3 at 50 °C. The experiment was made under unstirring condition.

Further increases in the current density, at potential more negative than -1.0 V (vs. Ag/AgCl), can be attributed to the hydrolysis of water expressed as follows:

$$2H_2O + 2e^- \rightarrow H_2 + 2OH^- \qquad E^o = -0.828 \text{ V vs. NHE} \qquad (3.5)$$

On reversing the direction of the potential sweep from -1.5 V (vs. Ag/AgCl), an anodic (peak 2) appeared at about -0.35 V (vs. Ag/AgCl). It is consistent with the oxidation of tin metal formed during the forward scan, i.e reverse of reaction (3.3) and (3.4). The low intensity of this oxidation peak indicates a small amount of metallic metal on the cathode. Consequently, it can be concluded that the large cathodic peak 1 is negligibly affected by the reduction of the Sn^{4+} ions in the solution. The forward and the reverse scans show crossover at potential approximately -0.4 V (vs. Ag/AgCl). The presence of the crossover between cathodic and anodic scan can be related to the characteristic of the nucleation and growth process [1].

The OH^- ions are generated on the cathode. They induce a local increase of the pH at the electrode vicinity. The OH^- ions react with Sn^{4+} ions to make the deposition of tin dioxide according to reaction (3.6).

$$Sn^{4+} + 4OH^- \rightarrow Sn(OH)_4 \rightarrow SnO_2 + 2H_2O \qquad (3.6)$$

The obtained cyclic voltammetry curve suggests that the potential for potentiostatic deposition of SnO_2 in the present experimental conditions ranges from -0.5 to -1.0 V (vs. Ag/AgCl). At voltage below -1.0 V, the electrodeposition cannot be achieved because of the hydrogen evolution reaction. The formation and release of hydrogen might hinder SnO_2 deposition on the ITO electrode.

3.1.2 Film cathodic electrodeposition

On the basis of the CV described above, we have performed the cathodic electrodeposition of SnO_2 films by varying the deposition voltage from -0.5 to -1.0 V (vs. Ag/AgCl). The deposition time is fixed at 300 seconds. The processing parameters are detailed in **Table 3.2**.

Table 3.2: Processing parameters used in the electrodeposition experiments

Electrolyte	**Condition**			**Deposition**	
	T (°C)	pH	Stirring	Potential (V vs. Ag/AgCl)	Time (s)
20 mM $SnCl_2.2H_2O$ 100 mM $NaNO_3$ 75 mM HNO_3	50	1.23	No	-0.5 to -1.0	300 (5 min)

Figure 3.2a shows the dependence of the total transferred charges as a function of deposition time for different deposition voltages. The deposition rate is slower at lower potential. At a fixed deposition potential, the growth rate is linear in time so there is no change in the rate of transfer electrons. However, at potential of -0.9 and -1.0V, a slight acceleration of the growth rate is observed after 50 s and 80 s, respectively.

Figure 3.2b and **Table 3.3** present the total transferred charge value corresponding to each deposition voltage for a deposition time of 5 min. The total passed charge density increases with the deposition potential, indicating that more NO_3^- ions are reduced resulting in more OH- groups generated on the electrode surface.

Table 3.3: Evolution of the total transferred charges at different voltages for 5 min deposition

Deposition potential (V)	**-0.5**	**-0.6**	**-0.7**	**-0.8**	**-0.9**	**-1.0**
Total passed charge (C/cm^2)	0.86	1.62	2.29	3.49	4.32	5.23

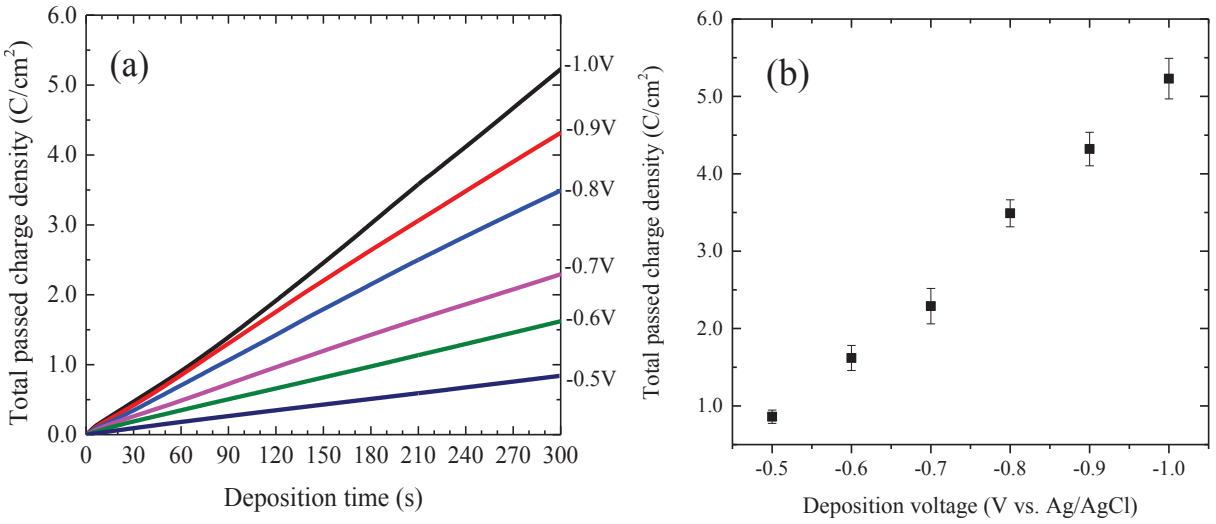

Figure 3.2: (a) Evolution of passed charge density as a function of deposition time, (b) Evolution of passed charge density as a function of deposition voltage for a deposition time of 5 minutes.

In the following part, we study the physical characteristics of the as-deposited films. The influence of the deposition voltage on their characteristics is further investigated.

3.1.3 Film characteristics

3.1.3.1 Morphology

SEM was used to investigate the morphology of the deposited films. Whatever the deposition voltage, the films present a nanoporous morphology that is composed of numerous nanoparticles as presented in the typical top-view SEM images in **Figure 3.3**. The sizes of the nanoparticles do not vary with the deposition potential and range from 20 to 100 nm. The formation of some cracks on the film surface could be attributed to high thermal tension during drying process in air. **Figure 3.4** shows SEM cross-sectional views of the as-deposited films obtained at different voltages. No significant change of the porosity is observed. The observed pore size varies from about 20 nm up to 1 µm. The film thickness is measured and reported as the function of the deposition potential (**Figure 3.5**). The film thickness increases from 1.9 to 4.1 µm when the applied potential is driven negatively from -0.5 to -1.0 V (vs. Ag/AgCl). More particularly, the thickness increases linearly in the -0.5 to -0.8 V (vs. Ag/AgCl) range, then a saturation value of 4 µm is reached. Because the range of the obtained thickness is in the micrometer range, we call these films **micrometer-thick films.**

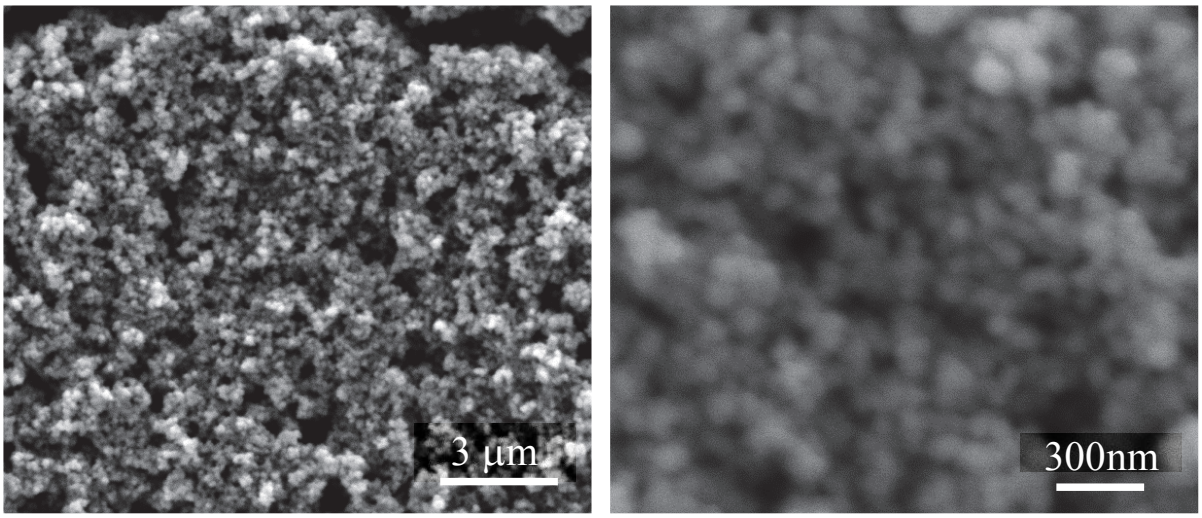

Figure 3.3: Typical top-view SEM images of SnO_2 films deposited for 5 minutes onto ITO coated glass electrode at voltage of -1.0 V (vs. Ag/AgCl)

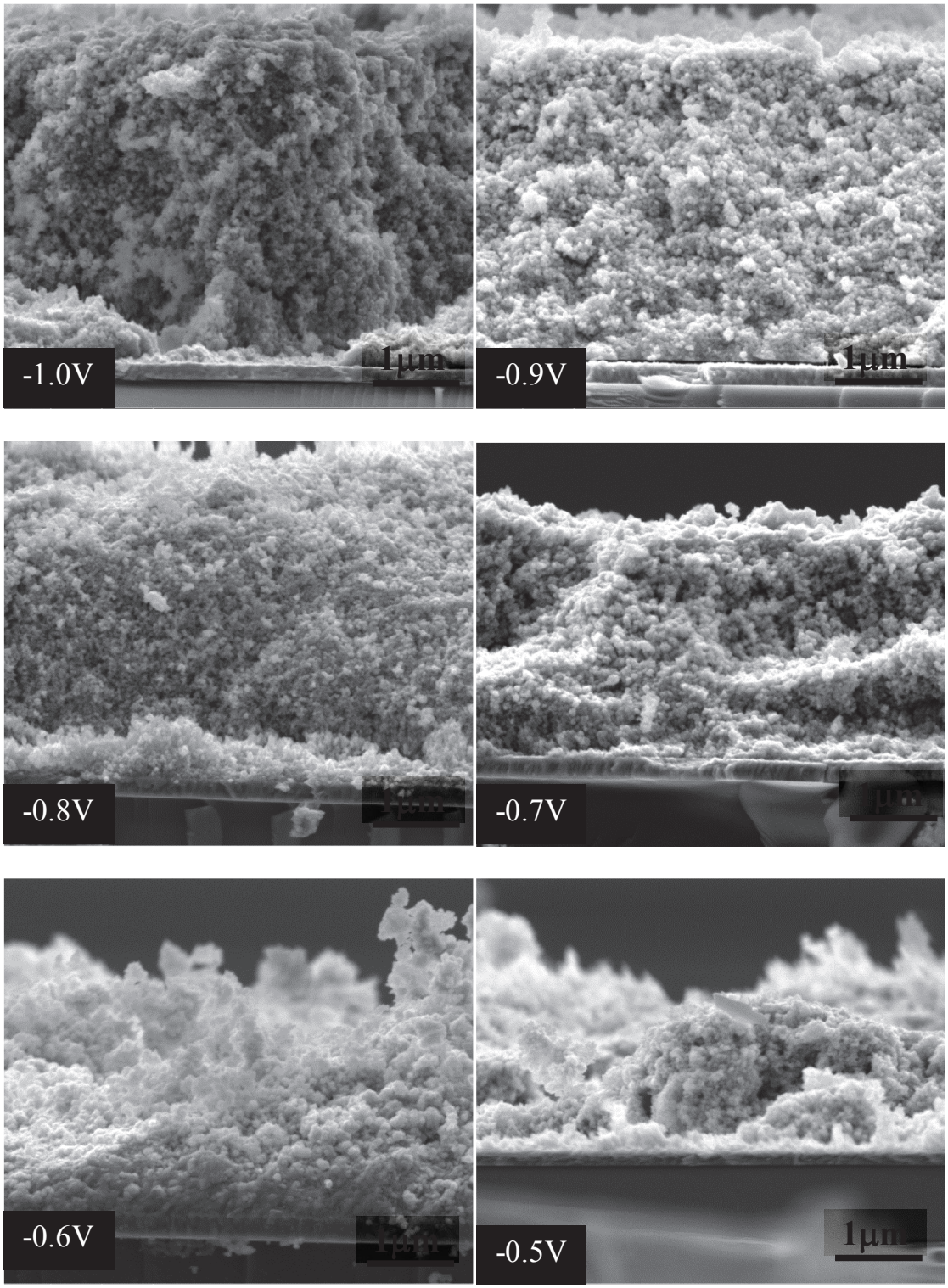

Figure 3.4: SEM images of SnO_2 films deposited for 5 minutes onto ITO coated glass electrode in a solution of 20 mM $SnCl_2.2H_2O$, 100 mM $NaNO_3$ and 75 mM HNO_3 at 50 °C under unstirring condition at voltage in the range of -1.0 to 0.5 V (vs. Ag/AgCl).

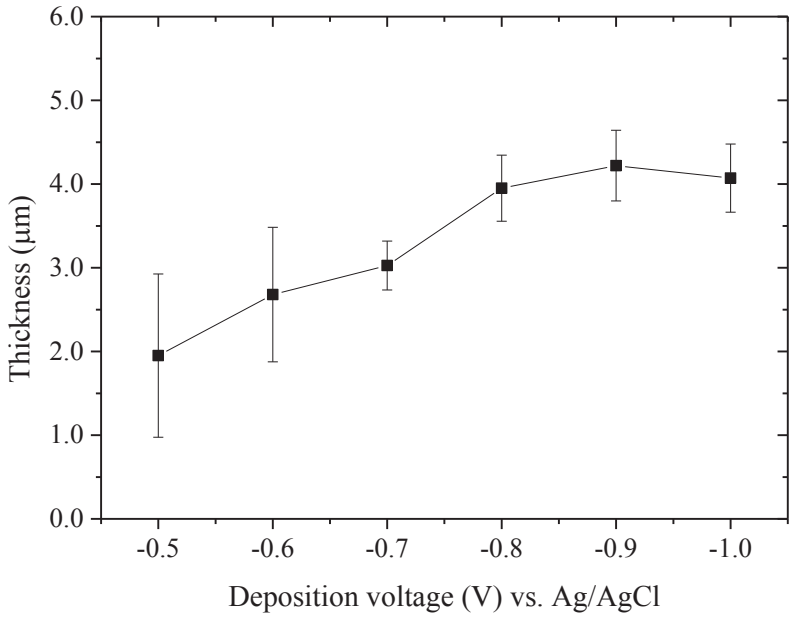

Figure 3.5: Evolution of the film thickness as a function of the deposition voltage with a fixed deposition time of 5 minutes.

3.1.3.2 Microstructure

The evolution of the microstructure organization of the as-deposited films according to the deposition potential can be deduced from XRD spectra (**Figure 3.6**). Except numerous peaks of the ITO substrate, the XRD patterns of the films show three broaden peaks located at 2θ equal to 26.3, 33.8 and 52.1°, respectively. Their positions and relative intensities according to different deposition voltages are showed in **Table 3.4**. These peaks correspond to the cassiterite tetragonal SnO_2 phase. Their relative intensities are similar to the value of powder as given in the ICDD 00-041-1445 file. It indicates that the obtained films exhibit a non-preferred oriented structure. When the applied voltage was driven negatively, the peaks of SnO_2 become more intense and well-defined.

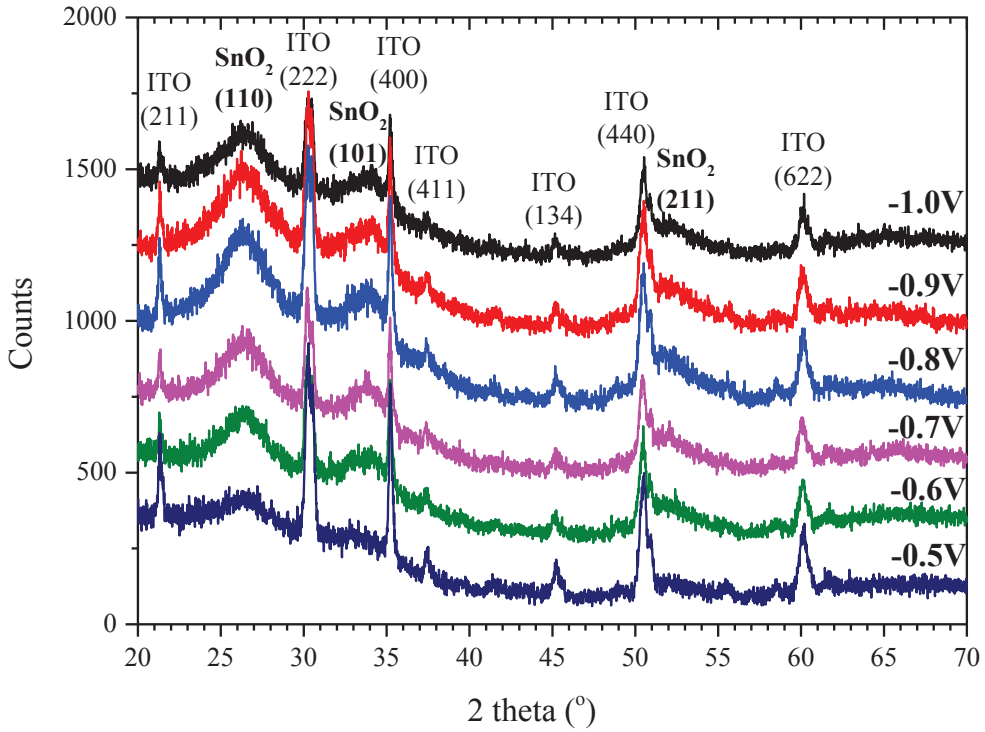

Figure 3.6: XRD spectra of SnO_2 films electrodeposited for 5 minutes onto ITO electrode at different deposition potentials.

The ratio of the integral peak intensity of SnO_2 (110) to ITO (222), I_{SnO2}/I_{ITO}, changes from 0.6 to 2.4 (**Figure 3.7**) when decreasing the potential from -0.5 to -1.0 V (vs. Ag/AgCl), indicating that the more negative potential electrodeposition was carried out, the more SnO_2 was deposited on ITO electrode surface. This result is in agreement with the increase of thickness as seen from SEM cross-section images (**Figure 3.4**). That is because a more negative applied voltage leads to a faster formation of OH^- ions on the electrode surface and consequently to a higher pH value near the electrode surface. As a result, it increased the deposition rate of SnO_2 coating.

Table 3.4: Data analysis from XRD patterns in Figure 3.6.

Samples	**Film thickness (µm)**	**Peak positions**			**Relative intensity of SnO_2 peaks**			**Grain size (nm)**	**I_{SnO2}/I_{ITO}**
		(110)	(101)	(211)	(110)	(101)	(211)		
ICDD-00-041-1445		***26.584***	***33.8695***	***51.766***	***100***	***75***	***57***	**-**	**-**
-0.5 V	1.95	26.218	33.783	-	100	65	-	7.1	0.6
-0.6 V	2.68	26.272	33.760	52.203	100	71	-	5.0	1.8
-0.7 V	2.91	26.317	33.732	52.057	100	70	-	4.6	2.0
-0.8 V	3.95	26.332	33.855	52.311	100	71	-	4.5	2.2
-0.9 V	4.22	26.323	33.881	52.186	100	72	-	4.4	2.2
-1.0 V	4.07	26.301	33.903	51.979	100	70	-	4.4	2.4

From the full width at the half maximum (FWHM) of the (110) peak, the size of coherent diffraction domain is calculated by the Scherrer formula. It slightly increases from 4.4 to 7.1 nm when driving the potential negatively from -0.5 to -1.0 V (vs. Ag/AgCl) (**Figure 3.7**).

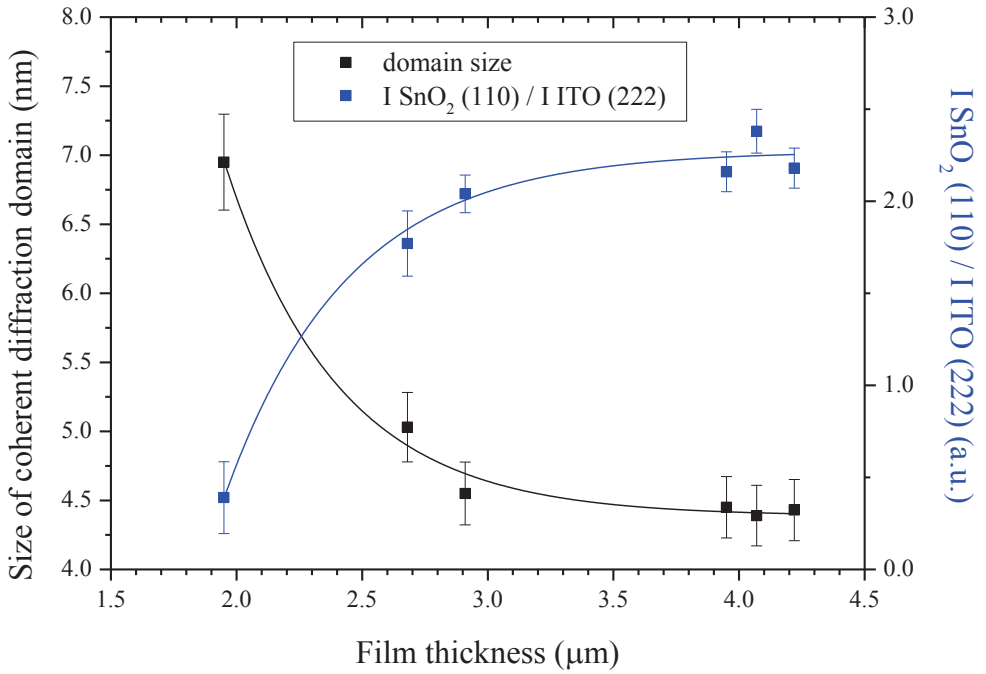

Figure 3.7: Evolution of the size of coherent diffraction domains and integral peak intensity of SnO_2 (110) to ITO (222) as a function of the film thickness for the nanoporous SnO_2 micrometer-thick films potentiostatically deposited for 5 minutes onto ITO electrodes.

3.1.3.3 Surface chemical composition

The composition and chemical states of the nanoporous micrometer thick film surfaces were investigated by XPS. Similar XPS results are obtained for all of the studied samples. Sn, O, C, Cl and In elements are detected at the film surfaces as can be observed in the survey spectrum (**Figure 3.8**). The presence of a small peak of Cl 1s is also observed. This element could come from the $SnCl_2$ of the electrolyte during deposition process. It might act as a dopant. On the other hand, the In signal arises from SnO_2-free area of ITO/glass substrate.

We focused on the Sn $3d_{5/2}$ peak in order to analyze the multi-valence states of Sn element. The binding energy was calibrated using C1s signal (284.5eV) from the sample surface. The Sn $3d_{5/2}$ peak of the as-deposited SnO_2 is slightly asymmetric. It is fitted with Gaussian function with FWHM of 1.7 eV. As can be seen, the dominant part of the peak can be attributed to Sn^{4+}

(486.83eV). A small peak accounts for metallic Sn at lower binding energy also can be observed. However, because the peak of Sn was not found in XRD patterns, the quantity of the simultaneously deposited Sn should be less than 3 mol.%. It proved that the reaction (3.4) took place simultaneously with the reduction of the nitrate ions.

Besides, XPS peak of O1s shows three chemical states of O. They include SnO_2 at binding energy of 530.6 eV, OH at 532.06 eV and CO contamination at 533.16 eV. Tin hydroxide was unstable with respect to tin oxide. As a result, a highly reversible dehydration was favored. The small peak belonging to OH proved that the dehydration from $Sn(OH)_4$ to SnO_2 was not completed and a small quantity of $Sn(OH)_4$ still existed on the deposited layer.

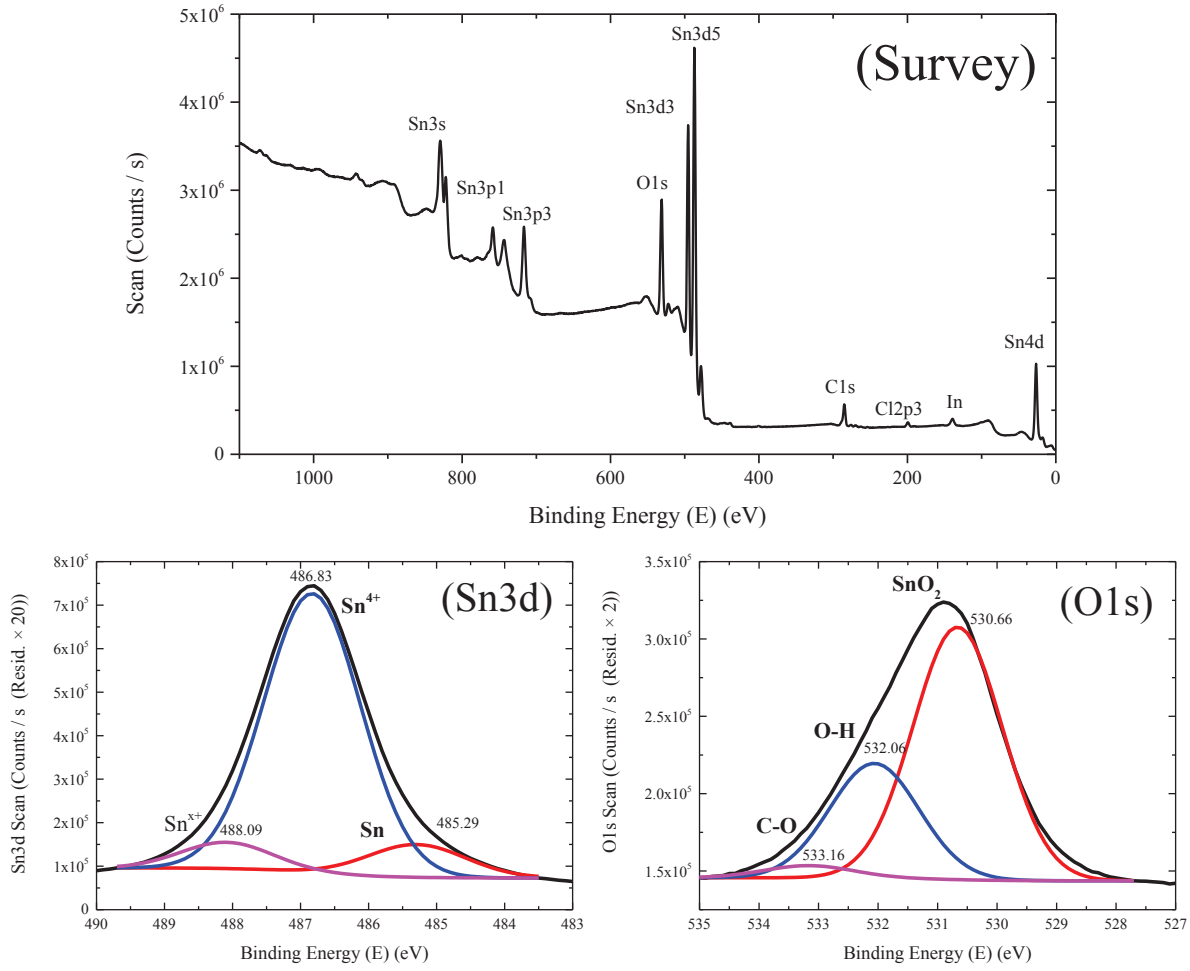

Figure 3.8: Typical XPS survey spectrum, Sn $3d_{5/2}$ and O1s peaks of the films deposited onto ITO/glass electrode at -1.0 V (vs. Ag/AgCl) for 5 minutes.

From the respective intensity of Sn^{4+} and SnO_2 peaks, we can calculate the $O:Sn^{4+}$ ratio according to the following relation:

$$\frac{O}{Sn^{4+}} = \frac{O\ peak\ area}{O\ sensitivity\ factor} \cdot \frac{Sn^{4+}\ peak\ area}{Sn^{4+}\ sensitivity\ factor} \qquad (3.7)$$

The respective atomic sensitivity factors of O1s and Sn3d are 0.66 and 4.3. The calculated $O:Sn^{4+}$ ratios range from 1.33 to 1.35 for applied voltages ranging from -0.5 to -1.0 V (vs. Ag/AgCl), respectively (**Figure 3.9**). Whatever the voltage, the $O:Sn^{4+}$ value does not vary significantly and is lower than the theoretical value 2 of SnO_2. The lack of oxygen can be explained by the uncompleted dehydration of the formed $Sn(OH)_4$. Another possible explanation is the difference in chemical composition between the extreme surface and the underlying layer, even if it is well-known that SnO_2 films are under stoichiometric in oxygen, due to oxygen vacancies. The latter is responsible for the n-doped characteristic of the semi-conducting properties of SnO_2.

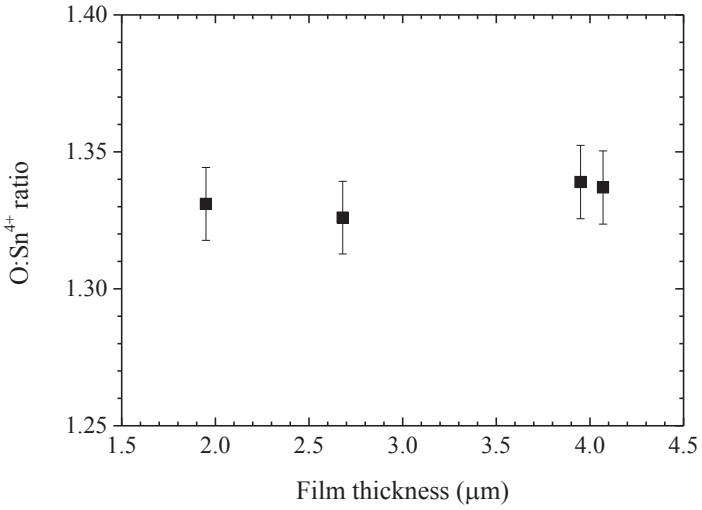

Figure 3.9: Evolution of calculated $O:Sn^{4+}$ ratio as a function of the film thickness for SnO_2 films electrodeposited for 5 minutes onto ITO electrodes.

In conclusion, the SnO_2 films potentiostatically electrodeposited in a range of potential going from -0.5 to -1.0 V (vs. Ag/AgCl) during 5 min, show a nanoporous morphology. No dependence of the porosity on the deposition voltage is found. The size of the nanoparticles ranges from 20 to 100 nm, and the pore size ranges from about 20 nm up to 1 µm. The film thickness varies as a function of the deposition voltage. When the deposition voltage decreases from -0.5 to -1.0 V (vs. Ag/AgCl), the film thickness increases from 1.9 to 4.1 µm. It is revealed from XRD patterns that the as-deposited SnO_2 films exhibit a SnO_2 tetragonal phase with a low degree of crystallinity. XPS results indicate that the film surface is understoichiometric in oxygen. Whatever the deposition potential, the calculated $O:Sn^{4+}$ ratio is approximately 1.3.

3.1.3.4 Electrochemical properties

The ac responses of the obtained micrometer-thick nanoporous SnO_2 films are examined with electrochemical impedance spectroscopy (EIS) and analyzed with the use of equivalent circuits. EIS measurements are carried out in a three-electrode electrochemical system as described in the experimental part. The processing parameters are detailed in **Table 3.6**. The reference electrode is a lab-made Ag/AgCl.

Table 3.6: Parameters of the impedance measurement for the micrometer-thick nanoporous films

Electrolyte	*Frequency range*	*Modulation*	*Applied voltage range V (vs. ref)*
Hybridization buffer without DNA molecules 0.5 M NaCl, 0.01 M PBS 0.01 M EDTA, (pH = 5.5)	100 mHz to 200 kHz	10 mV	-0.5 to 0.5

A similar trend of the impedance evolutions with the different applied voltages is found for all studied samples (see Annex 1). The representative Nyquist plots obtained for the 4.07µm- thick nanoporous film (deposited at -1.0V (vs. Ag/AgCl)) with applied voltages varying from -0.5 to 0.5 V (vs. ref) are showed in **Figure 3.10**.

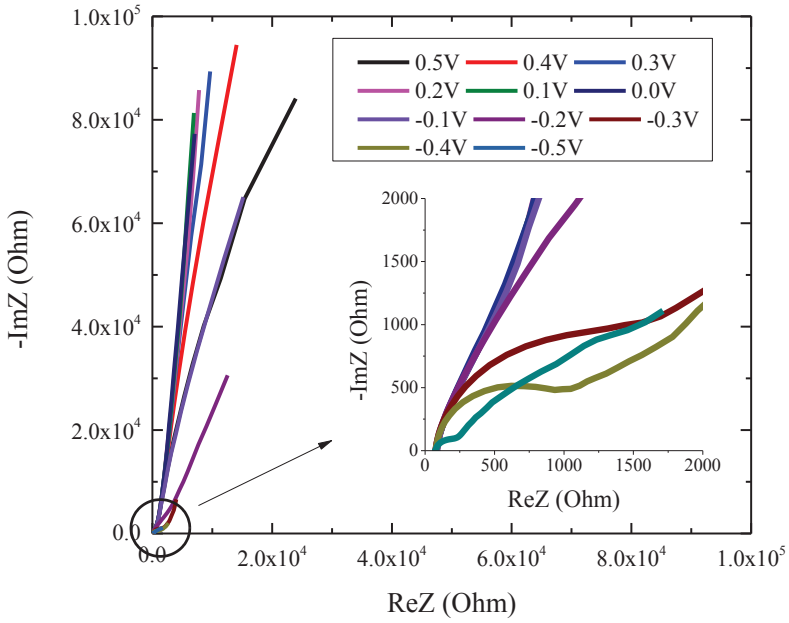

Figure 3.10: Nyquist plots obtained for the 4.07µm- thick -nanoporous film. The impedance curves are recorded at voltages ranging from -0.5 and 0.5 V (vs. ref).

As can be seen, the 4.07-µm-thick-nanoporous SnO_2 film exhibits a large voltage dependent impedance response. Depending on both the applied voltage and frequency range, different shapes of the Nyquist diagrams are obtained as presented in the following **Table 3.7**. Four main domains of voltage can be distinguished.

Table 3.7 Evolution of the shape of the impedance curves as a function of applied voltage at high and low frequency regions for the 4.07 µm-thick nanoporous film.

V (vs. ref) / Freq.	-0.5	-0.4 to -0.3	-0.2 to 0.4	0.5
High frequencies	*small semicircle*	*small semicircle*	straight line with slope of 60°	straight line with slope of 60°
Low frequencies	*large semicircle*	nearly vertical straight line	nearly vertical straight line	*large semicircle*

In order to understand the physical basis of the impedance response, the impedance data are analyzed using equivalent circuit models with discrete elements. As schematically depicted in **Figure 3.11**, the SnO_2-electrode/electrolyte interface can be divided into several physical regions going from the electrolyte bulk to the ITO bulk film:

- Ohmic resistance of the electrolyte bulk.
- The double-layer at the surface of the SnO_2 electrode.
- The space charge layer in the sub-surface of the SnO_2 film.
- Ohmic resistances of ITO and SnO_2 bulk films.

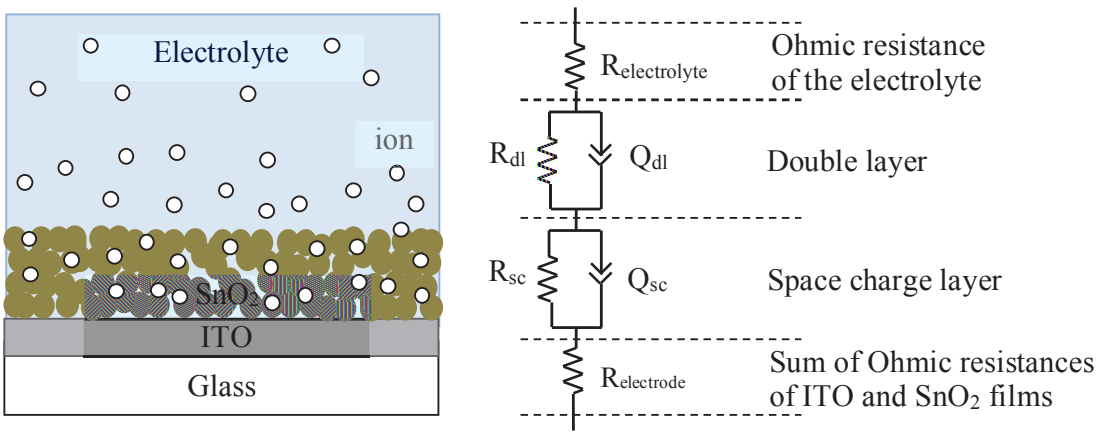

Figure 3.11: Schema of the electrode/electrolyte interface and electrical used for modeling

The global electrochemical behavior varies with applied voltage. The contribution of these elements differs according to the applied voltage. Three main domains of voltage are emphasized:

At applied potentials ranging from -0.5 to -0.3 V (vs. ref):

The Nyquist diagrams show two different frequency domains (**Figure 3.12**):

- **High frequencies:** The increase of the semicircle diameter at high frequency region, corresponding to the increase of both real and imaginary components of the impedance, can be attributed to the development of a depletion layer in the SnO_2 sub-surface when increasing the applied voltage from -0.5 to -0.3 V (vs. ref).
- **Low frequencies**: At applied voltage of -0.5 V (vs. ref), the large semicircle at low frequencies could be due to some electrochemical reactions, i.e. hydrogen evolution, occurring at the electrode surface. At applied voltages ranging from -0.4 to -0.3 V (vs. ref), no hydrogen evolution reaction occurs, and the impedance curves show a nearly vertical straight line corresponding to the charge of the electrode under polarization.

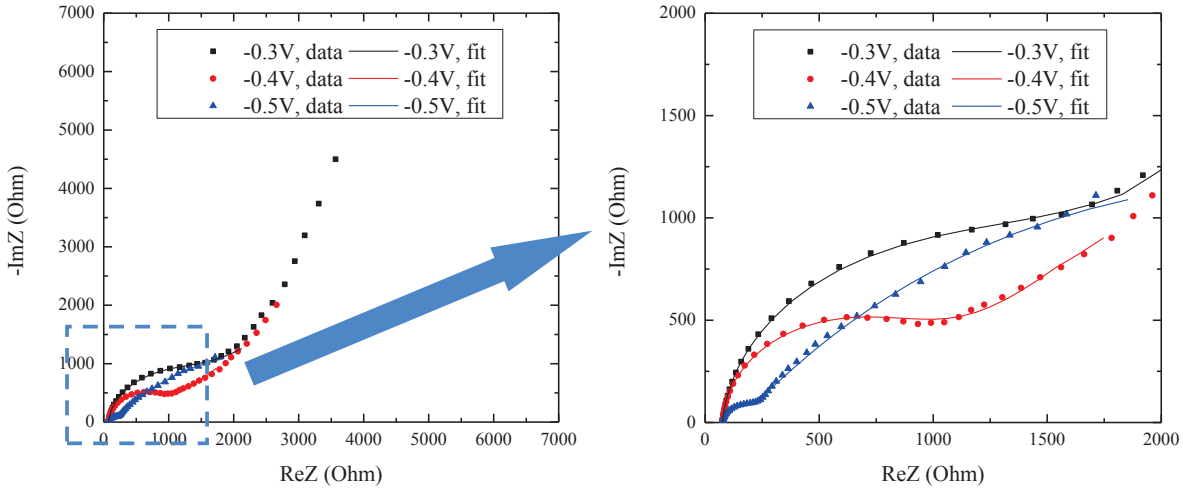

Figure 3.12: Nyquist plots and their corresponding modeling curves for the 4.07µm- thick - nanoporous film. The impedance curves are recorded at potentials ranging from -0.5 to -0.3 V (vs. ref.).

Two different equivalent circuits are used to model these electrical responses of the SnO_2 nanoporous electrode at applied voltage of -0.5 V (vs. ref) and at potentials ranging from -0.4 to -0.3 V (vs. ref) (**Figure 3.13a** and **b**).

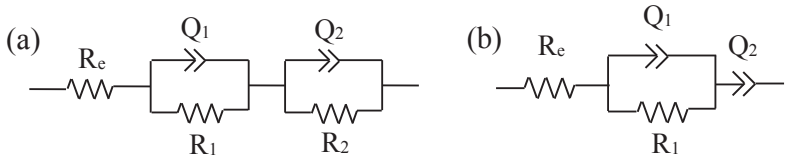

Figure 3.13: Equivalent circuits used to fit the impedance data obtained at applied voltages of (a) -0.5 V and (b) from -0.4 to -0.3 V (vs. ref)

At applied voltage -0.5 V (vs. ref), the first equivalent circuit R_e (Q_1, R_1) (Q_2, R_2) provides a reasonably good fit to the data (**Figure 3.12**).

- The resistance R_e at highest frequency is sum of the ohmic and bulk resistances of the electrolyte and electrode material including ITO and SnO_2 films.

- The first parallel element circuit (Q_1, R_1) is responsible for the high frequency small semicircle related to the space charge region. Therefore, R_1 and C_1 (extracted from Q_1) are understood as the resistance and the capacitance of the space charge layer, respectively.

- The second parallel element circuit (Q_2, R_2) is responsible for the large semicircle at lower frequencies related to a hydrogen evolution reaction at electrode/electrolyte interface. R_2 and C_2 (extracted from Q_2) can be considered as a charge transfer resistance through the double layer and the double layer capacitance, respectively.

At applied voltages ranging from -0.4 to -0.3 V (vs.ref), the second parallel element circuit (Q_2, R_2) is replaced by Q_2 (**Figure 3.13b**) which models the capacitive behavior of the electrode at lower frequencies.

The results of electrical parameter values used for fitting impedance curves are reported in **Table 3.8**.

Table 3.8: Electrical parameters values obtained for fitting impedance for the 4.07 µm thick film (deposited at -1.0V vs. Ag/AgCl).

Applied voltage (V vs. ref)	R_e (Ω)	high frequency		low frequency	
		C_1 (µF)	R_1 (Ω)	C_2 (µF)	R_2 (Ω)
-0.5	62.81	21.71	120.5	359	2955
-0.4	62.76	12.69	1194	-	-
-0.3	62.78	13.72	2422	-	-

(For all the complete fitting data, see Annex2-A1)*

- Within the considered applied voltage range, the value of R_e stays constant at 62.8 Ω (**Table 3.8)**. It results from the sum of ohmic resistances which are intrinsic characteristics of the electrolyte and electrode materials (ITO and SnO_2 film). Consequently, R_e is not frequency and voltage dependant.
- When driving the applied potential positively from -0.5 to -0.3 V (vs. ref), the diameter of the first small semicircle observed at high frequencies increases drastically, resulting an increase of the space charge transfer resistance R_1 from 120 to 2422 Ω. Besides the

capacitance C_1 decreases from 21.7 to 13.7 µF. The changes of R_1 and C_1 feature the growth of a highly insulating depletion layer within n-type SnO_2 electrode.

At applied voltages ranging from -0.2 to 0.4 V (vs. ref):

- The previous high frequency semicircle is invisible. It is replaced by a straight line with a slope approximately of 1 and a nearly vertical line at low frequencies. It indicates the complete absence of any space charge component at these potentials (**Figure 3.14a**). It might be due to very high insulating property of the space charge layer.

- This variation of the impedance with frequency is well known and commonly observed for porous conducting films [2-3]. In most cases, the double transmission lines model is used to explain the electrochemical behavior. According to the model proposed by Bisquert and Garcia-Belmonte [2], the straight line with a slope of 1 at high frequency can be considered as Warburg impedance and it relates to the ions migration through the porous structure of the film. The vertical line is consistent with a capacitive behavior corresponding to the charge of the porous film under polarization.

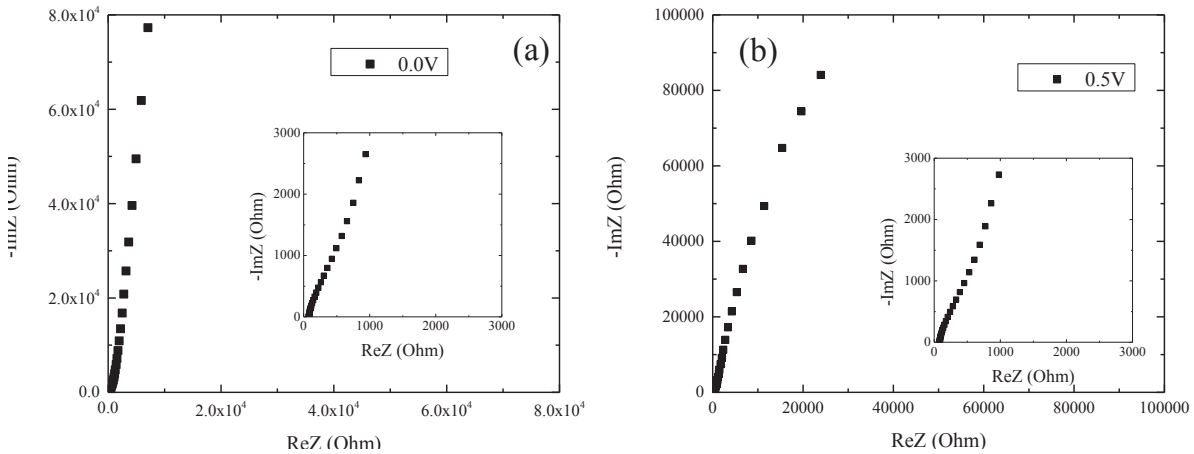

Figure 3.14: Nyquist plots for the 4.07µm- thick -nanoporous film deposited at -1.0 V. The impedance curves are recorded at voltages of (a) 0 and (b) 0.5 V (vs. ref.).

At applied voltage of 0.5 V (vs. ref):

- The Nyquist diagram presents two frequencies domains (**Figure 3.14b**). As above, the high frequency domain shows a straight line with a slope of approximately 1 corresponding to a Warburg impedance. The low frequency region shows the start of a semicircle which should express an electrochemical reaction, likely the oxygen evolution reaction.

In conclusion, the nanoporous SnO_2 micrometer-thick films exhibit a largely voltage-dependent impedance. In the whole explored range of applied potentials going from -0.5 to 0.5 V (vs. ref), it seems that only the potential of -0.5 V (vs. ref) is the most adequate to exploit the impedance behavior for the next studies. At this potential, the first small semicircle at high frequencies is related to the space charge layer. The second large semicircle at lower frequencies involves a charge transfer resistance related to the hydrogen evolution reactions.

3.1.4 DNA detection

The same functionalization process is carried out for all deposited films. This process is detailed in the experimental part. The main parameters such as DNA probe and target concentrations used in this process are detailed in **Table 3.9**.

Table 3.9: Parameters of the functionalization and impedance measurement processes

Functionalization parameters			**Impedance measurement parameter**			
Silanization	$C_{DNA\ probe}$ *(μM)*	$C_{DNA\ target}$ *(μM)*	*Electrolyte*	*Frequency range*	*Modulation*	*Applied voltage range*
Liquid phase deposition	10	2	0.5 M NaCl 0.01 M PBS 0.01 M EDTA (pH = 5.5)	100 mHz to 200 kHz	10 mV	-0.5 to 0.5 (V vs.ref)

3.1.4.1 Non-faradic impedance detection

Prior, we remind that the term "non-faradic detection" means that no redox compound is added in the electrolyte. The impedance measurements are systematically carried out after each main step of the functionalization process:

(i) after film silanization,
(ii) after probe grafting (ss-DNA),
(iii) after DNA hybridization (ds-DNA).

The applied processing parameters are presented in **Table 3.9**. The electrolyte used for impedance analyses is the pure hybridization buffer solution without the presence of target DNA with a volume of 0.5 ml per measurement.

As for the bare films discussed in previous section, the bio-modified nanoporous SnO_2 film exhibits a large voltage dependent impedance response. Depending on both the applied voltage

and frequency range different shapes of the Nyquist diagrams are obtained. In the following, the evolution of the impedance upon stepwise modification is discussed according to different ranges of applied voltage.

<u>At applied voltages from -0.5 to -0.4 V (vs. ref)</u>

The overall electrochemical behavior of the bio-modified films upon the stepwise functionalization does not change compared to the one of bare SnO_2 film. Their Nyquist diagrams present two frequency domains (**Figure 3.15**):

- A high-frequency small semicircle related to the space charge layer is still observed.
- A second semicircle at low frequency region related to the hydrogen evolution reaction only appears at potentials of -0.5 and -0.4 V (vs. ref).

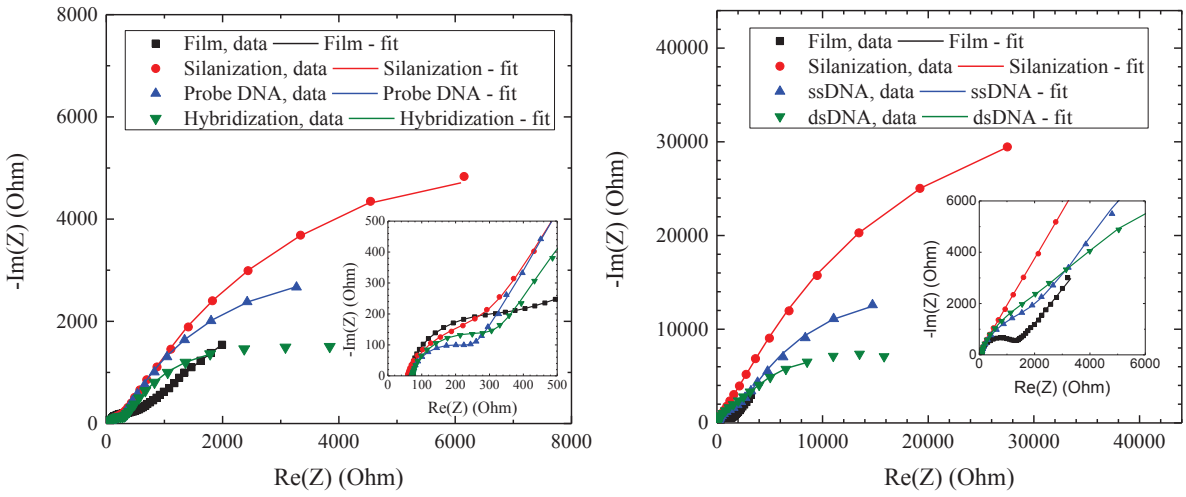

Figure 3.15: Nyquist plots of bio-modified 3.95µm-thick- SnO_2 nanoporous film after each modification step. Applied voltages are of (a) -0.5 and (b) 0.4 V (vs. ref).

However, significant changes in the impedance modulus are obtained upon the stepwise modification of the SnO_2 electrode at any applied potential. These changes are induced by the molecular layer immobilized on the film surface. As schematically depicted in **Figure 3.16**, in comparison to the bare film, a parallel element of (Q_{org} and R_{leak}) is added reflecting the properties of the molecular layer and its associated electrical double layer. C_{org} is the capacitance of this organic layer and R_{leak} reflects the penetration of the electrolyte through this molecular layer.

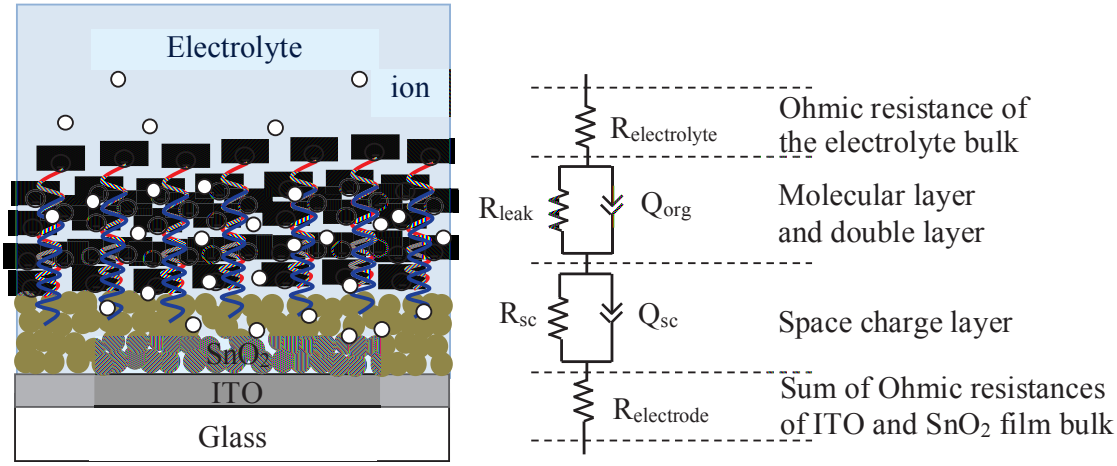

Figure 3.16: Schema of the bio-modified electrode/electrolyte interface and electrical circuit used for modeling.

In spite of the presence of the additional molecular layer, as for bare films, the impedance curves of the bio-modified films are well fitted with the equivalent circuit R_e (R_1, Q_1) (R_2, Q_2) described in **Figure 3.13a** and in **Figure 3.16**.

- The resistance R_e at highest frequency is still the sum of the ohmic and bulk resistances of the electrolyte and electrode material including ITO and SnO_2 films.
- The first parallel element circuit (Q_1, R_1) is responsible for the high frequency small semicircle related to the space charge region.
- The second parallel element circuit (Q_2, R_2) is responsible for the large semicircle at lower frequencies. It is related to the charge transfer through the molecular layers and their associated electrical double layer [4, 5].

In this study, we emphasize on **the evolution of the real parts of the impedance** including **the space charge layer resistance, R_1** and **the charge transfer resistance, R_2**. By monitoring the changes in these resistances before and after DNA hybridization we can get the information about different modification steps of the SnO_2 based DNA sensors. **We remind that R_1, R_2 can be determined from Nyquist plot modeling and after extrapolation of the semicircles until the ReZ axis.** Then, we calculate the variation of the resistance expressed as $\Delta R/R$ for all studied films as follow:

$$\frac{\Delta R}{R} = \frac{|R\ (\text{before hybridization}) - R\ (\text{after hybridization})|}{R\ (\text{before hybridization})} * 100\% \qquad (3.10)$$

The resistance values R_1 and R_2 obtained after analyzing impedance data and their variation $\Delta R_1/R_1$ and $\Delta R_2/R_2$ after DNA hybridization with complementary target DNA at applied potentials

of -0.5 and -0.4 V (vs. ref.) are reported in **Table 3.10a** and **3.10b**, respectively, for all the micrometer-thick films.

Table 3.10a: Resistance values of the equivalent circuit used for Nyquist plot modeling of all the micrometer-thick films for the impedance curves obtained at voltage of -0.5 V (vs. ref).

Deposition voltage (V)	Film thickness (μm)	R_e (Ω)		R_1 (Ω)		**$\Delta R_1/R_1$ (%)**	R_2 (Ω)		**$\Delta R_2/R_2$ (%)**
		ssDNA	dsDNA	ssDNA	dsDNA		ssDNA	dsDNA	
-1.0	4.07	66.6	61.3	79.39	101.7	**28±2**	8821	5027	**-43±4**
-0.9	4.22	65.1	67.3	1509	1648	**9±1**	11156	8794	**-21±4**
-0.8	3.95	71.3	74.1	248	337	**36±2**	7908	3729	**-53±5**
-0.7	2.91	67.3	65.8	637.1	699.2	**10±2**	7242	4482	**-38±5**
-0.6	2.68	66.5	68.4	102.4	109.2	**6±1**	7712	4257	**-45±5**
-0.5	1.95	67.8	70.2	2130	2221	**4±1**	10927	7388	**-32±4**

(For all the complete fitting data, see Annex2-A1)*

Table 3.10b: Resistance values of the equivalent circuit used for Nyquist plot modeling for of all the micrometer-thick films the impedance curves obtained at voltage of -0.4 V (vs. ref).

Deposition voltage (V)	Film thickness (μm)	R_e (Ω)		R_1 (Ω)		**$\Delta R_1/R_1$ (%)**	R_2 (Ω)		**$\Delta R_2/R_2$ (%)**
		ssDNA	dsDNA	ssDNA	dsDNA		ssDNA	dsDNA	
-1.0	4.07	66.7	61.3	3403	3496	**3±1**	41013	16620	**-59±5**
-0.9	4.22	65.2	67.3	8085	9076	**12±2**	43352	40929	**-6±3**
-0.8	3.95	71.3	74.1	4629	5408	**17±2**	32585	14696	**-55±5**
-0.7	2.91	69.2	67.11	9632	10402	**8±2**	25147	19541	**-22±3**
-0.6	2.68	66.7	68.4	2005	2694	**35±2**	19771	13057	**-34±4**
-0.5	1.95	68.0	71.3	6913	5330	**23±2**	53656	43789	**-18±3**

(For all the complete fitting data, see Annex2-A1)*

From these tables, it is noteworthy that reproducible results are obtained at the two values of applied potential (-0.5 to -0.4 V (vs. ref)). The main observations are the following.

- R_e does not vary significantly during the different functionalization steps. Its value remains in the 68 to 70 Ω range. In contrary, R_1 and R_2 change after stepwise modification of the film surface.

- After the step of silanization, the resistance R_1 does not change significantly while R_2 increases considerably (calculation is not reported here). The large increase of R_2 could be due to the coverage of the non-charged and hydrophobic APTES layer on the electrode surface which hinders electrochemical reaction occurred at the electrode/electrolyte interface.

- After immobilization of ss-DNA, (C_{probe} = 10 μM) onto the silanized surface, the charge transfer resistance R_2 decreases. Indeed, the negatively charged ss-DNA could facilitate the ionic current between electrolyte and electrode. From the comparison between **Table 3.8** and **Table 3.10a** in the case of the 4.07 μm- thick film, we note that the value of R_1 is not affected significantly by the addition of ss-DNA. Its value stays in range from 80 to 100 Ω. However, the R_2 value exhibits a real modification upon ss-DNA grafting. It indicates that the molecular layer strongly affects the ionic transport. As a result, the conditions of hydrogen evolution at voltage of -0.5 V (vs. ref) on the film surface are modified.

- Finally, the DNA hybridization with complementary target DNA molecules (C_{target} = 2 μM) results in a slight increase of R_1 ranging between 5 - 35% and a systematic decrease of R_2 ranging between 20 - 58%.

    - The slight increase of space charge layer resistance R_1 upon DNA hybridization might be originated from a slight field effect phenomenon. The negative charges of DNA strands grafted on the film surface repel the electrons within the film from the sub-surface into the bulk of the film, resulting in an increase of space charge layer resistance.

    - On the other hand, the decrease of the charge transfer resistance R_2 upon DNA hybridization could be explained by some external phenomena. First, the hydrophilic character of ds-DNA can partially facilitate the ionic molecules of electrolyte to reach the electrode surface following their infiltration into the porous structure. Another possible reason is based on the change of strand conformation of the ss-DNA compared to the ds-DNA. According to Piro et al. [6], ss-DNA strands behave as random coil. The electrode surface is partially blocked upon probe grafting. On the contrary, after hybridization, the ds-DNA behave as a rigid helicoidal chain as presented in **Figure 1.13**. Therefore, the electrode surface is liberated after hybridization.

To figure out how the resistances R_1 and R_2 change with the different film thicknesses, we plot the $\Delta R_1/R_1$ and $\Delta R_2/R_2$ as a function of the film thickness for both applied voltage of -0.5 and -0.4V (vs. ref) as presented in **Figure 3.17**.

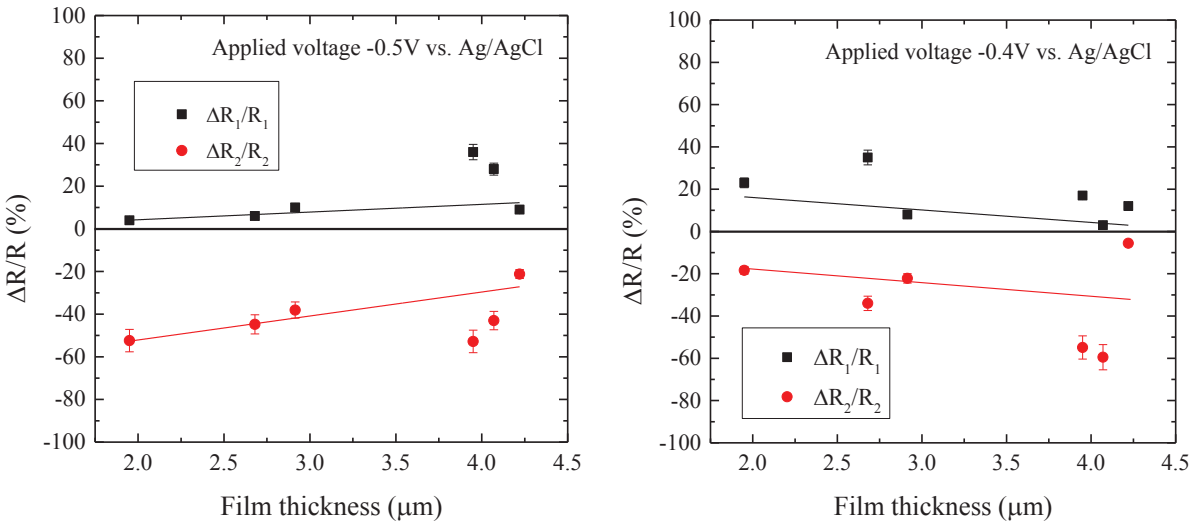

Figure 3.17: Evolution of the calculated space charge resistance $\Delta R_1/R_1$ and charge transfer resistance $\Delta R_2/R_2$ upon DNA hybridization as a function of film thickness at applied potential (left) -0.5 and (right) -0.4 V (vs. ref).

In the whole micrometer range of the film thickness, whatever the applied potential (-0.5 or -0.4 V (vs. ref)), no drastic variation of R_1 and R_2 is observed. Only some slight variations can be noted within the experimental value dispersion. Notably, at applied potential of -0.5 V (vs. ref), the space charge resistance R_1 exhibits a slight increase from 3 to 15% and the charge transfer resistance ranges between -30 to -50%.

At applied voltage of -0.3 V (vs. ref)

- The impedance curves of the modified SnO_2 porous films polarized at -0.3 V (vs. ref) show only one big semicircle at low frequency (**Figure 3.18**). The invisibility of the high frequency semicircle could be due to the condition in which the charge transfer resistance is much larger than the space charge resistance. In fact, the rate of the hydrogen evolution is slowed down when the applied potential is driven positively. The slow reaction rate could also be attributed to the thick depletion space charge layer at this applied voltage. DNA hybridization leads to a slight decrease of the charge transfer resistance.

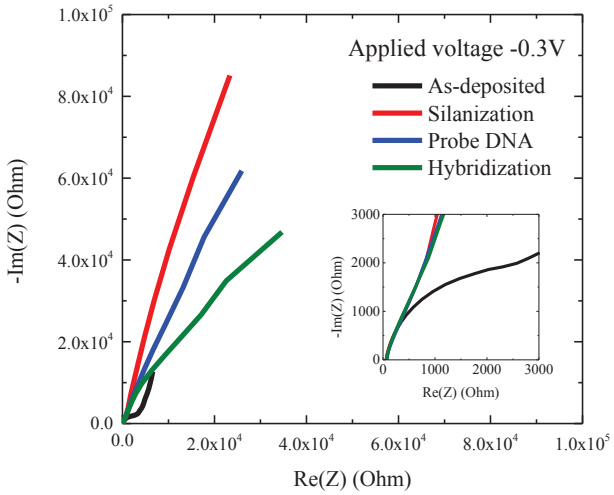

Figure 3.18: Nyquist plots of bio-modified SnO_2 nanoporous film after each modification step. Film thickness is 3.95µm. Applied voltage is -0.3V (vs. ref).

At applied voltages raging from -0.2 to 0.4 V (vs. ref)

- As for the bare films, the impedance spectra of the bio-modified electrode correspond to the behavior of a capacitance (**Figure 3.19-left**). No significant changes of the impedance upon DNA hybridization are observed at these applied voltages.

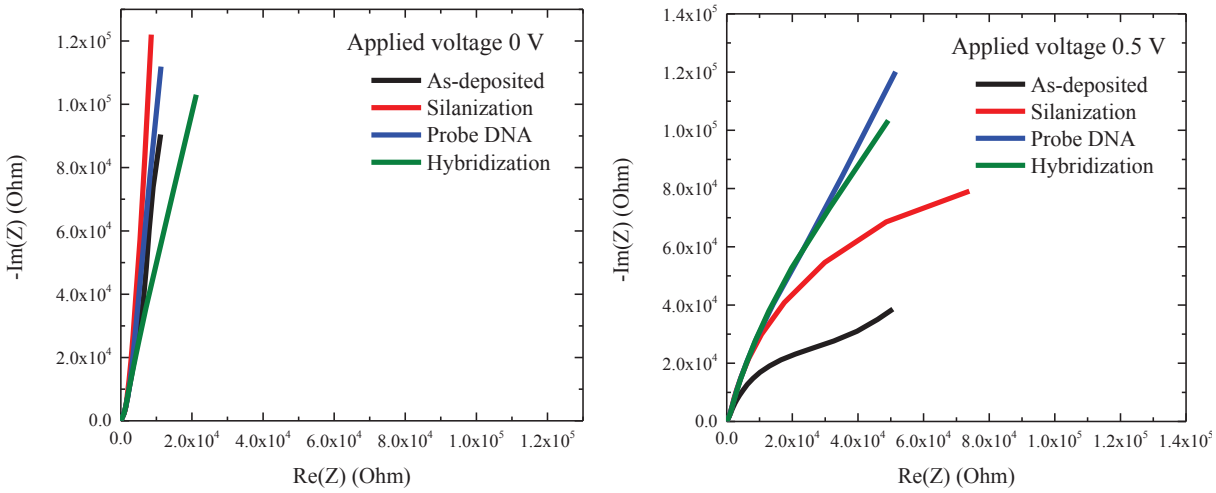

Figure 3.19: Nyquist plots of bio-modified SnO_2 nanoporous film after each modification step. Film thickness is 3.95µm. Applied voltages are of (a) 0 and (b) 0.5V (vs. ref).

At applied voltage of 0.5 V (vs. ref)

- At positive potential 0.5 V (vs. ref), the oxygen evolution reaction occurring at the DNA-modified electrode surface produces the large semicircle at low frequency region (**Figure 3.19-left**). As for bare SnO_2 film, the charge transfer resistance is high due to slow reaction rate. DNA hybridization leads to a slight decrease of the charge transfer resistance with the same reasons as for hydrogen evolution reaction at negative applied potentials.

3.1.4.2 Fluorescence detection

DNA hybridization is also detected using fluorescence microscopy. **Figure 3.20** presents a typical top view image obtained by epifluorescence microscope after DNA hybridization with Cy3 labeled complementary DNA targets on a 4.07 µm thick film.

From this micrograph, two observations can be made. First, at the center of the DNA drop spot (zone 1), the fluorescence intensity distribution is discontinuous and discrete. Second, the border of the drop is not sharp. A gradient in fluorescence intensity is observed. These observations are different from the one obtained from a dense 2D SnO_2 surface which provided an homogeneous intensity inside the DNA drop with a sharp border. The difference must be associated to the nanoporous morphology which considerably modifies the hydrophilic characteristic of the surface. Indeed, this kind of surface is much more hydrophilic than 2D surface, causing a capillary effect and a spreading of the DNA droplet on the surface as schematically presented in **Figure 3.21**.

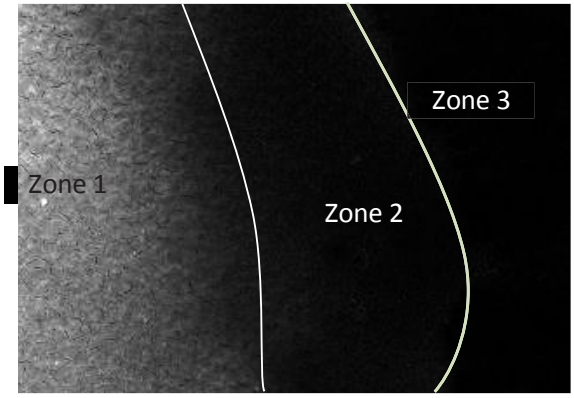

Figure 3.20: Fluorescence micrograph after hybridization to complementary DNA target molecules obtained for 4.07 µm thick nanoporous SnO_2 film.

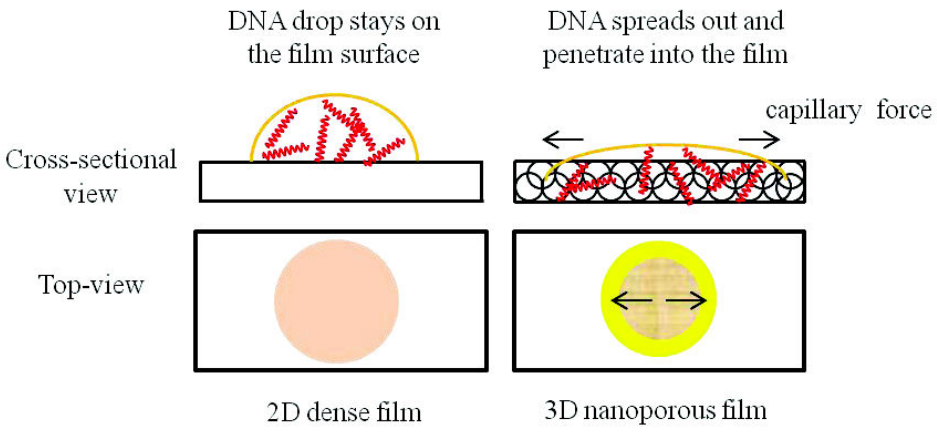

Figure 3.21: Schema of the different DNA probe drop behavior applied onto 2D dense and 3D nanoporous surfaces

In conclusion, DNA hybridization performed on the SnO_2 micrometer-thick nanoporous films obtained under different deposition potentials during 5 min, led to a variation of impedance, notably a change of ReZ at high and low frequencies. Indeed, based on the calculation of the resistances by equivalent fitting, DNA hybridization induces an increase in space charge layer resistance R_1 and a strong decrease in charge transfer resistance R_2. The slight increase of R_1 is explained by a field effect phenomenon in which the negative charges of the DNA increase the space charge layer width in the semiconductive SnO_2 sub-surface. On the other hand, hydrophilic characteristic of ds-DNA and the change in conformational structure result in a decrease of charge transfer resistance R_2 ranging between -30 to -50 %. Moreover, we confirm that the applied voltage of -0.5V (vs. ref) is the most relevant for the impedance curve exploitation. For this reason, in the following impedance analyses, only this potential will be chosen.

In the case of optical detection, a non-uniform fluorescence signal is observed with a gradient of the border due to capillary effect. Besides, no significant influence of the thickness in range from 1.95 to 4.22 µm on the sensing signals is found.

3.2 Influence of the passed charge density: from micrometer to nanometer-thick-films

3.2.1 Film cathodic electrodeposition

Although the passed charge density Q does not affect the kinetic and the thermodynamic of the electrochemical reaction, Q is proportional to the amount of NO_3^- reduced at the electrode surface to generate OH^- group. Consequently, it relates to the amount of the SnO_2 deposited on the cathode. The aim of the experiments is to investigate the influence of Q on both the morphology and the electrochemical properties of the nanoporous SnO_2 films.

The films are potentiostatically deposited by the same process at a fixed deposition potential of -1.0 V (vs. Ag/AgCl) with increased passed charge densities: 0.2, 0.4, 0.8 and 3.9 C/cm^2. The processing parameters are presented in **Table 3.11**. The deposition potential of -1.0 V (vs. Ag/AgCl) has been chosen, because at this potential, the films exhibit a homogeneous surface and a better adherence onto the ITO substrates.

Table 3.11: Processing parameters used in the electrodeposition experiments

Electrolyte	Condition			Deposition		
	T (°C)	pH	Stirring	Voltage (V vs. Ag/AgCl)	Range of charge density (C/cm^2)	Corresponding deposition time
20 mM $SnCl_2.2H_2O$ 100 mM $NaNO_3$ 75 mM HNO_3	50	1.23	No	-1.0	0.2 0.4 0.8 3.9	14±1 s 36±2 s 76±2 s 300 s

3.2.2 Film characteristics

3.2.2.1 Morphology

Figure 3.22 shows the morphology conducted using SEM of the as-deposited films. From the top view images, it seems that the particle size does not change significantly when increasing passed charge density, going from 20 to 50 nm. Elsewhere, the sample deposited with Q = 3.9 C/cm^2 presents the same pore sizes as previous micrometer-thick-films, from 20 nm to 1 µm. However, the pores are not well observed in the other films by SEM. The observations indicate a higher porosity and an increase of the pore size when the passed charge density increases from 0.2 to 0.8 C/cm^2. Besides, the film thickness, determined from cross-sectional SEM images, increases linearly from 220±10 nm to 4.2±0.3 µm. (**Figure 3.23**). Due to this wide range of film thickness obtained by changing the passed charge density, we call this part "**from nanometer to micrometer-thick nanoporous films**".

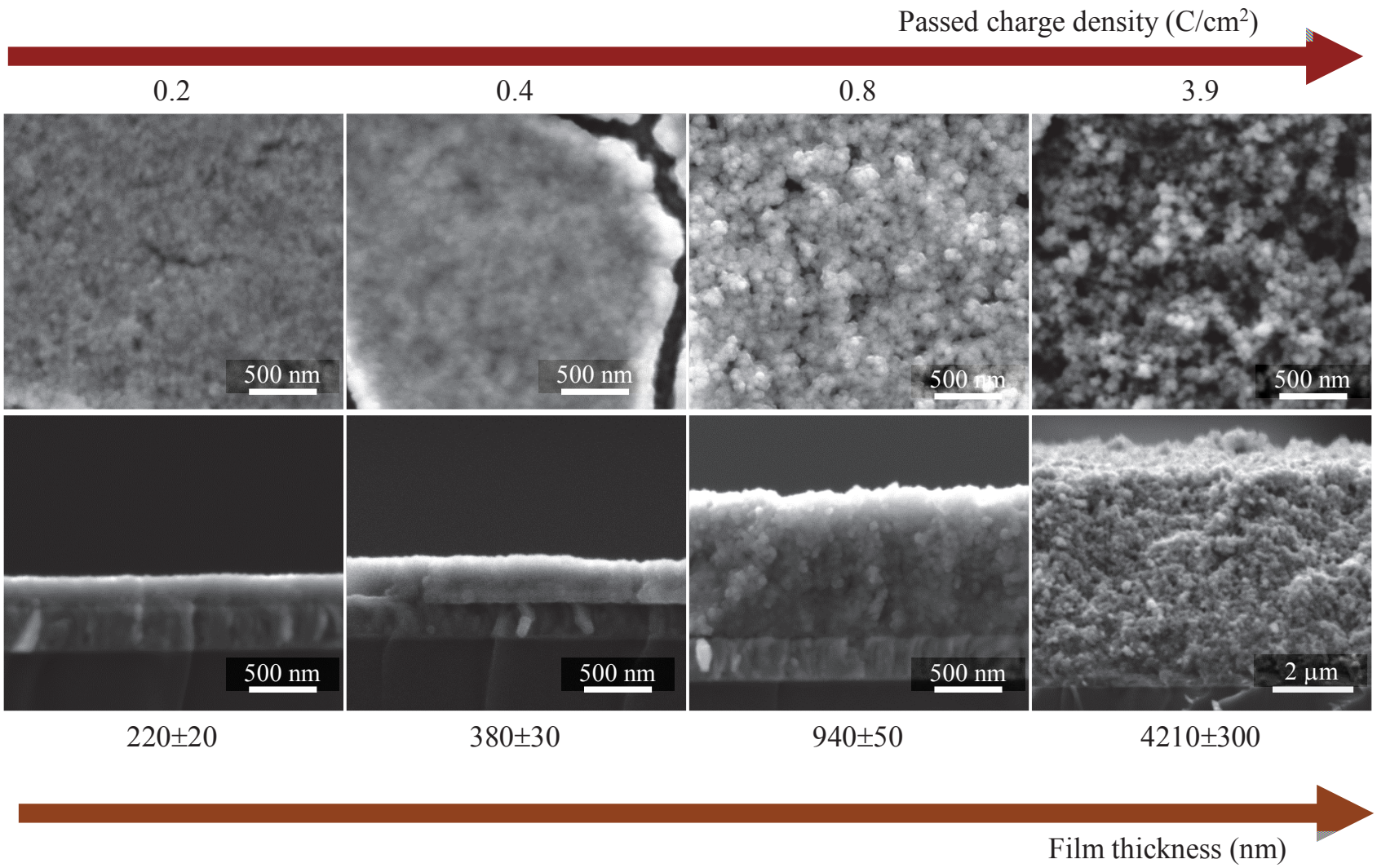

Figure 3.22: SEM images of SnO_2 films deposited onto ITO electrode at -1.0 V (vs. Ag/AgCl) with different passed charge density

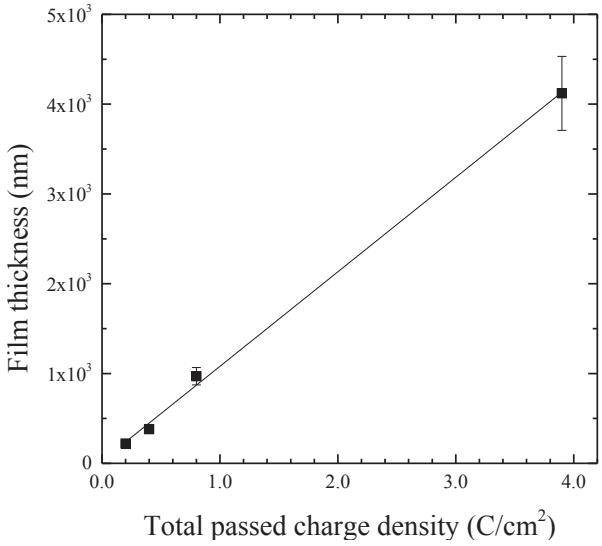

Figure 3.23: Evolution of the deposited film thickness with total transferred charge density.

Due to the difficulty of observing and measuring efficiently the pore size from the SEM images, the morphology of the 940 nm-thick-film is further characterized by HRTEM observation. The cross-section TEM image reveals much better the local nanoporous structure of the film with highly dispersed SnO_2 nanoparticles (**Figure 3.24**). The SnO_2 nanoparticles are nearly spherical. Their size is in the range of 5 to 15 nm. The average pore size is approximately 10 nm.

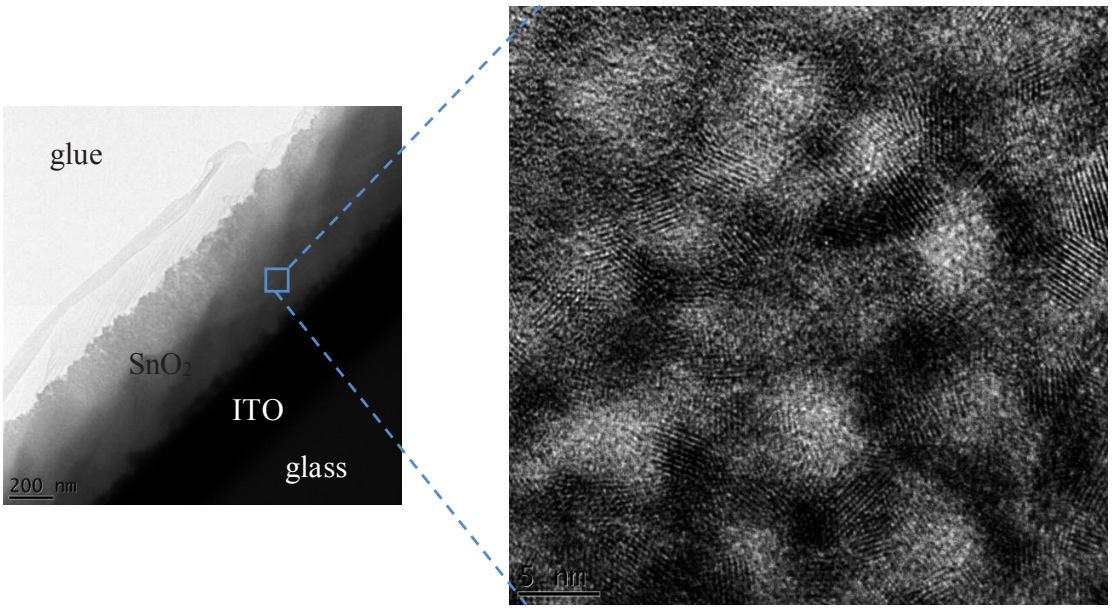

Figure 3.24: Cross-section HRTEM images of the 940nm-thick film deposited at -1.V (vs. Ag/AgCl) with Q = 0.8C/cm²

3.2.2.2 Microstructure

Figure 3.25a shows the XRD spectra of the as-deposited films. Except the pattern of the thickest film (Q = 3.9 C/cm^2) showing three peaks of tetragonal SnO_2, i.e. (101), (101) and (211) at 2θ = 26.3, 33.8 and 52.1°, respectively, the other spectra show the peaks of the ITO substrate without any peaks of SnO_2. The grazing incidence diffraction (GID) spectra of these samples exhibit very broad peaks of SnO_2 (110) and (101) at about 26.5° and 33.7°, respectively (**Figure 3.25b**). It indicates the poor crystalline and rather amorphous nature of these electrodeposited SnO_2 films due to nanosized effect. This result is in agreement with Chang et al. [7] and Hosono et al. [8]. The higher is the thickness, the higher is the relative intensity SnO_2 peak (110) compared to the peak of ITO (222).

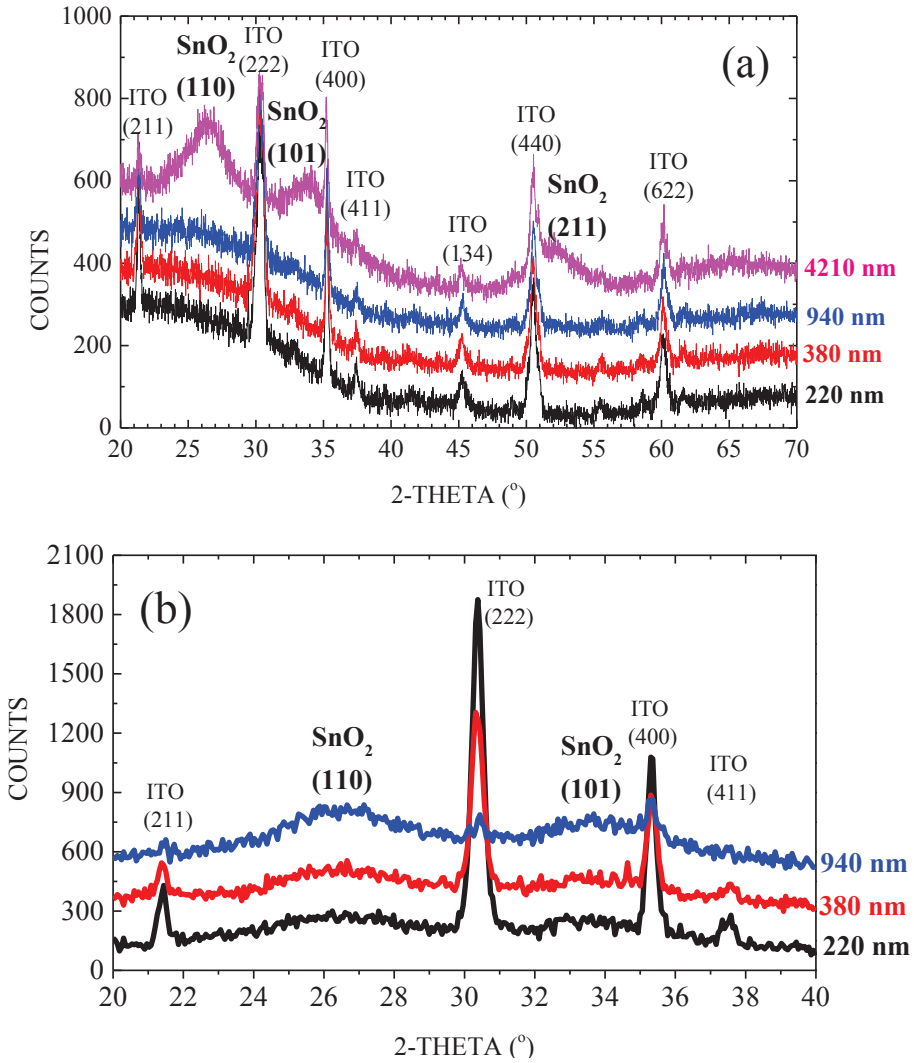

Figure 3.25: (a) XRD and (b) GID spectra of the films deposited onto ITO electrode at -1.0 V (vs. Ag/AgCl) with different passed charge densities.

Figure 3.26 shows the selected area electron diffraction (SAED) pattern of the corresponding measured area (HRTEM image). The electron diffraction, with a ring pattern, reveals the polycrystalline nature of the electrodeposited SnO_2. The d-spacing values calculated from the rings diameter are 0.345, 0.265 and 0.224 nm, belonging to the (110), (101) and (211) planes of tetragonal SnO_2. In addition, the hollow diffracted rings confirm a low crystallinity of the deposited nanoporous film.

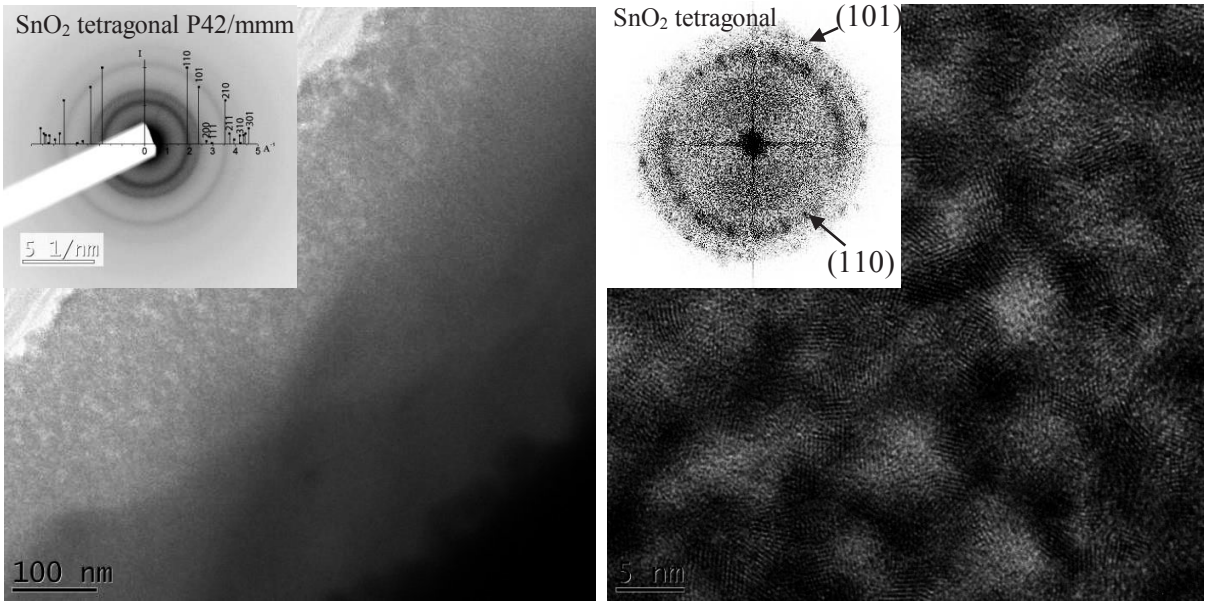

Figure 3.26: HRTEM images with their corresponding diffraction patterns.

In conclusion, at a fixed deposition potential of -1.0 V (vs. Ag/AgCl), the thickness of the SnO_2 nanoporous films can be well controlled by monitoring the total charge transfer density Q. The film thickness increases linearly with Q, from 220±20 to 4210±300 nm. SEM and TEM observation shows a nanoporous morphology of the films with the pore size from 10 nm to several hundred nm. Besides as for the micrometer-thick films, the XRD results confirm a poor crystallinity of the films.

3.2.2.3 Electrochemical properties

The impedance analyses of the as-deposited films exhibiting a wide range of thickness going from 220 nm to 4.2 µm are carried out. These analyses are conducted only at a fixed dc potential of -0.5 V (vs. ref) instead of at different potentials as in the previous part for micrometer-thick films. In addition and importantly, the hybridization buffer does not include EDTA, so that the measured pH of the solution changes from 5.5 to 7.0. The processing parameters are detailed in **Table 3.12**.

Table 3.12: Parameters of the impedance measurement process.

Electrolyte	*Frequency range*	*Modulation*	*Applied voltage V (vs. ref)*
0.5 M NaCl, 0.01 M PBS (pH = 7.0)	10 mHz to 200 kHz	10 mV	-0.5

The obtained Nyquist plots are presented in **Figure 3.27a**. The corresponding evolutions of the real part (ReZ) and imaginary part (-ImZ) as a function of frequency are presented in **Figure 3.27 (b) and (c)**, respectively.

The nanoporous SnO_2 film exhibit a large thickness-dependent impedance. Apart the 4.2 µm-thick film which exhibits two semicircles (a small arc at high frequency region and a large arc at low frequency region), impedance spectra of the thinner films display only one semicircle. This transformation can be explained by the increasing importance of the charge transfer resistance through the double layer (see schema in **Figure 3.11**) compared to the space charge layer resistance when both the film thickness and porosity decrease. Besides, the semicircle diameter decreases when increasing the film thickness.

The equivalent circuit used for data fitting R_e (Q_1, R_1) for the thinner films is presented in **Figure 3.28**. The resistance R_e is the sum of both the electrolyte and the electrode ohmic resistances. The parallel element circuit (Q_1, R_1) is responsible for the observed semicircle. Extracted electrical parameters from the modeling are showed in the **Table 3.13**.

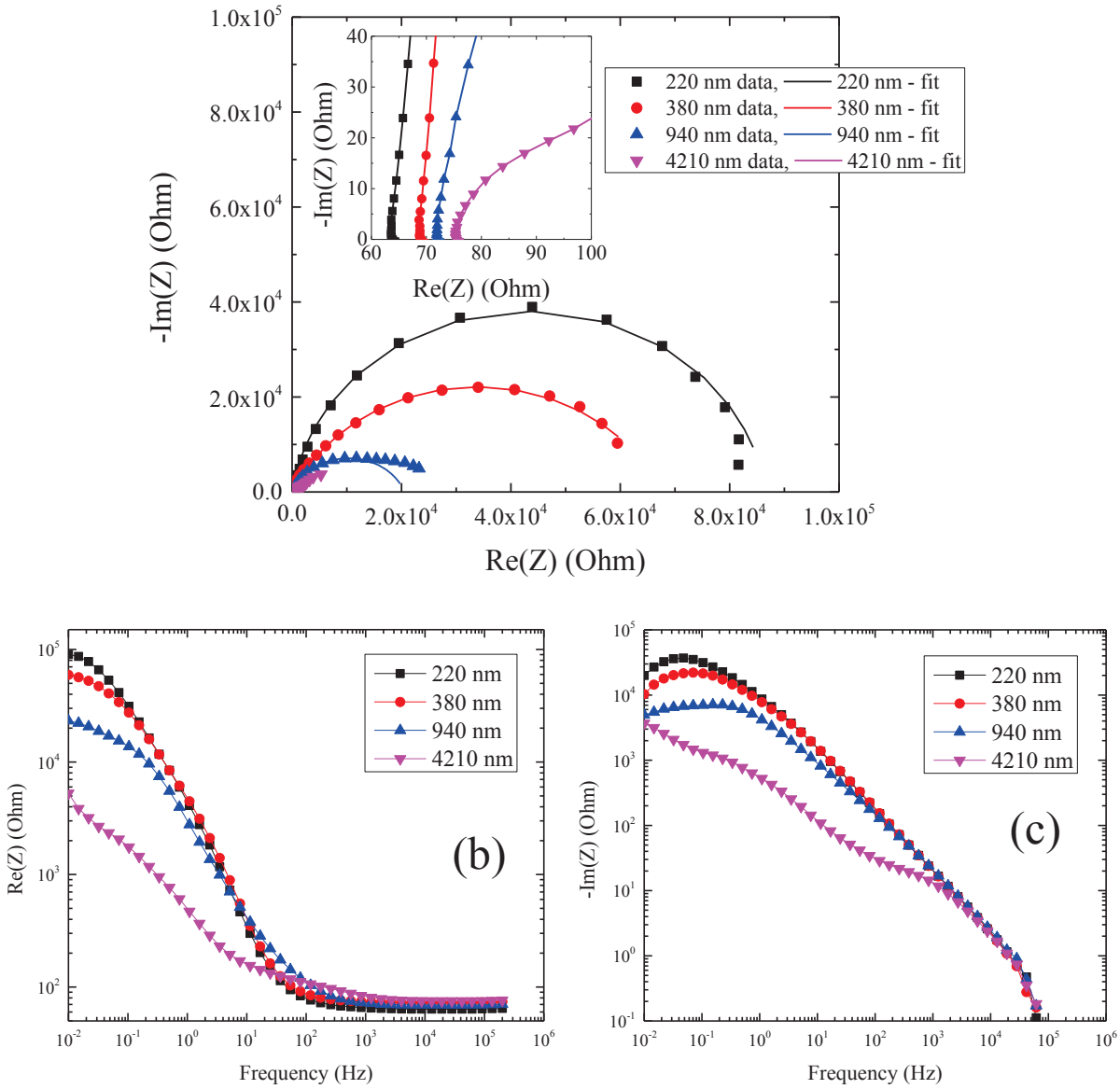

Figure 3.27: Impedance spectra (V = -0.5 V vs. ref) for electrodeposited onto ITO coated glass electrode with different film thicknesses. (a) Nyquist plots, (b) Re(Z) as a function of the frequency, and (c) –Im(Z) as a function of frequency.

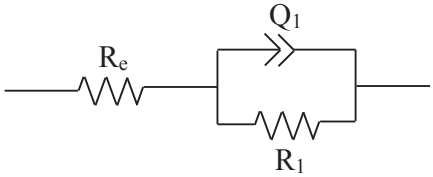

Figure 3.28: Equivalent circuit used to fit the thin SnO_2 films

Table 3.13: Components values of the equivalent circuit used for Nyquist plot modeling of the nanoporous SnO_2 electrode with different film thickness.

Q (C/cm^2)	Film thickness	R_e (Ω)	Q_1 (low frequency)		Q_2 (high frequency)		R_1 (Ω)
			C_1 (μF)	α_1	C_2 (μF)	α_2	
0.2	210 nm	64.61	23.37	0.779	-	-	84782
0.4	380 nm	70.40	26.29	0.772	-	-	66496
0.8	920 nm	73.90	38.15	0.810	-	-	21276
3.9	4210 nm	76.42	107.3	0.796	539	0.620	4025

(For all the complete fitting data, see Annex2-A2)*

From **Figure 3.27a** and **Table 3.13**, we observed that the resistance R_e increases with the film thickness and then saturates above film thickness of 1 μm. This evolution is shown in **Figure 3.29a**. We assume that the resistance of the electrolyte does not change between the experiments. Consequently, the increase of R_e is mainly due to the increase of the SnO_2 film resistance with the film thickness.

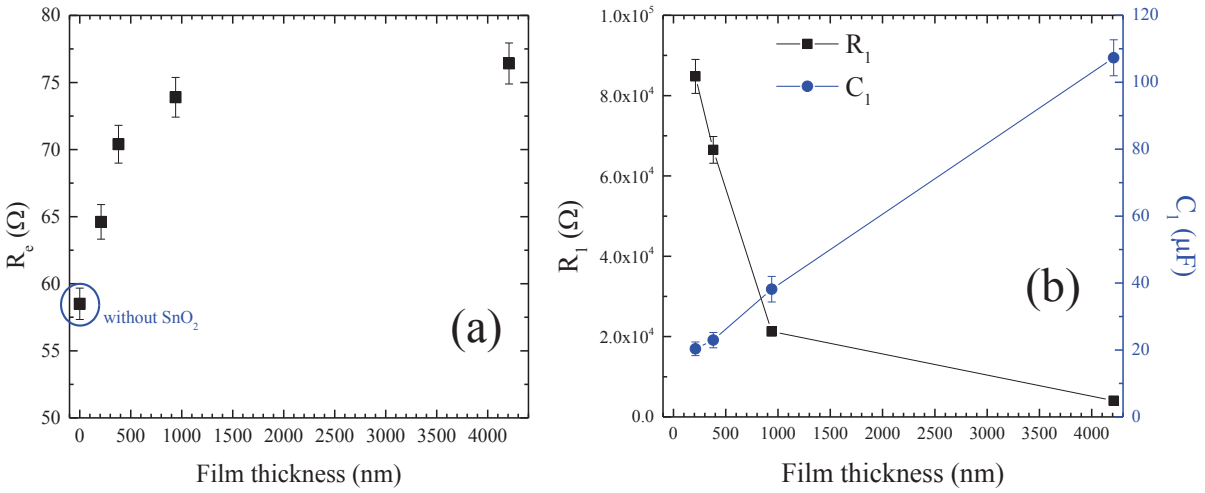

Figure 3.29: Evolution of the calculated (a) resistance R_e; (b) resistance R_1 and capacitance C_1 as a function of film thickness.

The variations of the calculated charge transfer resistance R_1 and capacitance C_1 with the film thickness are shown in **Figure 3.29b**. R_1 decreases sharply when the film thickness increases to 940 nm, and then gradually decreases for higher thickness values.

The drop of R_1 can be explained in term of a higher porosity of the thicker films. Generally, AC impedance of the films is related to their grain sizes, grain boundaries. Increment of porosity improves the real surface areas and consequently, the ionic interaction at electrolyte-electrode

interface resulting in low R_1. In contrast to R_1, regarding to the change of the capacitance C_1, an increase is observed. C_1 exhibited a slightly enhancement when the film thickness increases from 220 to 920 nm, while drastically rising when the film thickness reach 4210 nm. The capacitance of the nanoporous SnO_2 thick film 4210 nm is almost 5 times higher than that of the thin film 220 nm.

This obtained behavior of impedance evolution is in agreement with early work [9] where nanoporous antimony-doped tin oxide (ATO)/FTO film show much smaller and almost negligible semicircles in the Nyquist plot in comparison to the FTO substrate.

In conclusion, in this wide range of film thickness going from 220 to 4210 nm, the impedance signal exhibited different electrochemical behavior with the film thickness. The first semicircle at high frequency related to the space charge layer appeared only in the case of the thickest film (4.2 µm). On the other hand, only one semicircle is obtained for thinner films, the thickness of which ranges from 220 to 940 nm. This semicircle could be related to the hydrogen evolution reaction. A decrease of the charge transfer resistance R_{ct} is obtained when film thickness increases.

3.2.3 Influence of the film thickness on the response signal of DNA detection

To evaluate the influence of the film thickness on the sensing performance of the DNA detection via impedance and fluorescence measurements, the same functionalization process is applied to these nanoporous SnO_2 films. The functionalization is similar to the one used previously with liquid phase silanization. EIS measurements are carried out at a fixed potential of -0.5 V (vs. ref) after silanization, DNA probe grafting and DNA hybridization in the case of complementary and non-complementary DNA targets. The processing parameters are detailed in **Table 3.14**.

Table 3.14: Parameters of the functionalization and impedance measurement processes

Functionalization parameters			**Impedance measurement parameters**			
Silanization	C_{probe} *(µM)*	C_{target} *(µM)*	*Electrolyte*	*Frequency range*	*Modulation*	*Applied potential V (vs. ref)*
Liquid phase deposition	10	2	0.5 M NaCl 0.01 M PBS (pH = 7.0)	10 mHz to 200 kHz	10 mV	-0.5

We have observed that the wettability of the films after silanization is strongly influenced by the film thickness. In the case of the thinnest film (220 nm), the DNA probe drop is not completely

absorbed into the film. The majority of the drop stays stably on the film surface during 2 hours of incubation at room temperature. The duration for the DNA drop to be totally absorbed into the film is dependant of the film thickness and porosity. It takes about 30 minutes for a drop to be totally absorbed into the 400- nm-thick-film. When increasing the film thickness to 1µm, the time needed is approximately 30 seconds. Finally, the drop is totally and immediately absorbed into the thickest film (4.2 µm).

3.2.3.1 Non-faradic impedance detection

Figure 3.30 presents the different Nyquist plots obtained from these SnO_2 nanoporous films after the main bio-modified steps, in the case of complementary hybridization (curves on the left) and non-complementary hybridization (curves on the right).

The electrochemical behavior is similar for all the studied films. As for the thick films in the previous part, the silanization induces a large increase of the semicircle diameter. The DNA probes grafting results in a decrease of the semicircle diameter. Similarly to micrometer-thick films, this decrease is amplified by the complementary DNA hybridization. On the other hand, the impedance curves show a small change when non-complementary hybridization is applied, showing the selectivity of the hybridization process.

We must notice a difference in the behavior of the Nyquist plots obtained for the present thickest film (4.2 µm) (**Figure 3.30**) and the micrometer-thick film obtained at -1.0 V (vs. Ag/AgCl) (in the 3.1.4.1 part, **Figure 3.15**). Previously, the Nyquist plot of the bio-modified nanoporous SnO_2 film was composed of 2 semicircles each corresponding to, from left to right, the space charge layer in the sub-surface and hydrogen evolution reaction at the electrode/electrolyte interface. However, in this case, only one semicircle after functionalization process is carried out onto the surface. The reason might come from the change in pH of the electrolyte. The pH 7.0 of the electrolyte used in this experiment is higher than that of the previous one, 5.5. It is noted that hydrogen evolution reaction is less efficient at higher pH resulting in a higher charge transfer resistance. Consequently, the first semicircle is not well-resolved and hindered by the second semicircle.

Complementary hybridization

Non-complementary hybridization

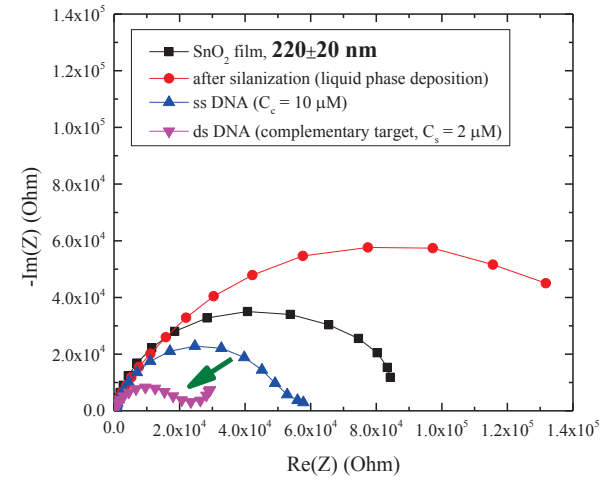

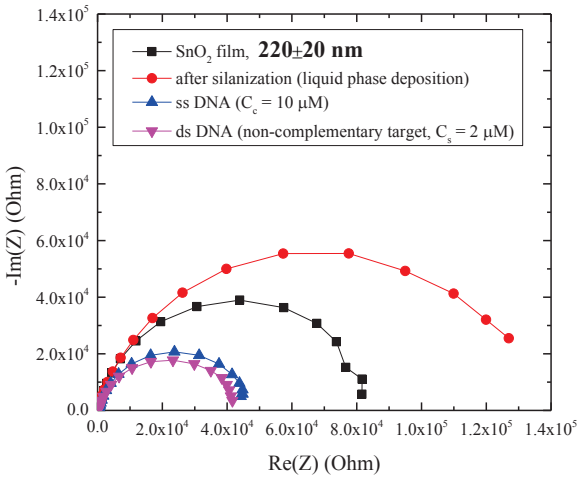

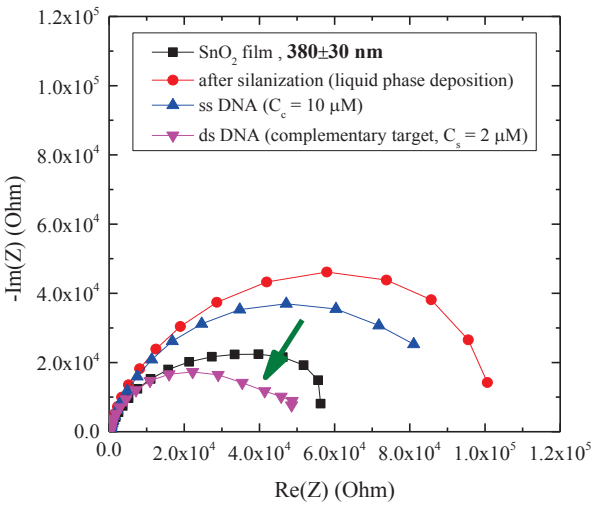

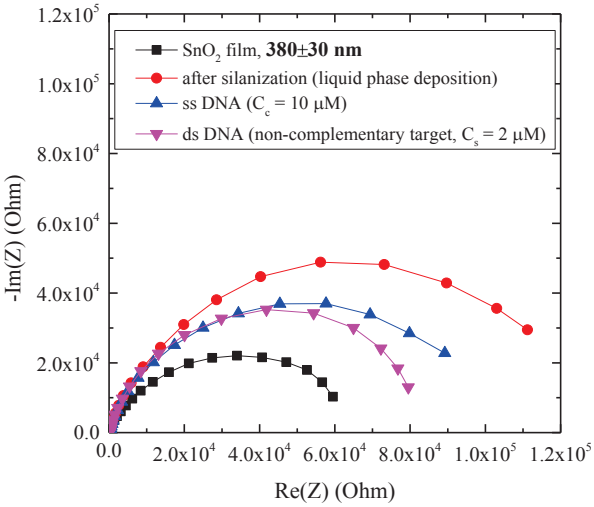

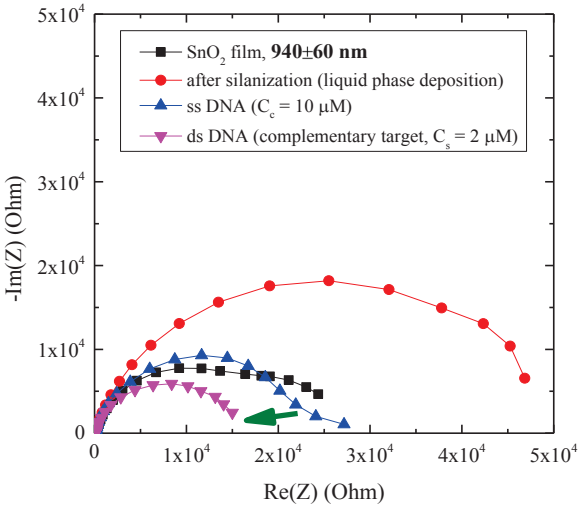

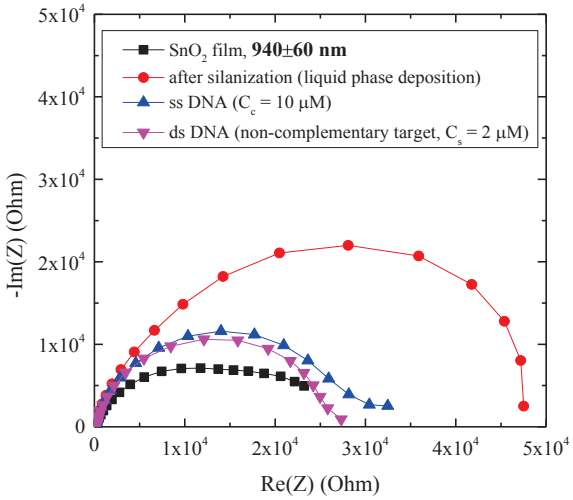

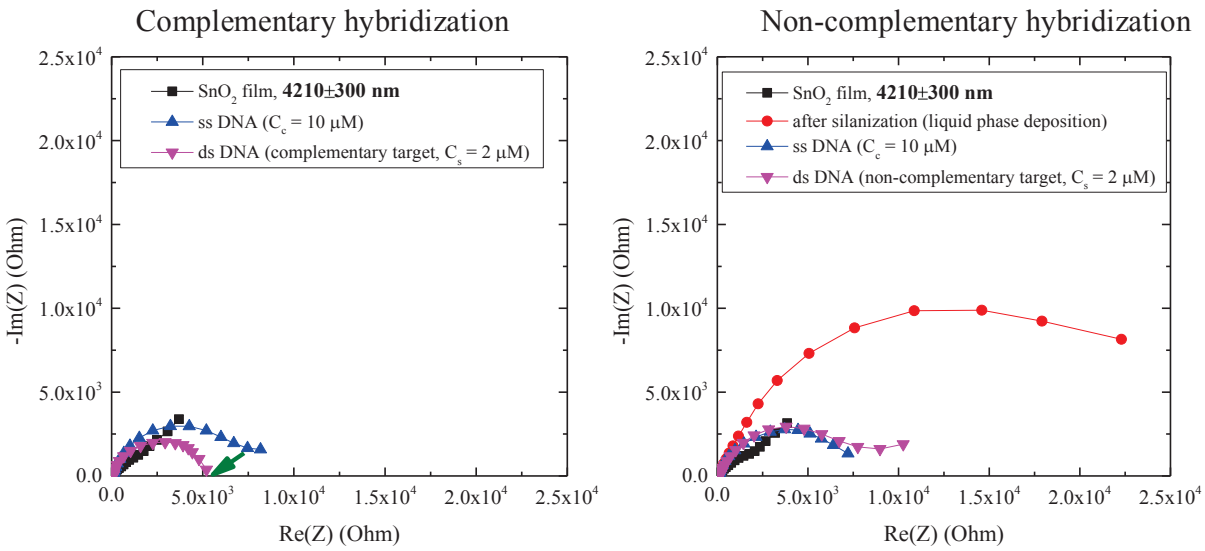

Figure 3.30: Nyquist plots of bio-modified SnO_2 nanoporous films deposited at -1.0 V (vs. Ag/AgCl) with increasing the film thickness: 220, 380, 940 and 4210 nm. DNA hybridization is performed with complementary (left) and non-complementary (right) DNA targets.

R_1 is determined from Nyquist plot modeling by using the equivalent circuit R_e (R_1Q_1) (**Figure 3.28**). The modeling parameters for these films with increasing thickness are shown in **Table 3.15**. In order to emphasize the influence of the film thickness on the decrease of the charge transfer resistance R_1 upon hybridization, $\Delta R_1/R_1$ is reported as a function of the film thickness (**Figure 3.31**).

Table 3.15: Calculated charge transfer resistance values obtained from the equivalent circuit used for Nyquist plot modeling

Film thickness (nm)	Type of DNA target molecules	R_1 (Ω)				$\Delta R_1/R_1$ (%)
		SnO_2 film	silanized	ss_DNA	ds_DNA	
220 ± 20	complementary	84782	146577	51974	24743	**-54±3**
	non-complementary	*87250*	*136078*	*45541*	*42543*	***-7±2***
380 ± 20	complementary	66496	115162	95137	43301	**-59±3**
	non-complementary	*67596*	*127038*	*101959*	*95300*	***-5±2***
940 ± 20	complementary	21276	47176	23047	15413	**-33±3**
	non-complementary	*20486*	*56258*	*28471*	*26605*	***-6±2***
4210± 300	complementary	4025	-	7381	4816	**-29±4**
	non-complementary	*5464*	*25377*	*7665*	*7910*	***-7±2***

(For all the complete fitting data, see Annex2-A2)*

The thinner and denser is the film, the more important is the decrease of R_1. The decrease of the charge transfer resistance R_1 is about -29±4 % for the thickest film (4.2 µm) and about -54±3 % for the thinnest film (220 nm). It can be concluded that the sensitivity to DNA hybridization decreases when the film thickness increases. The decrease is not more effective above a thickness value of 1 µm. The more sensitive films are the denser and the thinner films.

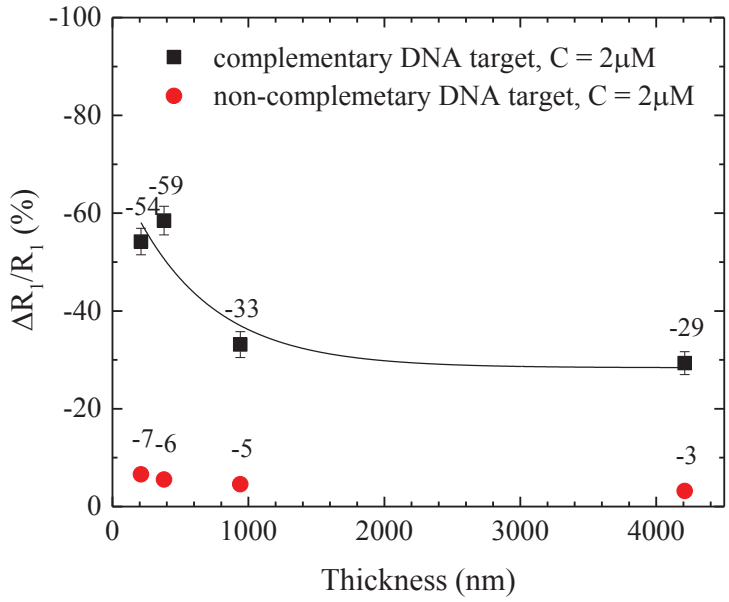

Figure 3.31: Evolution of the charge transfer resistance variation $\Delta R_1/R_1$ of the biomodified SnO_2 nanoporous films as a function of film thickness at applied potential -0.5 V (vs. ref).

3.2.3.2 Fluorescence detection

Fluorescence measurements are also performed on the corresponding samples after impedance analysis. The micrographs of the films with increasing thickness (**Figure 3.32)** present a fluorescence signal in the case of complementary DNA hybridization, while non-complementary hybridization provides no signals of fluorescence.

In the case of complementary hybridization, we note that the fluorescence intensity inside and outside of the DNA drop which corresponds to background, increases proportionally with the film thickness. The increase in the background fluorescence intensity could be attributed to a higher capillary force in the case of the thicker film, which could cause the absorbed probe DNA drop to spread out in a larger volume of the film.

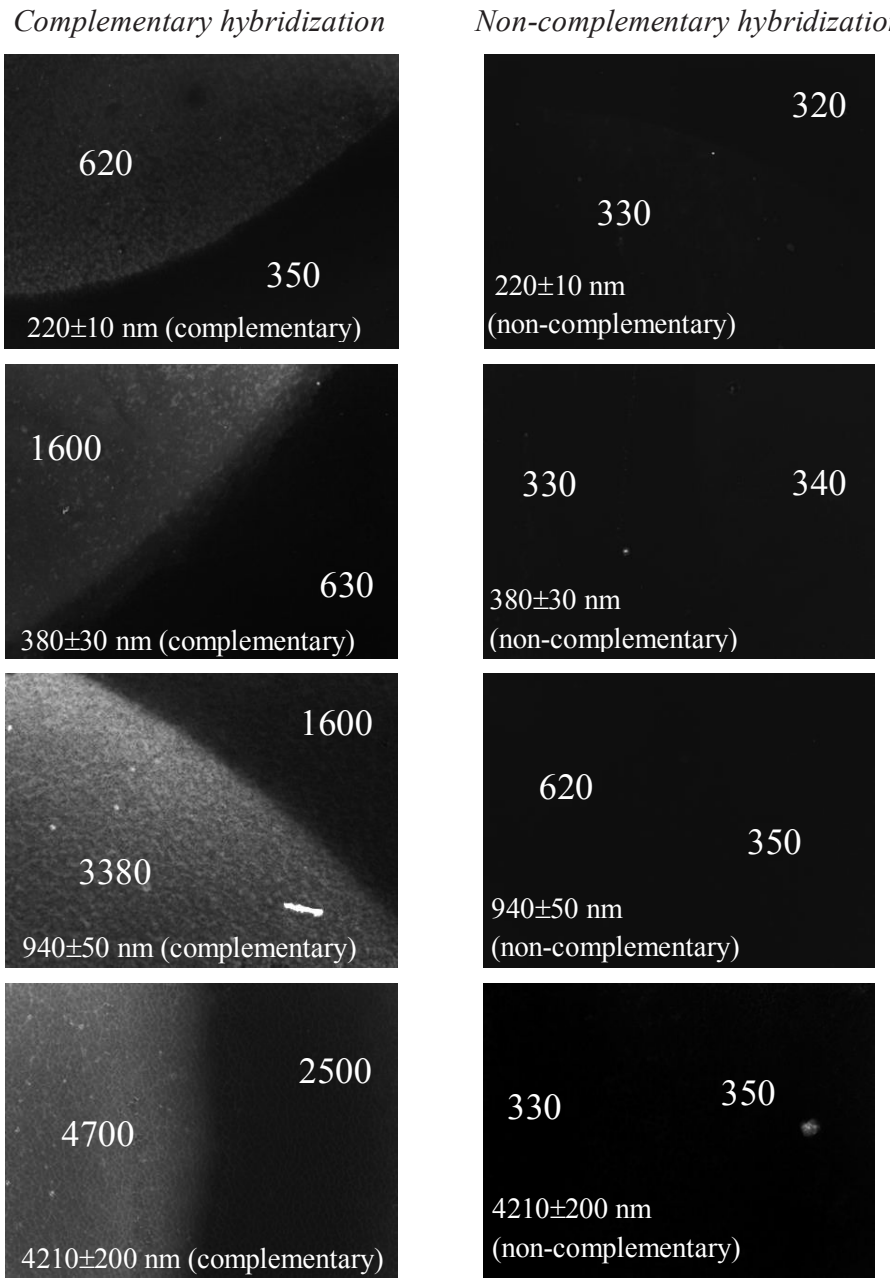

Figure 3.32: Fluorescence micrographs after hybridization of Cy3 labeled targets in the case of complementary and non-complementary DNA hybridization obtained for the SnO_2 nanoporous films as a function of film thickness: 220, 380, 940 and 4210 nm.

The evolution of the fluorescence intensity as a function of the film thickness is showed in **Figure 3.33**. As did for impedance, the fluorescence intensity is strongly dependant on the film thickness. It sharply increases with the film thickness up to about 1 μm thick and then seems to saturate. It is

striking that the obtained fluorescence evolution is totally opposite to that of impedance (**Figure 3.31**).

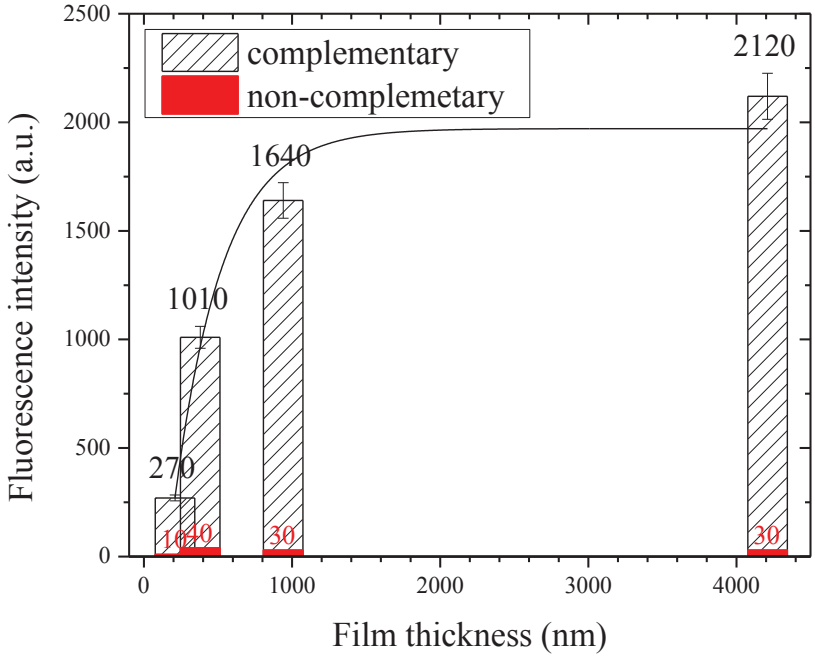

Figure 3.33: Evolution of fluorescence intensity of the biomodified SnO_2 nanoporous films as a function of film thickness.

To further investigate the DNA distribution within the nanoporous film structure, the confocal laser scanning microscope is used on the 4.2 µm-thick film. The confocal mode enables to take pictures on different focusing plans. A picture set is taken from the bottom plan up to 10 µm with steps of 0.25 µm. By assembling the 40 pictures, a 3D reconstructed picture of the surface can be created (**Figure 3.34**) showing a thickness of the fluorescent layer of about 5.0 µm. From this result, it can be concluded that the target DNA molecules infiltrate within the SnO_2 nanoporous film and successfully hybridized to DNA probes into the nanoporous structure. The difference between this thickness and the film thickness (4.2 µm) is due to a vertical light scattering phenomenon. In the case non-complementary DNA target, a very weak fluorescence signal is found, which demonstrates the high selectivity of the process performed using nanoporous SnO_2 sensing matrix.

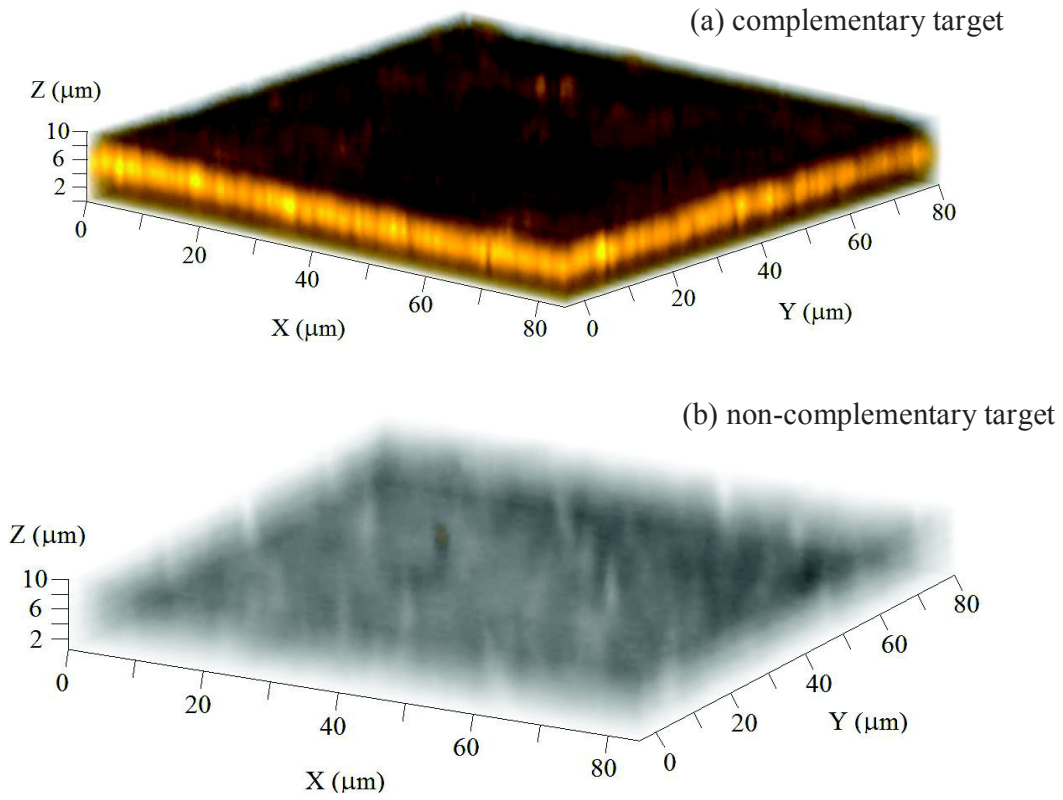

Figure 3.34: 3D constructed view of fluorescent DNA on 4.2 µm-thick nanoporous SnO_2 films obtained by confocal scanning laser fluorescence microscopy. (a) complementary and (b) non-complementary DNA target molecules with concentration of 2 µM.

To explain the exactly opposite trend between the impedance and the fluorescence results (**Figure 3.35**), we must clarify that the change of the impedance and the change of the fluorescence intensity are not due to similar factors. The fluorescence intensity strongly depends on the number of DNA probes and targets immobilized into the porous films. This number increase with the film thickness up to a certain limit. On the other hand, the change of impedance is based on the percentage of the surface area which is influenced by DNA hybridization. We hypothesize that due to much larger specific surface area, the DNA probe and target molecules absorbed into the thick film should be much higher than the thin one, leading to higher fluorescence signal. However, because of very high specific area, the percentage of the surface area in which DNA probe is grafted is lower for the thick film than the thinner one. Consequently, the free DNA surface is higher and the impedance signal becomes less important when the film thickness increases.

P.S: Some new points have been added in **Figure 3.35**. They come from a complementary study aiming to the influence of the deposition potential between -0.5 to -1.0 V (vs. Ag/AgCl) at a fixed charge density of 0.2 C/cm^2 on the film characteristics. We found that these new conditions of

deposition have no significant influence on the film characteristics (thickness, morphology, microstructure), and on the DNA detection signals. That is why we added these new points.

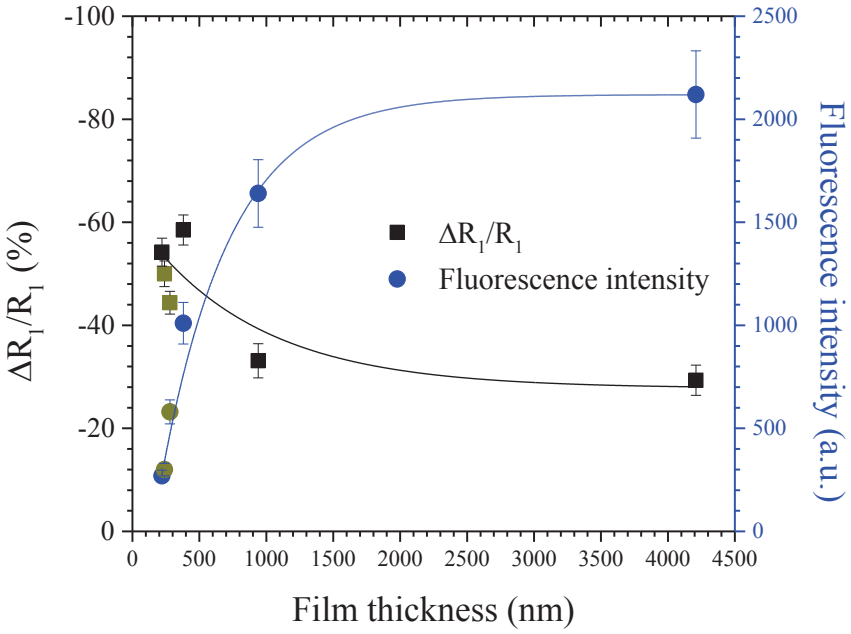

Figure 3.35: Evolution of the charge transfer resistance $\Delta R_1/R_1$ and fluorescence intensity of the biomodified SnO_2 nanoporous films as a function of film thickness.

In conclusion, in the wide range of film thickness going from 220±20 nm to 4.2±0.2 µm, both the impedance and fluorescence response signals of the DNA sensors based on nanoporous SnO_2 films are strongly dependent on the film thickness. Below a threshold thickness value of about 1.0 µm, opposite trends are found for the two different ways of detection. The EIS decreases and the fluorescence intensity increases when increasing the film thickness. However, above the thickness threshold value, no significant variation is observed for both signals, showing a saturation regime. 3D-constructed-view of fluorescent DNA on nanoporous SnO_2 films obtained by confocal scanning laser fluorescence microscopy demonstrated that the target DNA molecules are infiltrated within the SnO_2 nanoporous film and successfully hybridized into the nanoporous structure.

As the 220±20 nm-thick SnO_2 film provides a higher impedance response signal upon DNA hybridization, we further investigate the characteristics of DNA biosensors based on this film in the following parts.

3.3 Characteristics of DNA biosensors based on SnO_2 nanoporous nanometer-thick films

3.3.1 Comparison between vapor and liquid phase deposition of APTES

As discussed in the state of the art chapter, the immobilization of the DNA probes on the film electrode needs to be well controlled to obtain high sensitive and selective DNA sensor. In the present work, the DNA probes are covalently grafted to the amino-silane (APTES) through a cross-linker (glutaraldehyde molecules). Silanization of the oxide films is performed traditionally in our laboratory by liquid phase deposition of a solution of silane diluted in 95% pure ethanol and 5% deionized water. However, the main issue of liquid treatment is the eventual ability of the precursor to copolymerize in the presence of water. As a result, an inhomogeneous organosilane monolayer can eventually be formed on the surface with aggregates [10-11]. To overcome this problem, the vapor phase deposition has been studied. The low density of the agent in vapor phase could reduce the aggregation formation. In addition, because the vapor is more effective than the solution in penetrating into the nanoporous structure of the films, it is expected that a superior organosilane monolayer is achieved and consequently, a better DNA surface coverage. As a result, the DNA detection performance should be enhanced.

In this part, two different methods of silanization are performed: liquid and vapor phase deposition of APTES, which are described in detail in the experimental part. To evaluate and to compare the efficiency of both methods on the sensitivity of the DNA hybridization detection, the experiments were carried out simultaneously on 2 similar 220±20 nm-thick SnO_2 films. The processing parameters are presented **Table 3.16**.

Table 3.16: Processing parameters of the applied functionalization and impedance measurement processes.

Film thickness	**Functionalization parameters**			**Impedance measurement parameters**			
220±20 nm	*Silanization*	*C_{probe} (μM)*	*C_{target} (μM)*	*Hybridization buffer*	*Frequency (Hz)*	*Modu-lation*	*V_{dc}*
	Liquid phase deposition	10	2.0	0.5 M NaCl, 0.01 M PBS (pH = 7.0)	10 mHz to 200 kHz	10 mV	-0.5 V (vs.ref)
	Vapor phase deposition						

3.3.1.1 Impedance response signal

For EIS measurement, the analyses are carried out at a fixed potential of -0.5 V (vs. ref.) The processing parameters are detailed in **Table 3.16**.

Figure 3.36 shows the Nyquist diagrams obtained after the main stepwise of the bio-modification process:

(i) after silanization: Liquid or Vapor phase deposition of APTES,

(ii) after DNA probes grafting,

(iii) after DNA hybridization of complementary DNA targets.

The obtained impedance results clearly show the importance of the silanization conditions. In the case of vapor phase silanization, the semicircle (red curve) presents a much larger diameter than that of liquid phase deposition. As previously, we perform the Nyquist plot modeling by using the equivalent circuit R_e (R_1Q_1) to determine the charge transfer resistance R_1 variation upon the stepwise modification.

The charge transfer resistance R_1 obtained from the impedance curve after silanization in vapor phase revealed a 3 times higher value than the one after silanization in the liquid phase (**Table 3.17**). It indicates that the deposited organosilane monolayer from vapor phase is more efficient on the nanoporous film surface than in the case of liquid phase.

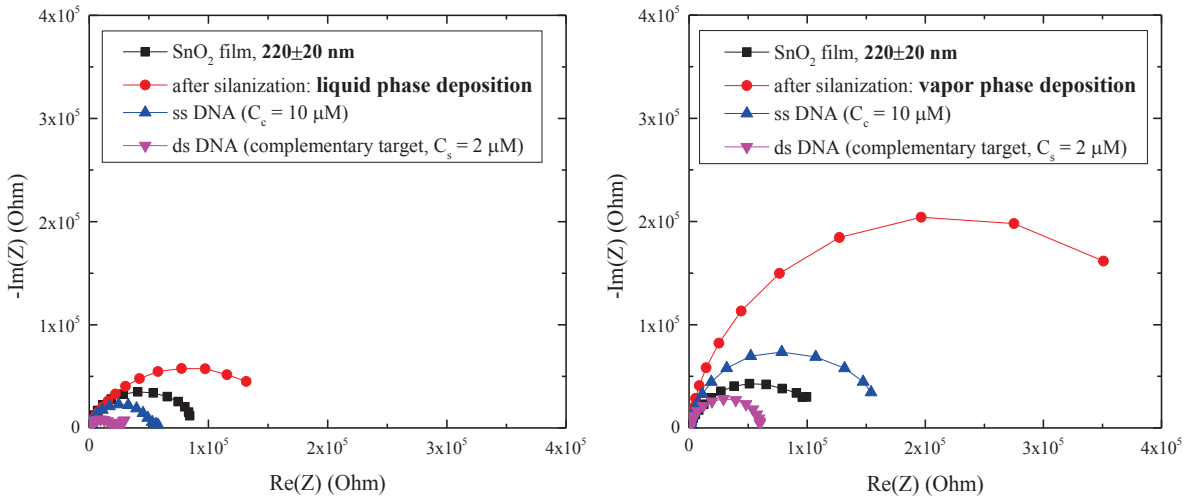

Figure 3.36: Nyquist plots of 220 nm-thick bio-modified SnO_2 nanoporous films with two different silanization processes: liquid phase (left) and vapor phase (right).

DNA hybridization is then performed on both film surfaces with the same processing parameters. With the same DNA target concentration of 2 µM, the change of charge transfer resistance $\Delta R_1/R_1$ upon DNA hybridization increases from -54±5% in the case of liquid phase deposition to -63±5% of vapor phase deposition. This nearly 10% increase of the EIS signal confirms that the sensitivity of the DNA detection can be improved significantly by using vapor phase silanization process.

Table 3.17: Charge transfer resistance R_1 values of the equivalent circuit used for Nyquist plot modeling for the impedance curves obtained at applied voltage of -0.5 V vs. ref

Film thickness (nm)	Silanization process	R_1 (Ω)				**$\Delta R_1/R_1$ (%)**
		SnO_2 film	silanized	ss_DNA	ds_DNA	
220 ± 20	Vapor phase deposition	96782	432768	95137	43301	**-63±5**
	Liquid phase deposition	82367	139221	54329	26077	**-54±5**

(For all the complete fitting data, see Annex2-A4)*

3.3.1.2 Fluorescence detection

The corresponding fluorescence micrographs of these samples (**Figure 3.37**) show a higher fluorescence intensity in the case of vapor phase deposition. Indeed, the fluorescence intensity increases almost 3 times from 270 to 840 compared to liquid phase process. It indicates that a significant increase in both the DNA probe density grafting and the hybridization efficiency is obtained after silanization in vapor phase than in case of liquid phase. The fluorescence results match with those of impedance.

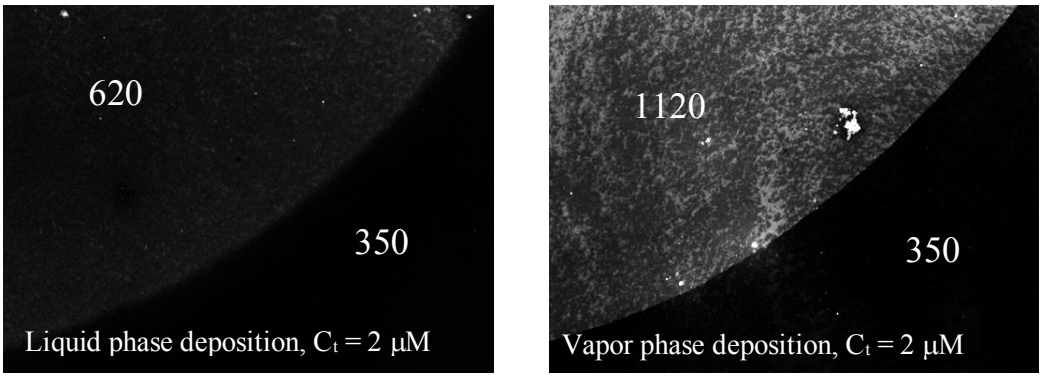

Figure 3.37: Fluorescence micrographs after complementary hybridization (C_{target} = 2 µM) on 220 nm-thick samples with different silanization processes: liquid (left) and vapor phase deposition (right).

3.3.2 Sensitivity

The sensitivity of these DNA sensors based on 220 nm-thick SnO_2 films is also studied electrically and optically using decreasing concentrations of complementary DNA target after either liquid phase or vapor phase silanization. To minimize the experimental dilution errors, the DNA target solution is prepared once at 2 µM and is then diluted to the desired lower concentrations down to 10 nM. The processing parameters are detailed in **Table 3.18**.

Table 3.18: Processing parameters of the applied functionalization and impedance measurement processes.

<table>
<tr><th>Film thickness</th><th colspan="3">Functionalization parameters</th><th colspan="4">Impedance measurement parameters</th></tr>
<tr><td rowspan="3">220±20 nm</td><td>Silanization</td><td>C_{probe} (µM)</td><td>C_{target} (µM)</td><td>Hybridization buffer</td><td>Frequency range</td><td>Modu-lation</td><td>V_{dc}</td></tr>
<tr><td>Liquid phase deposition</td><td rowspan="2">10</td><td rowspan="2">1.0
0.5
0.1
0.01</td><td rowspan="2">0.5 M NaCl
0.01 M PBS
(pH = 7.0)</td><td rowspan="2">10 mHz to 200 kHz</td><td rowspan="2">10 mV</td><td rowspan="2">-0.5
(V vs. ref)</td></tr>
<tr><td>Vapor phase deposition</td></tr>
</table>

3.3.2.1 Impedance response signals

Nyquist plots of bio-modified SnO_2 nanoporous thin films are shown in **Figure 3.38**. For all the studied samples, the DNA hybridization induces a decrease of the semicircle diameter. Besides, the decrease of DNA target concentration leads to larger semicircles upon DNA hybridization. At the lowest DNA target concentration, $C_t = 0.01$ µM, a weak change in the diameter of the semicircle upon DNA hybridization is observed.

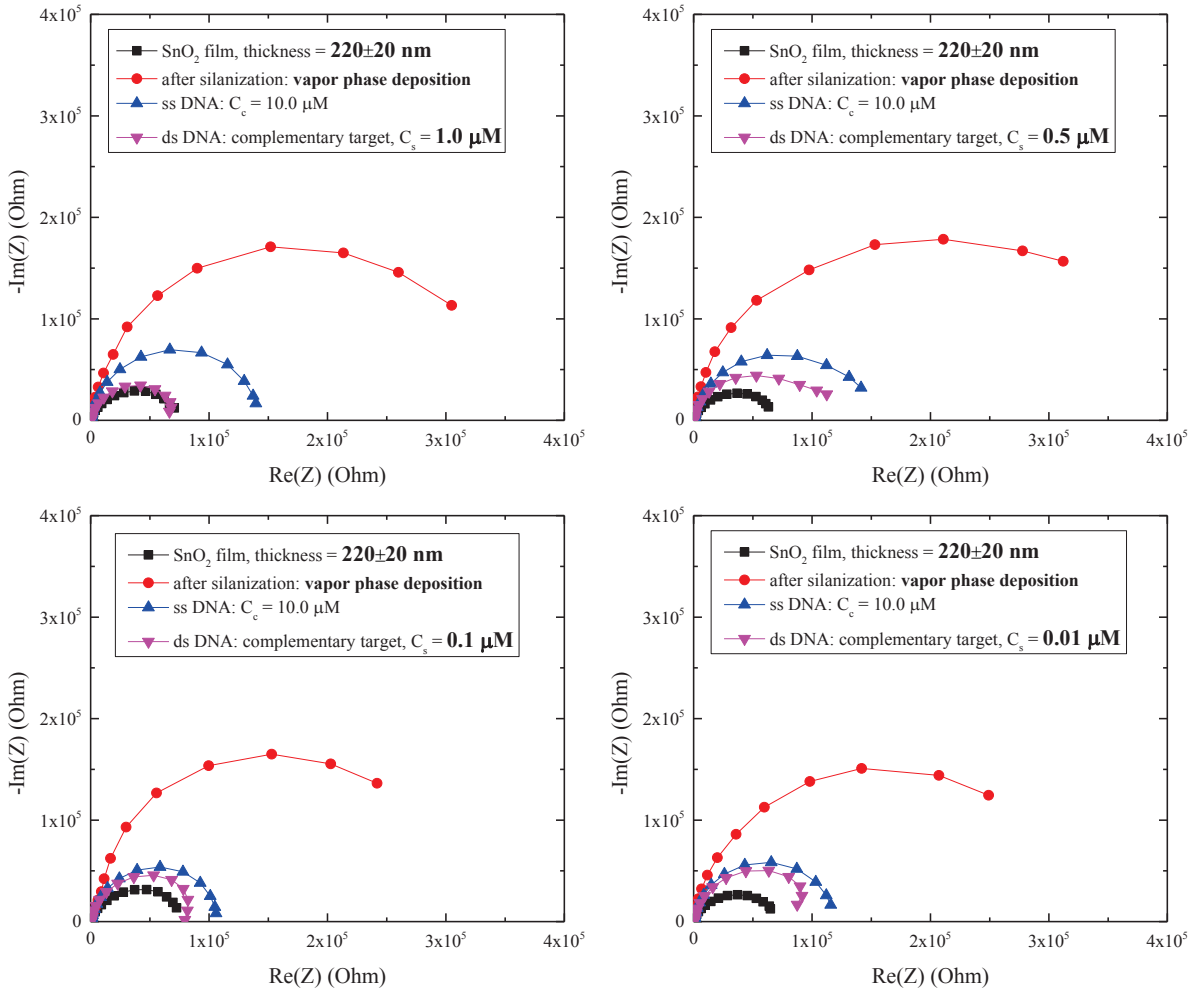

Figure 3.38: Nyquist plots of bio-modified SnO_2 nanoporous films after different stepwise of bio-modification in the case of vapor phase silanization. The DNA hybridization is performed with decreasing DNA target concentrations: 1.0, 05, 0.1 and 0.01 µM. EIS measurements are performed at voltage of -0.5 V (vs. ref).

After Nyquist plot modeling using the equivalent circuit R_e (R_1, Q_1), we calculate the values of charge transfer resistance R_1 upon DNA hybridization, after vapor (**Table 3.19a**) and liquid (**Table 3.19b**) phase silanization.

Table 3.19a: Vapor phase silanization: calculated charge transfer resistance R_1 from Nyquist plot modeling for decreasing DNA target concentrations.

Film thickness (nm)	$C_{DNA\ target}$ (μM)	R_1 (Ω)				**$\Delta R_1/R_1$ (%)**
		SnO_2 film	silanized	ss_DNA	ds_DNA	
220 ± 20	1.0	76453	370742	147929	76689	**-48±5**
	0.5	75310	377590	143687	97006	**-33±3**
	0.1	81101	416567	121467	99531	**-18±3**
	0.01	79987	393879	126847	111929	**-11±3**

(For all the complete fitting data, see Annex2-A4)*

Table 3.19b: Liquid phase silanization: calculated charge transfer resistance R_1 from Nyquist plot modeling for decreasing DNA target concentrations.

Film thickness (nm)	$C_{DNA\ target}$ (μM)	R_1 (Ω)				**$\Delta R_1/R_1$ (%)**
		SnO_2 film	silanized	ss_DNA	ds_DNA	
220 ± 20	1.0	97419	144626	47492	34015	**-28±5**
	0.5	97926	151935	45305	37707	**-17±3**
	0.1	95509	135238	43923	41441	**-7±2**

(For all the complete fitting data, see Annex2-A4)*

The decrease of the charge transfer resistance $\Delta R_1/R_1$ has been plotted as a function of DNA target concentration (**Figure 3.39)** in the case of both silanization processes: vapor and liquid phase deposition.

In the case of vapor phase silanization, the decrease of the charge transfer resistance $\Delta R_1/R_1$ is systematically wider, from 10 to 20 %, than in the case of liquid phase silanization. Indeed, in the first case it ranges from -48±5 to -11±3 % when decreasing DNA target concentration from 1 μm down to 10 nM, whereas, it decreases only from -28±5 to -7±2 % when decreasing DNA target concentration from 1 μm down to 100 nM in the case of liquid phase silanization. As expected, even for low DNA target concentrations, the infiltration of the organosilane molecules into the nanopores is facilitated in the case of gas phase, which plays a role in the sensitivity enhancement of the DNA sensor. Importantly, the detection limit of the SnO_2 nanoporous film reaches 10 nM of DNA target concentration in the case vapor phase process, which is not achieved in the case of liquid phase method.

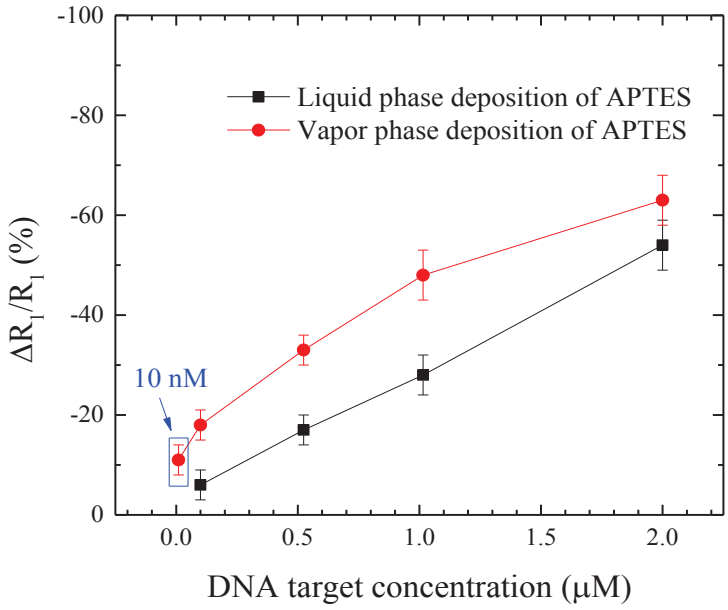

Figure 3.39: Evolution of the calculated charge transfer resistance $\Delta R_1/R_1$ of the biomodified SnO_2 nanoporous films as a function of target DNA concentration in the case of vapor (red curve) and liquid phase silanization (black curve).

3.3.2.2 Fluorescence signal

From **Figure 3.40**, the lower the DNA target concentration is, the less contrasted the DNA drop is. For an acquisition time of 2s, **Figure 3.41** exhibits a linear dependence between the DNA target concentration and the fluorescence intensity. For the lowest DNA target concentration of 0.01 µM, the DNA hybridization is only optically detected in the case of the film silanized by vapor phase deposition. In the case of liquid phase silanization, the hybridization area cannot be traced by fluorescence optical microscopy.

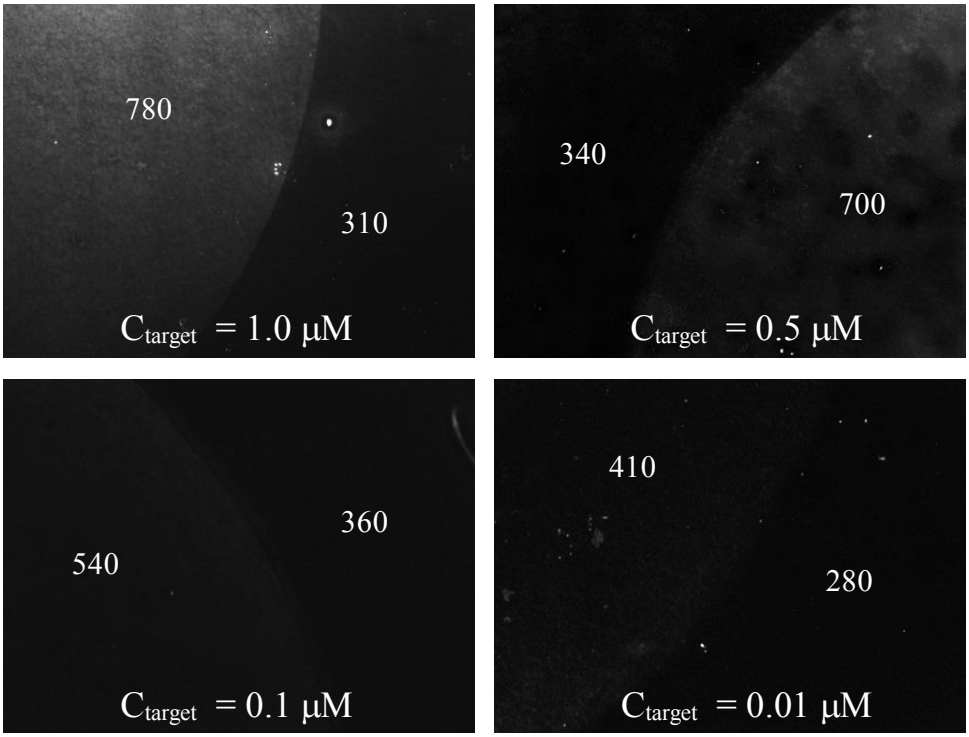

Figure 3.40: Fluorescence micrographs after hybridization of complementary DNA target labeled with Cy3 with different DNA target concentrations from 1.0 to 0.01µM. Silanization is carried out by vapor phase deposition.

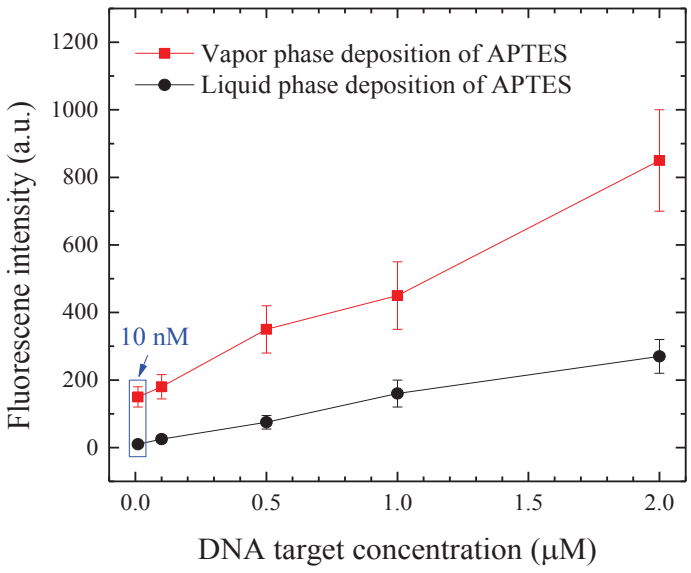

Figure 3.41: Evolution of the fluorescence intensity of the biomodified SnO_2 nanoporous films as a function of target DNA concentration in the case of vapor (red curve) and liquid phase silanization (black curve).

In conclusion, the comparison between the liquid and vapor phase processes for grafting APTES on the nanoporous SnO_2 films showed that vapor-phase method is more efficient. Indeed, the vapor is more effective than the solution in penetrating into the nanopores of the films. As a result, the DNA sensors built on vapor-treated silane layer exhibit a higher sensitivity than those produced on liquid-treated silane. The detection limit of DNA target concentration is 10 nM.

3.3.3 Calibration

It is to be kept in mind that not all DNA target molecules applied to the surface are hybridized with the DNA probe immobilized on the electrode surface. To investigate the percentage of DNA target molecules which actually joined the hybridization process, fluorescence calibration experiments are carried out.

For calibrating samples, the 220 nm-thick nanoporous films are functionalized with the same process by vapor phase deposition of APTES followed by glutaraldehyde grafting. Then, the DNA target drops with different concentrations are applied directly onto the surface without the presence of the DNA probes molecules. These samples are then kept in ambient condition until the hybridization buffer solution is completely evaporated leaving DNA target molecules on the surface without rinsing. To minimize the experimental errors, the DNA target solution is first prepared at 2 μM. It is then diluted by adding hybridization buffer solution to desired lower concentrations at 1, 0.5, 0.1, 0.01 μM.

The fluorescence intensity (I_F) of these drops is measured and plotted as a function of the number of DNA target molecule (**Figure 3.42**).

The number of DNA target molecule (N) could be determined from solution concentration as below:

$$N = N_A \, C_M \, V \qquad (3.11)$$

where, N_A is the Avogadro constant ($N_A = 6.02 \times 10^{23}$), C_M is the DNA concentration of the drop, and V is volume of the drop (V = 2 μL).

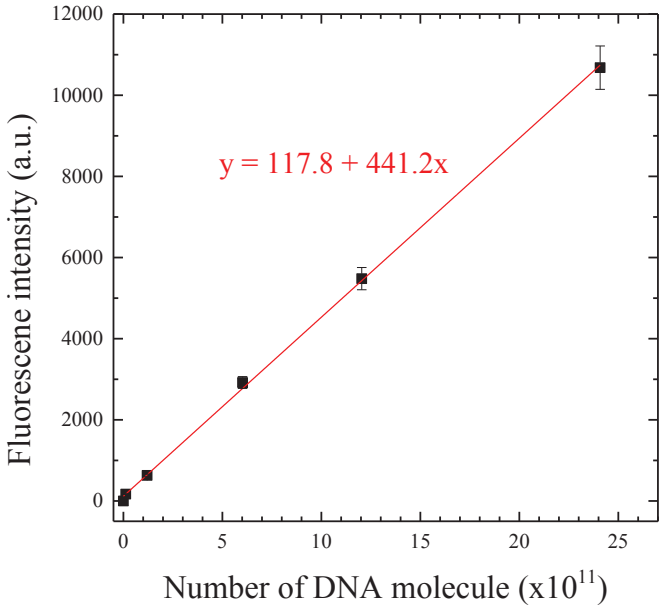

Figure 3.42: Calibrated fluorescence intensity as function of number of DNA target molecules.

In order to have an accurate calibration, linear fits are performed in two distinct ranges: at high concentration from 0.5 to 2.0 µM and low concentration from 0.01 to 0.5 µM. From obtained calibration lines, the real number of DNA target molecule (N_{sample}) captured at the surface are determined from the obtained fluorescence signal ($I_{F,\ sample}$) at each concentration of DNA target as presented at **Table 3.20**. As can be seen, the percentage of the DNA target hybridized with the probe DNA is low and increases when decreasing the initial concentration.

Table 3.20: Percentage of DNA target hybridized to the grafted probe determined by calibration

C_{target} (µM)	N (x 10^{11})	I_F (a.u.)	$I_{F,sample}$ (a.u.)	N_{sample} (x 10^{11})	N_{sample}/N (%)
2	24.08	10680	850	1.66	6.9
1	12.04	5680	450	0.75	6.3
0.5	6.02	2920	350	0.53	8.7
0.1	1.20	630	180	0.14	11.7
0.01	0.12	170	130	0.03	23.0

3.3.4 Selectivity

To further study the selectivity of the hybridization detection based on 220 nm-thick-nanoporous SnO_2 sensing matrix, new hybridizations are also carried out with 1- and 2-base mismatch DNA

target sequences in which the middle base(s) is (are) replaced by its complement (the formula of the mutation targets are detailed in the experimental part). To compare the obtained signals, the same process is applied to similar samples. The concentration of the all DNA targets is fixed at 2 µM. The silanization is carried out in vapor phase deposition technique. The processing parameters are detailed in **Table 3.21**.

Table 3.21: Parameters of the functionalization and impedance measurement processes

Functionalization parameters				**Impedance measurement parameters**			
Silanization	*C_{probe} (µM)*	*C_{target} (µM)*	*Types of DNA target*	*Electrolyte*	*Frequency range*	*Modula-tion*	*Applied voltage*
Vapor phase deposition	10	2.0	1-base mismatch 2-base mismatch	0.5M NaCl 0.01M PBS (pH = 7.0)	10mHz to 200kHz	10mV	-0.5 V (vs. ref)

3.3.4.1 Impedance signal responses

Nyquist plots of bio-modified SnO_2 nanoporous thin films in which DNA hybridization are performed with 1- and 2-base mismatch DNA target are shown in **Figure 3.43**. The DNA hybridization causes a decrease in charge transfer resistance for all types of DNA target. As expected, the EIS response generated from 1-base mismatch shows a higher decrease in diameter of the semicircle compared to that of 2-base mismatches.

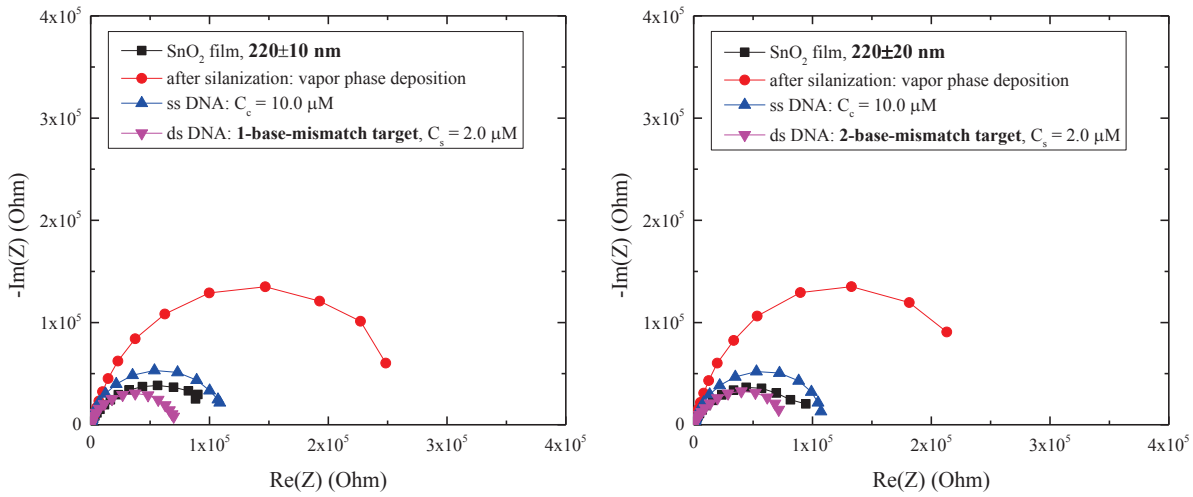

Figure 3.43: Nyquist plots of bio-modified SnO_2 nanoporous thin film in which DNA hybridization are performed with 1- (left) and 2-base mismatch (right) DNA target

To evaluate the selectivity of the process, we compare the different variations of the charge transfer resistance $\Delta R_1/R1$ obtained in the different cases (**Figure 3.44**). $\Delta R_1/R_1$ for 1- and 2-base-mismatch DNA targets are -34 and -21%, respectively. The use of non-complementary DNA target shows a -6% decrease, which can be attributed to non-specific adsorption of DNA target. In comparison with the fully complementary hybridization signal, the loss of signal is -58±5 in the case of 1-base mismatch and -71±5 in the case of 2-base mismatch.

Table 3.22: Calculated charge transfer resistance R_1 values of the equivalent circuit used for Nyquist plot modeling for the impedance curves obtained in the cases of 1- and 2-base mismatch hybridization at applied voltage of -0.5 V (vs. ref).

Film thickness (nm)	$C_{DNA\ target}$ (µM)	Type of DNA target molecules	R_1 (Ω)				**$\Delta R_1/R_1$ (%)**
			SnO_2 film	silanized	ss_DNA	ds_DNA	
220 ± 20	2.0	1-base mismatch	98742	316254	120292	79007	**-34±5**
		2-base mismatch	97249	304519	109624	86879	**-21±4**

(For all the complete fitting data, see Annex2-A5)*

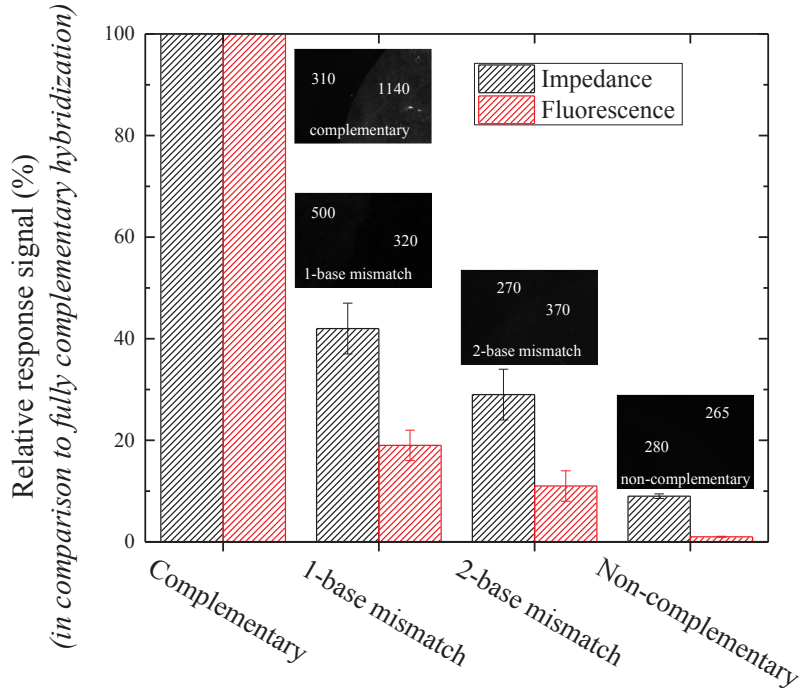

Figure 3.44: Relative EIS and fluorescence signals (in comparison to fully complementary hybridization) when DNA hybridization are performed with different types of DNA target: 1-, 2-base mismatch and non-complementary.

3.3.4.2 Fluorescence signals

To further support the results observed in impedance measurements, the selectivity of the films has also been studied optically by fluorescence optical microscopy. **Figure 3.44** gives the fluorescence intensity on the corresponding films after measuring impedance. The complementary target shows a highest signal at 920. The mismatch-DNA exhibits a lower signal, 180 and 100 for 1-base and 2-base mismatch respectively. The lowest signal 15 is obtained when non-complementary target is used. In comparison with the fully complementary hybridization signal, the loss of fluorescence signals is -81±3 % in the case of 1-base mismatch and 89±3 % in the case of 2-base mismatch. The fluorescence results are totally matched with those of impedance, which demonstrates the high selectivity of the process on nanoporous SnO_2 sensing matrix.

In conclusion, the impedance and fluorescence response signals are strongly dependent on the types of the target DNA molecules applied to the surface. It demonstrates a high selectivity of the process on nanoporous SnO_2 films.

3.3.5 Reusability

The reusability of the device is tested from dehybridization-rehybridization cycles. For DNA dehybridization, the electrode surface is exposed to a solution of 0.1 M NaOH for 30 min and then thoroughly rinsed by deionized water. After each hybridization and dehybridization process, fluorescence and impedance measurements are performed to evaluate the state of the sample.

The processing parameters regarding impedance measurements are detailed in **Table 3.23**. The films are the 220 nm-thick nanoporous films which have been silanized in vapor phase to give the sensor a better signal response.

Table 3.23: Parameters of the functionalization and impedance measurement processes for a 220 nm-thick nanoporous SnO_2 film submitted to reusability test.

Functionalization parameters			**Impedance measurement parameters**			
Silanization	C_{probe} (μM)	C_{target} (μM)	*Electrolyte*	*Frequency*	*Modulation*	V_{dc}
Vapor phase deposition	10	2.0	0.5 M NaCl 0.01 M PBS (pH = 7.0)	10 mHz to 200 kHz	10 mV	-0.5 V (vs. ref)

Figure 3.45 and **3.46** show the evolution of the fluorescence intensity and the Nyquist diagrams, respectively, after each step of hybridization and denaturation.

- After the first hybridization, the fluorescence signal intensity is 920 (**Figure 3.45**) and the calculated charge transfer resistance R_1 decrease is -62% (**Figure 3.46, from black to red curve**). These values are in agreement with the previous values found for such 220 nm-thick-nanoporous films.
- After the first dehybridization, the fluorescence intensity dramatically decreases of 97% to 30, which is in relation to the removal of fluorescence DNA targets. The impedance (**blue curve**) increases to a value slightly inferior to the previous one obtained for ssDNA (**black curve**). It indicates some changes in surface state, either probe damage or probe removal.
- After the second hybridization, the fluorescence intensity is only 230, which is 75% lower than that of the first hybridization. And, the impedance decreases of 52% back to the previous value corresponding to ds-DNA (**pink curve**).
- After the second dehybridization, the impedance (**green curve**) increases to a value completely different from the original curve of ss-DNA (**black curve**). It confirms a strong change in the state of the ss-DNA layer.
- After the third hybridization, no fluorescent drop is found on the film surface and the decrease of the impedance is just 20%. It is believed that the third hybridization failed.

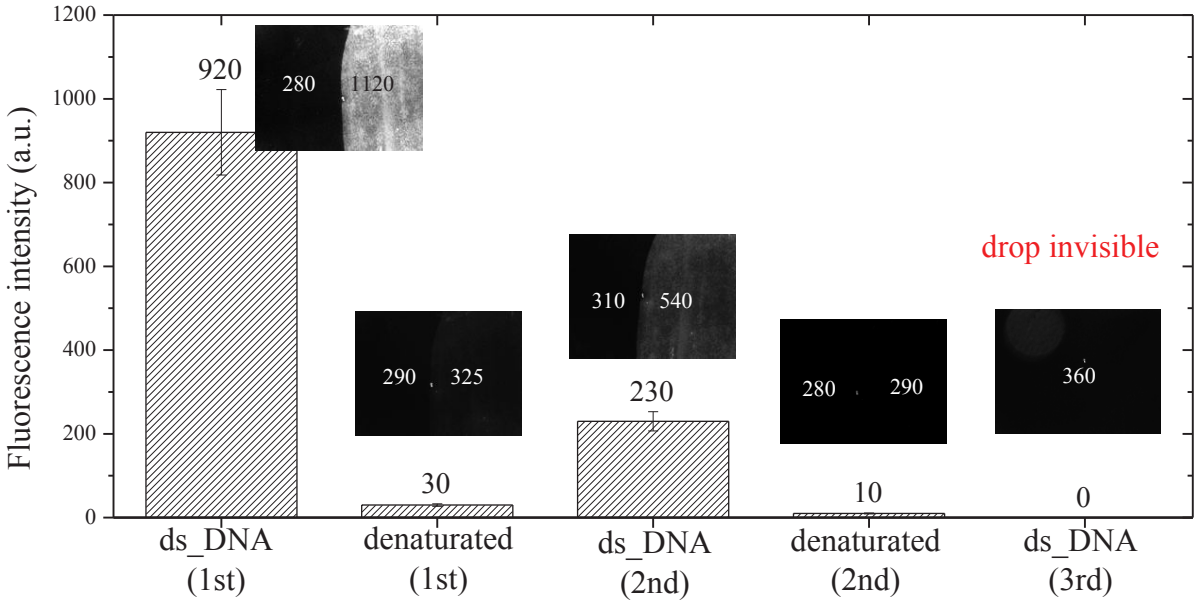

Figure 3.45: Evolution of the fluorescence intensity along 3 consecutive cycles of hybridization/denaturation experiments

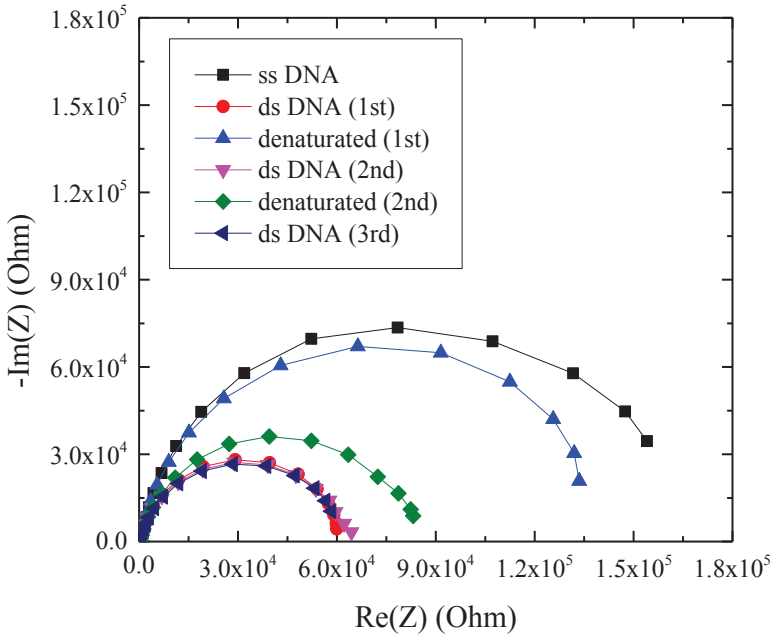

Figure 3.46: Nyquist plots of the bio-modified films obtained at 3 cycles of hybridization/denaturation experiments

In this study, several points are emphasized. The fluorescence signals seem to be more relevant to describe the real DNA state than the impedance signals. The decrease in fluorescence intensity according to stepwise process shows that the amount of fluorescent DNA target molecules is less and less important. The hybridization efficiency is strongly reduced from the second DNA hybridization.

On the other hand, the impedance changes are not in agreement with the fluorescence signals. They seem to be related to other phenomena. They can be originated from the accumulation of salts which are left and trapped inside the porous structure following the first and the second dehybridization. In our case, these salts might be either NaOH from the denaturating solution or NaCl from the electrolyte of impedance measurement.

These results show that in these conditions of dehybridization, the reusability of the SnO_2 nanoporous based DNA sensor is impossible. In order for our sensor to be reusable, it is necessary to have an effectively cleaning process to remove the trapped salts from the pores and a proper storage method. Another way of dehybridization should be tested, particularly, by heating the sensors up to the $T_{melting}$ of DNA. This method would enable to avoid the effect of the trapped salts responsible to the impedance changes.

REFERENCES

[1] S. B. Sadale and P. S. Patil, "Nucleation and growth of bismuth thin films onto fluorine-doped tin oxide-coated conducting glass substrates from nitrate solutions", *Solid State Ionics,* vol. 167, pp. 273-283, 2004.

[2] J. Bisquert, G. Garcia-Belmonte, F. Fabregat-Santiago, N. S. Ferriols, P. Bogdanoff, and E. C. Pereira, "Doubling Exponent Models for the Analysis of Porous Film Electrodes by Impedance. Relaxation of TiO_2 Nanoporous in Aqueous Solution", *The Journal of Physical Chemistry B,* vol. 104, pp. 2287-2298, 2000.

[3] D. D. Macdonald, "Reflections on the history of electrochemical impedance spectroscopy", *Electrochimica Acta,* vol. 51, pp. 1376-1388, 2006.

[4] W. Cai, J. R. Peck, D. W. van der Weide, and R. J. Hamers, "Direct electrical detection of hybridization at DNA-modified silicon surfaces", *Biosensors and Bioelectronics,* vol. 19, pp. 1013-1019, 2004.

[5] W. Yang, J. E. Butler, J. N. Russell, and R. J. Hamers, "Interfacial Electrical Properties of DNA-Modified Diamond Thin Films: Intrinsic Response and Hybridization-Induced Field Effects", *Langmuir,* vol. 20, pp. 6778-6787, 2004.

[6] B. Piro, J. Haccoun, M. C. Pham, L. D. Tran, A.Rubin, H. Perrot, and C. Gabrielli, "Study of the DNA hybridization transduction behavior of a quinone-containing electroactive polymer by cyclic voltammetry and electrochemical impedance spectroscopy", *Journal of Electroanalytical Chemistry,* vol. 577, pp. 155-165, 2005.

[7] S.-T. Chang, I.-C. Leu, and M.-H. Hon, "Preparation and characterization of nanostructured tin oxide films by electrochemical deposition", *Electrochemical and solid-state letters,* vol. 5, pp. C71-C74, 2002.

[8] E. Hosono, S. Fujihara, H. Imai, I. Honma, and H. Zhou, "Fabrication of highly porous and micropatterned SnO_2 films by oxygen bubbles generated on the anode electrode", *Chem Commun (Camb),* pp. 2609-11, 2005.

[9] S. Sharma, A. M. Volosin, D. Schmitt, and D.-K. Seo, "Preparation and electrochemical properties of nanoporous transparent antimony-doped tin oxide (ATO) coatings", *Journal of Materials Chemistry A,* vol. 1, pp. 699-706, 2013.

[10] S. Fiorilli, P. Rivolo, E. Descrovi, C. Ricciardi, L. Pasquardini, L. Lunelli, L. Vanzetti, C. Pederzolli, B. Onida, and E. Garrone, "Vapor-phase self-assembled monolayers of aminosilane on plasma-activated silicon substrates", *J Colloid Interface Sci,* vol. 321, pp. 235-41, 2008.

[11] G.-Y. Jung, Z. Li, W. Wu, Y. Chen, D. L. Olynick, S.-Y. Wang, W. M. Tong, and R. S. Williams, "Vapor-Phase Self-Assembled Monolayer for Improved Mold Release in Nanoimprint Lithography", *Langmuir,* vol. 21, pp. 1158-1161, 2005.

CHAPTER IV: Label-free DNA biosensors based on SnO_2 NWs

4.1 Preparation of SnO_2 nanowires (NWs)

The elaboration of the 1D SnO_2 NWs is based on a two-step-process which is described in the experimental part. The first step is the template-free electrodeposition of Sn NWs on the ITO/glass electrode. The second step deals with converting these deposited Sn NWs to form SnO_2 NWs by thermal oxidation.

4.1.1 Electrodeposition of Sn NWs

4.1.1.1 Cyclic voltammetry

To investigate the mechanism responsible for the formation of Sn NWs on the ITO-film electrode, cyclic voltammetry is performed without stirring at a scan rate of 50 $mV.s^{-1}$. The processing parameters are detailed in **Table 4.1**.

Table 4.1: Processing parameters used in cyclic voltammetry test.

Electrolyte	Condition			Cyclic voltammetry		
	T (^oC)	pH	Stirring	Working electrode	Scan rate (mV/s)	E_{oc} (mV)
20 mM $SnCl_2.2H_2O$ in deionized water	20	2.30	-	ITO/glass	50	-60

The addition of $SnCl_2.H_2O$ into deionized water results in a colloidal solution due to the hydrolysis of $SnCl_2$ to form $Sn_4(OH)_6Cl_2$ given by the equation [1-2]:

$$4SnCl_2 + 2H_2O \leftrightarrow Sn_4(OH)_6Cl_2 + 2HCl \qquad (4.1)$$

The measured pH of 2.30 of the colloidal solution consisting of $SnCl_2.2H_2O$ in deionized water is related to the presence of the product HCl in the solution according to reaction 4.1. Consequently, it confirms the formation of tin complex $Sn_4(OH)_6Cl_2$ in the $SnCl_2$ solution.

Figure 4.1 shows a typical cyclic voltammogram recorded onto an ITO working electrode at room temperature. The arrows show the scan direction. The potential is scanned from open-circuit potential E_{oc} (at -60 mV), reversed at -1.5V to 0V, and terminated at E_{oc}. The current-voltage curve is characteristic of metal deposition and oxidation process.

Tin deposition is related to the flow of cathodic current below -0.5 V (vs. Ag/AgCl) on the forward scan. However, the deposition of Sn metal does not result from Sn^{2+} ions reduction according to

the reaction 3.4 in this case. Alternatively, it could be caused by the reduction of the tin complex $Sn_4(OH)_6Cl_2$. However, no paper has been reported on electrochemical reduction of such compound. We propose that the $Sn_4(OH)_6Cl_2$ tin complex is electrochemically reduced on the ITO electrode surface according to the reaction 4.2 as below:

$$Sn_4(OH)_6Cl_2 + 8e^- \rightarrow 4Sn + 2OH^- + 6Cl^- \quad (4.2)$$

On the reverse scan toward more positive potentials, a well-defined oxidation peak appears at -0.15 V (vs. Ag/AgCl), which is associated to the reoxidation of the deposited Sn on the electrode surface.

From the obtained voltammogram, the electrodeposition of Sn could be performed from the reduction of the $Sn_4(OH)_6Cl_2$ tin complex at potentials ranging from -0.5 to -1.2 V (vs. Ag/AgCl).

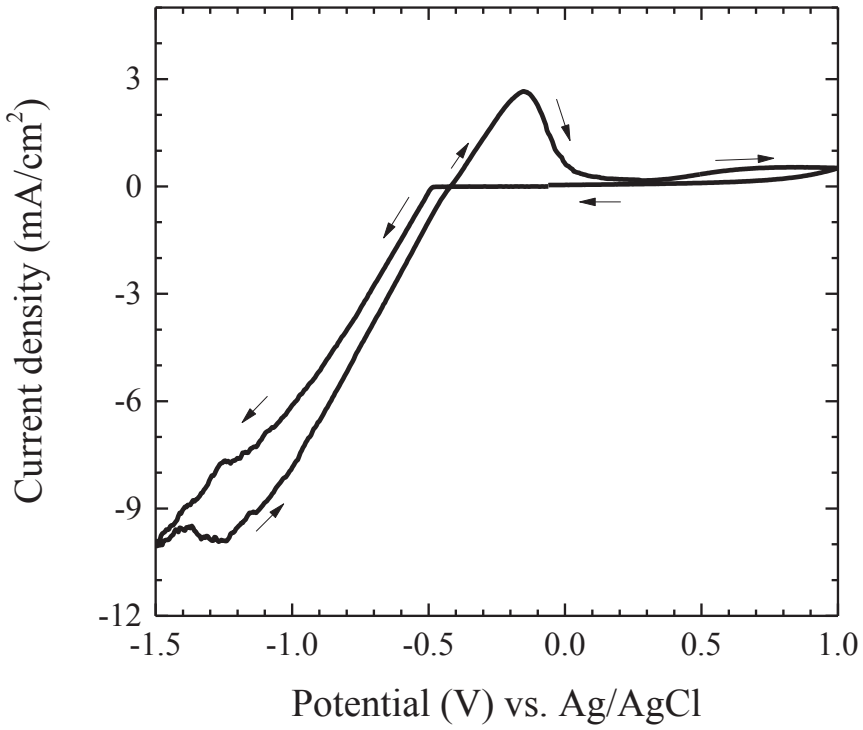

Figure 4.1: Cyclic voltammogram recorded onto an ITO working electrode (scan rate 50mV/s at room temperature) obtained in a solution of 20 mM $SnCl_2.2H_2O$ in deionized water.

4.1.1.2 Cathodic electrodeposition

The Sn deposits are electrodeposited galvanostatically by applying a cathodic current density of 5 $mA.cm^{-2}$ for 20s on ITO electrode. The processing parameters are detailed in **Table 4.2**.

Table 4.2: Processing parameters used in Sn NW electrodeposition process.

Electrolyte	Condition			Deposition parameters		
	T (^oC)	pH	Stirring	WE	Current density	Time (s)
20 mM $SnCl_2.2H_2O$ in deionized water	20	2.30	No	ITO/glass	5 $mA.cm^{-2}$	20

4.1.1.3 Characteristics

a. Morphology

The top-view and corresponding cross-sectional-view SEM images of the deposited layers at different magnifications are shown in **Figure 4.2**. Three different populations of Sn morphology can be observed on the ITO surface: nanowires, nanoparticles and large crystallites. The wire-shaped Sn nanostructures exhibit a diameter of 180±20 nm and a length in the range of 800 nm to 1.2 µm. The sizes of the Sn nanoparticles are ranging from 20 to 100 nm. Finally, large crystallites showing an average size of several micrometers are visible.

Elsewhere, we also studied the electrochemical deposition of Sn in a solution of 20 mM $SnCl_2.2H_2O$ and 75 mM HCl. In this case, there is no NW growth. Only the growth of nanoparticles and large crystallites is observed. It is concluded that adding HCl can suppress the hydrolysis of $SnCl_2$, and $Sn_4(OH)_6Cl_2$ tin complex no longer exists in $SnCl_2$ solution. So, in this case only Sn^{2+} cations are present in the electrolyte. It confirms that the presence of $Sn_4(OH)_6Cl_2$ tin complexe is a key factor in the Sn nanowires growth process.

The obtained multiple morphology of electrodeposited Sn is similar to that reported by Thierry's group [3-4] who electrochemically grew Sn nanowires. In their work, the nanotubular morphology is responsible for the formation of Sn nanowires which is not the case here. In our work, the Sn NWs are template-free electrodeposited onto the ITO electrode surface.

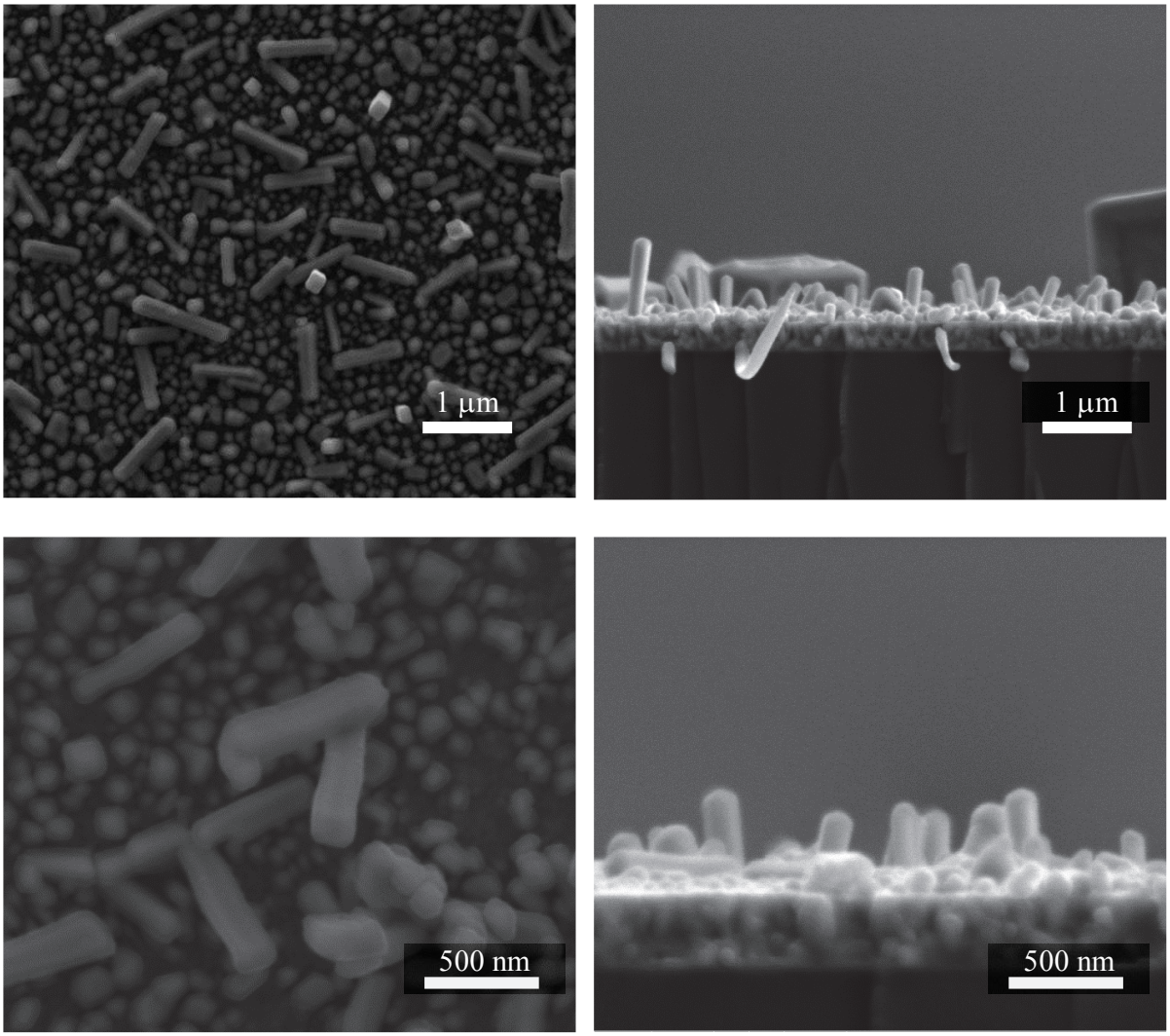

Figure 4.2: SEM top-view (left) and corresponding cross-sectional view (right) of the Sn nanostructures electrodeposited galvanostatically from a solution of 20 mM $SnCl_2.2H_2O$.

b. Microstructure

The XRD pattern of the deposited Sn nanostructures is presented in **Figure 4.3**. To observe the low-intense peaks more clearly, the X-ray intensity is plotted on a logarithmic scale. The X-ray diffraction pattern show the reflections corresponding to the body-centered tetragonal phase of Sn (ICDD File No: 00-004-0673) (see **Table 4.3**). The peaks can be assigned to the diffraction from (200), (101), (220), (211), (112) and (400) crystal planes as labeled on the curve. The small peak

width indicates a good crystallinity with a large grain size of deposited Sn. The crystallite size calculated by the Scherrer formula from the FWHM of the (101) peak is 140±10 nm.

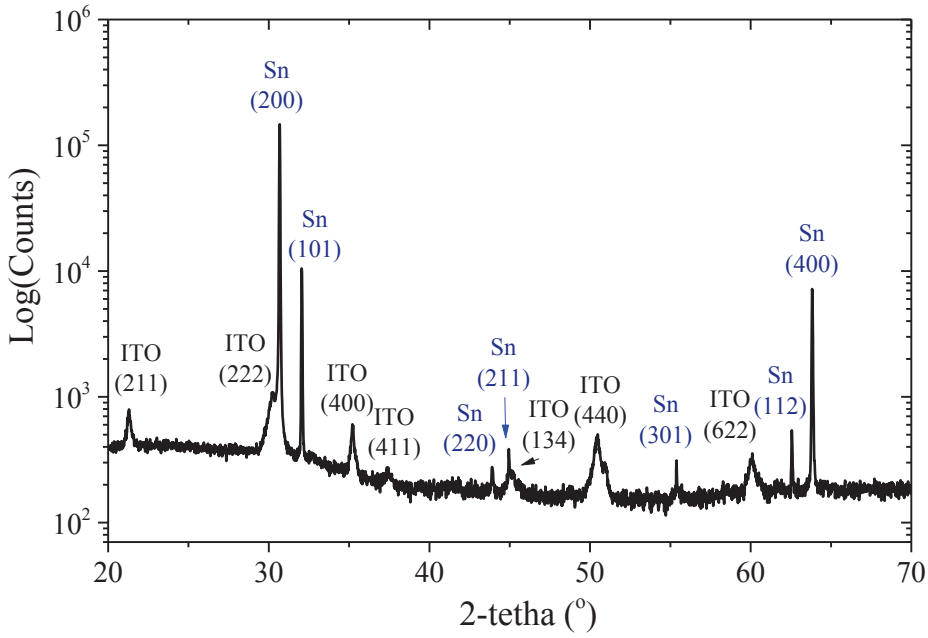

Figure 4.3: XRD pattern of the Sn nanostructures deposited galvanostatically onto an ITO working electrode in a colloidal solution comprising 20mM $SnCl_2.2H_2O$.

From the measured relative intensities of the peaks **(Table 4.3)**, and in comparison with the powder file (No: 00-004-0673), it can be deduced that the <100> planes perpendicular to the substrate plane are the most abundant planes of the crystalline Sn nanostructures and a preferred orientation <100> is favored.

Table 4.3: Data analysis from XRD pattern in Figure 4.3.

Peaks	ICDD 00-004-0673			Electrodeposited Sn nanostructures		
	Intensity	2-tetha (°)	d-spacing	Intensity	2-tetha (°)	d-spacing
200	100	30.640	2.916	100	30.686	2.911
101	90	32.017	2.793	18.2	32.066	2.789
220	34	43.882	2.062	0.61	43.928	2.059
211	74	44.905	2.017	0.25	44.953	2.015
301	17	55.343	1.659	0.21	55.377	1.658
112	23	62.524	1.484	0.21	62.579	1.483
400	13	63.807	1.458	4.8	63.842	1.457

4.1.2 Thermal oxidation to form SnO_2 NWs

The next step is the fabrication of SnO_2 NWs by oxidizing the electrodeposited Sn NWs. The thermal oxidation process used to convert Sn NWs to SnO_2 NWs without the loss of the structure is carried out by a process published elsewhere [5]. This process approximates rhetorical growth and thermal oxidation (RGTO) including two steps. The Sn NWs are first annealed at 200°C, which is close to the melting point of Sn, for 2h in ambient atmosphere. The aim of this step is to coat a thin supporting oxide layer on the surface of Sn NWs. In the second step, the Sn NWs are completely oxidized by further annealing at 500°C for 1h. To evaluate the efficiency of this process, the Sn NWs are also oxidized directly at 500°C for 1h. The obtained results of the two parallel processes are compared and assessed.

4.1.2.1 Morphology

The corresponding morphology obtained after each step of the thermal oxidation process is shown from SEM images in **Figure 4.4**.

After the first step of heat-treatment at 200°C for 2h (**Figure 4.4-top**), the morphology of the NWs keeps quite the same as the as-deposited one (**Figure 4.2**). The Sn NWs have a diameter of 180±20 nm and a length in the range of 800 nm to 1.1 µm (shape ratio between 4 to 7).

After the second heat-treatment at 500°C for 1h, the final SnO_2 NWs exhibit an increase in the diameter and a decrease in the length compared to initial Sn NWs (**Figure 4.4-middle**). The SnO_2 NWs have diameters in the range of 140 to 250 nm and lengths in the range of 500 to 800 nm.

The size variation of the NWs is due to the density change on going from Sn to SnO_2 [5]. The evolution of the NWs dimensions after each step of the annealing process is exhibited in **Figure 4.5**.

Elsewhere, the SnO_2 layer obtained from 1-step thermal oxidation process at 500°C for 1h shows a nearly smooth continuous thin film accompanied with several large crystalline on the surface (**Figure 4.4-bottom**). This morphology proves that the Sn NWs are melted and coalesced during this heat-treatment process. It is demonstrated that the prior formation of the thin oxide skin at 200°C is vital and necessary to preserve the nanowire morphology during the thermal oxidation process.

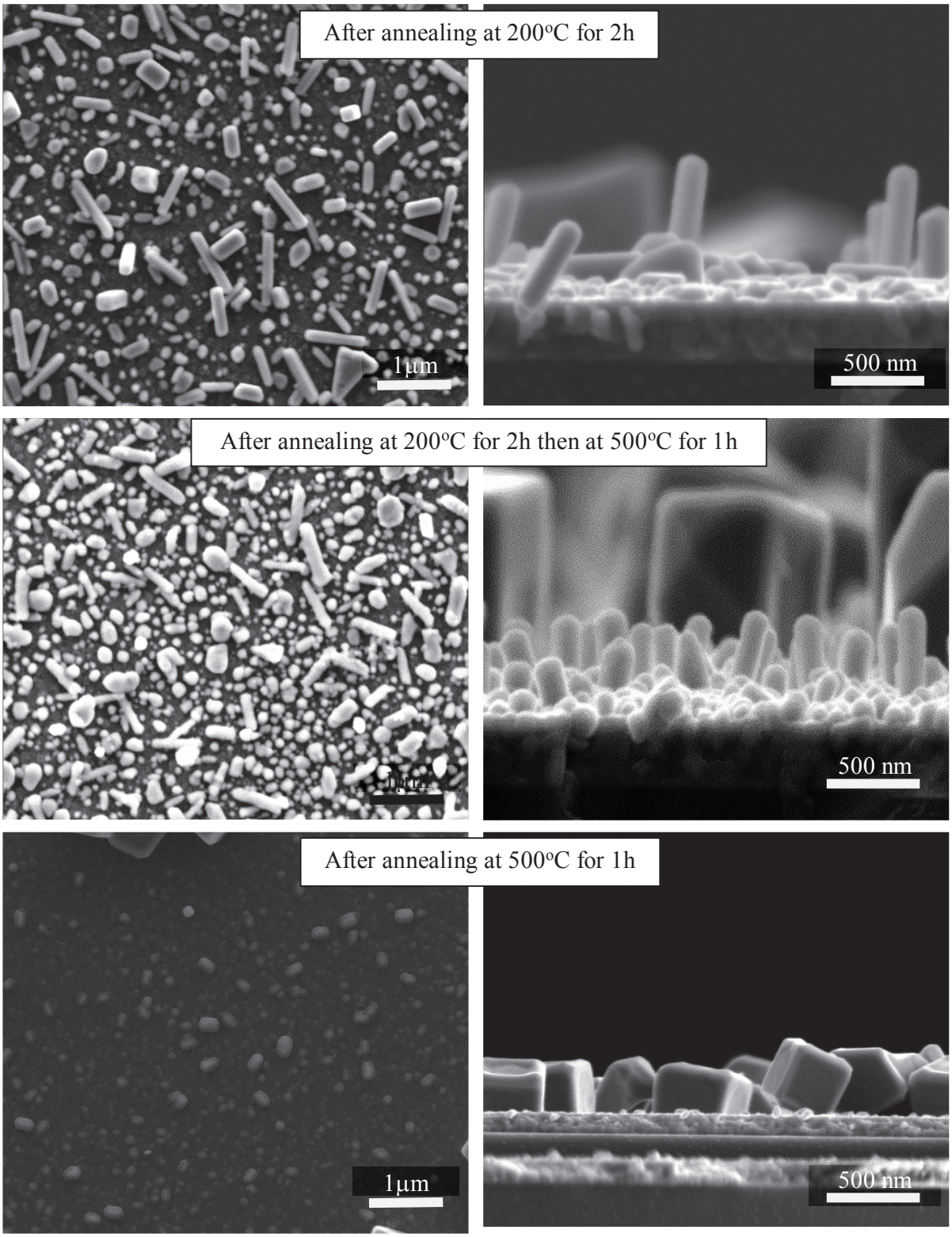

Figure 4.4: Top-view (left) and cross-sectional (right) SEM images of the Sn nanostructures obtained after each step of thermal oxidation process.

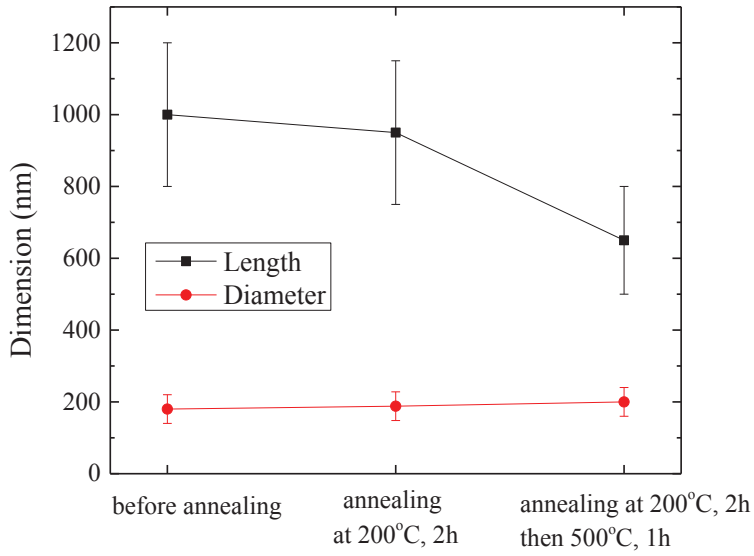

Figure 4.5: Evolution of the NWs sizes after each step of the thermal oxidation process.

The morphology of the deposit after 2-step annealing is further characterized by localized TEM observation after thinning the sample**. Figure 4.6** shows the cross-sectional TEM bright images of the nanoparticles and the NWs presence on the surface. As already noticed from SEM images, the nanoparticles exhibit a nearly spherical shape. Their size ranges from 30 to 100 nm. Besides, the length and the diameter of the observed SnO_2 NW is 531 and 102 nm, respectively. Morever, by scratching the samples, more SnO_2 NWs could be observed and the lengths and diameters range 600±200 nm and 100±50 nm, respectively.

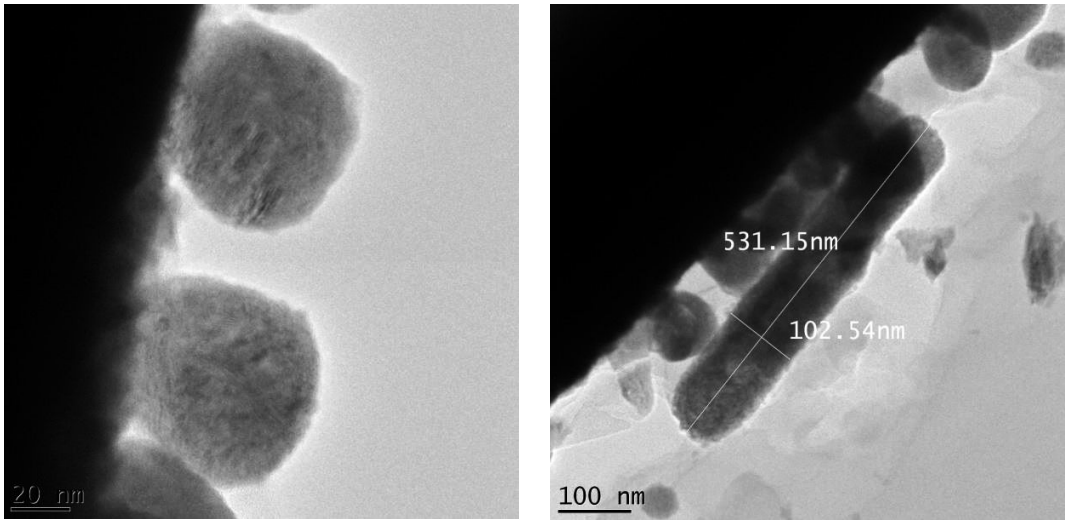

Figure 4.6: Cross-sectional TEM images of some SnO_2 nanoparticles and NWs on ITO surface after 2-step annealing.

4.1.2.2 Microstructure

Figure 4.7 presents the changes in the XRD spectra after each step of the thermal oxidation process. After 2 hour annealing at 200ºC, the XRD pattern (**Figure 4.7 –top**) is similar to that obtained for the as-deposited Sn NWs (**Figure 4.3**) indicating that the amount of the formed SnO_2 on the Sn NWs surface is negligible.

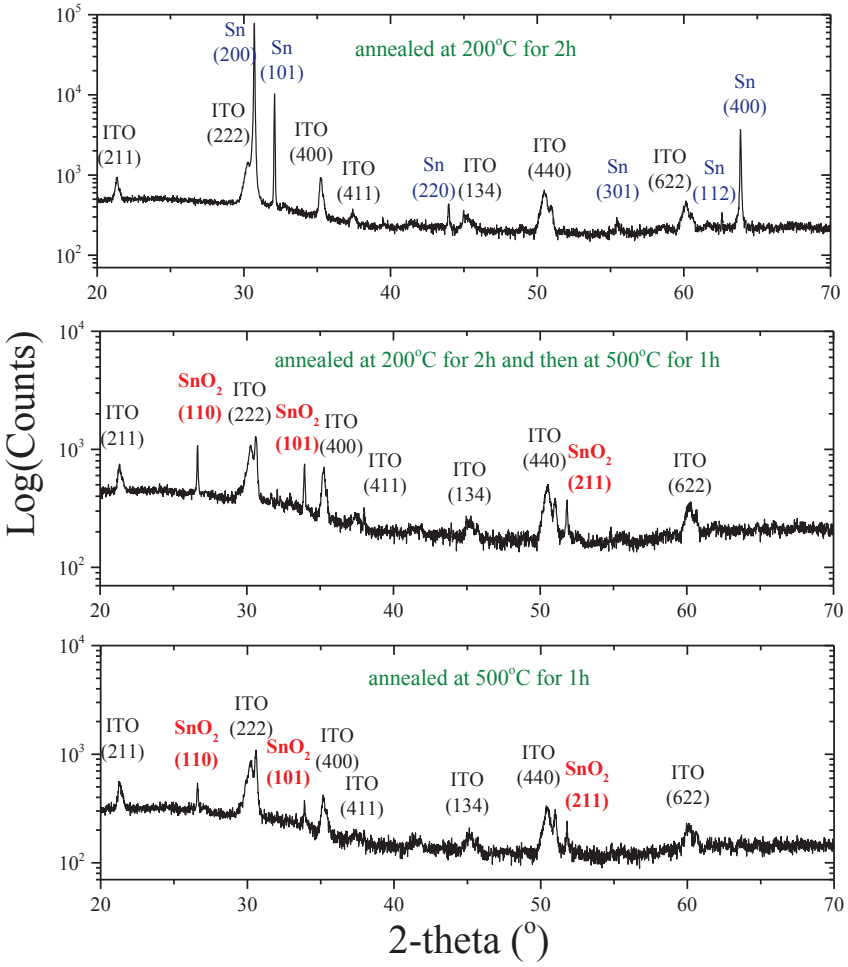

Figure 4.7: XRD spectra of the product after each step of the thermal oxidation process.

Further annealing at 500 ºC for 1 hour leads to the complete oxidation of the Sn into casseterite tetragonal SnO_2 phase as can be observed from the XRD pattern (**Figure 4.7 –middle**). The Sn peaks are disappeared and are replaced by 3 peaks of SnO_2 including (110), (101) and (211) peaks located at 2θ equal to 26.6, 33.9 and 51.8, respectively. Their relative intensity (**Table 4.4**) shows <101> planes are the most dominant planes of the crystalline SnO_2 deposit. The calculated crystallite size from the FWHM of peak SnO_2 (101) using Scherrer formula is 112 nm.

Performing the 1-step oxidation mode directly at 500°C for 1 hour produces similar X-ray pattern to that of 2-step process (**Figure 4.7–bottom**).

Table 4.4: Data analysis from XRD pattern in Figure 4.7-middle.

Peaks	**ICDD 00-041-1445**			**SnO_2 deposit**		
	Intensity	2-theta (°)	d-spacing	Intensity	2-theta (°)	d-spacing
110	100	26.584	3.347	100	26.642	3.343
101	75	33.870	2.643	66	33.931	2.640
211	57	51.766	1.764	30	51.828	1.762

The typical bright field HRTEM micrographs and their corresponding selected area electron diffraction (SAED) patterns of the nanoparticles and the SnO_2 NWs are shown in **Figure 4.8a** and **b**, respectively.

- The co-deposited SnO_2 nanoparticles with a ring pattern exhibit a polycrystalline structure.
- The SnO_2 NWs with a dot pattern appear to be single crystalline with the (110) preferred orientation. Besides, from the Fourier transform of the HRTEM image (**Figure 4.8a, right**) the interatomic plane distance of 0.334 nm can be calculated. It appears that the growth direction is <110>.

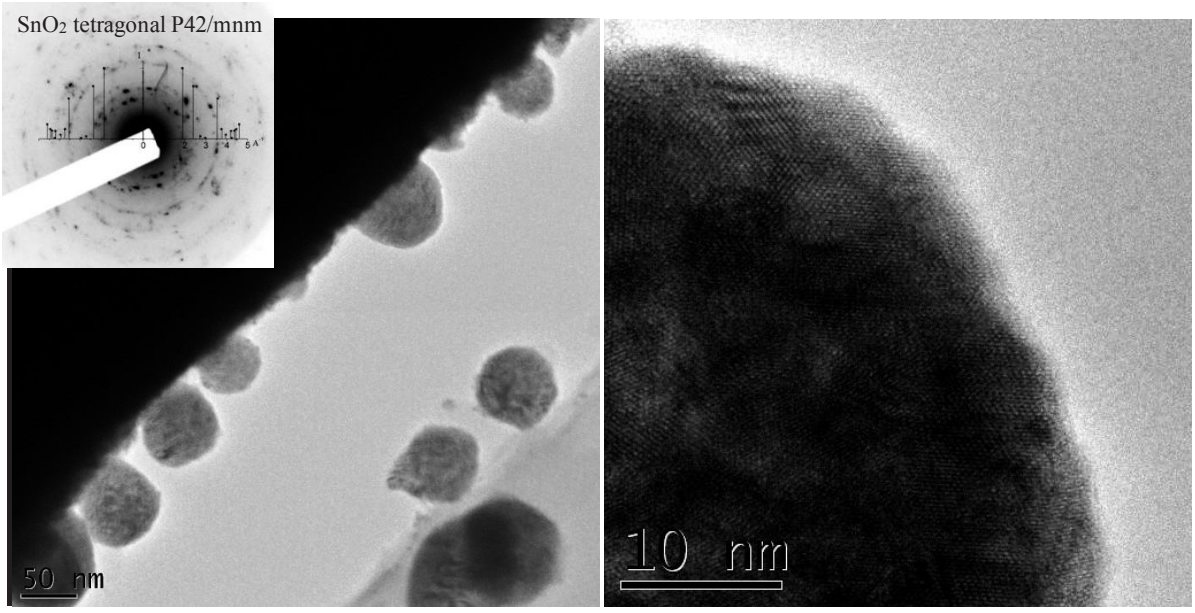

Figure 4.8a: Typical high-resolution TEM images with their corresponding SAED patterns of the co-deposited SnO_2 nanoparticles

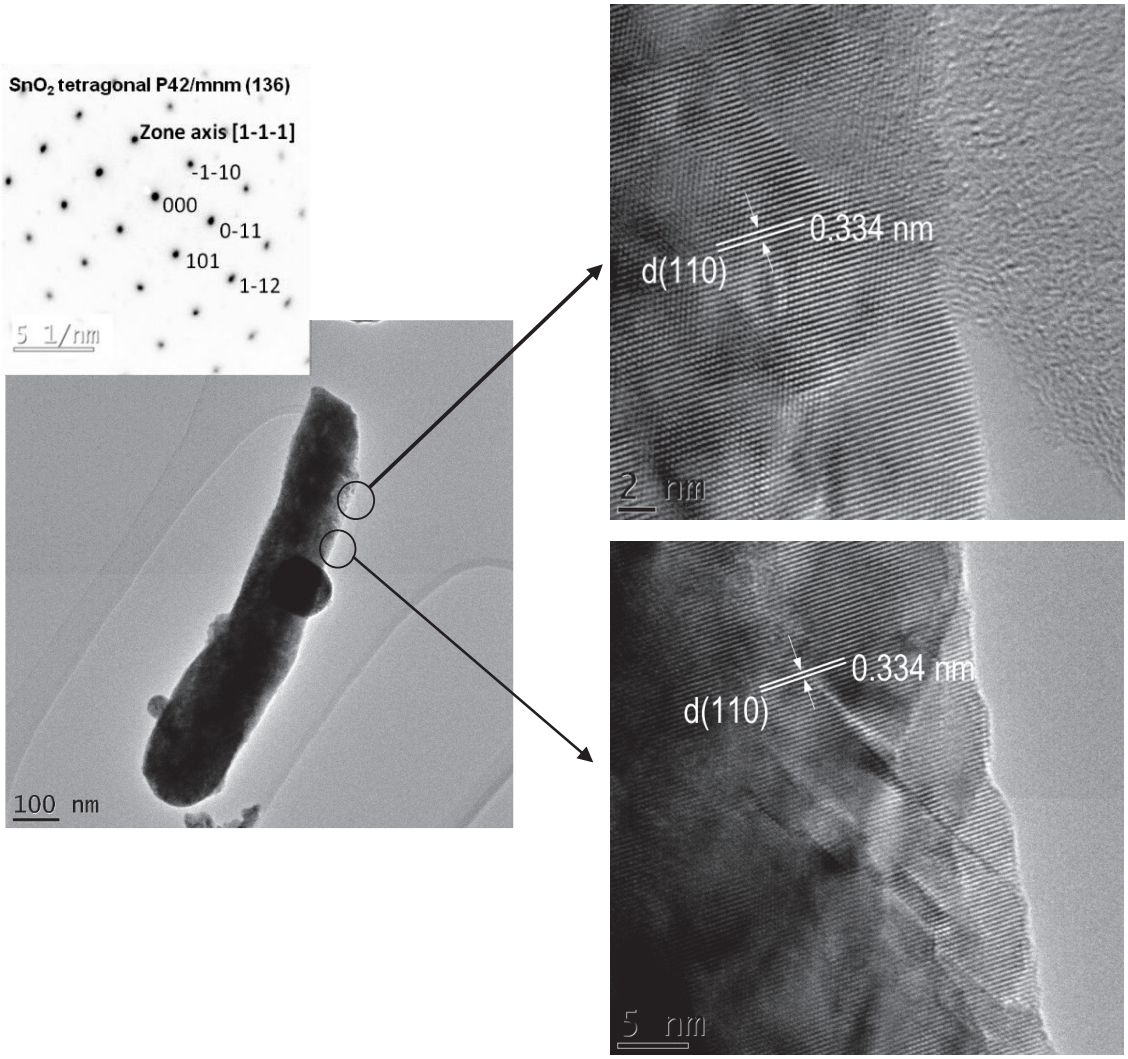

Figure 4.8b: Typical high-resolution TEM images with their corresponding SAED patterns of the deposited SnO_2 NWs

In conclusion, the SnO_2 NWs are successfully synthesized onto ITO electrode by a 2-step process consisting of template-free electrodeposition of Sn NWs which are then thermally oxidized to form SnO_2 NWs. The SnO_2 NWs have diameters in the range of 140 to 250 nm and lengths in the range of 500 to 850 nm (shape ratio ranges from 4 to 7). In addition to the NWs, SnO_2 nanoparticles appear on the surface. The nanoparticles show a polycrystalline structure, their diameter ranges from 30 to 100 nm. Further investigation should be made to optimize the electrodepostion process to obtain SnO_2 NW with a higher shape ratio perfectly controlled.

4.1.2.3 Impedance characterization of SnO_2 NWs

We characterize the electrochemical behavior of the elaborated SnO_2 NWs using EIS. A typical Nyquist plot recorded at applied voltage of -0.5V (vs. ref) is presented in **Figure 4.9a**.

The impedance curve can be described as the convolution of two semicircles: a small arc at high frequency region and a larger arc in the low frequency region. The presence of these two impedimetric elements is found to be more pronounced in the Bode plot, phase angle as a function of frequency (**Figure 4.9b**).

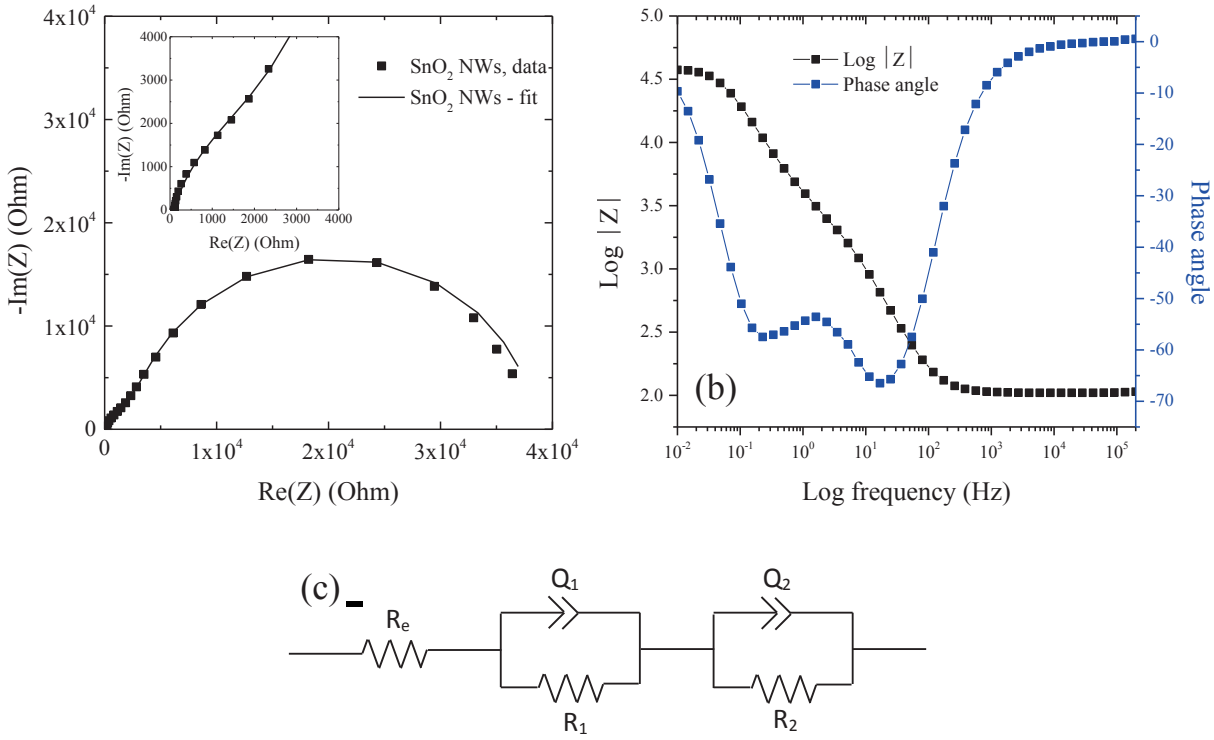

Figure 4.9: (a) Nyquist plot and (b) corresponding Bode plot of SnO_2 NWs/ITO electrode, (c) the equivalent circuit model used for fitting the data.

The obtained impedance response can be interpreted using an equivalent circuit (**Figure 4.9c**) which consists of 3 elements in series:

- At the highest frequency, the resistance R_e is the sum of the ohmic resistances of the electrolyte bulk and the electrode (ITO and SnO_2 bulk).

Because a discontinuous layer of SnO_2 is formed onto the ITO surface, two interfaces are considered including ITO/electrolyte and SnO_2/electrolyte interfaces (**Figure 4.10**), the former being less important compared to the latter.

- The first parallel element circuit (Q_1, R_1) represents the first semicircle at high frequency. C_1 (extracted from Q_1) is the double layer capacitance of the ITO/electrolyte interface, and R_1 is the polarization resistance through ITO/electrolyte interface.

- The second parallel element circuit (Q_2, R_2) represents the large semicircle at lower frequencies. C_2 (extracted from Q_2) is the double layer capacitance of the SnO_2/electrolyte interface and R_2 is the polarization resistance through SnO_2/electrolyte interface.

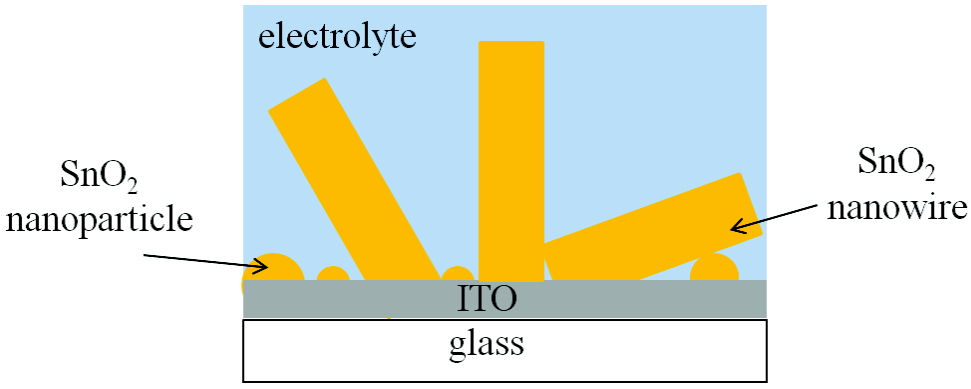

Figure 4.10: Schematic of the electrolyte/electrode interfaces

Table 4.5 presents the calculated values of the different electrical parameter values of the equivalent circuit used for Nyquist plot modeling. These values are calculated from three independent SnO_2 NWs/ITO samples. The variation between the results is less than 10% showing a good reproducibility between samples.

Table 4.5: Electrical parameter values obtained for fitting the Nyquist plots obtained in the case of bare SnO_2 NWs.

Sample	R_e (Ω)	R_1 (Ω)	C_1 (µF)	α_1	R_2 (Ω)	C_2 (µF)	α_2
1	98.0	2981	33.54	0.89	32706	58.35	0.91
2	98.1	2779	31.99	0.90	31236	58.91	0.91
3	98.6	2704	31.04	0.90	31324	58.86	0.91

(For all the complete fitting data, see Annex2-B1)*

4.2 DNA sensor fabrication based on SnO_2 NWs

The process used to functionalize SnO_2 NWs is the same as the one for nanoporous films with chemical vapor phase deposition of APTES. The vaporized APTES is expected to enhance the detection signal with SnO_2 NWs.

As for the nanoporous SnO_2-based DNA sensors, the impedance is systematically measured before the main steps of the functionalisation process. The electrolyte is the pure hybridization buffer solution without DNA target. The processing parameters are detailed in **Table 4.6**.

Table 4.6: Parameters of the functionalization and impedance measurement processes

Functionalization parameters				**Impedance measurement parameters**			
Silanization	*C_{probe} (μM)*	*C_{target} (μM)*	*Types of DNA target*	*Hybridization buffer*	*Frequency range*	*Modula-tion*	*Applied voltage*
Vapor phase deposition	10	2.0 1.0 0.5 0.1 0.01 0.002	Complementary	0.5 M NaCl 0.01 M PBS (pH = 7.0)	10 mHz to 200 kHz	10mV	-0.5 V (vs. ref)

4.2.1 Sensitivity

4.2.1.1 Impedance response signals

Figure 4.11 presents the changes in the Nyquist plots of the bio-modifed SnO_2 NWs after the main steps of functionalization:

(i) after silanization,

(ii) after probe grafting (ss-DNA),

(iii) after DNA complementary hybridization (ds-DNA).

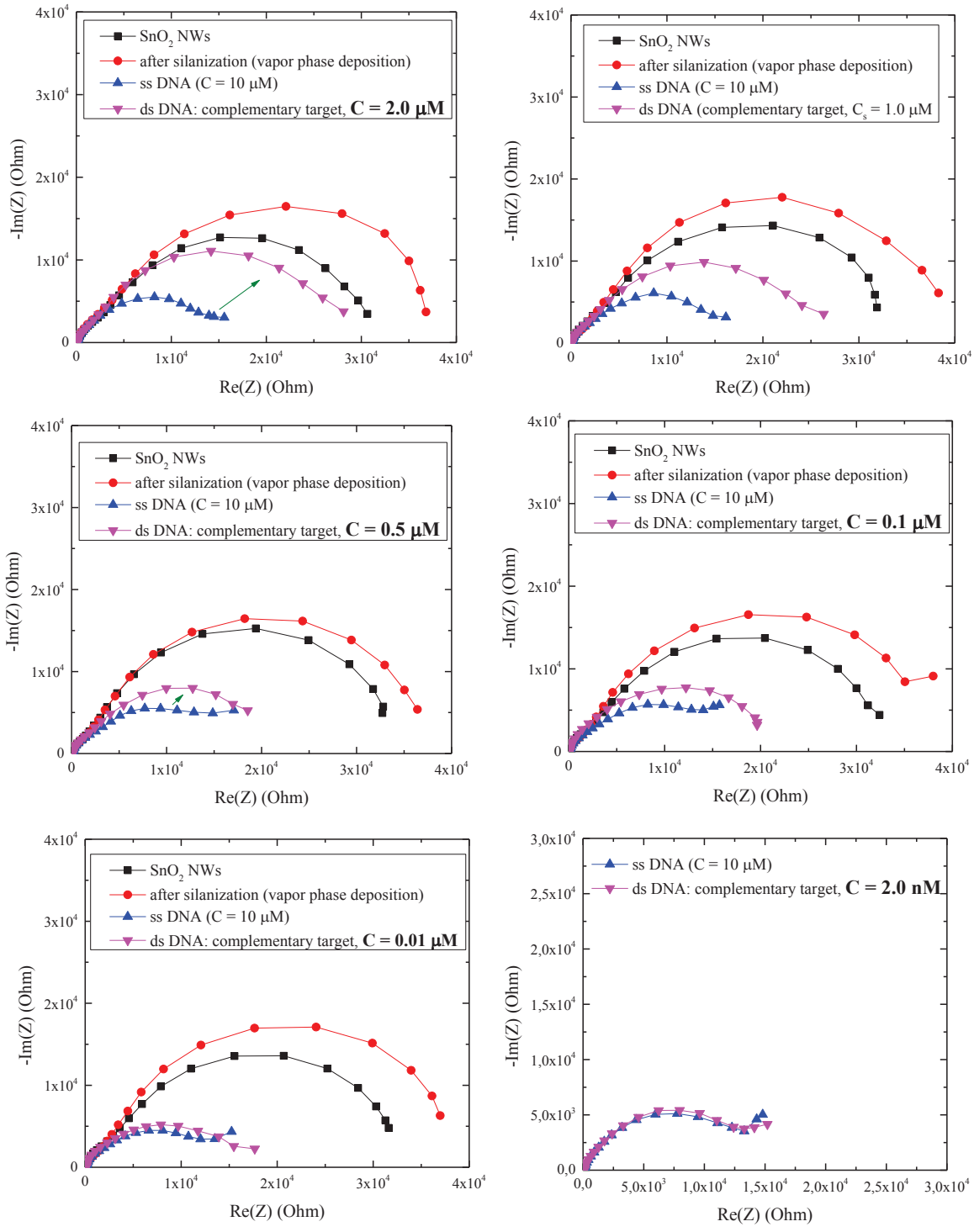

Figure 4.11: Nyquist plots of bio-modified SnO_2 NWs in which DNA hybridization is performed with different DNA target concentrations: 2.0, 1.0, 0.5, 0.1, 0.01 and 0.002 µM. EIS measurements are performed at voltage of -0.5 V (vs. ref).

As for the bare SnO_2 NWs, two semicircles are observed in all the impedance curves. However, significant differences in electrochemical behavior are observed upon the stepwise modification of the SnO_2 NW electrode.

- As for the nanoporous SnO_2 films, the deposition of the APTES leads to an increase of the impedance of the electrode, probably due to the fact that APTES is a non charged-layer and acts as a blocking or passivating thin layer.

- A drastic decrease in the impedance is observed after immobilization of DNA probes. Similar trend was observed for nanoporous films.

- Finally, contrarily to the nanoporous SnO_2 films, with the capture of the complementary DNA targets, **the diameter of the second semicircle increases considerably**, depending on the concentration of DNA target. Besides, the first semicircle at higher frequencies varies negligibly upon DNA hybridization. This general behavior is systematically found whatever the target DNA concentration, showing the reproducibility of the samples and the functionalization process.

As for the bare SnO_2 NW, the impedance curves are best fitted with the equivalent circuit $R_e(R_1,Q_1)(R_2Q_2)$. It is reminded that the deposit of SnO_2 NWs on ITO electrode surface is discontinuous (**Figure 4.10**). The first R_1C_1 (extracted from Q_1) circuit reflects the small semicircle at high frequency region induced by the polarization at the ITO/electrolyte interfaces. The second R_2C_2 (extracted from Q_2) circuit accounts for the big semicircle at low frequency region, which is caused by the polarization at the SnO_2/electrolyte interface. The modeling parameters of the equivalent circuit are presented in **Table 4.7**.

Table 4.7: Different resistance values, R_e, R_1 and R_2, calculated from the use of the equivalent circuit for Nyquist plot modeling obtained for DNA modified SnO_2 NW electrode.

C_{target} (μM)	R_e (Ω)			R_1 (Ω)			R_2 (Ω)		
	silanized	**ssDNA**	**dsDNA**	**silanized**	**ssDNA**	**dsDNA**	**silanized**	**ssDNA**	**dsDNA**
2.0	99.23	97.8	97.5	1435	1752	1814	38924	12564	24843
1.0	107.12	96. 8	97.5	1663	2101	2083	42111	12431	22022
0.5	106.84	98.4	97.5	1444	1955	2160	38924	12588	17796
0.1	106.65	97.1	90.65	1657	1994	1907	39994	13605	17955
0.01	106.80	96.6	97.0	1636	2183	2068	40057	10748	12152
0.002	-	97.9	97.9	-	1807	1793	-	13479	14124

(For all the complete fitting data, see Annex2-B1)*

- The resistances R_e increase from 98±1.5 Ω for the bare electrodes to ~106 Ω for the silanized electrodes. Its value then decreases to 97.5 ±1.0 Ω after DNA probe grafting and keeps the same upon DNA hybridization.

- The resistance R_1 of the ITO/electrolyte interface does not change significantly upon hybridization. $\Delta R_1/R_1$ is about 1%.

- The increase of R_2 upon DNA hybridization is the most striking result. This increase is 97% for C_{target} of 2 µM, and 13% for C_{target} of 0.01 µM. The complete evolution of $\Delta R_2/R_2$ as a function of DNA target concentration is plotted in **Figure 4.12**. The increase of the R_2 upon hybridization can be linked to a field effect phenomenon as discussed in the case of micrometer-thick nanoporous SnO_2 films, notably, regarding the evolution of the first semicircle (part 3.1.4.1). The accumulation of more negative charges after DNA hybridization induces an increase of the thickness of the space charge layer in the sub-surface of the SnO_2 NWs. As a result, the impedance increases.

Moreover, we have tested with lower concentration at 2 nM but a negligible change of R_2, about 4%, is found.

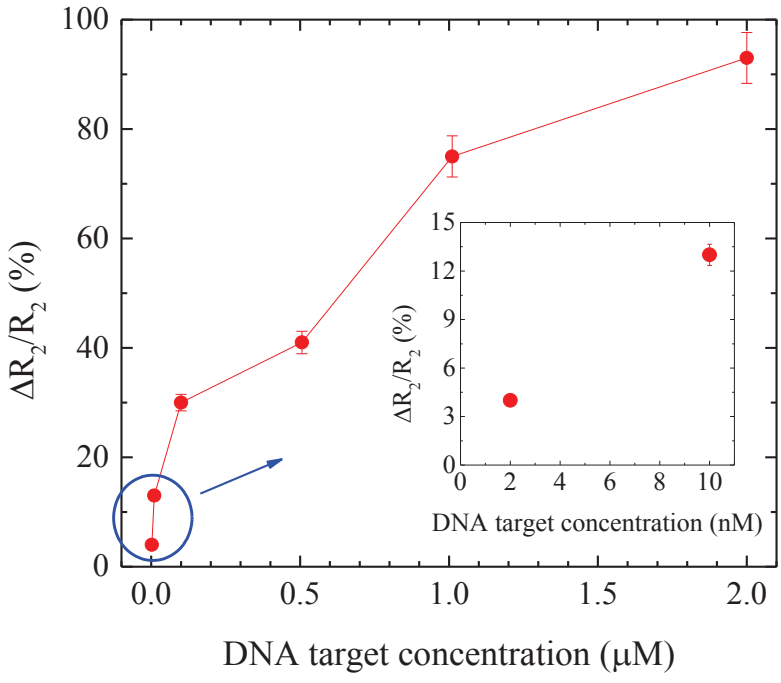

Figure 4.12: Evolution of the charge transfer resistance $\Delta R_2/R_2$ of the biomodified SnO_2 NWs as a function of DNA target concentration.

4.2.1.2 Fluorescence response signals

For each sample, the impedance results are systematically confirmed by fluorescence measurements. **Figure 4.13** exhibits the corresponding fluorescence micrographs. A big difference in fluorescence intensity is found between the region where DNA probes are immobilized and the rest part of the electrode surface. It proves the successful hybridization between the complementary targets and the immobilized DNA probe. Similarly to nanoporous SnO_2 films, the fluorescence distribution inside the DNA drop is discrete and non-continuous with many bright spots inside fluorescence region.

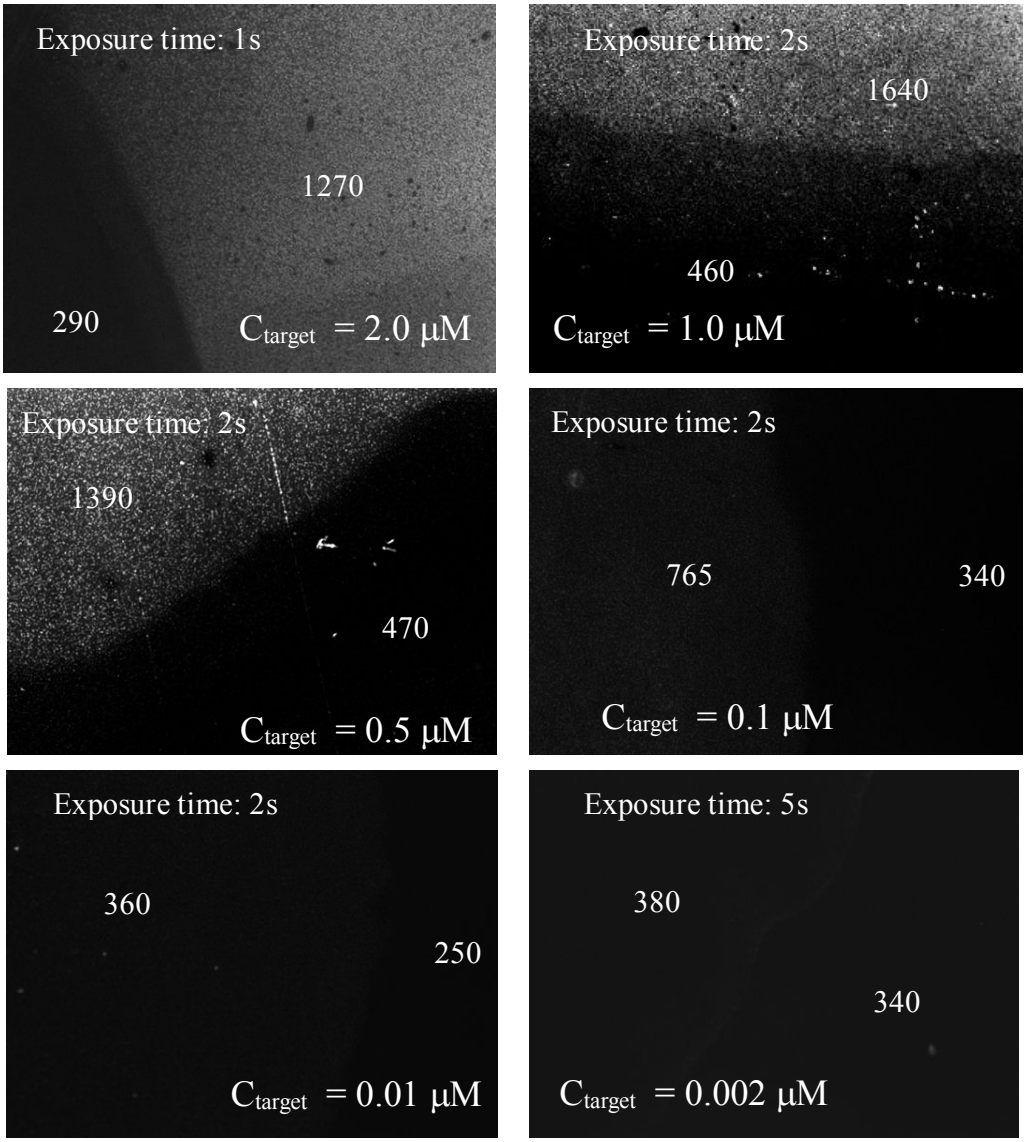

Figure 4.13: Fluorescence micrographs after complementary hybridization with Cy3 labeled DNA targets with different concentration going from 10 nM to 2.0 μM on SnO_2 NWs electrode.

Indeed, the top-view SEM images of the SnO_2 NWs deposit (**Figure 4.4**) revealed the simultaneous formation of nanoparticles along with NWs. Because of their difference in morphology, they do not show the same sensitivity to the DNA hybridization. With a higher specific surface area, the fluorescence should be more intense on a NW. Each brighter spot could correspond to one NW or a group of them. Besides, a gradient in fluorescence intensity is observed at the drop border. It results from an important capillarity effect which was already observed for nanoporous SnO_2 film (**Figure 3.20**). The deposited SnO_2 NWs is highly hydrophilic even after silanization was carried out. Importantly, by increasing the acquisition time to 5 seconds, the DNA hybridization could be traced by the fluorescence microscopy for the DNA target concentration of 2 nM. The result demonstrates the high sensitivity to the detection of DNA hybridization on SnO_2 NWs. The average fluorescence signal intensity increases with the DNA target concentration (**Figure 4.14**).

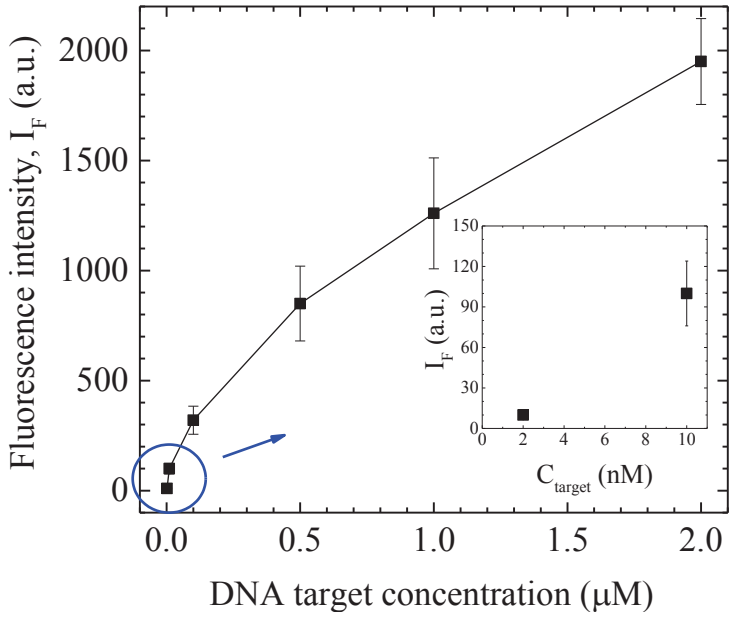

Figure 4.14: Fluorescence intensity of bio-modified SnO_2 NWs after DNA hybridization as a function of DNA target concentration.

The confocal laser microscope is used to observe the repartition of DNA molecules on the SnO_2 NWs. **Figure 4.15** presents a 3D view of the surface which is created by assembling fluorescence pictures took from 15 consecutive focusing plans with a step of 0.41 μm. When the focusing plan is far away from the ground, the fluorescence intensity of the SnO_2 nanoparticles on the surface decreases while the one of the NWs does not change. It is noted that the height of the fluorescence signal is always much higher than that of the NWs due to vertical light scattering effect. In our case, the length of the NWs is about 1.0 μm and the fluorescence is still visible up to 4.0 μm away

from the surface. From this result, an important conclusion can be drawn. The DNA molecules are successfully immobilized along the SnO_2 NWs.

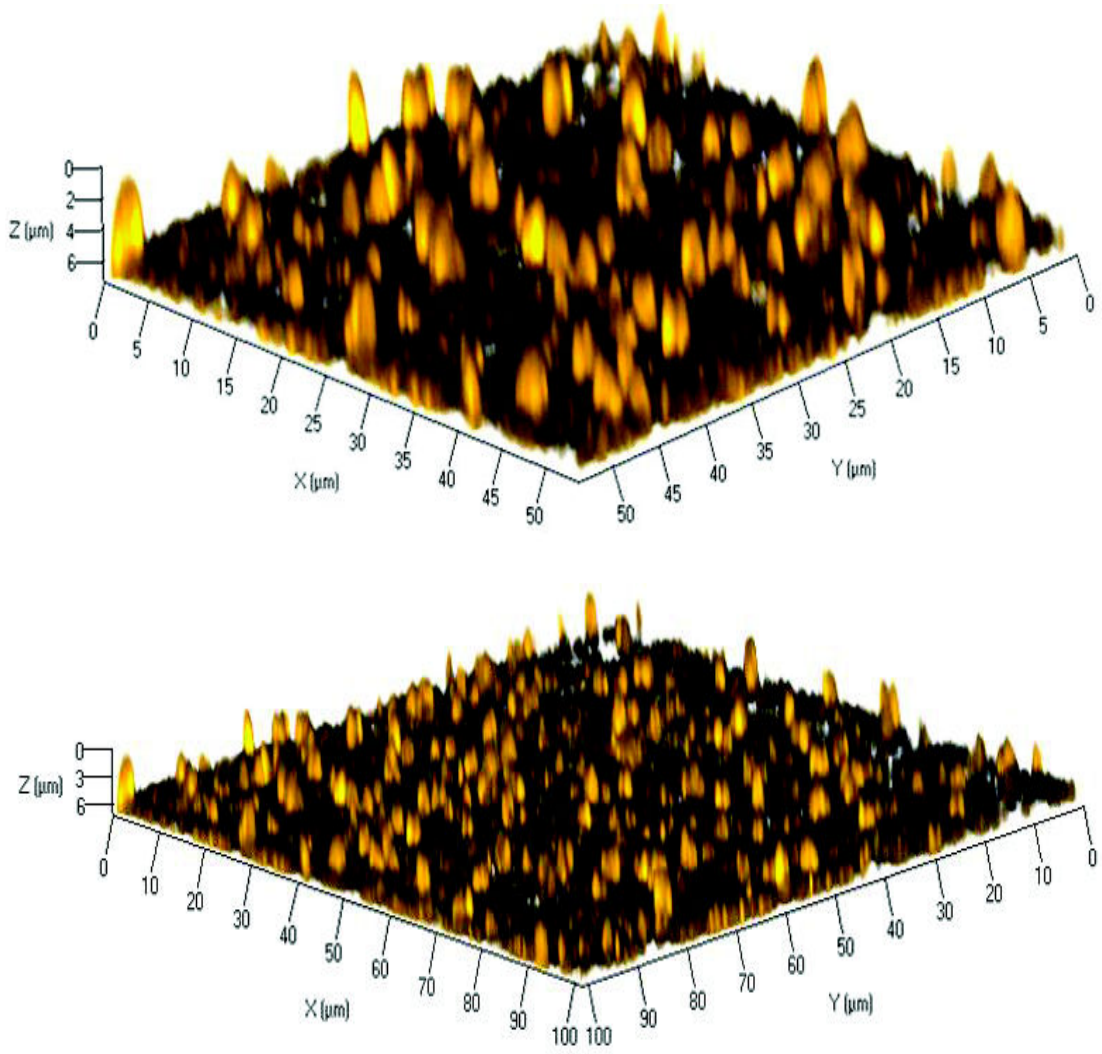

Figure 4.15: 3D constructed view of fluorescent DNA on SnO_2 NWs at different scales obtained by confocal scanning laser fluorescence microscopy with DNA target concentration of 0.5 µM.

In conclusion, contrary to nanoporous films, both the electrical and optical signals show a similar tendency (**Figure 4.16**). The limit of impedance detection is 10 nM. On the other hand, a lower DNA target concentration of 2 nM could be detected on the SnO_2 NWs layer by fluorescence microscopy. Importantly, from 3D view using confocal scanning laser fluorescence microscopy it is found that DNA molecules are mainly located along the SnO_2 NWs.

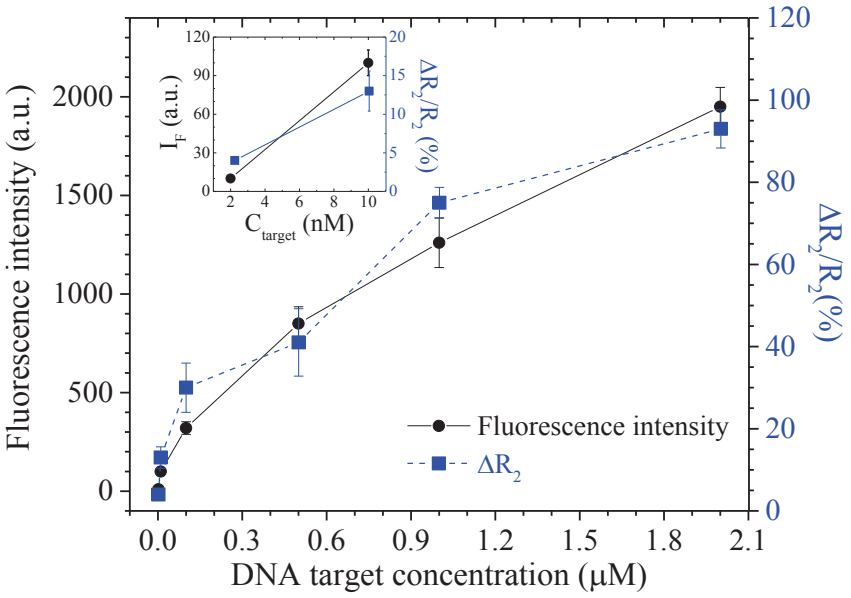

Figure 4.16: Evolution of the charge transfer resistance $\Delta R_2/R_2$ and the fluorescence intensity of the biomodified SnO_2 NWs as a function of target DNA concentration.

4.2.2 Selectivity of SnO_2 NWs based DNA biosensors

The selectivity of the process on the SnO_2 NWs based DNA sensor has also been tested as for nanoporous SnO_2 thin films by performing hybridization with non-complementary, 1- and 2-base mismatch DNA target molecules, the formula of which are detailed in experimental part. The experiments are performed with the same process and the DNA target concentration is fixed at 2 µM. The processing parameters are detailed in **Table 4.8**.

Table 4.8: Parameters of the functionalization and impedance measurement processes

Functionalization parameters				**Impedance measurement parameters**			
Silanization	*C_{probe} (µM)*	*C_{target} (µM)*	*Types of DNA target*	*Hybridization buffer*	*Frequency range*	*Modula-tion*	*Applied voltage*
Vapor phase deposition	10	2.0	non-complementary 1-base mismatch 2-base mismatch	0.5 M NaCl 0.01 M PBS (pH = 7.0)	10 mHz to 200 kHz	10 mV	-0.5 V (vs. ref)

4.2.2.1 Impedance response signals

Figure 4.17 shows the Nyquist plots of the bio-modifed SnO_2 NWs before and after DNA hybridization with different kinds of DNA target molecules: 1-base mismatch, 2-base mismatch and non complementary. Two semicircles are observed in all the impedance curves. Whatever the DNA target molecules, the impedance increases upon DNA hybridization following the general behavior of SnO_2 NWs based DNA sensor.

The impedance curves are fitted with the equivalent circuit $R_e(R_1,Q_1)(R_2Q_2)$ and the modeling parameters of the equivalent circuit are presented in **Table 4.9**.

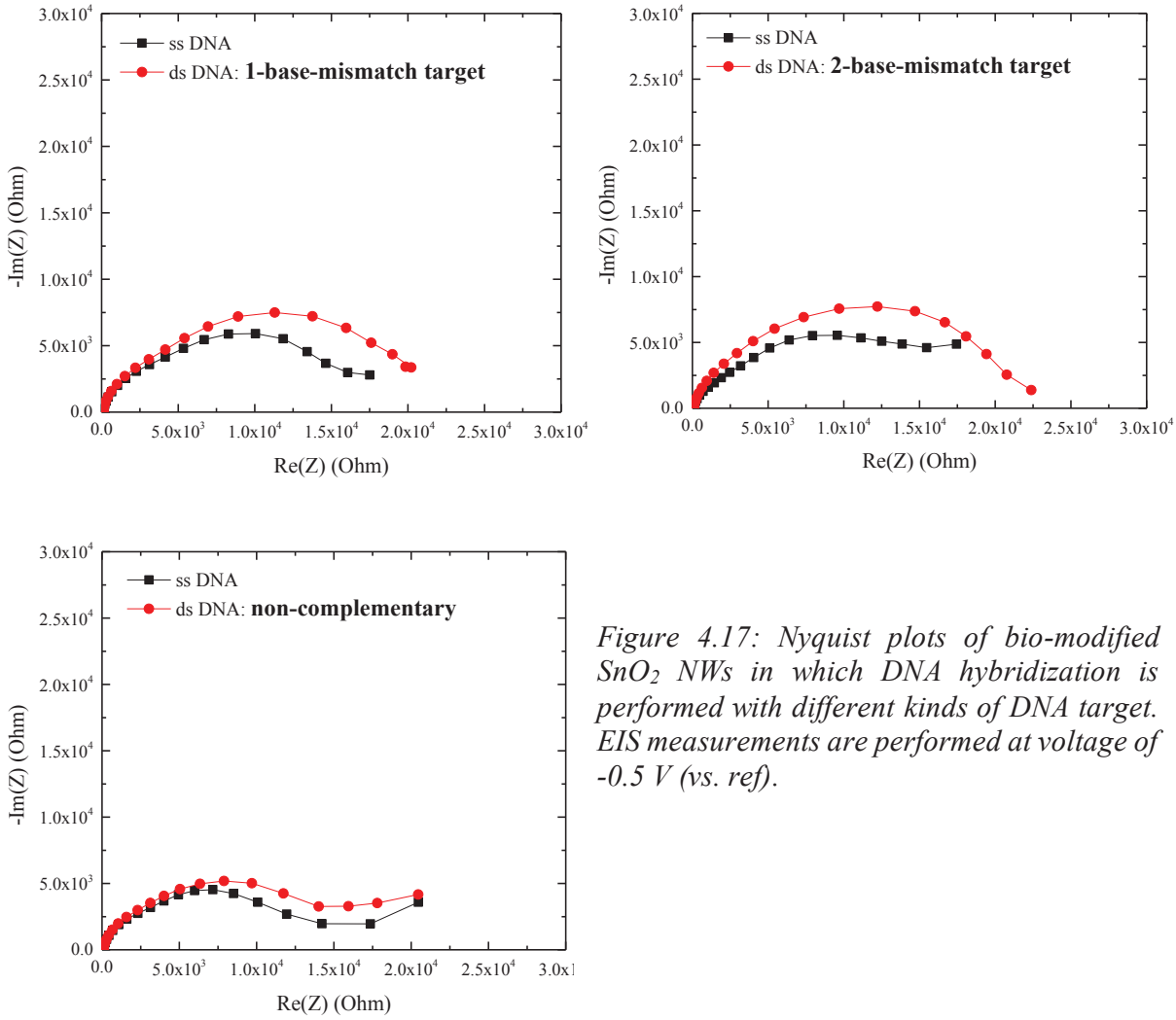

Figure 4.17: Nyquist plots of bio-modified SnO_2 NWs in which DNA hybridization is performed with different kinds of DNA target. EIS measurements are performed at voltage of -0.5 V (vs. ref).

Table 4.9: Different resistance values R_e, R_1 and R_2 of the equivalent circuit used for Nyquist plot modeling for the impedance curves obtained at applied voltage of -0.5 V (vs. ref).

DNA target molecules	R_e (Ω)		R_1 (Ω)		$\Delta R_1/R_1$ (%)	R_2 (Ω)		$\Delta R_2/R_2$ (%)
	ssDNA	dsDNA	ssDNA	dsDNA		ssDNA	dsDNA	
1-base mismatch	90.89	90.81	3353	3253	0	13564	17345	**27±3**
2-base mismatch	97.08	90.65	2515	2679	1	14494	16977	**19±3**
Non-complementary	91.02	91.24	3301	3314	0	10967	11733	**6±2**

(For all the complete fitting data, see Annex2-B2)*

The evolution of the charge transfer resistance $\Delta R_2/R_2$ of bio-modified SnO_2 NWs upon DNA hybridization with different types of DNA targets is reported in **Figure 4.18**. Reductions of 72% of impedance signal between fully complementary and 1-base mismatch and 80% in the case of 2-base mismatch are obtained, respectively. Finally, a negligible increase (6%) of R_2 is found in case of non-complementary hybridization. It can be concluded that the process on SnO_2 NWs shows a high selectivity to DNA hybridization. We can note that these reduction values are higher than those obtained for 220 nm-thick nanoporous film. It indicates that the SnO_2 NWs are more efficient for the selectivity.

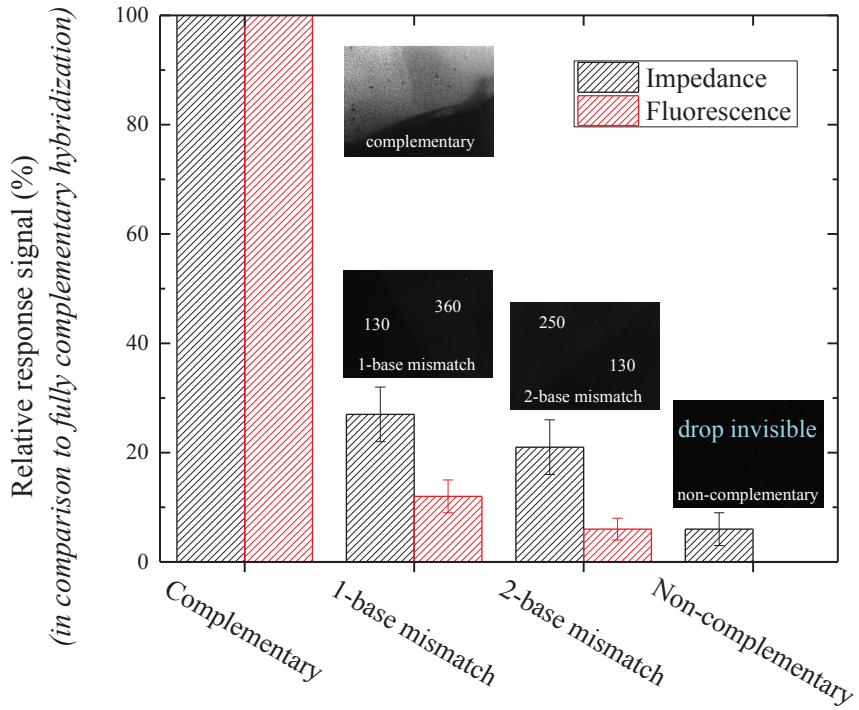

Figure 4.18: Relative EIS and fluorescence signals (in comparison to fully complementary hybridization) when DNA hybridization are performed with different types of DNA target: 1-, 2-base mismatch and non-complementary.

4.2.2.2 Fluorescence response signals

The selectivity of the process on the SnO_2 NWs has also been studied optically by fluorescence microscopy. **Figure 4.18** presents the different fluorescence signal intensity obtained for different types of DNA target molecules. In agreement with impedance results, the fluorescence intensity drastically decreases of 88% and 94% when 1- and 2-base mismatch DNA targets are used. Finally, in the case of non complementary target, the area where the DNA probes are immobilized could not be traced even when the high resolution laser scanning fluorescence microscopy is used.

In conclusion, both impedance and fluorescence results have demonstrated the high selectivity of the process on SnO_2 NWs to detect DNA hybridization.

4.3 Comparisons of the response signals to DNA hybridization according to the different morphologies of SnO_2 electrodes

Three kinds of comparison can be made from the impedance variation upon DNA hybridization following the 3D or 1D nanostructure morphology.

4.3.1 Comparison 1: Hybridization-induced impedance changes

Typical Nyquist plots obtained from the DNA probe grafted SnO_2 electrodes (i) before and (ii) after complementary DNA hybridization are showed in **Figure 4.19**. In order to compare with the behavior of a 2D surface, we have reported the previous results of impedance obtained by A. Zebda [6] in **Figure 4.19d**.

The tendency of impedance change induced by DNA hybridization is different according to the morphologies. Indeed, the impedance measurements show that DNA hybridization induces a decrease in the diameter of the large semicircle for both 3D-SnO_2 nanoporous micrometer- (**Figure 4.19 a**) and 3D-nanometer-thick films (**Figure 4.19 b**), while, an opposite tendency is obtained for both the 1D-SnO_2 NWs (**Figure 4.19c**) and 2D-SnO_2 dense surface film (**Figure 4.19 d**). In this case, a systematic increase of the semicircle diameter is obtained upon DNA hybridization.

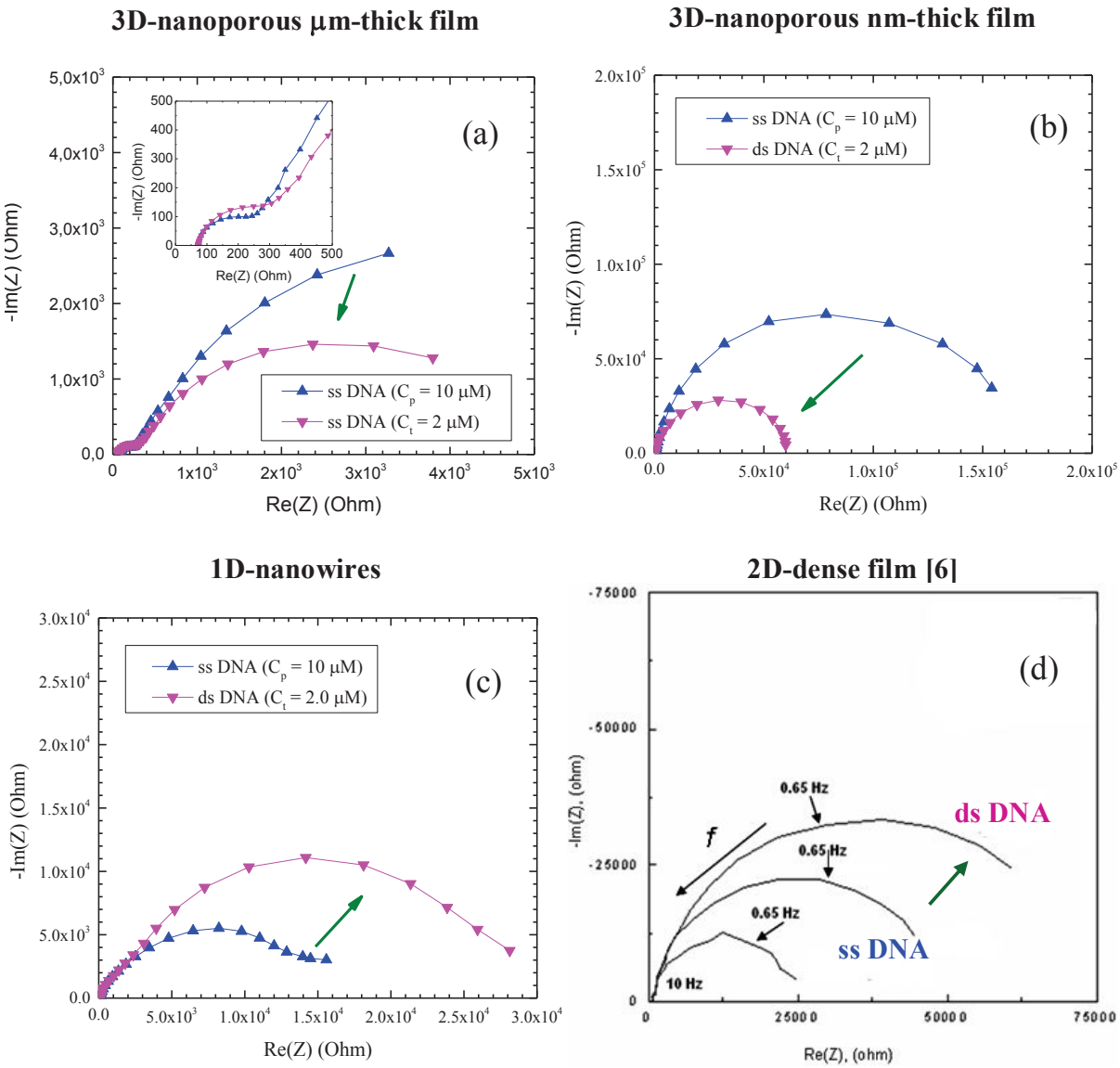

Figure 4.19: Evolution of Nyquist plots of ssDNA probe grafted SnO_2 electrodes (i) before and (ii) after complementary DNA hybridization, in the case of (a) micrometer and (b) nanometer thick 3D nanoporous films, (c) 1D nanowires, (d) 2D dense film surface [6].

To explain these different tendencies, we consider that the interfacial charge distribution is different according to the morphology.

As schematically depicted in **Figure 4.20**, in the case of 3D-nanoporous films, the DNA strands and the ionic species are located **within the film thickness**, while both in the case of 1D-NW and 2D-dense film, the DNA and ionic species are located **above the film surface**. As a result, their local and immediate environment is completely different.

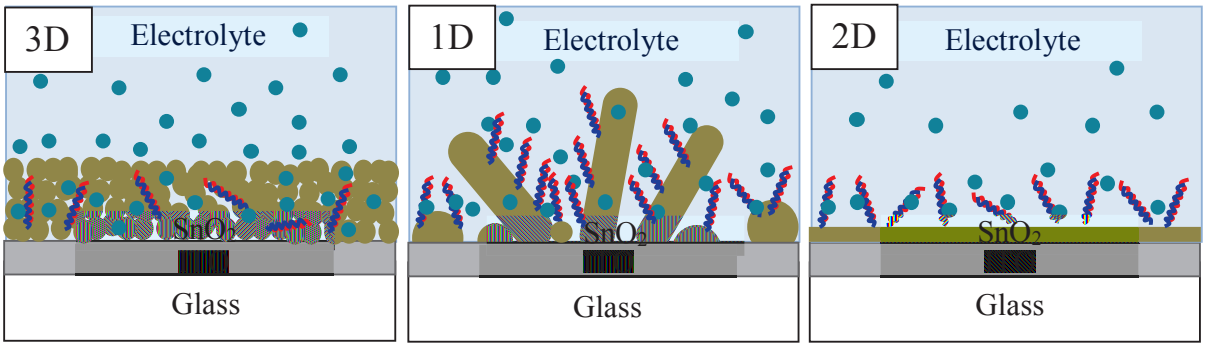

Figure 4.20: Schema of the electrode/electrolyte interfaces following the different nanostructured SnO_2 electrodes: 3D (nanoporous), 1D (nanowires) and 2D surface.

In the case of 3D-nanoporous films, as already discussed in previous chapter (part 3.1.4), the decrease of the impedance upon DNA hybridization can be explained by some external phenomena. Notably, the hydrophilic character of ds-DNA can partially facilitate the ionic species of electrolyte to reach the electrode surface following their infiltration into the porous structure. As a result, the impedance decreases.

In the case of 1D NWs and 2D dense film surface, other phenomena contribute to the increase of the impedance. First we suggest that a low dimensional environment such as 1D or 2D-surface reduces the possibility of charge exchanges at the electrode surface. Besides, as it was previously described for 2D-surfaces [6], the increase of the impedance upon DNA hybridization in the case of 1D-NWs can be originated from a field effect phenomenon. By this way, the negative charges of DNA strands grafted on the NW surface repel the electrons within the NW from the sub-surface into the bulk of the NW, resulting in an increase of the space charge layer resistance and in the impedance.

4.3.2 Comparison 2: Sensitivity

The sensitivity of the DNA sensors based on these different SnO_2 morphologies is compared. In **Table 4.10**, we report the impedance changes upon DNA hybridization when decreasing the DNA target concentration for all the morphologies. At a DNA target concentration of 2.0 µM, the impedance change upon DNA hybridization is more important for the 1D SnO_2 NWs than for the 3D-nanoporous film.

By performing complementary hybridization at lower DNA target concentrations, we observe that the EIS detection limit of the 3D-nanoporous nm-thick film is 10 nM, while the 1D-SnO_2 NWs can reach down to 2 nM. Besides, at each DNA target concentration, the 1D-SnO_2 NWs-electrode

gives higher fluorescence signal than that of 3D-nanoporous nm-thick film. This shows a higher sensitivity in the case of the 1D morphology than for the 3D one.

Table 4.10: Sensitivity of DNA sensors based on different nanostructured SnO_2 electrodes from both EIS and fluorescence signals.

$C_{DNA\ target}$ (µM)	**3D-nanoporous µm-thick film**		**3D-nanoporous nm-thick film**		**1D-SnO_2 NWs**		**2D-dense film**	
	$\Delta R_2/R_2$ (%)	I_f (a.u.)	$\Delta R_1/R_1$ (%)	I_f (a.u.)	$\Delta R_2/R_2$ (%)	I_f (a.u.)	$\Delta R_1/R_1$ (%)	I_f (a.u.)
2.0	29±5	2100± 200	-63±5	850±50	97±5	1950±300	Not studied	
1.0	Not studied		-48±5	450±70	77±5	1260±200	50±20	-
0.5			-33±3	350±40	41±5	850±100	Not studied	
0.1			-18±3	180±30	32±4	320±50		
0.01			-11±3	120±30	13±2	100±20		
0.002			negli-gible	negli-gible	4±2	10±2		

From the **Table 4.10**, compared to the 2D-surface, the 1D-NW morphology seems to provide a higher sensitivity for a DNA concentration of 1 µM. However the gap is quite low as the difference is in the order of experimental errors. This implies that further investigations should focus on (i) a better control of both density and shape ratio of the NWs, and on (ii) a thorough study of the relationship between the NW characteristics and the signal response upon DNA hybridization in order to enhance the field effect phenomenon and thus the sensitivity of the device.

4.3.3 Comparison 3: Selectivity

Both impedance and fluorescence measurements confirm the high selectivity of the hybridization process on both nanostructured SnO_2 electrodes: 3D nanoporous nm-thick film and NWs. The obtained results (see **table 4-11**) show a good correlation between the response signals of both electrical and optical detections according to the different kinds of hybridization.

Table 4.11: Selectivity of DNA sensors based on different nanostructured SnO_2 electrodes

Types of DNA target	$C_{DNA\ target}$ (μM)	**3D nanoporous nm-thick film**		**1D SnO_2 NWs**	
		ΔR decrease* (%)	I_f decrease* (%)	ΔR decrease* (%)	I_f decrease* (%)
1-base mismatch	2.0	58±5	81±3	72±5	88±5
2-base mismatch		71±5	89±3	80±5	94±5
non-complementary		91±2	99±2	94±3	-

(the decrease of the response signal is compared to that of complementary hybridization with the same DNA target concentration of 2 μM)*

REFERENCES

[1] J. D. Donaldson, W. Moser, and W. B. Simpson, "321. Basic tin(II) chloride", *Journal of the Chemical Society (Resumed),* pp. 1727-1731, 1963.

[2] H.-T. Fang, X. Sun, L.-H. Qian, D.-W. Wang, F. Li, Y. Chu, F.-P. Wang, and H.-M. Cheng, "Synthesis of Tin (II or IV) Oxide Coated Multiwall Carbon Nanotubes with Controlled Morphology", *The Journal of Physical Chemistry C,* vol. 112, pp. 5790-5794, 2008.

[3] D. Thierry, H. Ilie, D. P. Yesudas, V. Florence, and K. Philippe, "Electrochemical fabrication of Sn nanowires on titania nanotube guide layers", *Nanotechnology,* vol. 19, p. 205601, 2008.

[4] I. Hanzu, T. Djenizian, G. F. Ortiz, and P. Knauth, "Mechanistic Study of Sn Electrodeposition on TiO_2 Nanotube Layers: Thermodynamics, Kinetics, Nucleation, and Growth Modes", *The Journal of Physical Chemistry C,* vol. 113, pp. 20568-20575, 2009.

[5] A. Kolmakov, Y. Zhang, and M. Moskovits, "Topotactic Thermal Oxidation of Sn Nanowires: Intermediate Suboxides and Core−Shell Metastable Structures", *Nano Letters,* vol. 3, pp. 1125-1129, 2003.

[6] A. Zebda, "Propriétés microstructurales et électriques d'électrodes d'oxydes SnO_2 et $Cdln_2O_4$: application à la détection électrochimique directe de l'hybridation de l'ADN", Docteur, Grenoble INP, Grenoble, 2007.

CONCLUSIONS

We performed the cathodic electrodeposition of SnO_2 nanostructured films. By changing relevant deposition parameters, two kinds of nanostructures are obtained: **3D nanoporous films** and **1D nanowires**. Both nanostructured films have been characterized in terms of morphology, microstructure and electrochemical properties. Then they were successfully functionalized to study DNA hybridization signal by EIS and fluorescence measurements. In the following, we summarize the different results obtained.

The **3D nanoporous films** are deposited under a potentiostatic regime. The film thickness can be varied by either the deposition voltage or the passed charge density. On the one hand, by decreasing the deposition potential from -0.5 to -1.0 V (vs. Ag/AgCl) at a fixed deposition time (300 sec), micrometer thick films are obtained. Their thickness ranges from 2 to 4 μm. On the other hand, by increasing the charge density from 0.2 to 3.9 C/cm^2 at a fixed potential (-1.0 V), a wide range of film thicknesses can be obtained, ranging from 220 nm to 4.2 μm.

In this range of film thickness, the films are composed of numerous nanoparticles, the size of which is comprised between 5 to 15 nm. The pore size ranges from 10 nm to several hundred nm. However, from SEM observations, the nanometer thick films reveal denser and more compact nanoporous morphology than the micrometer thick films. Whatever the film thickness, the study of the XRD patterns reveals a poorly crystallized tetragonal SnO_2 phase. The chemical composition of the extreme surface deduced by XPS shows an oxygen depleted stochiometry. A decrease of the impedance, and more particularly of the calculated charge-transfer, is obtained when the film thickness increases in agreement with an increase in the surface area of the electrode accessible to the electrolyte.

For this whole range of nanoporous film thicknesses, DNA hybridization leads to a systematic **decrease of the calculated charge-transfer resistance**. The signal strongly depends on the film thickness up to a threshold value of about 1.0 μm, above which no significant variation is observed. The thinnest films (220 nm) provide the highest variation.

A strictly opposite tendency is found for fluorescence signal detection. Indeed, it increases with the film thickness and does not change significantly above 1 μm. 3D-constructed views obtained by confocal scanning laser fluorescence microscopy demonstrated that the target DNA molecules infiltrate within the film and successfully hybridized inside the nanoporous structure.

The comparison between the liquid and vapor phase processes for APTES grafting has been performed on the thinnest nanoporous SnO_2 films. It reveals that the vapor-phase method is more effective than the solution method in penetrating into the nanopores of the films. As a result, the

DNA sensors built on vapor-treated silane layers exhibit a higher sensitivity than those treated by liquid phase. The EIS detection limit is 10 nM of DNA target concentration. The obtained response signals from 1- and 2-base mismatch DNA hybridizations demonstrated the selectivity of the process.

To the best of our knowledge, this is the first time that **1D nanowire nanostructures** were fabricated by a template-free process. The latter is a two step deposition process which involves (i) the electrodeposition under a galvanostatic mode of Sn nanowires followed by (ii) a thermal oxidizing process. The resulting SnO_2 nanowires are found in a population of round and well-defined nanocrystallites. They exhibit a shape ratio ranging from 4 to 7. Their diameter ranges from 140 to 250 nm and their lengths from 500 to 850 nm. The study of their microstructure revealed a dense and monocrystalline structure with a strong <110> preferred orientation.

Contrary to the 3D nanoporous films, the DNA hybridization performed on these 1D nanostructures induces a systematic **increase of the charge-transfer resistance**, depending on the DNA target concentration. Importantly, from 3D view obtained by confocal scanning laser fluorescence microscopy, it is found that DNA molecules are mainly located along the SnO_2 NWs. Both the electrical and optical signals showed higher variations upon DNA hybridization than in the case of the thinnest nanoporous films. The EIS detection limit is 2 nM. Finally, similarly to the thinnest nanoporous SnO_2 films, the impedance and fluorescence measurements for 1- and 2-base mismatch hybridizations demonstrated the selectivity of the process.

From a more general point of view, this strongly experimental study emphasizes the importance of both the **microstructural and morphological organizations** of the sensing material on the impedimetric signal upon DNA hybridization. Indeed, following the dimensionality of the nanostructure, the EIS signal can be completely different and opposite in relation with either external or internal causes, as illustrated in the present work.

Indeed, similarly to the previous study of A. Zebda on polycrystalline and dense 2D SnO_2 surfaces, in the present case, the EIS response signal obtained from monocrystalline 1D nanowires shows an increase of the impedance. It is explained by an internal cause, namely, the field effect phenomenon. The addition of negatively charged DNA molecules upon hybridization leads to an increase of the space charge layer thickness at the nanowire surface. On the contrary, in the case of a quasi-amorphous 3D nanoporous matrix, the DNA hybridization leads to a decrease of the impedance. In this case, the field effect does not play any predominant role. This decrease is explained by an external cause: the penetration of hydrophilic and charged double-stranded DNA molecules within the nanoporous matrix volume. This enhances the transport of ionic species inside the electrode volume. As a result, the impedance of this complex interface is reduced.

Further studies should be conducted to investigate in more detail the exact influence of the sensing matrix morphology: pore and nanoparticle sizes as well as their density in the case of nanoporous morphology, density and shape ratio in the case of nanowire morphology… Besides, computational modeling and simulation of the local electric field involving the ion distribution as well as the DNA distribution within the different nanostructures would help to predict and understand the impedance behavior.

SnO_2 nanowires seem to be promising transduction elements for impedance signal upon DNA hybridization. Beyond the biosensor field, other kinds of sensors such as pH or gas sensors, or other application fields such as energy storage could benefit from such sensing materials. That is why it would be interesting to go further in the control of their fabrication using the successful process of template-free electrodeposition that we developed in this study. Indeed, the influence of fabrication parameters regarding the electrodeposition and annealing steps should be analyzed. It could open the way for further experiments to obtain a better control of their morphology and shape ratio, as well as their electrical properties by the introduction of doping elements.

ANNEXES

Annex 1: Nyquist plots of for the SnO_2 nanoporous films potentiostatically electrodeposited at -0.6, -0.7, -0.8 and -0.9V (vs. Ag/AgCl) for 5 min.

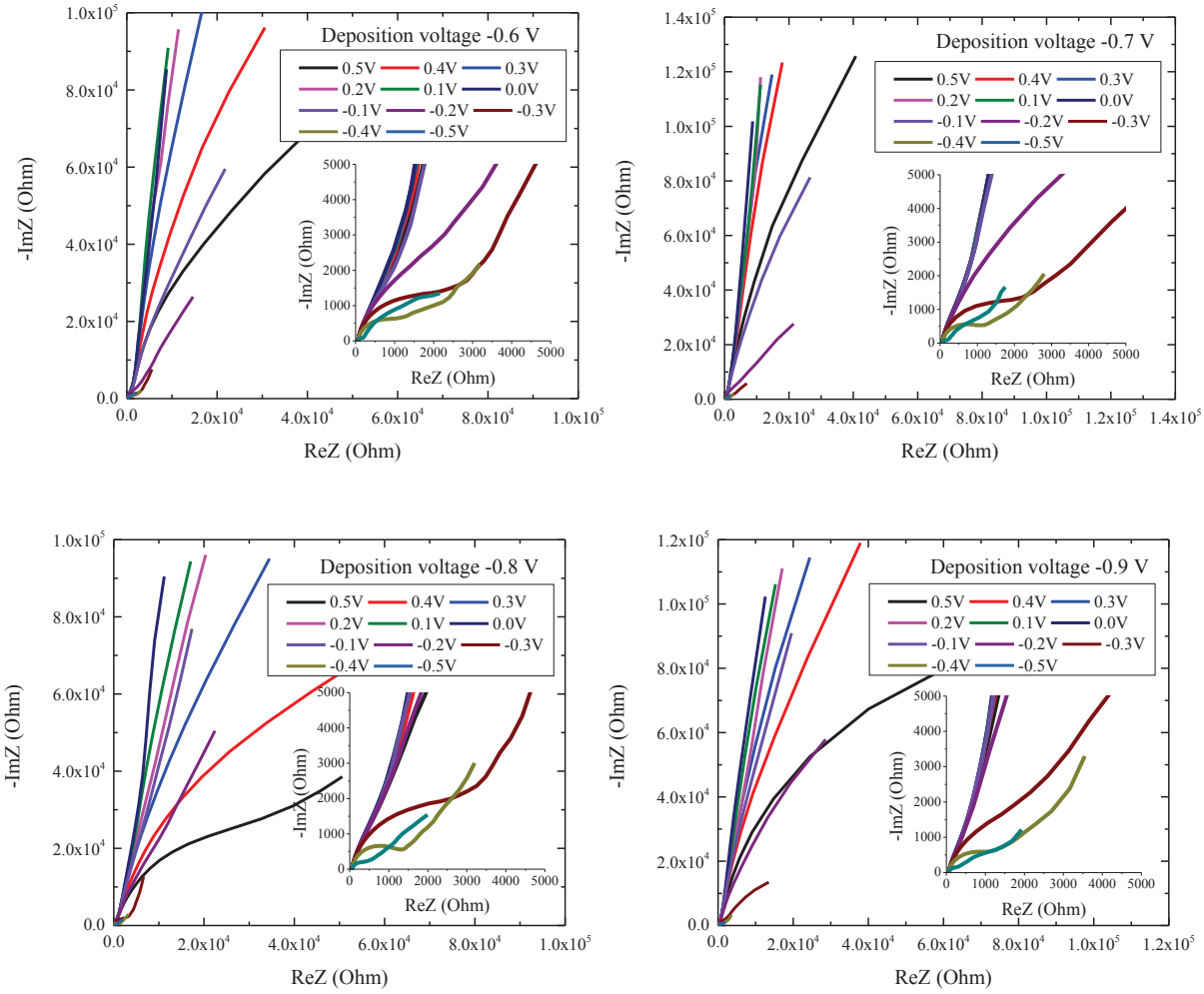

Nyquist plots for the SnO_2 nanoporous films potentiostatically electrodeposited at -0.6, -0.7, -0.8 and -0.9V (vs. Ag/AgCl) for 5 min. The impedance curves are recorded at potential ranging from -0.5 and 0.5 V (vs. ref).

Annex 2: Equivalent fitting parameters

A. Nanoporous films

A1. Micrometers thick-films: Influence of deposition potential

- At applied potential of -0.5 V (vs. ref)

Deposition potential	Thickness (μm)	Steps	R_e (Ω)	R_1 (Ω)	C_1 (μF)	α_1	R_2 (Ω)	C_2 (μF)	α_2
-0.5 V (vs. Ag/AgCl)	1.95	Bare film	-	-	-	-	-	-	-
		Silanization	-	-	-	-	-	-	-
		ss-DNA	67.8	2130	71.2	0.774	10927	133	1
		ds-DNA	70.2	2221	66.3	0.779	7388	156	1

Deposition potential	Thickness (μm)	Steps	R_e (Ω)	R_1 (Ω)	C_1 (μF)	α_1	R_2 (Ω)	C_2 (μF)	α_2
-0.6 V (vs. Ag/AgCl)	2.68	Bare film	67.1	169.4	15.8	0.930	3143	244	0.755
		Silanization	60.4	156.2	13.1	1	9571	189	0.759
		ss-DNA	66.5	102.4	21.7	0.877	7712	208	0.763
		ds-DNA	68.4	109.2	6.5	0.995	4257	361	0.802

Deposition potential	Thickness (μm)	Steps	R_e (Ω)	R_1 (Ω)	C_1 (μF)	α_1	R_2 (Ω)	C_2 (μF)	α_2
-0.7 V (vs. Ag/AgCl)	2.91	Bare film	62.8	197.9	16.81	0.886	2692	296	0.790
		Silanization	76.1	140.0	60.6	0.737	10254	140	0.750
		ss-DNA	67.3	637.1	19.5	0.874	7242	133	0.723
		ds-DNA	65.8	699.2	18.1	0.886	4482	202	0.798

Deposition potential	Thickness (μm)	Steps	R_e (Ω)	R_1 (Ω)	C_1 (μF)	α_1	R_2 (Ω)	C_2 (μF)	α_2
-0.8 V (vs. Ag/AgCl)	3.95	Bare film	69.8	488.3	29.5	0.866	13837	243	0.631
		Silanization	60.1	330.6	92.3	0.765	24569	137	0.779
		ss-DNA	71.3	248.7	31.5	0.816	7908	199	0.780
		ds-DNA	74.1	337.2	26.0	0.787	3729	258	0.833

Deposition potential	Thickness (μm)	Steps	R_e (Ω)	R_1 (Ω)	C_1 (μF)	α_1	R_2 (Ω)	C_2 (μF)	α_2
-0.9 V (vs. Ag/AgCl)	4.22	Bare film	68.6	180.2	19.5	0.960	2070	290	0.741
		Silanization	76.8	679.1	26.8	0.890	16972	86.7	0.703
		ss-DNA	65.1	1509	21.5	0.950	11156	90.2	0.753
		ds-DNA	67.3	1648	19.9	0.830	8794	116	0.887

Deposition potential	Thickness (μm)	Steps	R_e (Ω)	R_1 (Ω)	C_1 (μF)	α_1	R_2 (Ω)	C_2 (μF)	α_2
-1.0 V (vs. Ag/AgCl)	4.07	Bare film	62.8	120.5	21.7	0.894	2955	359	0.758
		Silanization	67.4	139.7	44.5	0.791	10946	107	0.792
		ss-DNA	66.6	79.39	28.8	0.996	8821	227	0.739
		ds-DNA	61.3	101.7	13.7	0.838	5027	240	0.794

- At applied potential of -0.4 V (vs. ref)

Deposition potential	Thickness (μm)	Steps	R_e (Ω)	R_1 (Ω)	C_1 (μF)	α_1	R_2 (Ω)	C_2 (μF)	α_2
-0.5 V (vs. Ag/AgCl)	1.95	Bare film	-	-	-	-	-	-	-
		Silanization	-	-	-	-	-	-	-
		ss-DNA	68.0	6913	62.4	0.728	53656	57.5	1
		ds-DNA	71.3	5330	46.5	0.737	43789	74.5	0.917

Deposition potential	Thickness (μm)	Steps	R_e (Ω)	R_1 (Ω)	C_1 (μF)	α_1	R_2 (Ω)	C_2 (μF)	α_2
-0.6 V (vs. Ag/AgCl)	2.68	Bare film	67.1	1283	10.1	0.949	-	-	-
		Silanization	60.6	1924	84.9	0.831	34606	53.6	0.875
		ss-DNA	66.6	2005	72.8	0.875	19771	62.9	0.838
		ds-DNA	68.5	2694	60.0	0.653	13057	89.2	0.904

Deposition potential	Thickness (μm)	Steps	R_e (Ω)	R_1 (Ω)	C_1 (μF)	α_1	R_2 (Ω)	C_2 (μF)	α_2
-0.7 V (vs. Ag/AgCl)	2.91	Bare film	62.8	1260	10.4	0.931	-	-	-
		Silanization	76.2	7757	10.1	0.774	33019	69.5	0.987
		ss-DNA	69.2	9632	31.4	0.790	25147	56.0	0.889
		ds-DNA	67.1	10402	29.3	0.758	19541	54.7	0.943

Deposition potential	Thickness (μm)	Steps	R_e (Ω)	R_1 (Ω)	C_1 (μF)	α_1	R_2 (Ω)	C_2 (μF)	α_2
-0.8 V (vs. Ag/AgCl)	3.95	Bare film	67.6	1473	10.0	0.933	-	-	-
		Silanization	60.2	2760	68.1	0.795	81318	30.3	0.853
		ss-DNA	71.3	4629	33.6	0.799	32585	47.1	0.852
		ds-DNA	74.1	5408	24.7	0.820	14696	62.9	0.906

Deposition potential	Thickness (μm)	Steps	R_e (Ω)	R_1 (Ω)	C_1 (μF)	α_1	R_2 (Ω)	C_2 (μF)	α_2
-0.9 V (vs. Ag/AgCl)	4.22	Bare film	68.7	1320	12.1	0.917	-	-	-
		Silanization	76.9	2981	57.2	0.810	53469	42.6	0.881
		ss-DNA	65.2	7085	43.8	0.728	43352	59.8	1
		ds-DNA	67.3	9076	33.4	0.780	40929	57.4	1

Deposition potential	Thickness (μm)	Steps	R_e (Ω)	R_1 (Ω)	C_1 (μF)	α_1	R_2 (Ω)	C_2 (μF)	α_2
-1.0 V (vs. Ag/AgCl)	4.07	Bare film	62.7	1194	12.7	0.909	-	-	-
		Silanization	67.4	1338	30.3	0.832	51917	60.1	0.887
		ss-DNA	66.7	1049	39.6	1	41013	57.1	0.763
		ds-DNA	61.3	2201	16.3	0.742	16620	67.1	0.933

A2. From nanometer to micrometer-thick films: Influence of passed charge density

- Complementary hybridization

Passed charge density (C/cm^2)	Thickness (μm)	Steps	R_e (Ω)	R_1 (Ω)	C_1 (μF)	α_1
0.2	220±20	Bare film	64.6	84782	23.4	0.779
		Silanization	70.6	146577	23.1	0.778
		ss-DNA	68.9	51974	20.6	0.904
		ds-DNA	68.4	24743	26.5	0.878

Passed charge density (C/cm^2)	Thickness (μm)	Steps	R_e (Ω)	R_1 (Ω)	C_1 (μF)	α_1
0.4	380±20	Bare film	70.4	66496	26.3	0.772
		Silanization	69.8	115162	24.5	0.858
		ss-DNA	64.3	95137	28.9	0.838
		ds-DNA	67.6	43301	32.3	0.878

Passed charge density (C/cm^2)	Thickness (μm)	Steps	R_e (Ω)	R_1 (Ω)	C_1 (μF)	α_1
0.8	940±40	Bare film	73.9	21276	38.15	0.829
		Silanization	66.4	41176	38.46	0.840
		ss-DNA	63.7	23047	43.76	0.854
		ds-DNA	68.1	15413	45.15	0.848

Passed charge density (C/cm^2)	Thickness (μm)	Steps	R_e (Ω)	R_1 (Ω)	C_1 (μF)	α_1	R_2 (Ω)	C_2 (μF)	α_2
3.9	4210±300	Bare film	76.4	230.9	107.3	1	4025	539	0.620
		Silanization	-	-	-	-	-	-	-
		ss-DNA	72.8	-	-	-	7381	233	0.869
		ds-DNA	70.0	-	-	-	4816	248	0.868

- Non-complementary hybridization

Passed charge density (C/cm^2)	Thickness (μm)	Steps	R_e (Ω)	R_1 (Ω)	C_1 (μF)	α_1
0.2	220±20	Bare film	74.0	87250	16.8	0.919
		Silanization	71.6	136078	23.0	0.784
		ss-DNA	68.9	45541	20.6	0.912
		ds-DNA	64.6	42543	18.3	0.899

Passed charge density (C/cm^2)	Thickness (μm)	Steps	R_e (Ω)	R_1 (Ω)	C_1 (μF)	α_1
0.4	380±20	Bare film	73.9	67596	26.5	0.737
		Silanization	59.69	127038	24.5	0.831
		ss-DNA	69.1	101959	29.5	0.804
		ds-DNA	65.9	95300	28.4	0.871

Passed charge density (C/cm^2)	Thickness (μm)	Steps	R_e (Ω)	R_1 (Ω)	C_1 (μF)	α_1
0.8	940±40	Bare film	70.5	20486	10.5	0.775
		Silanization	65.7	56258	35.5	0.841
		ss-DNA	69.3	28471	37.0	0.867
		ds-DNA	75.9	26605	36.5	0.879

Passed charge density (C/cm^2)	Thickness (μm)	Steps	R_e (Ω)	R_1 (Ω)	C_1 (μF)	α_1	R_2 (Ω)	C_2 (μF)	α_2
3.9	4210±300	Bare film	79.6	552	528	0.796	5464	923	0.749
		Silanization	66.5	-	-	-	25377	133	0.849
		ss-DNA	65.8	-	-	-	7665	277	0.798
		ds-DNA	70.3	-	-	-	7910	101	0.815

A3. Nanometer-thick films: Influence of deposition potential

- Complementary hybridization

Deposition potential (vs. Ag/AgCl)	Thickness (μm)	Steps	R_e (Ω)	R_1 (Ω)	C_1 (μF)	α_1
-0.5 V	No	Bare film	70.4	53382	24.8	0.769
		Silanization	65.0	70784	24.8	0.792
		ss-DNA	66.9	39875	21.4	0.820
		ds-DNA	67.0	25125	24.2	0.865

Deposition potential (vs. Ag/AgCl)	Thickness (μm)	Steps	R_e (Ω)	R_1 (Ω)	C_1 (μF)	α_1
-0.6 V	240±20	Bare film	70.0	29489	20.1	0.765
		Silanization	68.9	78336	19.6	0.899
		ss-DNA	71.2	32788	29.2	0.900
		ds-DNA	67.9	16411	29.5	0.894

Deposition potential (vs. Ag/AgCl)	Thickness (μm)	Steps	R_e (Ω)	R_1 (Ω)	C_1 (μF)	α_1
-0.8 V	270±20	Bare film	61.7	37204	29.7	0.808
		Silanization	71.3	93694	21.4	0.863
		ss-DNA	74.0	49564	25.9	0.851
		ds-DNA	69.5	29737	26.7	0.845

- Non-complementary hybridization

Deposition potential (vs. Ag/AgCl)	Thickness (μm)	Steps	R_e (Ω)	R_1 (Ω)	C_1 (μF)	α_1
-0.5 V	No	Bare film	66.7	57640	28.1	0.754
		Silanization	68.3	72576	19.3	0.817
		ss-DNA	66.1	41534	24.2	0.819
		ds-DNA	68.2	40163	23.4	0.845

A4. Sensitivity

- Liquid phase deposition

Thickness (μm)	C_{target} (μM)	Steps	R_e (Ω)	R_1 (Ω)	C_1 (μF)	α_1
220±20	1.0	Bare film	64.6	97419	23.7	0.762
		Silanization	66.3	144626	20.1	0.916
		ss-DNA	68.7	47492	20.7	0.893
		ds-DNA	64.0	34015	24.8	0.886

Thickness (μm)	C_{target} (μM)	Steps	R_e (Ω)	R_1 (Ω)	C_1 (μF)	α_1
220±20	0.5	Bare film	63.8	97926	22.8	0.800
		Silanization	66.5	151935	22.3	0.869
		ss-DNA	69.0	45305	20.6	0.911
		ds-DNA	68.4	37707	23.0	0.911

Thickness (μm)	C_{target} (μM)	Steps	R_e (Ω)	R_1 (Ω)	C_1 (μF)	α_1
220±20	0.1	Bare film	66.7	95509	21.7	0.818
		Silanization	66.9	135238	18.0	0.932
		ss-DNA	64.4	43923	20.4	0.901
		ds-DNA	66.2	41441	20.5	0.903

- Vapor phase deposition

Thickness (μm)	C_{target} (μM)	Steps	R_e (Ω)	R_1 (Ω)	C_1 (μF)	α_1
220±20	2.0	Bare film	78.5	96782	19.3	0.825
		Silanization	69.9	432768	16.6	0.945
		ss-DNA	60.7	95137	17.6	0.946
		ds-DNA	59.8	43301	19.5	0.941

Thickness (μm)	C_{target} (μM)	Steps	R_e (Ω)	R_1 (Ω)	C_1 (μF)	α_1
220±20	1.0	Bare film	79.2	76453	19.1	0.824
		Silanization	75.0	370740	14.7	0.930
		ss-DNA	74.6	147929	16.3	0.992
		ds-DNA	73.8	76689	17.4	0.939

Thickness (μm)	C_{target} (μM)	Steps	R_e (Ω)	R_1 (Ω)	C_1 (μF)	α_1
220±20	0.5	Bare film	79.3	75310	19.4	0.811
		Silanization	75.4	377590	14.6	0.929
		ss-DNA	73.0	143687	13.9	0.944
		ds-DNA	72.3	97006	16.7	0.945

Thickness (μm)	C_{target} (μM)	Steps	R_e (Ω)	R_1 (Ω)	C_1 (μF)	α_1
220±20	0.1	Bare film	79.2	81101	19.5	0.816
		Silanization	71.7	416567	15.7	0.910
		ss-DNA	61.9	121467	12.7	0.939
		ds-DNA	62.0	99531	13.9	0.941

Thickness (μm)	C_{target} (μM)	Steps	R_e (Ω)	R_1 (Ω)	C_1 (μF)	α_1
220±20	0.01	Bare film	80.8	79987	18.8	0.816
		Silanization	74.9	393879	14.9	0.929
		ss-DNA	74.1	126847	16.5	0.945
		ds-DNA	75.2	111929	16.8	0.948

A5. Selectivity

Thickness (μm)	Type of DNA target	C_{target} (μM)	Steps	R_e (Ω)	R_1 (Ω)	C_1 (μF)	α_1
220±20	1-base mismatch	2	Bare film	79.0	95298	22.1	0.829
			Silanization	74.9	330742	14.9	0.932
			ss-DNA	62.2	115084	14.2	0.944
			ds-DNA	64.3	97006	18.9	0.938

Thickness (μm)	Type of DNA target	C_{target} (μM)	Steps	R_e (Ω)	R_1 (Ω)	C_1 (μF)	α_1
220±20	2-base mismatch	2	Bare film	77.4	109335	22.5	0.791
			Silanization	74.9	347531	14.9	0.929
			ss-DNA	74.6	86879	14.1	0.821
			ds-DNA	72.9	61963	25.0	0.877

A6. Reusability

Thickness (μm)	C_{target} (μM)	Steps	R_e (Ω)	R_1 (Ω)	C_1 (μF)	α_1
220±20	2.0	ss-DNA	77.6	113123	19.3	0.825
		1st ds-DNA	79.2	446752	16.6	0.945
		1st denaturation	68.6	141271	16.4	0.961
		2st ds-DNA	67.6	62274	18.0	0.926
		2st denaturation	68.4	84119	18.3	0.915
		3rd ds-DNA	66.4	61901	18.2	0.947

B. Nanowires

B1. Sensitivity

C_{target} (μM)	Steps	R_e (Ω)	R_1 (Ω)	C_1 (μF)	α_1	R_2 (Ω)	C_2 (μF)	α_2
2.0	Bare film	98.5	1807	32.0	0.933	32894	64.9	0.898
	Silanization	99.2	1435	32.7	0.912	38245	65.3	0.915
	ss-DNA	97.8	1752	31.8	0.990	12564	64.5	0.938
	ds-DNA	97.5	1814	33.5	0.954	24843	51.7	0.915

C_{target} (μM)	Steps	R_e (Ω)	R_1 (Ω)	C_1 (μF)	α_1	R_2 (Ω)	C_2 (μF)	α_2
1.0	Bare film	98.0	3287	36.5	0.872	37151	57.5	0.908
	Silanization	107.1	1663	32.0	0.946	42111	66.9	0.880
	ss-DNA	96.8	2101	32.4	0.955	12431	74.0	0.919
	ds-DNA	97.5	2083	33.1	0.954	22022	61.2	0.904

C_{target} (μM)	Steps	R_e (Ω)	R_1 (Ω)	C_1 (μF)	α_1	R_2 (Ω)	C_2 (μF)	α_2
0.5	Bare film	99.0	1898	31.2	0.927	34259	60.3	0.912
	Silanization	106.8	1444	32.0	0.933	38924	64.9	0.898
	ss-DNA	98.4	1955	33.1	0.952	12588	87.1	0.894
	ds-DNA	97.5	2160	33.5	0.960	17796	63.9	0.905

C_{target} (μM)	Steps	R_e (Ω)	R_1 (Ω)	C_1 (μF)	α_1	R_2 (Ω)	C_2 (μF)	α_2
0.1	Bare film	98.2	2981	33.5	0.888	32706	58.4	0.912
	Silanization	106.7	1657	31.8	0.946	39994	64.6	0.882
	ss-DNA	97.1	1994	32.1	0.969	13605	83.1	0.878
	ds-DNA	90.7	1907	33.2	0.968	17955	69.1	0.891

C_{target} (μM)	Steps	R_e (Ω)	R_1 (Ω)	C_1 (μF)	α_1	R_2 (Ω)	C_2 (μF)	α_2
0.01	Bare film	98.6	2704	31.0	0.906	31324	58.9	0.912
	Silanization	106.7	1636	31.5	0.949	40507	63.0	0.881
	ss-DNA	96.6	2183	32.8	0.961	10748	88.3	0.894
	ds-DNA	91.2	2068	27.1	0.959	10758	69.2	0.952

C_{target} (μM)	Steps	R_e (Ω)	R_1 (Ω)	C_1 (μF)	α_1	R_2 (Ω)	C_2 (μF)	α_2
0.002	ss-DNA	97.8	807.3	55.0	1	13479	54.0	0.850
	ds-DNA	95.6	793.6	59.1	1	14124	50.3	0.841

B2. Selectivity

Type of DNA target	C_{target} (μM)	Steps	R_e (Ω)	R_1 (Ω)	C_1 (μF)	α_1	R_2 (Ω)	C_2 (μF)	α_2
Non-complementary	0.002	ss-DNA	91.02	3301	30.4	0.933	10967	85.8	0.922
		ds-DNA	91.24	3314	31.0	0.948	11733	73.6	0.932

Type of DNA target	C_{target} (μM)	Steps	R_e (Ω)	R_1 (Ω)	C_1 (μF)	α_1	R_2 (Ω)	C_2 (μF)	α_2
1- base mismatch	0.002	ss-DNA	90.89	3253	31.6	0.956	13564	75.3	0.891
		ds-DNA	90.81	3353	33.4	0.949	17345	64.5	0.902

Type of DNA target	C_{target} (μM)	Steps	R_e (Ω)	R_1 (Ω)	C_1 (μF)	α_1	R_2 (Ω)	C_2 (μF)	α_2
2- base mismatch	0.002	ss-DNA	97.08	2515	35.4	1	14494	81.0	0.821
		ds-DNA	90.65	2679	38.6	0.932	16977	51.4	0.921